LBNL-57514

Controlled Electron Injection into Plasma Accelerators and Space Charge Estimates*

Gwenaël J. Fubiani

L'OASIS Laboratory
Accelerator and Fusion Research Division
Lawrence Berkeley National Laboratory
University of California
Berkeley, California 94720

Ph.D. Thesis

September 2005

* This work was supported by the Director, Office of Science, High Energy Physics, U.S. Department of Energy under Contract No. DE-AC02-05CH11231.

To Irma, my mother, my grand-father Emile and the rest of my family.

Abstract

Controlled Electron Injection into Plasma Accelerators and Space Charge Estimates

by

Gwenaël G. J. Fubiani

Doctor of Philosophy in Physics

Lawrence Orlando Berkeley National Laboratory

Doctor Wim P. Leemans, Chair

Plasma based accelerators are capable of producing electron sources which are ultra-compact (a few microns) and high energies (up to hundreds of MeVs) in much shorter distances than conventional accelerators. This is due to the large longitudinal electric field that can be excited without the limitation of breakdown as in RF structures. The characteristic scalelength of the accelerating field is the plasma wavelength and for typical densities ranging from $10^{18} - 10^{19}$ cm^{-3}, the accelerating fields and scalelength can hence be on the order of $10 - 100$ GV/m and $10 - 40$ μm, respectively. The production of quasi monoenergetic beams was recently obtained in a regime relying on self-trapping of background plasma electrons, using a single laser pulse for wakefield generation. In this dissertation, we study the controlled injection via the beating of two lasers (the pump laser pulse creating the plasma wave and a second beam being propagated in opposite direction) which induce a localized injection of background plasma electrons. The aim of this dissertation is to describe in detail the physics of optical injection using two lasers, the characteristics of the electron beams produced (the micrometer scale plasma wavelength can result in femtosecond and

even attosecond bunches) as well as a concise estimate of the effects of space charge on the dynamics of an ultra-dense electron bunch with a large energy spread.

Acknowledgements

There are many people that I wish to thank for valuable help they gave me during the course of my PhD. It was overall a great experience for me, I learned a lot in many areas and this work confirmed my deep passion for science in general.

My great thanks to my adviser Wim Leemans. He gave me such a great opportunity by inviting me to come to l'OASIS group as a PhD student. He was always present for both the good and doubtful times when the results were not (yet) the ones I was hoping for. He made me work on a few complementary topics which allowed me to get great insight on the field of laser plasma physics as a whole. I am especially grateful to him for this because it will clearly help me tremendously during my carrier as a physicist.

I wish to thank Eric Esarey, Carl Schroeder and Brad Shadwick for the long discussions and great help they provided me with. Without them, my theoretical understanding would not have been as deep. I wish to thank Eric in particular for proposing the new idea, among others, of optical beam injection combined with a density gradient, which inspired the work of Chapter 4 and also for helping me to study the physics of space charge.

I wish to thank Gerald Dugan for his tremendous help on the topic of space charge. We shared many useful discussions on the topic and spent a long time together deriving the basic set of equations for the shell method [Chapter 5, Section 5.3 and Appendix H] and the envelope equation for beams with cylindrical shape [Chapter 5, Section 5.5.2 and Appendix K]. It was a wonderful experience working with him.

I owe my appreciation to Drs. François Amiranoff, Jean-Louis Bobin, Guy

Bonnaud, Joël LeDuff, Patrick Mora, Vladimir Tikhonchuck for taking the time to be on my committee and also Drs. Guy Bonnaud and Patrick Mora for reading this dissertation.

In addition, I would like to thank Dr. Joël LeDuff for making me aware of the possibility to pursue a PhD in l'OASIS group. It was such a great opportunity.

I wish to express my gratitude to Irmita for all her encouragement during my PhD.

I am indebted to my family (especially my mom) and friends (Jeroen, Aarash, Richard, Nicolas, Thomas, Sylvain, Florent, Manoel, Sebastien, John, ...) for all the support they have provided me with and for everything they have done for me.

Lastly, many thanks to all the members of l'OASIS group that I didn't mention directly. It was an amazing experience working with you all. I will sincerely always remember the great time spent during my stay in Berkeley.

GWENAEL FUBIANI

Lawrence Berkeley National Laboratory,
Berkeley, july 2005

Table of Contents

Chapter 1

Introduction

Contents

1.1 Laser applications

The laser (acronym of **l**ight **a**mplification by **s**timulated **e**mission of **r**adiation) was first demonstrated in the 1960s [1]. They are devices that generate or amplify electromagnetic radiation, ranging from the long infrared region up through the visible region and extending to the ultraviolet and recently even to the X-ray region. The invention of the laser was the beginning of a very important scientific revolution. The sharply focusable beams of coherent light are suitable for a wide variety of applications. Lasers have been used in industry for cutting and boring metals and other materials, and for inspecting optical equipment. In medicine, they have been used in surgical operations.

Lasers have been used in many areas of scientific research. In inertial confinement fusion [2, 3] for instance, small hollow spherical capsules are filled at high pressure with an equal mixture of deuterium and tritium, and then chilled to cryogenic temperatures, so that the D-T gas freezes as a thin, solid coating on the inside of the capsule wall. Suspended by a thin plastic film at the center of a metal cavity called a hohlraum, these spherical capsules can be injected into the center of a target chamber. There, in a few billionths of a second, lasers can be used to heat the interior of the hohlraum cavity to temperatures several hundred times the temperature of the sun, vaporizing the surface of the plastic shell into an extremely high pressure plasma. Alternatively, direct-drive targets have no hohlraum, and lasers heat the capsule surface directly.

The capsule, transformed into vaporized plasma, reaches pressures of hundreds of millions of atmospheres. As the plasma expands outward like rocket exhaust, it accelerates the thin layer of D-T radially inward, to velocities of 300 to 400 kilometers per second. The residual D-T gas from the center of the capsule, heated by the denser D-T that surrounds and compresses it, reaches peak temperatures over 100 million degrees Celsius, sufficient to ignite a propagating fusion reaction. Just as a match can light firewood, this hot spot ignites a fusion burn wave that propagates out into the denser D-T. By releasing seventy or more times the energy originally needed to compress and heat the fuel, this dynamic process provides the basis for generating inertial fusion energy.

Lasers also opened the field of nonlinear optics, which is concerned with the study,

among others, of such phenomena as the frequency doubling of coherent light by certain crystals [4], X-ray production, harmonic generation or THz radiation in plasmas ([5–8] and references therein).

Laser-Plasma interactions are also extensively studied in the field of accelerator physics. Testing of new theories in high-energy physics (to find super-symmetric particles as a mean of testing string theory, the Higgs boson, etc.) requires the development of particle accelerators capable of producing particle beams with multi-TeV energies. In conventional accelerators based on radio-frequency technology, the size of the accelerating field is limited by breakdown of the structure media. Breakdown occurs when the electric field is sufficiently large to allow (secondary) emission of electrons from the walls of the accelerator cavity. These cavities typically are limited to accelerating fields around 100 MV/m. This limit on the maximum electric field means that studies of fundamental particle physics requires facilities 10s of Km in scale. A technology capable of higher gradients will hence be required in order to prevent machines from becoming excessively large. High gradients would also open new applications for moderate energy accelerators in medicine, material science, and other fields by rendering such machines of laboratory scale. Plasma-Based accelerators are not limited by electrical breakdown and therefore are a promising canditate for the next generation of compact high energy electron source. The use of plasma as an accelerating medium has been investigated for more than two decades ([9–11] and references therein) and significant progress has been made.

The basic idea behind plasma-based accelerators is to excite a longitudinal wave in a plasma with phase velocity near the speed of light. Injected charge particles can then gain energy from the large longitudinal electric field of the plasma wave. The availability of intense radiation sources allows one to consider the excitation of plasma waves by a laser pulse. The plasma can act as a transformer, generating a large longitudinal electric field for acceleration from the large transverse field of a laser pulse [10]. The production of a high gradient longitudinal (accelerating) electric field requires the use of high intensity short pulse lasers [12]. Furthermore, applications benefit greatly from such lasers which are operating at high repetition rate.

1.2 The chirped pulse amplification method

State of the art short pulse lasers can be as short as a few femtoseconds (1 fs = 10^{-15} s) or high power (about a petawatt, i.e., 10^{15} W). Note that a terawatt (10^{12} W) laser can be a tabletop system and available also to small laboratories. By focusing these lasers, intensities up to 10^{22} W/cm^2 [13] were attained.

The first constrain on the femtosecond laser medium is the requirement of a large bandwidth $\Delta\nu$, where $\nu = \omega/(2\pi)$. Since $\Delta\nu\ \tau \simeq 1$ (the uncertainty principle), where τ is the laser duration, one requires a laser wavelength bandwidth of $\Delta\lambda \simeq 42$ nm for a laser with carrier wavelength $\lambda_0 = 0.8\ \mu$m to have a pulse duration $\tau \simeq 50$ fs [$\tau \simeq \lambda_0^2/(c\Delta\lambda)$]. Since the temporal and spectral behavior of the electromagnetic fields are related through the Fourier transform, the laser bandwidth $\Delta\nu$ and the laser duration τ are related by,

$$\Delta\nu\ \tau \geq K\ . \tag{1.1}$$

The inequality in (1.1) is known as "Fourier limited" and is satisfied for pulses without frequency modulation (such as chirping). $K = 2\ln 2/\pi$ for a Gaussian pulse of the form,

$$E_{\rm env}(t) = E_0 \exp[-(2\ln 2)t^2/\tau^2]\ . \tag{1.2}$$

One of the most practical media for a very short laser pulse is the Ti-sapphire crystal. The spectral emission bandwidth of this crystal is very broad with a maximum at about 800 nm. The dramatic increase in power of the femtosecond laser pulses became possible after the introduction of the *chirped pulse amplification* (CPA) technique by Strickland & Mourou [14] applied to laser technology (developed more than 40 years ago for radar devices). In chirped pulse the frequency of the electromagnetic wave varies with time. The time-dependence of the laser electric field E can be described by

$$E(t) = \frac{1}{2}\left(E_{\rm env}(t)\exp[i\phi(t)]\exp(i\omega_0 t) + \text{c.c}\right)\ , \tag{1.3}$$

where "c.c" is the complex conjugate, ω_0 is the laser carrier frequency and $\phi(t)$ is the time-dependent phase so that the time-dependent laser frequency ω is,

$$\omega(t) = \omega_0 + \frac{d\phi(t)}{dt} \equiv \omega_0 + f(t)\ , \tag{1.4}$$

If $f(t) \neq$ constant, then the laser pulse is *frequency modulated*, or *chirped*. For example, consider a Gaussian pulse with a linear chirp, i.e., $f(t) = at$, then the laser electric field is given by

$$E(t) \propto E_0 \exp[-(2\ln 2)\,(1+ia)\,t^2/\tau^2]\,, \tag{1.5}$$

and the product of τ with the bandwidth is

$$\Delta\nu\ \tau = \frac{2\ln 2}{\pi}\sqrt{1+a^2}\,. \tag{1.6}$$

Without chirp ($a = 0$), the bandwidth times the pulse duration is equal to the Fourier limited value $2\ln 2/\pi = 0.44$, while with chirping this value is increased by a factor $\sqrt{1+a^2}$.

In the CPA scheme, the output femtosecond laser pulse from the oscillator is first stretched in time (chirped in frequency), then amplified and finally re-compressed. The stretching and compression are obtained by using a pair of gratings (prism). The grating pairs can be arranged to separate the output pulse spectrum in such a way that the different wavelengths follow different paths through the optical system. This enables pulse compression by using the reverse procedure. The sub-nanojoule output from the oscillator is stretched in time by a factor of $\sim 10^4$, and then the pulse energy is amplified by a factor $\sim 10^6$ in a smaller system and up to 10^{10} in the larger systems. After the amplification process, the laser pulse is re-compressed to nearly its initial value. In this way one can achieve a tabletop system with peak power > 1 TW. The pulse duration is increased in order to avoid damage to the crystal and to the optics, and to avoid nonlinear distortions to the spatial and temporal beam profile. CPA method combined with a high density ($\sim 10^{19}$ cm^{-3}) gas (plasma) has made it possible to study high energy electron production on a tabletop.

Next, an overview of basic-plasma-based accelerator concepts is presented. The mechanisms for plasma wave generation are reviewed, and the limitations of such accelerators is discussed. This will provide motivation for the subsequent chapters and the theoretical work presented in this dissertation.

1.3 Overview of plasma-based accelerator concepts

The laser-wakefield-accelerator (LWFA) method*, first proposed by Tajima and Dawson in 1979 [15], uses a single intense ($\gtrsim 10^{18}$ W/cm^2) short (on the order of a plasma period, i.e., $\lesssim 1$ ps) laser pulse which travels through an underdense plasma ($\omega_p/\omega_0 \ll 1$, where ω_p is the plasma frequency and ω_0 the laser frequency). The ponderomotive force (radiation pressure) associated with the laser pulse envelope expels electrons from the region of the laser pulse. If the laser pulse length is of order the plasma wavelength, the ponderomotive force of the laser will excite a near resonant, large amplitude plasma wave with phase velocity v_ϕ approximately equal to the group velocity of the laser pulse $v_g \simeq c\sqrt{1-\omega_p^2/\omega_0^2}$, which is near the speed of light for an underdense plasma [10]. For intensities $> 5 \times 10^{18}$ W/cm^2, laser pulse evolution through the interaction with the nonlinear plasma index of refraction may result in self-injection of background plasma electrons into the plasma wave [16, 17], leading to high energy beam production. This method of injection relies on a laser-plasma instability which greatly reduce the accelerator shot-to-shot reproducibility. Other methods of injection may be preferred relying on a multi-laser pulse process with intensities typically $< 10^{18}$ W/cm^2, the colliding pulse injection scheme (CPI) [18–22] which will be discussed extensively throughout this dissertation.

The self-modulated laser-wakefield-accelerator (SM-LWFA) also relies on a laser-plasma instability to excite plasma waves. The SM-LWFA uses a high-intensity laser pulse propagating though a high-density plasma such that the laser pulse length is long compared to the plasma wavelength. The laser power is typically somewhat larger than the critical power for relativistic self-focusing $P > P_{\rm crit} \simeq 17(\omega_0/\omega_p)^2$ GW such that the laser can modify the index of refraction of the plasma to overcome diffraction [9]. In this high-density plasma regime, the laser pulse undergoes a self-modulation instability which causes the pulse to become axially modulated at the plasma period. The modulated laser pulse produces a large amplitude resonantly-driven plasma wave [10]. The trapping and acceleration of electrons from the background plasma has been demonstrated experimentally in the SM-LWFA experiments at several laboratories [8, 16, 23–31] observing energies up to 200 MeV. Accelerating gradients as large as 100 GV/m have been produced. It was found that the number of electrons versus

*for a review on plasma based accelerators see Esarey *et al.* [9]

Table 1.1: Parameters of the SM-LWFA experiments reported worldwide.

Group	λ_0 (μm)	a_0	τ (fs)	n_0 ($\times 10^{19}$ cm^{-3})	Q (nC)	T_e (MeV)
MPQ	0.8	1.35	200	20	3.2	3.3
LBNL	0.8	2.6	~ 50	$1.5-3$	≤ 10	$3.3-4.6$
LOA	0.82	1.2	30	2.5	5	18
U-Tokyo	0.79	2.1	50	$0.7-3$	/	10
NRL	1.054	2.36	400	1.4	/	<30 MeV el.
Rutherford	1.054	2	800	1.5	/	<50 MeV el.
Michigan	1.053	1.78	400	$1.4-2.9$	/	/

energy produced in those single-beam experiments fits either a single or a double exponential decay law $dN/dE \propto \exp(-E/T_e)$, where T_e is the electron temperature. Table 1.1 summarizes the setup and the experimental results reported by different groups worldwide, where Q is the total accelerated electron beam charge, n_0 the plasma density, T_e the electron temperature, τ the laser pulse duration and a_0 the normalized laser vector potential with $a_0 \simeq 8.6 \times 10^{-10}\lambda_0[\mu\text{m}]I_0^{1/2}[\text{W/cm}^2]$ and I_0 is the pulse intensity. Most of those experiments had an acceleration length (i.e., after self-injection of background plasma electrons into the plasma wave) greater than the dephasing length, which is the typical distance a trapped electron will take to overcome the accelerating region of the plasma wave. This led to phase mixing inside the electron bunch; in other words, structures from within are smoothed out. However recent experiments having acceleration lengths matching the dephasing length have reported observation of fine structure within the electron beam and production in some cases of high quality, compact, high energy electron sources with charge up to 300 pC [32–34]. However, the production of quality electron beams suffers from a relatively high degree of fluctuations shot-to-shot. This may again be explained from the fact that these beams are produced through a laser-plasma instability and hence depend on the fragile link between laser pulse evolution and inhomogeneities within the plasma.

Controlled injection is therefore studied as a way of producing a stable high quality electron source. As mentioned above, this may be done through the use of multiple laser pulses (two or three depending on the configuration), each with a moderate intensity in order to avoid dark currents.

1.4 Summary and outline

The aim of this dissertation is to describe the concept of an electron injector that uses a single injection laser pulse colliding with a pump laser pulse in a plasma [21, 22]. The pump pulse generates a large amplitude laser wakefield (plasma wave). The counterpropagating injection pulse collides with the pump laser pulse to generate a beat wave (interference term) with a slow phase velocity. The ponderomotive force of the slow beat wave is responsible for injecting plasma electrons into the wakefield near the back of the pump pulse. Test particle simulations indicate that significant amounts of charge can be trapped and accelerated ($\sim 10 - 200$ pC). For higher charge, beam loading limits the validity of the simulations. The accelerated bunches are ultrashort (~ 10 % of the plasma wavelength) with good beam quality (relative energy spread of a few percent at a mean energy of ~ 10 MeV and a normalized rms emittance on the order 0.4 mm.mrad). The effects of interaction angle and polarization are also explored, e.g., efficient trapping can occur for near-collinear geometries. Beat wave injection using a single injection pulse has the advantages of simplicity, ease of experimental implementation, and requires relatively modest laser intensity $\sim 10^{18}$ W/cm^2.

The electron sources provide very high charge density beams and theoretical studies of the transport of such electron bunches in vacuum is necessary. The effects of space charge forces and energy spread on longitudinal and transverse bunch properties are evaluated for various bunch lengths, energies and amount of charge. A comprehensive summary and limitations of analytical methods available for the simulation of the wide variety of beam distributions generated by plasma-based accelerators is also provided for both beam produced by colliding pulse injection as well as the high charge, large energy spreads compact electron bunches produced by SM-LWFA experiments. The various methods discussed are respectively: envelope equations [35], semi-analytical approach using ellipsoidal shells [36], poisson solver and a 3-D point-to-point interaction code.

The dissertation is separated into six different chapters:

- Chapter 2 derives analytically the basic set of equations describing laser and plasma evolution.

- Chapter 3 uses partly the results of Chap. 2 for the description of the colliding pulse injection scheme (CPI). The injection process as well as the accelerated electron beam quality will be discussed together with the use of circularly (linearly) polarized laser pulses and non-collinear geometries.

- Chapter 4 extend the discussion on optical injection combined with a negative plasma density gradient as a mean of increasing the charge per electron bunches while conserving the overall high beam quality.

- Chapter 5 provide a comprehensive summary of space charge effects associated with high charge density beams. The combined effects of large energy spread on beam transport will be underlined.

- Lastly, Chap. 6 presents conclusions and directions for future work.

Chapter 2

Analytical description of laser-plasma interactions

Contents

2.1 Introduction

In this Chapter, a comprehensive summary of the equations describing laser-plasma evolution which are used throughout the dissertation will be presented. The cold fluid-Maxwell equation system will be introduced and reduced to give a basic set of equations valid in the linear regime. Limitations and possible generalization of this technique will further be discussed.

For a more general introduction, Appendix A gives a summary of the theoretical analysis starting from the N-body problem and leading to the fluid equations. Klimontovitch and Vlasov equations together with ensemble averaging is discussed.

2.2 Normalization of the cold fluid-Maxwell equations

In the following theoretical analysis, relevant to plasma based accelerators, ions are considered immobile such that the plasma is modeled as an electron fluid in a neutralizing ion background n_{i0}. Ions typically moves on a time scale on the order of a pico-second, meanwhile the laser-plasma interaction phenomenons we are interested in, are essentially due to electron motion on a faster time scale. For practical purposes it is useful to normalize the fluid-Maxwell equation and also to rewrite the equation of motion in terms of the ponderomotive potentials, which will be defined later in the text. Starting from the unnormalized Maxwell equations

$$\nabla \cdot \mathbf{E} = -4\pi e \left(n_e - n_i\right) \tag{2.1}$$

$$\nabla \cdot \mathbf{B} = 0 \tag{2.2}$$

$$\nabla \times \mathbf{E} = -\frac{\partial \mathbf{B}}{\partial ct} \tag{2.3}$$

$$\nabla \times \mathbf{B} = -4\pi e n_e \beta_e + \frac{\partial \mathbf{E}}{\partial ct} \tag{2.4}$$

where $\beta = \mathbf{V}/c$ is the fluid normalized velocity, $\mathbf{V}$ the fluid velocity defined in (A.37), n_e is the electron density, $n_i = Z^* n_0$ is the ion density which are assumed immobile, Z^* the ionization state on the atom ($Z = Z^*$, for a fully ionized gas, with Z the atomic number). Next $Z = 1$ will be assumed for simplicity. Rewriting Maxwell's

equations in terms of the potentials, we have

$$\mathbf{E} = -\nabla\Phi - \frac{\partial \mathbf{A}}{\partial ct} \tag{2.5}$$

$$\mathbf{B} = \nabla \times \mathbf{A} \tag{2.6}$$

and the Coulomb gauge is used $\nabla \cdot \mathbf{A} = 0$. Introducing the normalized potential $\phi = e\Phi/m_e c^2$, where m_e is the electron rest mass, Eq (2.1) becomes

$$\boxed{\nabla^2 \phi = k_p^2 \left(n_e/n_0 - 1\right)} \tag{2.7}$$

which is the normalized Poisson's equation. $k_p = \omega_p/c$ is the plasma wave number and $\omega_p = \sqrt{4\pi n_0 e^2/m_e}$. Taking the curl of Eq (2.3), we get an equation for the vector potential $\mathbf{A}$

$$\nabla \times \nabla \times \mathbf{A} = -4\pi e n_e \beta - \frac{\partial}{\partial ct}\left(\nabla\Phi + \frac{\partial \mathbf{A}}{\partial ct}\right) \tag{2.8}$$

$$\left(\nabla^2 - \frac{\partial^2}{\partial c^2 t^2}\right)\mathbf{A} = 4\pi e n_0 \beta \, \frac{n_e}{n_0} + \frac{\partial}{\partial ct}\nabla\Phi \tag{2.9}$$

where $\nabla \times \nabla \times \mathbf{A} = -\nabla^2 \mathbf{A}$ (in the Coulomb gauge) has been used. Next introducing the normalized vector potential $\mathbf{a} = e\mathbf{A}/m_e c^2$, Eq. (2.9) becomes

$$\boxed{\left(\nabla^2 - \frac{\partial^2}{\partial c^2 t^2}\right)\mathbf{a} = k_p^2 \; \beta \; \frac{n_e}{n_0} + \frac{\partial}{\partial ct}\nabla\phi} \tag{2.10}$$

which is the normalized wave equation. It describes the evolution of the laser field in the plasma. The last equation of interest, is the cold fluid equation of motion.

$$\left(\frac{\partial}{\partial t} + \mathbf{V} \cdot \nabla\right)\mathbf{P} = -e\left(\mathbf{E} + \beta \times \mathbf{B}\right) \tag{2.11}$$

Rewriting (2.11) in terms of the potentials then normalizing using the expression for $\mathbf{a}$ and ϕ, we get

$$\left(\frac{\partial}{\partial ct} + \beta \cdot \nabla\right)\mathbf{u} = \nabla\phi + \frac{\partial \mathbf{a}}{\partial ct} - \beta \times \left(\nabla \times \mathbf{a}\right) \tag{2.12}$$

where the normalized momentum $\mathbf{u}(\mathbf{x},t) = \mathbf{P}(\mathbf{x},t)/m_e c$ was introduced. Using the vector identity

$$(\mathbf{u}\cdot\nabla)\,\mathbf{u} = \nabla u^2/2 - \mathbf{u}\times(\nabla\times\mathbf{u}) \tag{2.13}$$

together with $u = \sqrt{\gamma^2-1}$, Eq. (2.12) becomes

$$\left(\frac{\partial}{\partial ct} - \frac{\mathbf{u}}{\gamma}\times\nabla\times\right)(\mathbf{u}-\mathbf{a}) = \nabla\,(\phi-\gamma) \tag{2.14}$$

where $\mathbf{F}_p = -\nabla\gamma$ is the generalized (and normalized) ponderomotive force. Eq. (2.14) can be further simplified as follow, first define the general vorticity $\Omega = \nabla\,(\mathbf{u}-\mathbf{a})$ and then take the curl of (2.14)

$$\frac{\partial\Omega}{\partial ct} - \nabla\times(\beta\times\Omega) = 0 \tag{2.15}$$

Eq. (2.15) has no source terms, which means that if at $t = 0$ the general vorticity $\Omega(\mathbf{x}, t=0) = 0$ then it will remain null at $t > 0$. This is equivalent to setting a gauge condition on $\mathbf{u}$, i.e., if Ω is chosen to be zero then,

$$\boxed{\mathbf{u} = \mathbf{a} + \nabla\psi} \tag{2.16}$$

and

$$\boxed{\frac{\partial\psi}{\partial ct} = \phi - \gamma + 1} \tag{2.17}$$

where ψ is equivalent to a generalized potential. The interesting feature of (2.16) is that it allows for a separation of electron motion inside the laser (transverse waves) with respect to the plasma wave (longitudinal waves). This is clearly seen by taking a Fourier transform of (2.16), e.g,

$$\tilde{\mathbf{u}} = \tilde{\mathbf{a}} + \mathbf{k}\tilde{\psi} \tag{2.18}$$

together with the coulomb gauge

$$\mathbf{k}\cdot\tilde{\mathbf{a}} = 0 \tag{2.19}$$

2.3 Single equation for laser-plasma interactions

The fluid-Maxwell's system of equation together with the cold fluid closure $\mathcal{P}_s = 0$ is closed, where $\mathcal{P}_s$ is the pressure tensor [for further details see Eq. (A.41) of Appendix A]. Therefore the full system can be reduced to one equation for the dimensionless electron fluid momentum $\mathbf{u}$ [37–40]. This is the aim of this section. From the gauge condition (2.16), we get a relation between the magnetic field $\mathbf{B}$ and $\mathbf{u}$ which is

$$\boxed{\frac{e\mathbf{B}}{m_e c^2} = \nabla \times \mathbf{u}} \tag{2.20}$$

From the momentum equation (2.17), we can deduce an expression for the electric field

$$-\nabla\phi - \frac{\partial \mathbf{a}}{\partial ct} = -\nabla\gamma - \frac{\partial \mathbf{u}}{\partial ct} \tag{2.21}$$

and

$$\boxed{\frac{e\mathbf{E}}{m_e c^2} = -\nabla\sqrt{1+u^2} - \frac{\partial \mathbf{u}}{\partial ct}} \tag{2.22}$$

Gauss's law (2.1) links the electron fluid momentum $\mathbf{u}$ to the electron density n_e, i.e.,

$$k_p^2\left(\frac{n_e}{n_0} - 1\right) = -\nabla\cdot\left(\frac{e\mathbf{E}}{m_e c^2}\right) = \nabla\cdot\left(\nabla\sqrt{1+u^2} + \frac{\partial \mathbf{u}}{\partial ct}\right) \tag{2.23}$$

and

$$\boxed{\frac{n_e}{n_0} = 1 + k_p^{-2}\nabla\cdot\left(\nabla\sqrt{1+u^2} + \frac{\partial \mathbf{u}}{\partial ct}\right)} \tag{2.24}$$

Lastly taking the temporal derivative of Eq. (2.22) and inserting the new expression in Eq. (2.4), we get

$$\nabla\times\nabla\times\mathbf{u} = -\frac{\partial}{\partial ct}\nabla\sqrt{1+u^2} - \frac{\partial^2\mathbf{u}}{\partial c^2t^2} - k_p^2\frac{\mathbf{u}}{\sqrt{1+u^2}}\frac{n_e}{n_0} \tag{2.25}$$

and finally

$$\boxed{\begin{aligned}\left(\frac{\partial^2}{\partial c^2t^2} + \nabla\times\nabla\times + \frac{k_p^2}{\sqrt{1+u^2}}\right)\mathbf{u} \;=\; & -\frac{\partial}{\partial ct}\nabla\sqrt{1+u^2} - \\ & \frac{\mathbf{u}}{\sqrt{1+u^2}}\nabla\cdot\left[\frac{\partial \mathbf{u}}{\partial ct} + \nabla\sqrt{1+u^2}\right]\end{aligned}} \tag{2.26}$$

This equation can be solved analytically in different ways. Perhaps one of the most common techniques would be to perform a *multiple scale* perturbation analysis [41] of Eq. (2.26) by noticing the scale separation between the laser (ω_0, k_0) and the plasma waves (ω_p, k_p). Multiple scale analysis of (2.26) has been studied in [37, 42] and references therein. It was used, among others, to derive the nonlinear wave equation for a long pulse propagating in an underdense plasma, quasi-static magnetic field generation and the self modulation instability.

Another analytical approach for solving (2.26) around an equilibrium solution is an asymptotic perturbation analysis where $\mathbf{u}$ is replaced by a (converging) Taylor series in the small parameter ϵ

$$\mathbf{u}(\mathbf{r}, t; \epsilon) = \sum_{i=0}^{+\infty} \epsilon^i \mathbf{u}_i \tag{2.27}$$

where

$$\mathbf{u}_n = \frac{1}{n!} \frac{\partial^n \mathbf{u}(\mathbf{r}, t; \epsilon)}{\partial \epsilon^n} \bigg|_{\epsilon=0}, \tag{2.28}$$

and $\mathbf{u}_0$ is an equilibrium solution of Eq. (2.26), i.e.,

$$\left(\nabla \times \nabla \times + \frac{k_p^2}{\sqrt{1+u_0^2}} \right) \mathbf{u}_0 = - \frac{\mathbf{u}_0}{\sqrt{1+u_0^2}} \nabla^2 \sqrt{1+u_0^2} \tag{2.29}$$

Next section we will focus in particular on asymptotic solutions for the case of a plasma initially at rest $\mathbf{u}_0 = \mathbf{0}$, i.e., $|\mathbf{a_0}| = \psi_0 = \phi_0 = 0$ and $n_{e0}/n_0 = 1$.

2.4 Wakefield generation in the linear regime

For the investigation of weak nonlinearities, Eq. (2.26) is expanded up to third order in the laser strength $\mathbf{a}$, assuming $|a| \ll 1$. Hence, it is written for the normalized fluid momentum

$$\mathbf{u} = \mathbf{u}_1 + \mathbf{u}_2 + \mathbf{u}_3 \tag{2.30}$$

where $\mathbf{u}_1 \sim O(\epsilon)$, $\mathbf{u}_2 \sim O(\epsilon^2)$, $\mathbf{u}_3 \sim O(\epsilon^3)$ and the approximations $(1+u^2)^{1/2} \simeq 1 + u^2/2$ and $(1-u^2)^{1/2} \simeq 1 - u^2/2$ were used. Here ϵ has been dropped simply because it is used for bookkeeping. Inserting (2.30) into (2.26) and sorting in power

of ϵ gives to order $O(\epsilon)$

$$\left(\frac{\partial^2}{\partial c^2 t^2} + \nabla \times \nabla \times + k_p^2\right) \mathbf{u}_1 = 0 \tag{2.31}$$

Using $\nabla \times \nabla \times \mathbf{u}_1 = \nabla(\nabla \cdot \mathbf{u}_1) - \nabla^2 \mathbf{u}_1$ and $\mathbf{u}_1 = \mathbf{a}_1 + \nabla\psi_1$, Eq. (2.31) becomes

$$\left(\frac{\partial^2}{\partial c^2 t^2} - \nabla^2 + k_p^2\right) \mathbf{a}_1 = 0 \tag{2.32}$$

$$\left(\frac{\partial^2}{\partial c^2 t^2} + k_p^2\right) \nabla\psi_1 = 0 \tag{2.33}$$

where $\mathbf{a}_1$ and $\nabla\psi_1$ are linearly independent. Matching Eq. (2.31) with the initial condition of an incoming laser pulse with carrier frequency λ_0, (2.31) gives the dispersion relation for that laser inside the plasma. This can be seen by taking a Fourier transform of (2.31), i.e.,

$$\left(-\omega^2/c^2 + k^2 + k_p^2\right) \tilde{\mathbf{a}}_1 = 0 \tag{2.34}$$

and

$$\beta_\phi = \omega/k = \eta^{-1} \tag{2.35}$$

$$\beta_g = \partial\omega/\partial k = \eta \tag{2.36}$$

where $\eta = \sqrt{1 - \omega^2/\omega_p^2}$ is the index of refraction. Eq. (2.33) has also no source term and matching the initial condition with a plasma at rest gives $\psi_1 = 0$. To second order in ϵ, Eq. (2.26) becomes

$$\left(\frac{\partial^2}{\partial c^2 t^2} + \nabla \times \nabla \times + k_p^2\right) \mathbf{u}_2 = -\nabla \frac{\partial}{\partial ct} \frac{u_1^2}{2} - \mathbf{u}_1 \nabla \cdot \frac{\partial \mathbf{u}_1}{\partial ct} \tag{2.37}$$

Replacing $\mathbf{u}_1 = \mathbf{a}_1$ and $\mathbf{u}_2 = \mathbf{a}_2 + \nabla\psi_2$ we get

$$\left(\frac{\partial^2}{\partial c^2 t^2} - \nabla^2 + k_p^2\right) \mathbf{a}_2 + \left(\frac{\partial^2}{\partial c^2 t^2} + k_p^2\right) \nabla\psi_2 = -\nabla \frac{\partial}{\partial ct} \frac{a_1^2}{2} \tag{2.38}$$

The source term of Eq. (2.38) is irrotational, this can be seen by taking a Fourier transform of (2.38), i.e.,

$$\left(k^2 + k_p^2 - \omega^2/c^2\right) \tilde{\mathbf{a}}_2 + \left(k_p^2 - \omega^2/c^2\right) \mathbf{k}\ \tilde{\psi}_2 = \omega \mathbf{k}\ \mathcal{F}(a_1^2/2) \tag{2.39}$$

where $\mathcal{F}(a_1^2/2)$ denotes the Fourier transform of $a_1^2/2$. Keeping in mind that $\mathbf{k}\cdot\tilde{\mathbf{a}}_2 = 0$ we have

$$\left(\frac{\partial^2}{\partial c^2 t^2} - \nabla^2 + k_p^2\right) \mathbf{a}_2 = 0 \tag{2.40}$$

$$\left(\frac{\partial^2}{\partial c^2 t^2} + k_p^2\right) \nabla\psi_2 = -\nabla \frac{\partial}{\partial ct} \frac{a_1^2}{2} \tag{2.41}$$

Eq. (2.40) has no source term and consequently $\mathbf{a}_2 = \mathbf{0}$. Looking for a solution of Eq. (2.41) specifically for the wakefield potential ϕ_2, we take the time derivative of (2.41) and replace

$$\frac{\partial\psi_2}{\partial ct} = \phi_2 - \frac{a_1^2}{2} \tag{2.42}$$

giving

$$\left(\frac{\partial^2}{\partial c^2 t^2} + k_p^2\right) \nabla\phi_2 = k_p^2 \nabla \frac{a_1^2}{2} \tag{2.43}$$

For a homogeneous plasma, we can further integrate this equation, assuming there is no potential (i.e., no plasma disturbance) in front of the laser pulse,

$$\left(\frac{\partial^2}{\partial c^2 t^2} + k_p^2\right) \phi_2 = k_p^2 \frac{a_1^2}{2} \tag{2.44}$$

This is the equation describing the wakefield generated by the incoming laser pulse. The source term is second order in $\mathbf{a}$, which implies that the driving force for the plasma oscillation is the *ponderomotive* force of the laser pulse. A general solution for Eq. (2.44) can be written as follow

$$\boxed{\phi_2(\mathbf{r}, t) = \omega_p \int_{-\infty}^{t} dt' \sin k_p(t - t')\ a_1^2(\mathbf{r}, t')/2} \tag{2.45}$$

In accordance with (2.26), the equation for the third-order value $\mathbf{u}_3$ has the form

$$\left(\frac{\partial^2}{\partial c^2 t^2} + \nabla \times \nabla \times + k_p^2\right) \mathbf{u}_3 = -\nabla \frac{\partial}{\partial ct} \left(\mathbf{u}_1 \cdot \mathbf{u}_2\right) + \mathbf{u}_1 \left[\left(k_p^2 - \nabla^2\right) \frac{u_1^2}{2} - \nabla \cdot \frac{\partial \mathbf{u}_2}{\partial ct}\right] \tag{2.46}$$

Introducing $\mathbf{u}_1 = \mathbf{a}_1$, $\mathbf{u}_3 = \mathbf{a}_3 + \mathbf{u}_{3L}$, where $\mathbf{u}_{3L} = \nabla\psi_3$ and using Eq. (2.42) gives

$$\left(\frac{\partial^2}{\partial c^2 t^2} - \nabla^2 + k_p^2\right) \mathbf{a}_3 + \left(\frac{\partial^2}{\partial c^2 t^2} + k_p^2\right) \mathbf{u}_{3L} = -\nabla \frac{\partial}{\partial ct} \left(\mathbf{a}_1 \cdot \mathbf{u}_2\right) + k_p^2 \mathbf{a}_1 \left(\frac{a_1^2}{2} - \frac{n_2}{n_0}\right) \tag{2.47}$$

Eq. (2.47) cannot simply be split into two independent equations (one for the light wave $\mathbf{a}_3$ and one for the electron motion inside the space charge wave $\nabla\psi_3$) because the last term on the right hand side (RHS) of the equation has both a rotational and an irrotational part. Further assuming an underdense plasma $\epsilon = \omega_p/\omega_0 \ll 1$, the procedure is to study (2.47) by performing an expansion into harmonics of $\mathbf{a}_3$ and $\nabla\psi_3$ then evaluating the contribution of the slow time scales (typically on the order $t \sim \omega_p^{-1}$) and fast time scales ($t \sim (n\omega_0)^{-1}$ where n is an integer) to the whole solution. This will be done in two main steps: (i) derive an equation for the third order plasma wave $\nabla^2\phi_3$ and perform a multiple scale expansion and (ii) using the equation of motion get an estimate for $\mathbf{u}_{3L}$ which will imply some simplifications of (2.47). Taking the divergence of Eq. (2.47) and using the third order longitudinal equation of motion

$$\frac{\partial \mathbf{u}_{3L}}{\partial ct} = \nabla(\phi_3 - \gamma_3) \tag{2.48}$$

one obtains an equation for the third order plasma wave,

$$\begin{aligned}\left(\frac{\partial^2}{\partial \zeta^2} + k_p^2\right) \left(\nabla_\perp^2 + \frac{\partial^2}{\partial \zeta^2}\right) \phi_3 \;\; &= \;\; k_p^2 \left(\nabla_\perp^2 + \frac{\partial^2}{\partial \zeta^2}\right) \left(\mathbf{a}_1 \cdot \mathbf{u}_2\right) \\ &\quad -k_p^2 \, \mathbf{a}_1 \cdot \frac{\partial}{\partial \zeta} \left(\nabla_\perp + \frac{\partial}{\partial \zeta} \mathbf{e}_z\right) \rho_2 \end{aligned} \tag{2.49}$$

where $\mathbf{e}_z$ is a unit vector, $\rho_2 = a_1^2/2 - n_2/n_0$ and we have transformed the equation in the frame comoving with the laser pulse, following the change of variable $\zeta \simeq z - ct$ and $t = \tau$. This is leading to the transformation $\partial/\partial ct = \partial/\partial c\tau - \partial/\partial\zeta$ and $\partial/\partial z = \partial/\partial\zeta$. For a matter of simplicity, the next level of approximation is to assume that the laser is slowly evolving in its frame, i.e., the $\partial/\partial\tau$ contribution is considered higher order

in $\epsilon = \omega_p/\omega_0$ (quasi-static approximation [9, 43]). We will focus only on the slow part and first order harmonics assuming higher order are negligible. All quantities (i.e., $\mathbf{a}$, ϕ, etc.) are expanded as follow

$$\begin{aligned} \mathbf{Q} &= \mathbf{Q}_0(\mathbf{r},\tau) + \frac{1}{2}\sum_{n=1}^{+\infty}\left[\mathbf{Q}_n(\mathbf{r},\tau)\exp(ink_0\zeta) + \text{c.c.}\right] \\ &\simeq \mathbf{Q}_s(\mathbf{r},\tau) + \frac{1}{2}\left[\mathbf{Q}_f(\mathbf{r},\tau)\exp(ik_0\zeta) + \text{c.c.}\right] \end{aligned} \tag{2.50}$$

where "c.c" stands for complex conjugate. Note that the laser pulse has only a fast component, i.e., $\propto \exp(ik_0\zeta)$. Inserting Eq. (2.50) into (2.49) provides an equation for the slow ϕ_{3s} without a source term. A non trivial solution leads to $\phi_{3s} = 0$. The first harmonic equation yields

$$\phi_{3f} \sim \epsilon^2\gamma_{3f} + O(\epsilon^3) \tag{2.51}$$

where $\gamma_{3f} = \mathbf{a}_{1f}\cdot\mathbf{u}_{2s}$ and $\epsilon = k_p/k_0$. In the latter calculation (fast term), we have assumed that $\nabla_\perp \sim k_p$, $\partial/\partial\zeta \sim k_0$ and $\epsilon \ll 1$. From (2.48) one can deduce that

$$\mathbf{u}_{3L\perp} \sim \epsilon(\phi_3 - \gamma_3) = -\epsilon\gamma_3 + O(\epsilon^3) \tag{2.52}$$

$$u_{3Lz} \sim \gamma_3 - \phi_3 = \gamma_3 + O(\epsilon^2) \tag{2.53}$$

leading to an estimate of

$$\left(\frac{\partial^2}{\partial(\omega_0 t)^2} + \epsilon^2\right)\mathbf{u}_{3L} = -\nabla\frac{\partial\gamma_3}{\partial(\omega_0 t)} + O(\epsilon^3) \tag{2.54}$$

up to third order in ϵ, where Eq, (2.54) has been normalized with respect to $\omega_0 = k_0 c$. Subtracting Eq (2.54) from (2.47) we obtain an approximate equation for the third order vector potential correct to order $\sim O(\epsilon^2)$

$$\boxed{\left(\frac{\partial^2}{\partial c^2 t^2} - \nabla^2 + k_p^2\right)\mathbf{a}_{3\perp} \simeq k_p^2\,\mathbf{a}_{1\perp}\rho_2} \tag{2.55}$$

where $a_{3z} \sim \epsilon a_{3\perp}$ has been used which was deduced from a multiple scale analysis of the Coulomb gauge $\nabla\cdot\mathbf{a}_3$. Finally inserting the solution for ρ_2 in integral form,

(2.55) becomes

$$\boxed{\begin{aligned}\left(\frac{\partial^2}{\partial c^2 t^2} - \nabla^2 + k_p^2\right)\mathbf{a}_{3\perp} &= \mathbf{a}_{1\perp}\left(k_p^2\,\frac{a_{1\perp}^2}{2} - \nabla^2\phi_2\right) \\ &= k_p^2\,\frac{\mathbf{a}_{1\perp}}{2}\left[a_{1\perp}^2 - \frac{c}{k_p}\nabla^2\int_{-\infty}^{t} dt'\sin k_p(t-t')\;a_{1\perp}^2\right]\end{aligned}} \tag{2.56}$$

Eq. (2.56) describes third harmonic generation as well as relativistic self-focusing, self-modulation instability and Raman scattering. This problems were discussed in several papers [for a review see [9] and references therein].

In Chapter 3 we will apply the results derived in this section for the analysis of electron bunches production in a plasma using two beating laser pulses. The laser pulses will be assumed non involving, i.e., $\mathbf{a}_3 \simeq \mathbf{0}$, which is a fairly good approximation in the standard regime where $L_0 \simeq \lambda_p$, with L_0 the laser pulse length, and particularly in the linear regime $|\mathbf{a}_{1i}| \ll 1$.

In Chapter 5, space charge effects for dense electron beams with large energy spread with be studied in great details. One of the mechanism for producing high energy electron beams using plasmas is the self-modulated laser-wakefield-accelerator (SM-LWFA) regime [9] in which the laser pulse length L is on the order or greater than the plasma wavelength. Laser pulse undergoing self-modulation and plasma wave evolution can be understood by solving Eq. (2.56) together with Eq. (2.44) (in the linear regime). However a general overview of the physical effect may be given; a sufficiently long interaction in time ($t \gg \omega_p^{-1}$) between the laser pulse and the plasma density modulation of the wake is necessary for the instability to build up from noise. The laser fields experience a local change of index of refraction, both radially and axially, due to the plasma density modulations. Regions where $\nabla\delta n > 0$ induce an increase of local laser energy whereas $\nabla\delta n < 0$ on the contrary enhance diffraction. This cause both the longitudinal and transverse laser envelope to become modulated at λ_p, which subsequently enhances the growth of the plasma wave, and the process proceeds in a highly nonlinear manner. The end result can be a fully self-modulated pulse. Associated with the periodic "beamlet" structure are large amplitude wake-fields which can self trap and accelerate electrons via direct wavebreaking, which for a cold one-dimensional (1D) plasma wave is $E_{\mathrm{WB}} = [2(\gamma_\phi - 1)]^{1/2}E_0 \gg E_0$, where

$v_\phi = c\beta_\phi = c(1 - \gamma_\phi^{-2})^{1/2}$ is the phase velocity of the plasma wave. When electrons become trapped in the fast wakefield, they become accelerated to high energies as they rotate up in momentum inside the separatrix of the wakefield.

Lastly, in Appendix B, a step further will be taken, that is multiple scale analysis will now be used to derive a new set of equations from the full non-linear Maxwell-fluid system of equations, which will be valid for arbitrary laser strength $|a|$. The main interest of this method is to provide a clear separation between the equation describing the laser evolution and the other quantities related uniquely to the plasma which occurs on a longer time scale. It will further be shown that assuming a moderate laser strength $|a| \ll 1$, allows reduction to the equations found in Sec. 2.4.

Chapter 3

Electron injection into plasma waves using two laser pulses

Contents

3.1 Introduction

Plasma-based accelerators [9] are capable of producing compact and high energy electron sources in much shorter distances than conventional accelerators due to the large longitudinal electric fields that can be excited without the limitation of breakdown as in RF structures. In a plasma, the accelerating fields of a plasma wave are on the order of the cold, nonrelativistic wavebreaking field $E_0 = m_e c\omega_p/e$, or $E_0[\mathrm{V/m}] \simeq 96(n_0[\mathrm{cm}^{-3}])^{1/2}$, where $\omega_p = (4\pi n_0 e^2/m_e)^{1/2}$ is the plasma frequency, n_0 is the plasma density, c is the speed of light, m_e the electron mass, and e the electron charge. The wavelength of the accelerating field is the plasma wavelength $\lambda_p = 2\pi c/\omega_p$, or $\lambda_p[\mathrm{m}] \simeq 3.3 \times 10^4\ (n_0[\mathrm{cm}^{-3}])^{-1/2}$. For example, a laser wakefield accelerator (LWFA) [9] in the standard regime, in which the laser pulse length L is matched to the plasma wavelength, $L \simeq \lambda_p$, typically has a density on the order of $n_0 \simeq 10^{18}$ cm^{-3} for a 100 fs pulse, which gives $E_0 \simeq 100$ GV/m and $\lambda_p \simeq 30$ μm. If a mono-energetic electron bunch is injected into a wakefield such that it is accelerated while maintaining a small energy spread, then it is necessary for the bunch to occupy a small fraction of the wakefield period, on the order of a few femtoseconds, which requires femtosecond accuracy in the injection process. To meet these requirements, a variety of laser injection methods have been proposed [18–20, 44–46].

Perhaps the most basic and simplest form of a laser-plasma injector is the self-modulated LWFA [9, 47], in which a single laser pulse, propagating in a relatively high density plasma (such that $L > \lambda_p$ and the laser pulse power exceeds the critical power for relativistic focusing), results in self-trapping and generation of a sub-ps electron bunch, however, with a large energy spread. Typically the self-trapped bunch is of high charge (up to 10 nC), with an energy distribution that can be modeled as a Boltzmann distribution with temperature in the few MeV range [16, 24, 27, 29, 30, 48]. One possible mechanism for self-trapping is direct wavebreaking of the plasma wakefield [49]. Since the phase velocity of the wakefield is near the speed of light, it is difficult to trap the background fluid electrons, which are undergoing the fluid oscillation that sustains the wakefield. Wavebreaking typically occurs at high wakefield amplitudes, i.e., amplitudes greater than the wavebreaking field, which for a cold one-dimensional (1D) plasma wave is $E_{\mathrm{WB}} = [2(\gamma_\phi - 1)]^{1/2} E_0 \gg E_0$, where $v_\phi = c\beta_\phi = c(1 - \gamma_\phi^{-2})^{1/2}$ is the phase velocity of the plasma wave. Alternatively,

self-trapping and acceleration can result from the coupling of Raman backscatter and Raman sidescatter to the wakefield [50]. When electrons become trapped in the fast wakefield, they become accelerated to high energies as they rotate up in momentum inside the separatrix of the wakefield. In the self-modulated regime, a large energy spread for the trapped electrons results because (i) some fraction of the background electrons are continually being swept up and trapped in the wakefield as the laser pulse propagates into fresh plasma, and (ii) typically the self-guided propagation distance of the laser pulse is much greater than the detuning length for trapped electrons. This implies that deeply trapped electrons will circulate many revolutions within the separatrix, again resulting in a large energy spread.

For many applications, a small energy spread is desired. This can be achieved by using a standard LWFA, in which the wakefield is produced in a controlled manner at an amplitude below the wavebreaking or self-trapping threshold. In principle, if a small energy spread electron bunch of duration small compared to λ_p is injected into the wakefield at the proper phase, then the bunch can be accelerated while maintaining a small energy spread. Umstadter *et al.* [18] first proposed using an additional laser pulse to inject background plasma electrons into the wave for acceleration to high energies. To generate ultrashort electron bunches with low energy spreads, the original laser injection method proposed by Umstadter *et al.* [18] (referred to as the LILAC scheme) utilizes two laser pulses which propagate perpendicular to one another. The first pulse (pump pulse) generates the wakefield via the standard LWFA mechanism, and the second pulse (injection pulse) intersects the wakefield some distance behind the pump pulse. The ponderomotive force $\mathbf{F} \simeq -(m_e c^2/\gamma)\nabla a^2/2$ of the injection pulse can accelerate a fraction of the plasma electrons such that they become trapped in the wakefield. Here γ is the relativistic Lorentz factor of the electrons and $a^2 \simeq 3.6\times10^{-19}(\lambda[\mu\mathrm{m}])^2 I[\mathrm{W/cm^2}]$ for a circularly polarized laser field, with λ the laser wavelength and I the laser intensity. Specifically, the axial (direction of propagation of the pump pulse along the z-axis) ponderomotive force of the injection pulse (propagating along the x-axis) scales as

$$F_{z,\mathrm{pond}} = -(m_e c^2/\gamma)(\partial/\partial z)a_1^2/2 \sim (m_e c^2/\gamma)a_1^2/r_1 \ , \tag{3.1}$$

where a_1^2 and r_1 are the normalized intensity and spot size of the injection pulse,

respectively. A simple estimate for the change of momentum that an electron will experience due to the ponderomotive force of the injection pulse is $\Delta p_z \simeq \tau_1 F_{z,\mathrm{pond}} \sim (mc^2/\gamma) a_1^2 \tau_1 / r_1$, where τ_1 is the injection pulse duration. It is possible for Δp_z to be sufficiently large that electrons are injected into the separatrix of the wakefield such that they become trapped and accelerated to high energies. To inject into a single plasma wave bucket, it is necessary for both the injection pulse spot size and pulse length to be small compared to the plasma wavelength, i.e., $r_1^2 \ll \lambda_p^2$ and $c^2\tau_1^2 \ll \lambda_p^2$. Simulations [18], which were performed for ultrashort pulses at high densities ($\lambda_p/\lambda = 10$ and $E_z/E_0 = 0.7$), indicated the production of a 10 fs, 21 MeV electron bunch with a 6% energy spread. However, high intensities ($I > 10^{18}$ W/cm^2) are required in both the pump and injection pulses ($a_0 \simeq a_1 \simeq 2$). It is important to note that in the work of Umstadter *et al.* [18], the pump pulse and the injection pulse do not overlap (in space and time) and a laser beat wave is not generated, as is discussed below.

Hemker et al. [44] also studied the LILAC injection scheme using 2D particle-in-cell simulations. They found that the wake generated by the transverse propagating injection pulse can play an important role in the trapping process and even exceed the amount of trapping produced by the ponderomotive force of the injection pulse alone. In addition, they varied the delay between the pump and injection pulses and found that the trapping can be enhanced when the two pulses overlap. However, the electric field polarizations of the two pulses were orthogonal in these simulations, i.e., no laser beat wave was generated when the two pulses overlapped.

Esarey *et al.* [19, 20] proposed and analyzed a colliding pulse injection (CPI) concept that uses three short laser pulses: an intense ($a_0^2 \simeq 1$) pump pulse (denoted by subscript 0) for plasma wave generation, a forward going injection pulse (subscript 1), and a backward going injection pulse (subscript 2). CPI is intrinsically different from the method of ponderomotive injection discussed above in that both the source and form of the ponderomotive force, responsible for injection, differs in these two methods. In ponderomotive injection, injection is the result of the ponderomotive force associated with the *envelope* (time-averaged intensity profile) of a single pulse. In CPI, injection is the result of the ponderomotive force associated with the *slow beat wave* of two intersecting pulses.

In CPI, the pump pulse generates a plasma wave with phase velocity near the

speed of light ($v_{p0} \simeq c$). The forward injection pulse travels at a fixed distance behind the pump pulse, which determines the position (i.e., phase) of the injected electrons. The injection pulses are orthogonally polarized to the pump laser pulse, such that the pump pulse and backward going injection pulse do not beat. When the injection pulses collide some distance behind the pump, they generate a slow ponderomotive beat wave of the form $a_1 a_2 \cos(\Delta k z - \Delta\omega t)$ (here $\Delta k = k_1 - k_2 \simeq 2k_0$) with a phase velocity $v_{pb} \simeq |\Delta\omega|/2k_0 \ll c$, where the frequency, wavenumber, and normalized intensity of the pulses are denoted by ω_i, k_i, and a_i ($i = 0, 1, 2$), respectively. Furthermore, it is assumed that $k_1 \simeq k_0$, $k_2 \simeq -k_0$, and $\omega_1 - \omega_2 = \Delta\omega \gg \omega_p$. The axial force associated with this beat wave scales as

$$F_{z,\mathrm{beat}} = -(m_e c^2/\gamma)(\partial/\partial z) a_1 a_2 \cos(2k_0 z - \Delta\omega t) \sim (m_e c^2/\gamma) 2k_0 a_1 a_2 \; . \tag{3.2}$$

During the time in which the two injection pulses overlap, a two-stage acceleration process can occur, i.e., the slow beat traps and heats background plasma electrons which, as a result of shifts in their momentum and phase, can be injected into the fast wakefield for acceleration to high energies.

The ratio of the axial force of the CPI beat wave to that of a single pulse in the ponderomotive injection scheme scales as

$$\frac{F_{z,\mathrm{beat}}}{F_{z,\mathrm{pond}}} \sim \frac{2k_0 a_1 a_2}{a_p^2/r_p} \; , \tag{3.3}$$

where the subscript p refers to the single ponderomotive injection pulse and the contribution of the relativistic Lorentz factor γ (which is different for the two cases) is neglected. For comparable injection pulse intensities ($a_1 \simeq a_2 \simeq a_p$), the ratio scales as $2k_0 r_p \gg 1$, i.e., the axial force of the beat wave is much greater than the ponderomotive force of a single pulse. Consequently, CPI using beat waves is much more effective for electron injection than relying on the ponderomotive force of the injection pulse alone. CPI can result in electron injection at relatively low intensities ($a_1 \sim a_2 \sim 0.2$), as well as at relatively low densities ($\lambda_p/\lambda \sim 100$), thus allowing for high single-stage energy gains. Furthermore, the CPI concept offers detailed control of the injection process: the injection phase can be controlled via the position of the forward injection pulse, the beat phase velocity via $\Delta\omega$, the injection energy via

the pulse amplitudes, and the injection time (number of trapped electrons) via the backward pulse duration.

In this Chapter, a simplified configuration of the CPI concept is proposed and analyzed that uses only two laser pulses with parallel polarizations: an intense pump pulse for wakefield generation and a single counterpropagating (or propagating at a finite angle) injection pulse. Injection is the result of the laser beat wave produced when the backward injection pulse collides with the trailing portion of the pump pulse. This configuration has the advantages of being easier to implement in comparison to the three-pulse CPI scheme, and of requiring less intensity in the injection pulse compared to the ponderomotive injection scheme, since injection is the result of the laser beat wave as opposed to the ponderomotive force of a single injection pulse.

In the following, analytical models and test particle simulations are used to describe the basic characteristics of the two-pulse CPI concept, such as the threshold for injection and the trapped bunch quality. Test particle simulations are carried out in three dimensions (3D) in which the fields of the laser pulses and their wakes are described analytically via linear theory. For high laser intensities ($a^2 > 1$), this model becomes inaccurate. To describe the nonlinear regime in 3D, as well as other nonlinear effects such as beam loading, requires self-consistent simulations such as can be done with particle-in-cell codes, which is beyond the scope of this chapter . Also explored are the effects of interaction angle and polarization on the injection process. These results are directly relevant to laser injection experiments being pursued at Lawrence Berkeley National Laboratory (LBNL) [51] and elsewhere.

3.2 Two-Pulse CPI: Fields

This section describes the fields used in the CPI simulations discussed below: (i) drive and injection laser pulse evolutions in the linear regime ($|\mathbf{a}_i| \ll 1$) and within the paraxial approximation (the latter assumes slow changes in the pulse envelope, i.e., Rayleigh length greater that the typical plasma size considered), (ii) wakefield generation and (iii) beatwave potential (plasma wave induced by the beating of the laser pulses).

3.2.1 Paraxial wave equation

The laser fields of the pump ($i = 0$) and injection ($i = 1$) laser pulses are described by the normalized vector potentials $\mathbf{a}_i = e\mathbf{A}_i/m_e c^2$. The 3D linear wave equation (2.32)

$$\left(\nabla^2 - \frac{\partial^2}{\partial c^2 t^2}\right)\mathbf{a} = k_p^2 \mathbf{a} \tag{3.4}$$

has a solution of the form

$$\hat{\mathbf{a}}_i(\mathbf{r}, t) = \frac{1}{2}\left\{\frac{1}{\sqrt{2\pi}}\iiint_{-\infty}^{+\infty} \mathrm{d}^3\mathbf{k}\ \tilde{\mathbf{a}}_i(\mathbf{k})\ \exp\left[-i\left(\mathbf{k}\cdot\mathbf{r} - \omega(k)t\right)\right] + \text{c.c}\right\} \tag{3.5}$$

along with

$$\omega(k) = \sqrt{\mathbf{k}^2 c^2 + \omega_p^2} \tag{3.6}$$

where c.c denotes the complex conjugate. In general this integral cannot be solved analytically. However for laser pulses with a slowly varying envelope compared to the carrier wavelength λ_0, there exists a set of gaussian modes that are exact solutions of Maxwell's equation. This can be shown as follows [52]: in terms of the independent variable $\zeta = z - \beta_g ct$ and z, the wave equation can be rewritten as

$$\left[\nabla_\perp^2 + 2\frac{\partial}{\partial\zeta\partial z} + \left(1 - \beta_g^2\right)\frac{\partial^2}{\partial\zeta^2} + \frac{\partial^2}{\partial z^2}\right]\mathbf{a}_i = k_p^2 \mathbf{a}_i \tag{3.7}$$

where β_g is the linear ($|\mathbf{a}_i| \ll 1$) group velocity of a laser pulse in a plasma, taken along the propagation axis. β_g is assumed to be a constant, i.e., local variations due to diffraction are neglected. Introducing the slowly-vary field envelope $\hat{\mathbf{a}}_i$, where $\mathbf{a}_i = \hat{\mathbf{a}}_i/2\exp[i(k_0 z - \omega_0 t)] + \text{c.c}$, ω_0 is the central frequency of the pulse and k_0 the central wave number, the wave equation becomes

$$\left[\nabla_\perp^2 + 2\left(ik_0 + \frac{\partial}{\partial\zeta}\right)\frac{\partial}{\partial z} + \left(1 - \beta_g^2\right)\frac{\partial^2}{\partial\zeta^2} + \frac{\partial^2}{\partial z^2}\right]\hat{\mathbf{a}}_i = k_p^2 \hat{\mathbf{a}}_i \tag{3.8}$$

For a short pulse of length L propagating in a plasma, the operators on the left side of the wave equation, Eq. (3.8), scale as follow: $\nabla_\perp \sim 1/r_0$, $\partial/\partial\zeta \sim 1/L$, $\partial/\partial z \sim 1/Z_R$ and $\beta_g \simeq k_0/k_z \simeq \left(1 - \omega_p^2/\omega_0^2 - \mathbf{k}_\perp^2/k_0^2\right)^{-1/2}$, e.g, using $\mathbf{k}_\perp \sim 2/r_0$ (for

a gaussian pulse) gives $\left(1-\beta_g^2\right) \simeq \omega_p^2/\omega_0^2 + 4/k_0^2 r_0^2$. The Rayleigh length $Z_R = k_0 r_0^2/2$ has been introduced.

Note that the last term on the left of Eq. (3.8), is typically small. This is true provided (i) $|\partial^2 \hat{\mathbf{a}}_i/\partial^2 z^2| \ll 2|\partial^2 \hat{\mathbf{a}}_i/\partial\zeta\partial z|$, which implies $L \ll 2Z_R$ and (ii) $|\partial^2 \hat{\mathbf{a}}_i/\partial z^2| \ll \left(1-\beta_g^2\right)|\partial^2 \hat{\mathbf{a}}_i/\partial\zeta^2|$, which implies $L^2/r_0^2 \ll \left(1+k_p^2 r_0^2/4\right)$. For an underdense plasma this equation can be further simplified. In the standard regime $L \simeq \lambda_p$ and $\epsilon = \omega_p/\omega_0 \ll 1$, we have $k_0 L \gg 1$ and $\left(1-\beta_g^2\right) \simeq O(\epsilon^2) \ll 1$. Eq. (3.8) becomes

$$\boxed{\left(\nabla_\perp^2 + ik_0\frac{\partial}{\partial z}\right)\hat{\mathbf{a}}_i = k_p^2 \hat{\mathbf{a}}_i} \tag{3.9}$$

which is the *paraxial* wave equation. Note that in Eq. (3.8), the terms $\partial^2 \hat{\mathbf{a}}_i/\partial\zeta\partial z$ and $\left(1-\beta_g^2\right)\partial^2 \hat{\mathbf{a}}_i/\partial\zeta^2$ represent corrections to the paraxial wave equation that account for short pulse and group velocity dispersion effect.

Solving the paraxial wave equation for a linear plasma response, the transverse laser fields (linearly polarized in the x-direction and propagating along the z-axis) are given by [37, 52, 53]

$$a_{xi}(r,\zeta_i) = \hat{a}_i(r,\zeta_i)\cos\psi_i \ , \tag{3.10}$$

with

$$\hat{a}_i(r,\zeta_i) = a_i(r_i/r_{si})\exp\left(-r^2/r_{si}^2\right)\sin\left(\pi\zeta_i/L_i\right) \ , \tag{3.11}$$

for $-L_i < \zeta_i < 0$ and zero otherwise, where $\zeta_0 = z - \beta_{g0}ct$ (forward comoving coordinate), $\zeta_1 = -z - \beta_{g1}ct$ (backward comoving coordinate), $\beta_{gi} = \eta_i$ is the linear group velocity, $\beta_{\phi i} = \eta_i^{-1}$ is the linear phase velocity, $\eta_i = \sqrt{1-\omega_p^2/\omega_i^2 - 4/(k_i r_i)^2}$ is the plasma index of refraction, $\psi_i = k_i(z-\beta_{\phi i}ct) + \alpha_i\ r^2/r_{si}^2 + \alpha_i - \tan^{-1}\alpha_i$ is the phase, $k_i = \omega_i/(\beta_{\phi i}c)$ is the wavenumber, ω_i is the frequency in vacuum, $r_{si}(z) = r_i\sqrt{1+\alpha_i(z)}$ is the spot size, r_i is the spot size at waist (here chosen to be $z = Z_{f_i}$), $\alpha_i(z) = (z-Z_{f_i})^2/Z_{R_i}^2$, $Z_{R_i} = k_i\eta_i r_i^2/2$ is the Rayleigh length, L_i is the pulse length, and a constant has been omitted in the definition of ψ_i that represents the initial position and phase of the laser pulse. The axial component of the laser field is

specified via $\nabla \cdot \mathbf{a}_i = 0$. Keeping only the leading order contributions gives

$$\begin{aligned} a_{zi}(r,\zeta_i) &= -\int_0^{\zeta_i} d\zeta_i' \partial a_{xi}(r,\zeta_i')/\partial x \\ &\simeq 2x[\hat{a}_i(r,\zeta_i)/(k_i r_{si}^2)]\,(\sin\psi_i - \alpha_i \cos\psi_i)\ . \end{aligned} \tag{3.12}$$

For simplicity, the notation $\langle a_i^2 \rangle$ is introduced to denote the time-averaged peak intensity of the laser pulse, which for a linearly polarized laser pulse of the form $a_i \cos\psi_i e_x$ is given by $\langle a_i^2 \rangle = a_i^2/2$ and for a circularly polarized laser pulse of the form $a_i(\cos\psi_i e_x + \sin\psi_i e_y)$ by $\langle a_i^2 \rangle = a_i^2$. Comparisons between linear and circular polarization will be done for equal values of the time-averaged peak intensity $\langle a_i^2 \rangle$. The weakly relativistic limit, sometimes referred to as the linear regime, corresponds to $\langle a_i^2 \rangle \ll 1$.

3.2.2 Wakefield generation

In the linear ($\langle a_i^2 \rangle \ll 1$) three-dimensional (3D) regime, wakefield generation can be examined using the cold fluid equations. In particular for linear polarization, the normalized electrostatic potential of the wakefield $\phi_i = e\Phi_i/m_e c^2$ is given by Eq. (2.44)

$$\left(\partial^2/\partial\zeta_i^2 + k_p^2\right)\phi_i \simeq k_p^2 \hat{a}_i^2/4\ , \tag{3.13}$$

where $k_p = \omega_p/c$ and $\partial^2/\partial c^2 t^2 = \beta_{gi}^2\ \partial^2/\partial\zeta_i^2 \simeq \partial^2/\partial\zeta_i^2 + O(\epsilon^2)$ is assumed (quasi-static). This is a valid approximation provided $\hat{\mathbf{a}}$ is a function of ζ_i only or slowly varying in $\tau = t$. Time-averaging has been performed over the fast laser oscillation (laser frequency), i.e., $\langle \hat{a}_i^2 \cos^2\psi_i \rangle = \hat{a}_i^2/2$. The solution to Eq. (3.13) [for a detailed calculation see Appendix C], using the vector potential of Sec. (3.2.1), is

$$\phi_i(r,\zeta_i) = k_p \int_0^{\zeta_i} d\zeta_i' \sin k_p(\zeta_i - \zeta_i')\hat{a}_i^2(r,\zeta_i')/4\ . \tag{3.14}$$

Specifically, Eq. (3.13) yields the potential generated inside the pulse ($-L_i < \zeta_i < 0$)

$$\phi_i = \frac{a_i^2}{8}\frac{r_i^2}{r_{si}^2} e^{-2r^2/r_{si}^2}\left[1 + \frac{(4\pi^2/k_p^2 L_i^2)\cos(k_p\zeta_i) - \cos(2\pi\zeta_i/L_i)}{(1 - 4\pi^2/k_p^2 L_i^2)}\right]\ , \tag{3.15}$$

and behind the pulse ($\zeta_i < -L_i$)

$$\phi_i = \frac{a_i^2}{4}\frac{r_i^2}{r_{si}^2}e^{-2r^2/r_{si}^2}\left(\frac{4\pi^2}{k_p^2 L_i^2}\right)\frac{\sin[k_p(\zeta_i + L_i/2)]\sin(k_p L_i/2)}{(1-4\pi^2/k_p^2 L_i^2)} \ . \tag{3.16}$$

For the resonant case $L = \lambda_p$, which corresponds to maximum wakefield generation,

$$\phi_i = \frac{a_i^2}{8}\frac{r_i^2}{r_{si}^2}e^{-2r^2/r_{si}^2}\left[1 - \cos(k_p\zeta_i) - (k_p\zeta_i/2)\sin(k_p\zeta_i)\right] \tag{3.17}$$

and

$$\phi_i = \frac{\pi a_i^2}{8}\frac{r_i^2}{r_{si}^2}e^{-2r^2/r_{si}^2}\sin(k_p\zeta_i) \ , \tag{3.18}$$

within and behind the pulse, respectively.

3.2.3 Beatwave potential

During the collision (overlap) of the two laser pulses, a beat wave space charge potential ϕ_b will be driven by the slow ponderomotive beat wave, i.e., in the linear regime,

$$\left(\partial^2/\partial ct^2 + k_p^2\right)\phi_b = 2k_p^2\langle \mathbf{a}_0 \cdot \mathbf{a}_1\rangle \ , \tag{3.19}$$

where,

$$\begin{aligned}
\mathbf{a}_i &= a_i F_i(\theta_i)\cos\psi_i \ \mathbf{e}_x, \ -\pi/2 < \theta_i < \pi/2 && (3.20)\\
\theta_i &= (\pi/L_i)(z - z_i - \beta_{gi}ct) && (3.21)\\
\psi_i &= k_i z - \omega_i t && (3.22)\\
F_i &= H(\pi/2 + \theta_i)H(\pi/2 - \theta_i) && (3.23)
\end{aligned}$$

and $\mathbf{e}_x$ is a unit vector. Square laser pulse profiles of length L_i, strength $\mathbf{a}_i$ and linear polarization have been assumed. Note that diffraction effects have been also neglected for simplicity. The averaging in Eq. (3.19) is done over the fast oscillation terms ($\propto \psi_1 + \psi_2$) because their contribution to the wake is significantly smaller due to the frequency typically much larger than ω_p, i.e., we get

$$\langle 2\mathbf{a}_0 \cdot \mathbf{a}_1\rangle = a_0 F_0 a_1 F_1 \cos\psi_b, \ \psi_b = \psi_0 - \psi_1 \tag{3.24}$$

where $\psi_b = \Delta k(z - \beta_b ct)$ is the beat wave phase, $c\beta_b = \Delta\omega/\Delta k$ is the beat wave phase velocity, $\Delta\omega = \omega_0 - \omega_1$, and $\Delta k = k_0 - k_2 \simeq 2k_0$ assuming $\Delta\omega \ll \omega_i$ and a counterpropagating geometry. Following Eq. (3.14) the solution for ϕ_b in integral form can be written as

$$\phi_b = (\omega_p/2)\int_{t_0}^{t} dt' \sin T \left\langle 2\mathbf{a}_0 \cdot \mathbf{a}_1 \right\rangle, \; T = \omega_p(t - t') \tag{3.25}$$

and

$$\phi_b = \begin{cases} 0, \; t < t_{\text{on}} \\ I_b(t' = t) - I_b(t' = t_{\text{on}}), \; t_{\text{on}} < t < t_{\text{off}} \\ I_b(t' = t_{\text{off}}) - I_b(t' = t_{\text{on}}), \; t > t_{\text{off}} \end{cases} \tag{3.26}$$

where $t_{\text{on}}(z)$ is the onset time of overlap of the two colliding laser pulses at a fixed position z, $t_{\text{off}}(z)$ end of overlapping time at position z and $I_b(t, t')$ has been introduced, i.e.,

$$I_b(t, t') = \int dt' \sin T \left\langle 2\mathbf{a}_0(t') \cdot \mathbf{a}_1(t') \right\rangle \tag{3.27}$$

with

$$\left\langle 2\mathbf{a}_0 \cdot \mathbf{a}_1 \right\rangle \sin T = (1/2)a_0 a_1 F_0 F_1 \left[\sin(\psi_b + T) - \sin(\psi_b - T)\right] \tag{3.28}$$

leading to,

$$I_b(t, t') = \frac{a_0 a_1}{2} F_0 F_1 \left[-\frac{\cos(\psi_b + T)}{\dot{\psi}_b + \dot{T}} + \frac{\cos(\psi_b - T)}{\dot{\psi}_b - \dot{T}} \right] \tag{3.29}$$

where

$$T = \omega_p(t - t'), \qquad \dot{T} = -\omega_p, \tag{3.30}$$

$$\psi_b = (k_1 - k_2)z - (\omega_1 - \omega_2)t', \qquad \dot{\psi}_b = -\Delta\omega = -(\omega_1 - \omega_2), \tag{3.31}$$

has been used. Inserting Eqs. (3.30)-(3.31) into Eq. (3.29) gives

$$I_b = \frac{a_0 a_1 F_0 F_1}{2} \left[-\frac{\cos\left[\psi_b + \omega_p(t - t')\right]}{\Delta\omega + \omega_p} - \frac{\cos\left[\psi_b - \omega_p(t - t')\right]}{\Delta\omega - \omega_p} \right] \tag{3.32}$$

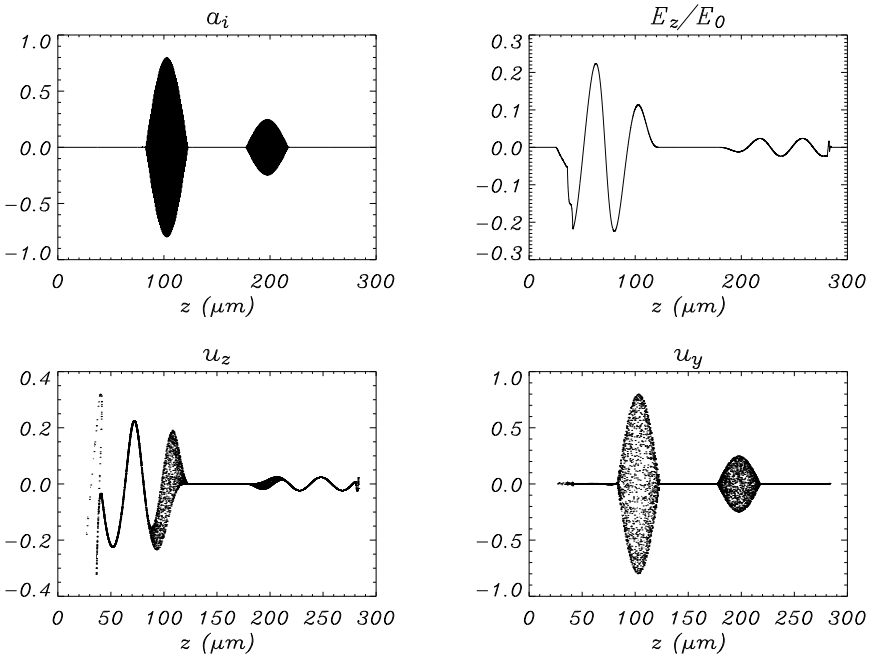

Figure 3.1: 1D PIC simulation using two linearly polarized half-sine laser pulses with normalized average vector potential $\langle a_0^2 \rangle = 0.32$ (drive pulse), $\langle a_1^2 \rangle = 3.125 \times 10^{-2}$ (backward pulse), laser full length (FWHM) $L_0 = L_1 = 20\ \mu$m (resonant), laser carrier frequency $\lambda_0 = \lambda_1 = 0.8\ \mu$m, grid size $\Delta x = \lambda_0/40 = 0.02\ \mu$m, 100 particles per cell and a plasma wavelength $\lambda_p = 40\ \mu$m, i.e., background density $n_0 = 6.9 \times 10^{17}$ cm^{-3}. Normalized vector potential a_i, wakefield E_z/E_0, transverse momentum u_y and axial momentum u_z is shown before collision.

and after further simplifications,

$$\boxed{I_b = \frac{a_0 a_1 F_0 F_1}{\Delta\omega^2 - \omega_p^2}[-\omega_p \cos\psi_b \cos\omega_p(t-t') - \Delta\omega \cos\psi_b \cos\omega_p(t-t')]} \tag{3.33}$$

As an example, analytical solutions for ϕ_b can be found in the linear limit (for the case of square pulse profiles, without diffraction) and equal frequencies $\Delta\omega = 0$. In this case,

$$I_b(t,t') = \frac{a_0 a_1 F_0 F_1}{\omega_p} \cos\psi_b \cos\omega_p(t-t'), \tag{3.34}$$

i.e., during the overlap $t_{\rm on} < t < t_{\rm off}$,

$$\phi_b = (a_0 a_1/4)\,[1 - \cos\omega_p\,(t - t_{\rm on})] \cos\psi_b\ , \tag{3.35}$$

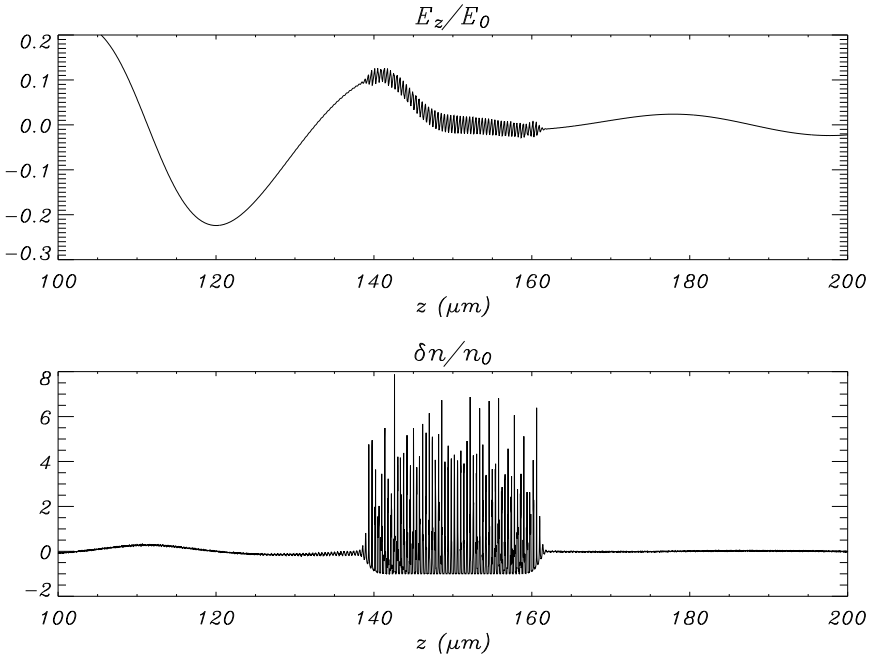

Figure 3.2: Normalized wakefield E_z/E_0 and density variation $\delta n/n_0$ is shown during head-on collision and for the parameters of Fig. 3.1. Note that the resolution within one period of the density inside the beatwave is sampled by 20 grid points and 100 macroparticles per cell.

and after interaction $t > t_{\rm off}$

$$\phi_b = (a_0 a_1/4)\left[\cos\omega_p\left(t - t_{\rm off}\right) - \cos\omega_p\left(t - t_{\rm on}\right)\right]\cos\psi_b \ . \tag{3.36}$$

Associated with ϕ_b is a density perturbation $\delta n_b = n_0 k_p^{-2}\nabla^2\phi_b$, equivalent to the scaling $\delta n_b/n_0 \simeq -(2k_0/k_p)^2\phi_b$. Strictly speaking, the linear solution given by Eq. (3.35) and Eq. (3.36) is only valid if $|\delta n_b/n_0| \ll 1$, or $(k_0/k_p)^2 a_0 a_1 \ll 1$, which is easily violated even for modest values of $a_0 a_1$ since $(k_0/k_p)^2 \gg 1$. However, the relation $\nabla^2\phi_b = k_p^2\delta n_b/n_0$ holds in the nonlinear limit and hence the scaling $|\phi_b| \sim (k_p/2k_0)^2|\delta n_b/n_0|$ holds even for large values of $\delta n_b/n_0$, assuming $\nabla^2\phi_b \sim 4k_0^2\phi_b$. In particular, as long as $|\delta n_b/n_0| \ll (2k_0/k_p)^2(a_0 a_1)$ [i.e., $(2k_0/k_p)^2(a_0 a_1) \sim 10^3$ in the simulations presented below], then $|\nabla\phi_b| \ll |\nabla a_0 a_1/2|$ (i.e., $|\phi_b| \ll a_0 a_1$) and the effects of the space charge potential of the beat wave ϕ_b can be neglected in comparison to the ponderomotive potential of the beat wave $a_0 a_1$. Hence, in the following test particle

simulations, ϕ_b is neglected. Note that this has been confirmed by Particle-In-Cell (PIC) simulations [54, 55]. Figure 3.1 shows a 1D-PIC simulation using the code VORPAL [56], where two counterpropagating linearly polarized laser pulses of equal frequencies $\Delta\omega = 0$, strength $\langle a_0^2 \rangle = 0.32$ and $\langle a_1^2 \rangle = 3.125 \times 10^{-2}$ propagate in an underdense plasma $\omega_0/\omega_p = 50$. The two pulses are seeding a resonant plasma wave, i.e., $L_0 = L_1 = \lambda_p$. The plot shows the normalized laser vector potential a_i, the normalized wakefield E_z/E_0 where E_0 is the cold nonrelativistic wave breaking field $E_0[\mathrm{V/m}] \simeq 96(n_0[\mathrm{cm}^{-3}])^{1/2}$, the transverse electron normalized momentum u_y and longitudinal u_z. The laser envelope was assumed to be a half-sine, i.e., of the form $a_{yi} = a_i \sin(\pi\zeta_i/L_i)\cos\psi_i$. Figure 3.2 shows normalized wakefield E_z/E_0, and normalized electron density $\delta n/n_0$ for the parameters of Fig. 3.1 and during collision of the two laser pulses. Inside the beating region we have $\delta n/n_0 \sim \delta n_b/n_0$ and the maximum density is found to be $|\delta n_b/n_0|_{\ \mathrm{max}} \simeq 8$ leading to a small amplitude electric field generation $|E_{zb}/E_0| \sim (k_p/2k_0)\ |\delta n_b/n_0|$ at a frequency $\omega_0/2$. This additionnal electric field is negligible and consequently will not induce trapping as stated above. Note that for two half-sine laser pulses linear theory predicts $\delta n_b/n_0 \sim (k_0/k_p)^2 a_0 a_1/2 \simeq 250$ for the laser-plasma parameters under consideration.

3.3 One-dimensional equation of motion

It is possible to derive an exact 1D equation of motion for an electron in the electromagnetic fields of the drive and injection laser pulse combined with the plasma wave. In this Section, we will transform the equations to the frame comoving with the beat wave phase velocity, enabling us to get an estimate for the contribution of the different fields to the overall electron motion. It will be shown that the electron trajectory is dominated by the interaction with the colliding laser pulse induced fields whereas the wakefield acts as a small perturbation. This separation of scales in the equation of motion will allow us to consider alternate analytical means, such as an island overlap criterion, providing a precise estimate of the trapping threshold for injection of background plasma electrons into the plasma wave *via* the interaction with colliding laser pulses. The latter will be discussed in the next sections.

From Eqs. (2.16)-(2.17), one can deduce the 1D equations of motion in a La-

grangian coordinate system,

$$\mathbf{u}_\perp = \mathbf{a}_\perp \,, \tag{3.37}$$

$$\frac{du_z}{dct} = \frac{\partial \phi}{\partial z} - \frac{u_\perp}{\gamma}\frac{\partial a_\perp}{\partial z} \,. \tag{3.38}$$

Inserting Eq. (3.37) into Eq. (3.38) and rewritting the latter as a function of the beat wave phase $\psi_b = \Delta k(z - \beta_b ct)$, we get

$$\boxed{\ddot{\psi}_b - \omega_T^2(\psi_b, \dot{\psi}_b)\sin\psi_b = \delta_L \omega_L^2(\psi_b, \dot{\psi}_b)\cos\epsilon\left[\psi_b + \frac{(\beta_b - \beta_\phi)\,\tau}{(1-\beta_b^2)\sqrt{\epsilon_T}}\right]} \,, \tag{3.39}$$

where β_ϕ is the phase velocity of the plasma wave, $\epsilon = k_p/\Delta k$, $\tau = \hat{\omega}_T t$, $\hat{\omega}_T = c\Delta k(1-\beta_b^2)\epsilon_T$ is the bounce frequency of an electron in a deeply trapped beat wave orbit (orbits in Hamiltonian sytems will be studied in Sec. 3.4),

$$\begin{aligned}
\omega_T^2 &= (1 + 2\epsilon_T \cos\psi_b)^{-1}\left[1 - (1-\beta_b^2)\,\epsilon_T\dot{\psi}_b^2 - 2\beta_b\epsilon_T^{1/2}\dot{\psi}_b\right]\left[1 - \beta_b\epsilon_T^{1/2}\dot{\psi}_b\right] \,, \\
\omega_L^2 &= (1 + \epsilon_T \cos\psi_b)^{-1/2}\left[1 - (1-\beta_b^2)\,\epsilon_T\dot{\psi}_b^2 - 2\beta_b\epsilon_T^{1/2}\dot{\psi}_b\right]^{3/2} \,, \\
\delta_L &= \epsilon_L\left[(1-\beta_b)^2\,\epsilon_T\right]^{-1} \,,
\end{aligned} \tag{3.40}$$

$\epsilon_T = a_0 a_1/(1 + a_0^2 + a_1^2)$, $\epsilon_L = \phi_0\epsilon/(1 + a_0^2 + a_1^2)^{-1/2}$ and $\dot{\psi}_b$ stands for $d\psi_b/d\tau$. In this model two circularly polarized squared laser pulse profiles have been assumed along with a wakefield of the form $\phi = \phi_0 \sin k_p\zeta$. A detailed derivation of Eq. (3.39) is done in Appendix D.

It is clear from Eq. (3.39) that the exact axial equation of motion has the form of a non linear equation for coupled pendulum with amplitude and velocity dependent frequencies $\omega_T(\psi_b, \dot{\psi}_b)$ and $\omega_L(\psi_b, \dot{\psi}_b)$ [57]. The parameter δ_L is typically small implying the main contribution to the electron motion is coming from the beat wave potential. The wakefield acts as a perturbation to the electron dynamics inside the beatwave. Typically a trapped electron will circulated a couple of times inside a beatwave orbit while the accumulated perturbation from the wake, which is equivalent to a DC field for the electron ($\lambda_b = \lambda_0/2 \ll \lambda_p$) will allow for the beatwave orbit to open and lead an electron to a trapped orbit of the wakefield. Trapping of a background electron is obviously dependent of the initial condition of the two colliding pulse.

Eq. (3.39) could be solved to some extend analytically using, for instance, a multiple scale perturbation technique [41]. A simpler argument, considering the plasma wave amplitude as a constant during the interaction time leading to injection, will be used in Sec. 3.5 to show the opening of the beatwave orbits. In Sec 3.6, We will study the full electron dynamics numerically for the case of linearly polarized laser pulses. A simplified analytical theory based on an island overlap criterion is presented next.

3.4 Phase space analysis

To gain a qualitative understanding of the basic process, a heuristic theory of injection and trapping is presented. Specifically, an approximate expression for the injection threshold can be obtained by considering the motion of an electron in the wakefield and the beat wave individually, and by using an island overlap criteria [58, 59]. Recall that the beat wave leads to formation of phase space buckets (separatrices) of width $2\pi/\Delta k \simeq \lambda_0/2$. This width is much shorter than the wakefield period (λ_p), thus allowing for a separation of spatial scales. In the following analytical treatment, electron motion will be described using a Hamiltonian approach in the limit of a broad laser pulse ($r_0 k_p \gg 1$ and neglecting diffraction effects) and assuming $\omega_p^2/\omega_i^2 \ll 1$ (such that the group and phase velocities are approximately c). Furthermore, circular polarization will be assumed, $\mathbf{a} = \sum_i \hat{a}_i(\cos\psi_i \mathbf{e}_x + \sin\psi_i \mathbf{e}_y)$, such that $a^2 = \hat{a}_0^2 + \hat{a}_1^2 + 2\hat{a}_0\hat{a}_1\cos\psi_b$ is independent of the fast laser phase ψ_i and only a function of the beat phase $\psi_b = \psi_0 - \psi_1 \simeq 2k_0 z - \Delta\omega t$.

To underline the heuristic character of using an overlap criterion, we quote a passage of Chirikov's paper [58]:
"A plausible condition for the occurrence of the stochastic instability [i.e., region in phase space where an electron can transit from one resonance (the beat wave orbits in our case) to another one (the wakefield orbits)] seems to be the approach of resonances down to the distance on the order of a resonance size. Such an approach was naturally called the *resonance overlap*. To be precise, the overlap of resonances begins when their separatrices touch each other. The possibility for a system to move from one resonance to another under the above condition is quite obvious. The problem is another one: how to calculate the condition of separatrix touching taking into account

a deformation of the separatrix by a neighboring resonance? The simplest method, a quite rough one, is to use the unperturbed resonance parameters, i.e., to consider each of the resonances as if another one were absent. It is clear that one expect to get in this way only an order of magnitude estimate. This criterion, thus, turn out to be a quite rough one, yet it is fairly efficient since the above procedure may be easily performed even in the case of a rather complicated system"

Following his comment the overlap criterion applied to colliding pulse interaction is believed to be the most appropriate under the condition $\delta_L \ll 1$. In the next Section, we will calculate analytically electron orbits inside the plasma wave.

3.4.1 Plasma wave

In the absence of the beat wave ($a_1 = 0$), the nonlinear motion of an electron in a plasma wave with relativistic phase velocity is described by the Lorentz equation, which in the 1D limit can be written in the following form [46]

$$\frac{d\psi}{d\omega_p t} = \frac{\partial H}{\partial u_z} = \frac{u_z}{\sqrt{\gamma_\perp^2(\psi) + u_z^2}} - \beta_\phi \ , \tag{3.41}$$

$$\frac{du_z}{d\omega_p t} = -\frac{\partial H}{\partial \psi} = \frac{\partial \phi}{\partial \psi} - \frac{1}{2\sqrt{\gamma_\perp^2(\psi) + u_z^2}} \frac{\partial \gamma_\perp^2}{\partial \psi} \ , \tag{3.42}$$

where $\mathbf{u} = \mathbf{p}/m_e c$ is the normalized electron momentum, $\gamma_\perp = (1 + \hat{a}^2)^{1/2}$, $\psi = k_p(z - v_\phi t)$ is phase of the plasma wave, $v_\phi = c\beta_\phi = c(1 - 1/\gamma_\phi^2)^{1/2}$ is the phase velocity of the plasma wave (approximately equal to the group velocity of the drive laser pulse), and

$$\boxed{H(u_z, \psi) = \sqrt{\gamma_\perp^2(\psi) + u_z^2} - \beta_\phi u_z - \phi(\psi)} \tag{3.43}$$

is the Hamiltonian. Here, $\phi(\psi)$ is the laser-driven plasma wave (wakefield) potential given by Eq. (3.14) and the subscript 0, denoting the pump laser pulse, has been omitted. In the above equations, the identity $\mathbf{u}_\perp = \mathbf{a}$ has been used, which is exact in 1D. Note that the Hamiltonian is time independent (a function of only ψ) and, therefore, is constant along any orbit.

The normalized axial momentum of an electron on an orbit (specified by the value

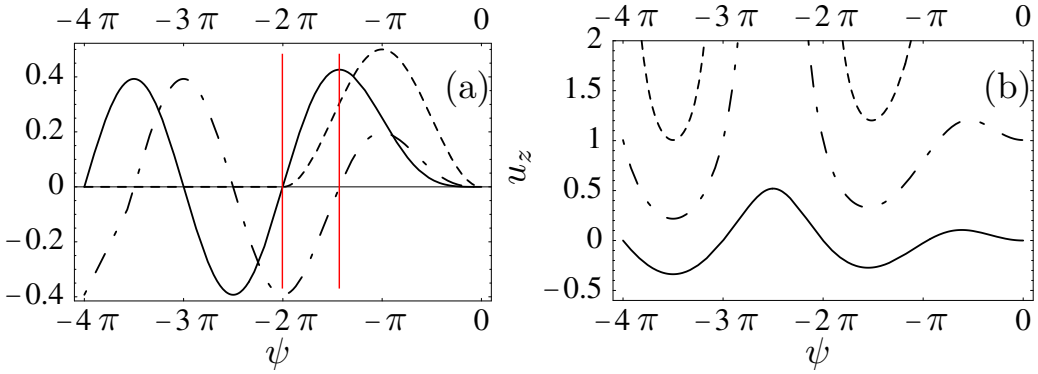

Figure 3.3: (a) Wakefield ϕ (solid line), drive laser pulse envelope $\langle a^2 \rangle$ (dashed line), and longitudinal electric field $E_z = -\partial_z \phi$ (dot-dashed line) for $L_0 = \lambda_p$ and $\langle a_0^2 \rangle = 0.5$. The focusing and accelerating region behind the first bucket of the plasma wave is shown between the solid red lines. (b) Phase space plot showing cold fluid orbit (solid line), trapped and focused orbit (dashed line), and trapped separatrix (dot-dashed line).

of H_c) in the plasma wave is found from Eq. (3.43) by setting $H = H_c$, where H_c is a constant, i.e.,

$$u_z(\psi) = \beta_\phi \gamma_\phi^2 \left(H_c + \phi\right) \pm \gamma_\phi \sqrt{\gamma_\phi^2 \left(H_c + \phi\right)^2 - \gamma_\perp^2} \; . \tag{3.44}$$

For example, assuming the plasma is initially cold (i.e., $u_z = 0$ in front of the laser pulse where $a^2 = \phi = 0$), the background electron fluid motion in the plasma wave is defined by the orbit $H_c = 1$. The Hamiltonian $H(u_z, \psi)$ exhibits fixed points ($du_z/dt = d\psi/dt = 0$) that are stable ("O" points) at $u_z = \gamma_\perp(\psi_o)\gamma_\phi\beta_\phi$, $\psi_o \simeq -1.47 - 0.60\, k_p L + 0.02\, k_p^2 L^2$ inside the drive pulse and $\psi_o = -\pi/2 - k_p L/2$ modulo 2π outside. Unstable fixed points ("X" points) lie at $u_z = \gamma_\phi \beta_\phi$ and $\psi_x = -3\pi/2 - k_p L/2$ modulo 2π. The boundary between trapped and untrapped orbits defines the separatrix orbit, which is specified by $H_c = H(\gamma_\phi \beta_\phi, \psi_x)$ and crosses the X-point.

Figure 3.3(a) shows wakefield ϕ (solid line), drive laser pulse envelope $\hat{a}^2$ (dashed line), and longitudinal electric field $E_z = -\partial_z \phi$ (dot-dashed line) for the parameters $L_0 = \lambda_p$ and $\langle a_0^2 \rangle = 0.5$ as obtained from Eqs. (3.17)-(3.18). The corresponding phase space orbits are plotted in Fig. 3.3(b) as obtained from Eq. (3.44). Shown are the cold fluid orbit, separatrix between trapped and untrapped orbits, and the trapped and focused (2D) separatrix.

Behind the drive laser pulse, the width of the separatrix is $\Delta\psi = 2\pi$, however, only half this region is accelerating (the left half for the case of the laser pulse propagating to the right). The width of the accelerating region of the wakefield is $\Delta\psi = \pi$ and extends from the O-point to the X-point. When two-dimensional (2D) effects are taken into consideration (specifically, the focusing and defocusing regions associated with the transverse electric field of the plasma wave), there exists only a region of width $\Delta\psi = \pi/2$ that is both accelerating and focusing (extending from the O-point to half the distance to the X-point). Hence, the "2D separatrix", defining the region of trapped orbits that are both accelerating and focusing, is given by $H_c = H(\gamma_\phi\beta_\phi, -\pi - k_pL/2 \text{ modulo } 2\pi) \equiv H_f$. For the case of a single injection pulse colliding with the pump pulse, trapping will occur within the first 2D separatrix, which typically extends from the O-point within the pump laser pulse to roughly half the distance to the first X-point immediately behind the pump pulse. This region of trapped orbits that are in the accelerating and focusing region of the wakefield are characterized by values of the Hamiltonian in the range $H_f = H(\gamma_\phi\beta_\phi, -\pi - k_pL/2 \text{ modulo } 2\pi) \leq H \leq H_o = H(\gamma_\phi\beta_\phi, \psi_o)$.

In the limit $\gamma_\phi^2(H_c+\phi)^2 \gg \gamma_\perp^2$, Eq. (3.44) can be expanded to yield $u_z = 2\gamma_\phi^2(H_c+\phi)$ and $u_z = \gamma_\perp^2/[2(H_c+\phi)] - (H_c+\phi)/2$ for the plus and minus portions of Eq. (3.44), respectively, assuming $\gamma_\phi^2 \gg 1$. These expressions are useful for evaluating $u_z(\psi)$ on the separatrix for values of ψ in the vicinity of the O-points.

3.4.2 Ponderomotive beat wave

The motion of the electron in the beat wave alone ($\phi = 0$) is described by the beat wave Hamiltonian [19, 20, 46]

$$\boxed{H_b(u_z, \psi_b) = \sqrt{\gamma_{\perp b}^2(\psi_b) + u_z^2} - \beta_b u_z - \phi_b(\psi_b)} \tag{3.45}$$

where $\gamma_{\perp b}^2(\psi_b) \simeq 1 + \hat{a}_0^2 + 2\hat{a}_0\hat{a}_1\cos\psi_b$ ($a_1^2 \ll a_0^2$ has been assumed), $\psi_b = (k_0 - k_1)(z - \beta_b ct)$ is the beat wave phase (note $k_1 < 0$ for the backward pulse), and $c\beta_b = \Delta\omega/(k_0 - k_1)$ is the beat wave phase velocity ($\Delta\omega = \omega_0 - \omega_1$ with, typically, $\Delta\omega^2 \ll \omega_0^2$ and $\beta_b^2 \ll 1$). In the following, the space charge potential driven by the beating of the two colliding pulses $\phi_b(\psi_b)$ will be neglected since ϕ_b is typically

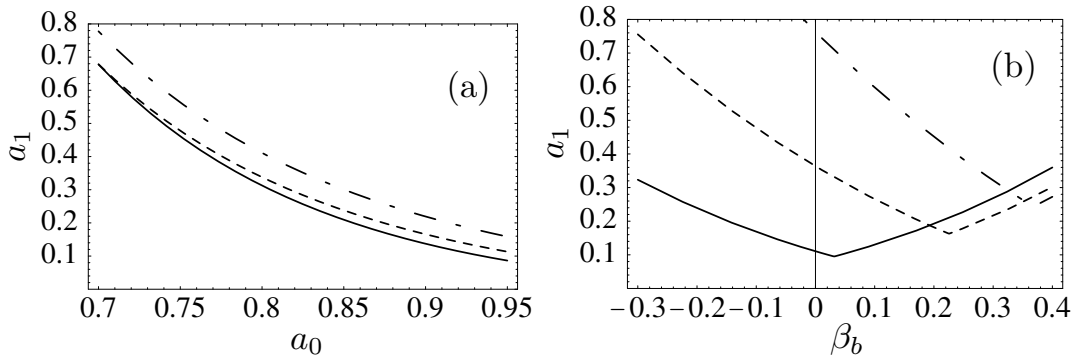

Figure 3.4: (a) Injection laser pulse amplitude a_1 versus pump laser pulse amplitude a_0 at threshold for $\psi_{\rm opt} = -3\pi/2$, $\beta_b \simeq 0.05$, $L_0 = \lambda_p$ (solid line), $L_0 = 9\lambda_p/8$ (dashed line), and $L_0 = 5\lambda_p/4$ (dot-dashed line). (b) Injection laser pulse amplitude a_1 versus β_b at threshold for $\psi_{\rm opt} = -3\pi/2$, $L_0 = \lambda_p$, $\langle a_0^2 \rangle = 0.9$ (solid line), $\langle a_0^2 \rangle = 0.64$ (dashed line), and $\langle a_0^2 \rangle = 0.49$ (dot-dashed line).

much smaller than the ponderomotive beat wave potential ($\hat{a}_0 \hat{a}_1$), as discussed above. Also, since $k_0 - k_1 \simeq 2k_0$ (i.e., the width of the beat wave separatrix is approximately $\lambda_0/2$), the spatial variation in the pulse envelopes $\hat{a}_{0,1}$, which are assumed to have pulse lengths much greater than λ_0, will be neglected.

The normalized axial momentum of an electron in the beat wave is

$$u_{z_b}(\psi_b) = \beta_b \gamma_b^2 H_{bc} \pm \gamma_b \sqrt{\gamma_b^2 H_{bc}^2 - \gamma_{\perp b}^2}\,, \tag{3.46}$$

where H_{bc} is a constant specifying a given orbit. The X-points are given by $\psi_{\rm x} = 0$ modulo 2π and the separatrix is specified by $H_b(\gamma_\perp \gamma_b \beta_b, 0) = \gamma_\perp(0)/\gamma_b$. The maximum and minimum normalized axial momenta of an electron on a trapped beat wave orbit (extrema of the separatrix) are

$$u_{b\pm} = \gamma_b \beta_b \gamma_{\perp b}(0) \pm 2\gamma_b \sqrt{\hat{a}_0 \hat{a}_1}\,. \tag{3.47}$$

3.4.3 Trapping threshold

Assuming circular polarization, an approximate threshold for injection into the wake-field can be estimated by applying a phase space separatrix overlap condition (i.e.,

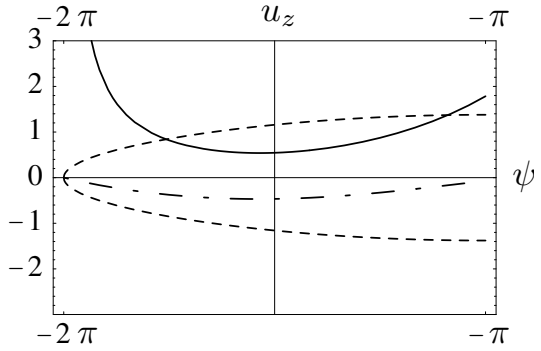

Figure 3.5: Phase-space (ψ, u_z) showing trapped and focused separatrix (solid line), cold fluid orbit (dot-dashed line), and maximum of the beat wave separatrix (dashed line) for $\langle a_0^2 \rangle = 0.9$, $\langle a_1^2 \rangle = 0.25$, $\beta_b = 0$, and $L_0 = \lambda_p$.

Chirikov island overlap criterion) [59]. Specifically, island overlap requires (i) the maximum momentum of the beat wave separatrix exceed the minimum momentum of the wakefield separatrix and (ii) the minimum momentum of the beat wave separatrix be less than the plasma electron fluid momentum, i.e.,

$$u_{b+} \geq u_z(H = H_f) \; , \tag{3.48}$$

$$u_{b-} \leq u_z(H = 1) \; . \tag{3.49}$$

If this occurs, then there exists a phase space path that can take an electron from the cold fluid orbit, through the beat wave separatrix, and finally on a trapped orbit within the 2D separatrix of the wakefield.

The trapping threshold can be solved analytically. In the limit $\beta_b \ll 1$, Eqs. (3.48) and (3.49) imply

$$2\hat{a}_0\hat{a}_1 \simeq \begin{cases} u_z(H_f)\left[u_z(H_f)/2 - \beta_b\sqrt{1+\hat{a}_0^2+u_z^2(H_f)/2}\right] \; , & \text{if } \beta_b \leq \beta_* \\ u_z(H=1)\left[u_z(H=1)/2 - \beta_b\sqrt{1+\hat{a}_0^2+u_z^2(H=1)/2}\right] \; , & \text{if } \beta_b > \beta_* \end{cases} \tag{3.50}$$

where

$$\beta^* = \frac{\left[u_z^2(H_f) - u_z^2(H=1)\right]/\sqrt{2}}{\left[u_z(H_f)\sqrt{2+2\hat{a}_0^2+u_z^2(H_f)} - u_z(H=1)\sqrt{2+2\hat{a}_0^2+u_z^2(H=1)}\right]} \; . \tag{3.51}$$

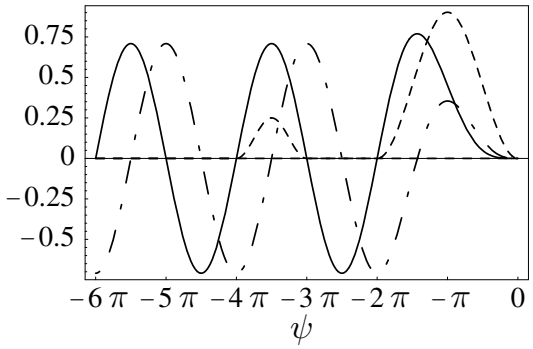

Figure 3.6: Wakefield ϕ (solid line), drive and injection laser pulses envelope $\langle a^2 \rangle$ (dashed line), and longitudinal electric field $E_z = -\partial_z \phi$ (dot-dashed line) for $L_0 = \lambda_p$, $\langle a_0^2 \rangle = 0.9$, $L_1 = \lambda_p/2$ and $\langle a_1^2 \rangle = 0.25$

Numerical solutions to the analytical estimation of the trapping threshold, Eqs. (3.48) and (3.49), are shown in Fig. 3.4. Note that, in Eqs. (3.48) and (3.49), $\hat{a}_0$ and ϕ are functions of ψ, i.e., the relative position within the pump laser pulse. The minimum value of a_1 required for trapping is plotted versus a_0 in Fig. 3.4(a) for different lengths of the drive pulse for $\beta_b = 0.05$ and $\psi = \psi_{\rm opt} = -3\pi/2$ (i.e., near the back of the pump pulse). Trapping is easiest (occurs for the lowest value of a_1 for a given a_0) when $L = \lambda_p$, which is the resonant case for wakefield generation that yields the largest wakefield amplitude (i.e., $\phi_0 \simeq 0.4$ for $L = \lambda_p$ and $\langle a_0^2 \rangle = 0.5$). Similarly, Fig. 3.4(b) shows the value of a_1 required for trapping as a function of the beat wave phase velocity β_b for several values of a_0 with $L_0 = \lambda_p$ and $\psi = \psi_{\rm opt} = -3\pi/2$. For these parameters, trapping is optimized for small positive values of β_p. Figure 3.5 shows an example of the phase space orbits (the 2D separatrix, the beat wave separatrix, and the fluid orbit) for a case where the island overlap condition is well satisfied ($\langle a_0^2 \rangle = 0.9$, $\langle a_1^2 \rangle = 0.25$, $\beta_b = 0.1$ and $L_0 = \lambda_p$).

3.5 Detailed study of the injection process for circularly polarized laser pulses

In this section we will analyse a specific configuration of optical injection using three circularly polarized laser pulses [19, 20]. The drive pulse is seeding the wakefield and an independent injection pulse is positioned at some specific location behind allowing

for a controlled injection of background plasma electrons as shown in Fig. 3.6. Adding a third laser provide more freedom regarding the selection of a region of phase-space. This configuration also has a pedagogic purpose, the two injection lasers are now independent of the plasma wave parameters, controlled by the drive pulse, and provide a clear understanding of the injection process and Chirikov island overlap criterion for the case of circularly polarized pulses.

Starting again from the equation of motion for broad laser pulses $k_p r_i \gg 1$, one may find an approximate expression for Eq. (3.39) assuming the wakefield amplitude is approximatelly a constant within the size of a trapped beatwave orbit, i.e.,

$$\frac{d\psi_b}{d(\Delta k c t)} = \frac{\partial H_b}{\partial u_z} = \frac{u_z}{\sqrt{\gamma_{\perp b}^2(\psi_b) + u_z^2}} - \beta_b \ , \tag{3.52}$$

$$\frac{du_z}{d(\Delta k c t)} = -\frac{\partial H_b}{\partial \psi_b} = \frac{k_p}{\Delta k}\frac{E_z(\psi_{\rm inj})}{E_0} - \frac{1}{2\sqrt{\gamma_{\perp}^2(\psi_b) + u_z^2}}\frac{\partial \gamma_{\perp b}^2}{\partial \psi_b} \ , \tag{3.53}$$

giving,

$$\boxed{H_b(u_z, \psi_b) = \sqrt{\gamma_{\perp b}^2(\psi_b) + u_z^2} - \beta_b u_z + \mu \psi_b} \tag{3.54}$$

where $\mu = \epsilon E_z(\psi_{\rm inj})/E_0$, $\epsilon = k_p/\Delta k \ll 1$, $\psi_{\rm inj} = k_p \zeta_{\rm inj}$ is the phase of injection and $\zeta_{\rm inj} = z_{\rm inj} - c t_{\rm inj}$. The coefficient μ is typically a small number and the Hamiltonian (3.54) gives an approximate description of the opening of the beatwave orbits induced by the plasma wave. Figure 3.7(a) shows the orbits in the frame comoving with the beatwave group velocity for the case $\mu = 0$, i.e., no plasma wave and (b) for $\mu = -0.07$ and shows a clear opening to the right ($\mu < 0$) of the orbits. In summary, trapping may occur the following way. In the region $-2\pi < \psi < -3\pi/2$, the plasma electrons are flowing backward ($u_z < 0$), the electric field is accelerating ($E_z/E_0 < 0$ giving $\mu < 0$) and consequently the beatwave orbits open to the right [Fig. 3.7] taking an electron from below to above the beatwave separatrix. Such an electron would acquire a positive axial momentum which is sufficiently high to be trapped and accelerated by the plasma wave. The open phase-space orbits provide a possible path by which the ponderomotive beatwave can lead to trapping of electrons in the plasma wave.

Note that for a sufficiently long interaction time between the colliding injection pulses, i.e., typically $\Delta t_{\rm int} \gg \tau_b$ where $\tau_b = 2\pi c/\hat{\omega}_T$ is the bounce time of a deeply trapped electron [see Sec. 3.3 for a definition of $\hat{\omega}_T$], even lower untrapped orbits such

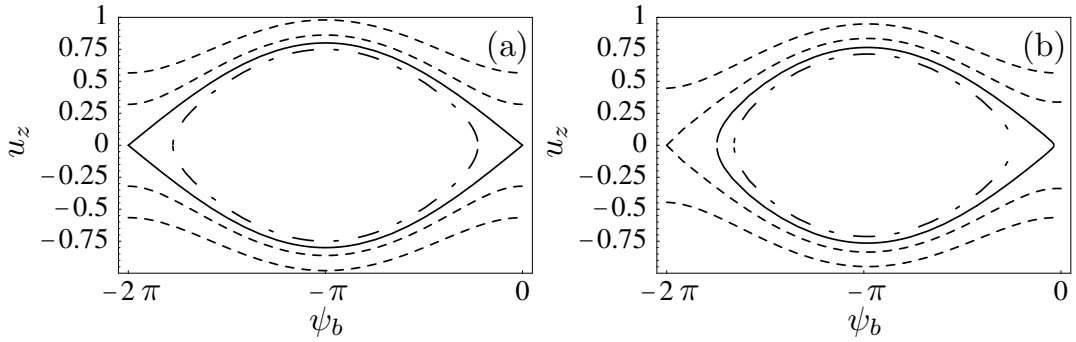

Figure 3.7: (a) Beat wave separatrix (solid line), trapped orbit (dot-dashed line) and untrapped orbits (dashed line) for squared laser pulses with $\langle a_1^2 \rangle = \langle a_2^2 \rangle = 0.16$ and $\mu = 0$. (b) Same orbits but for $\mu = -0.07$ showing distortion of the beat wave orbits in phase space due to the presence of the plasma wave $\mu \neq 0$. With $\mu < 0$ the bucket open to the right.

as, for instance, the one drawn in Fig. 3.7(b) may end-up trapped by one of the next beatwave buckets as shown in Fig 3.11. As long as the electric field is accelerating, i.e., $\mu < 0$, the perturbation carried out by the wakefield will provide an increase of the mean energy of the electrons, or in other words will pull electrons up in phase-space.

Next we provide an estimate for the accuracy of the island criterion overlap, we assume that $\Delta t_{\rm int} \sim \tau_b$ such that the opened orbit shown in Fig. 3.7(b) is assumed to be the new separatrix between the trapped and untrapped region of the beatwave buckets. One may deduce the equation for $u_{zb}(\psi_b)$ from Eq. (3.54), e.g,

$$u_{zb\pm}(\psi_b) = \beta_b \gamma_b^2 \left(H_{bc} - \mu\psi_b\right) \pm \gamma_b \sqrt{\gamma_b^2 \left(H_{bc} - \mu\psi_b\right)^2 - \gamma_{\perp b}^2(\psi_b)} \; . \tag{3.55}$$

Using the value of the Hamiltonian for the separatrix in the unperturbed case derived in Sec. 3.4.2,

$$H_{bc} = \gamma_{\perp b}(-2\pi)/\gamma_b \; , \tag{3.56}$$

provides an estimate for the trajectory of an electron with the same total energy when $\mu \neq 0$. Introducing (3.56) into Eq. (3.55) yields,

$$\begin{aligned} u_{zb\pm}^{\rm un}(\psi_b) \;\; = \;\; & \beta_b \gamma_b \left[\gamma_{\perp b}(-2\pi) - \mu\psi_b\gamma_b\right] \pm \\ & \gamma_b \sqrt{\gamma_{\perp b}^2(-2\pi) - \gamma_{\perp b}(\psi_b) - 2\gamma_{\perp b}(-2\pi)\mu\psi_b\gamma_b + \mu^2\psi_b^2\gamma_b^2} \; . \end{aligned} \tag{3.57}$$

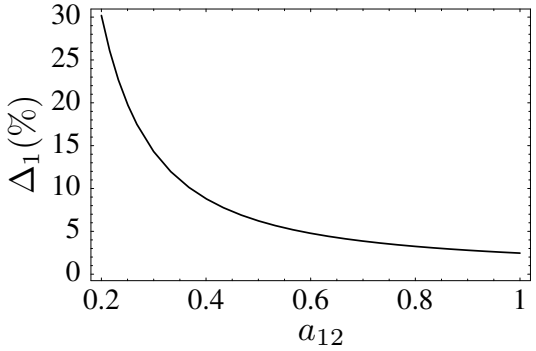

Figure 3.8: Relative difference Δ_1 between $u_b^{\rm pb}$ and $u_b^{\rm un}$ as a function of injection laser strengh assuming $a_1 = a_2 = a_{12}$ and $\mu = -0.07$

giving a maximum (minimum) value for $u_{zb\pm}^{\rm un}$ at location $\psi_b = -\pi$, and

$$u_{b\pm}^{\rm un} = \beta_b\gamma_b\left[\gamma_{\perp b}(-2\pi) - \pi|\mu|\gamma_b\right] \pm 2\gamma_b\sqrt{a_1a_2}\sqrt{1 - \frac{\pi|\mu|\gamma_b\gamma_{\perp b}(-2\pi)}{2a_1a_2}}\ , \tag{3.58}$$

where the term $\mu^2\psi_b^2\gamma_b^2$ was assumed negligibly small. Equation (3.58) may also be rewritten using the notations of Sec. 3.3,

$$\boxed{u_{b\pm}^{\rm un} = \beta_b\gamma_b\gamma_{\perp b}(-2\pi)\left(1 - \pi\gamma_b\epsilon_L\right) \pm 2\gamma_b\sqrt{a_1a_2}\sqrt{1 - \frac{\pi\delta_L}{2\gamma_b}}} \tag{3.59}$$

where $\delta_L = |\mu|\gamma_{\perp b}(-2\pi)\gamma_b^2/(a_1a_2)$. Following the same procedure, the Hamiltonian for the new separatrix is found to be

$$H_{bc} = \gamma_{\perp b}(-2\pi)/\gamma_b + 2\pi|\mu|\ , \tag{3.60}$$

giving,

$$\boxed{u_{b\pm}^{\rm pb} = \beta_b\gamma_b\gamma_{\perp b}(-2\pi)\left(1 - \pi\gamma_b\epsilon_L\right) \pm 2\gamma_b\sqrt{a_1a_2}\sqrt{1 + \frac{\pi\delta_L}{2\gamma_b}}} \tag{3.61}$$

and

$$\boxed{\Delta u_b = \left|\ u_{b\pm}^{\rm pb} - u_{b\pm}^{\rm un}\ \right| = \pi\delta_L\sqrt{a_1a_2} + O(\delta_L^2)} \tag{3.62}$$

Equation 3.62 provides an important result, confirming the fact that a small pertur-

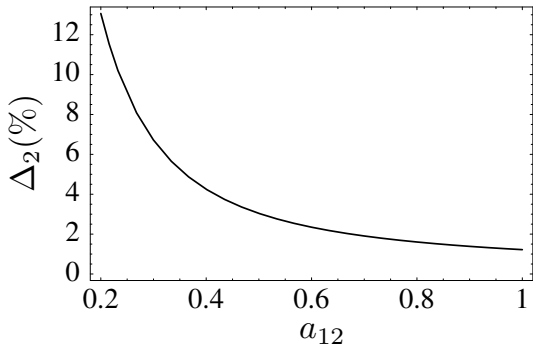

Figure 3.9: Relative difference Δ_2 between $u_b^{\rm pb}$ and $u_b^{\rm un}(\delta_L = 0)$ as a function of injection laser strengh assuming $a_1 = a_2 = a_{12}$ and $\mu = -0.07$

bation $\delta_L \ll 1$ [either a small wake amplitude $E_z(\psi_{\rm inj})/E_0$, a very underdense plasma $\epsilon \ll 1$ or a large value of a_i] prevents a large opening of the orbits, or in other words, lowers the phase-space volume from which background plasma electrons are trapped. Figure 3.8 plots the relative difference $\Delta_1 = (u_b^{\rm pb} - u_b^{\rm un})/(u_b^{\rm pb} + u_b^{\rm un})/2$ in percent as a function of injection laser strengh assuming $a_1 = a_2 = a_{12}$, which shows the narrowing of the opened phase-space region as a_{12} increases.

The island overlap criterion assumes that trapping readily occurs when the *unperturbed* wake and beatwave separatrices touch each other. From Eq. (3.59) taking $\delta_L = 0$ [equivalent to Eq. (3.47)] describing the maximum (minimum) excursion of an electron in phase-space for the unperturbed case $\mu = 0$ (no plasma wave), one may provide an estimate of the validity of the criterion by comparing $u_b^{\rm un}(\delta_L = 0)$ with $u_b^{\rm pb}$. Figure 3.9 shows the relative difference $\Delta_2 = [u_b^{\rm pb} - u_b^{\rm un}(\delta_L = 0)]/[u_b^{\rm pb} + u_b^{\rm un}(\delta_L = 0)]/2$ in percent as a function of injection laser strength assuming again $a_1 = a_2 = a_{12}$. The most relevant information provided by Δ_2 is the fact that the criterion actually *underestimates* the trapping threshold for *squared profile laser pulses*. Recall that in this derivation we assumed $\Delta t_{\rm int} \sim \tau_b$. Longer interaction times, allowing a slow trapping process through multiple beatwave bucket [Fig 3.10] will increase Δ_2, i.e., worsen the prediction from the criterion. Note also that, as pointed out in Sec. 3.3, the criterion is particularly accurate when $\delta_L \ll 1$ and a moderate interaction time (short injection pulses). The latter point also means that the energy spread of the injected beam will be minimized (trapping through multiple buckets increases the distance in phase-space between trapped electrons). In summary a small energy spread beam

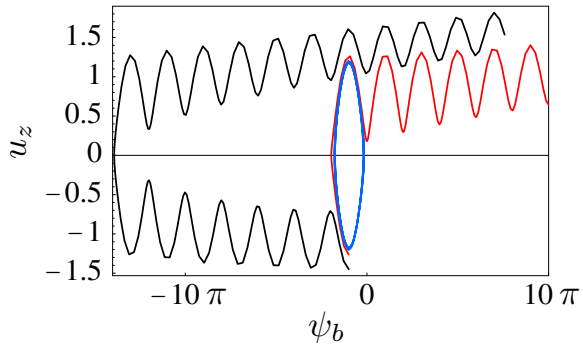

Figure 3.10: Trapping though multiple beatwave buckets.

may be injected into the plasma wave provided:

- Injection laser strength near injection threshold. It may be important not to inject background plasma electrons into deeply trapped beatwave orbits, as those electrons will be released at the end of the interaction time and may increase energy spread depending on the number of revolutions within the trapped orbit.

- Short injection laser pulses to lower interaction time and consequently minimize energy spread through multiple beatwave bucket injection.

- The injection pulse comoving with the drive pulse must be short, again to minimize interaction time but the (third) colliding pulse may be long. Using a long pulse will reduce the wakefield amplitude and will also allow for injection of a greater number of background plasma electrons.

For the moment the discussion assumed plane laser waves or a square pulse profile. Including the effect of a more realistic envelope such as a longitudinal Gaussian or half-sine profile will result in slightly different trapping conditions. A short injection pulse leads to a non-adiabatic process in the sense that $\mid \partial\gamma_{\perp b}(\psi_b,\psi)/\partial\psi_b \mid \sim \mid \partial\gamma_{\perp b}(\psi_b,\psi)/\partial\psi \mid$ in the equation of motion (3.53), where a laser pulse of the form $\mathbf{a}_i = \hat{a}_i(\psi)(\cos\psi_i\mathbf{e}_x + \sin\psi_i\mathbf{e}_y)$ has been assumed with $\hat{a}_i(\psi)$ the envelope profile, $\mathbf{e}_x$ and $\mathbf{e}_y$ unit vectors. The beatwave Hamiltonian is now time dependent $H_b(u_z,\psi_b,t)$ and an analytical solution becomes intractable. Solving the equations of motion numerically, using a particle tracking code [the method will be described in great detail next section], it is found that the island overlap criterion on the contrary

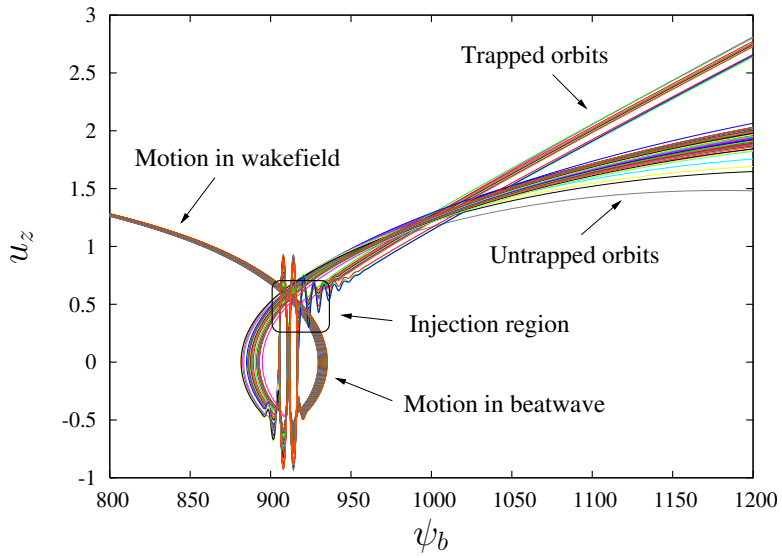

Figure 3.11: Trajectories in beatwave rest frame is shown for the three-pulse colliding pulse scheme assuming a half-sine longitudinal laser envelope profile and broad laser pulses ($k_p r_i \gg 1$). Laser-plasma parameters: a drive laser (subscript 0) normalized vector potential $\langle a_0^2 \rangle = 0.9$, length $k_p L_0 = 2\pi$, frequency $\omega_0/\omega_p = \omega_1/\omega_p = 50$, injection pulse (subscript 1) normalized vector potential $\langle a_1^2 \rangle = \langle a_2^2 \rangle = 0.25$, length $k_p L_1 = \pi/2$, backward propagating injection pulse (subscript 2) length $k_p L_2 = 4\pi$ and frequency $\omega_2/\omega_p = 42.5$.

overestimates the trapping threshold. Figure. 3.11 provides a detailed description of the injection process using three circularly polarized laser pulses with a half-sine longitudinal envelope profile (in this frame electrons move from left to right) for a drive laser (subscript 0) normalized vector potential $\langle a_0^2 \rangle = 0.9$, length $k_p L_0 = 2\pi$, frequency $\omega_0/\omega_p = \omega_1/\omega_p = 50$, injection pulse (subscript 1) normalized vector potential $\langle a_1^2 \rangle = \langle a_2^2 \rangle = 0.25$, length $k_p L_1 = \pi/2$, backward propagating injection pulse (subscript 2) length $k_p L_2 = 4\pi$, frequency $\omega_2/\omega_p = 42.5$ and assuming broad laser pulses, i.e., $k_p r_i \gg 1$ giving a beatwave normalized group velocity $\beta_b \simeq 0.08$:

(i) Before interaction with the two injection pulses, background plasma electrons follow the cold fluid orbit.

(ii) The colliding laser pulses parameters are chosen such as to be close to injection threshold into the plasma wave.

(iii) Electrons interact with the ponderomotive force of the injection pulse. This

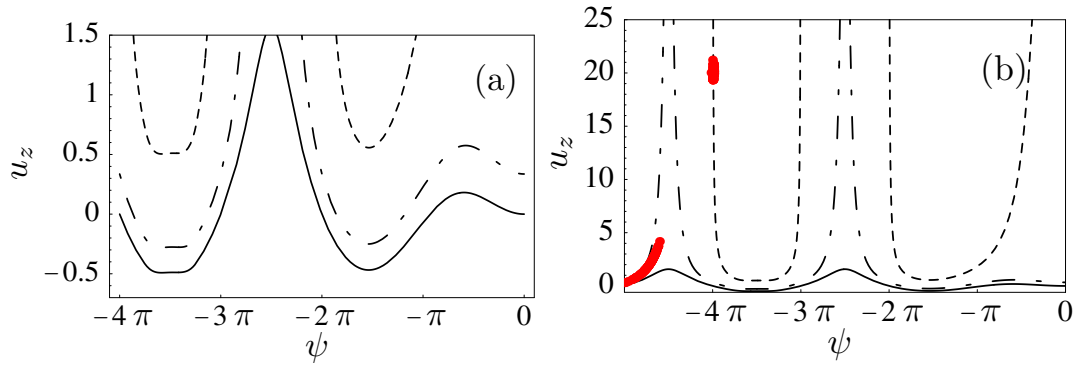

Figure 3.12: Phase space plot showing cold fluid orbit (solid line), trapped and focused orbit (dashed line), and trapped separatrix (dot-dashed line) for the laser-plasma parameters of Fig. 3.11. (a) zoom of the interaction region showing the flattening of the separatrices due to the presence of the injection laser pulse and (b) trapped and focused electron beam (red color) showing a clear separation in phase space with respect to the untrapped background plasma electrons

motion is dominant and the plasma wave simply acts as a perturbation ($\delta_L \ll 1$) opening the orbits.

(iv) A clear separation in phase-space is observed between background plasma electrons and electrons injected into trapped and focused orbits.

(v) The injected beam is very compact (typically a fraction of the plasma wavelength λ_p, on the order $\sim 10\%$) with a small energy spread.

Note that for the parameters of Fig. 3.11 the trapping threshold is found to be for injection laser strengths $\sqrt{a_1 a_2} \simeq 0.45$ which is greater than the predicted value using the island overlap criterion $\sqrt{a_1 a_2} \simeq 0.25$ [a quarter of the distance between the trapped and focused orbit (dashed-line) and the cold fluid orbit (solid line) in Fig. 3.12(a). Note the flattening of the separatrices due to the presence of the co-moving injection pulse]. Figure 3.12(b) plots the trapped and focused electron beam along with the cold fluid orbit, trapped and trapped and focused separatrices showing a clear separation in phase space with respect to the untrapped background plasma electrons. The trapped bunch is ultra-short with a small energy spread and was injected into a trapped and focused orbit. Recall that this example assumed broad laser pulse transverse profiles $k_p r_i \gg 1$, identical to a 1-D description. In 3-D, some

off-axis electrons will be also injected which will introduce energy spread, or in other words a head to tail correlation in phase-space. However, the electrons lying in a defocussing phase will slowly depart away from the longitudinal axis leaving a clean trapped and focused electron bunch (e.g, isolated in phase-space).

In the next section, the results of test particle simulations are presented for the linear polarized laser fields discussed in Sec. 3.2. For linear polarization, an analytic theory of the trapping threshold is complicated by the fact that a^2 is no longer independent of the fast laser phases, i.e., $a^2 = \hat{a}_0^2 \cos^2\psi_0 + \hat{a}_1^2 \cos^2\psi_1 + \hat{a}_0\hat{a}_1[\cos\psi_b + \cos(\psi_0 + \psi_1)]$. One consequence is that the wake separatrix now contains fine scale structure since the quantity $\gamma_{\perp 0}^2 = 1 + \hat{a}_0^2 \cos^2\psi_0$ oscillates between $1 + a_0^2$ and unity. Similarly, the beat wave separatrix becomes "fuzzy" because of contributions from wave components with phases $\cos 2\psi_0$, $\cos 2\psi_1$, and $\cos(\psi_0 + \psi_1)$. Furthermore, simulations of the motion of test particles in the beat wave from two counterpropagating, linear polarized laser pulses indicates that the particle orbits can become chaotic [60], as discussed in Section 3.8. The result is that the trapping threshold is lower than that predicted by circular polarization theory [46], as is apparent in the simulations discussed below.

3.6 Simulation results

This section describes results from a 3D particle tracking code in which the electromagnetic fields for the laser pulses and their corresponding wakefields are specified analytically as described in Sec. 3.2.

In the following simulations, the plasma was modelled by a group of test electrons initially at rest and loaded randomly in a three dimensional spatial region of length λ_p and transverse radius $\lambda_p/2$, uniformly about the z-axis, corresponding to a volume $V_0 = \pi\lambda_p^3/4$. This spatial region was chosen to be ahead of the pump laser pulse, and timed with respect to the initial position of the injection pulse such that when the two pulses collide, the test electrons fill the entire region in which trapping may occur. After the collision, various properties of the trapped electron bunch were monitored as function of propagation time, such as the mean energy, the energy spread, the root-mean square (rms) bunch length, and the trapping fraction. Here, the trapping

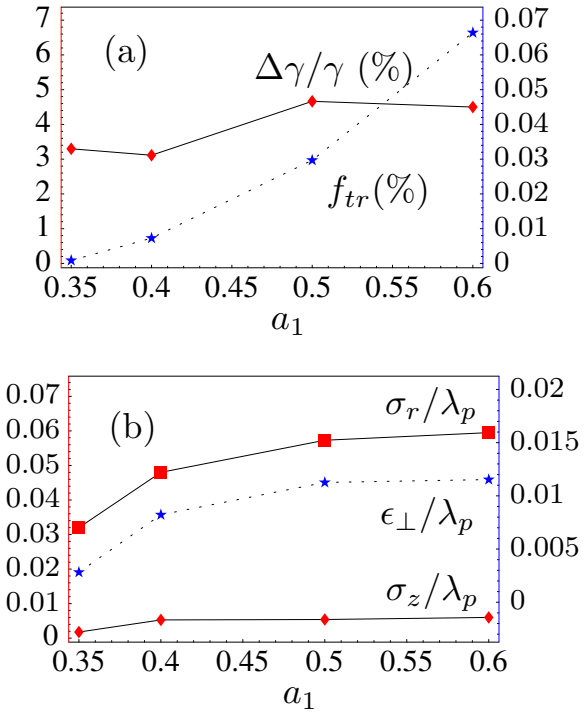

Figure 3.13: (Color) Trapped bunch parameters versus a_1 (for two collinear, counter-propagating laser pulses with equal polarization, $\langle a_0^2\rangle = 0.5$, $\omega_0/\omega_p = 50$, $L_0 = 9\lambda_p/8$, $\omega_1/\omega_p = 50$, $L_1 = \lambda_p/2$, and $\omega_p t = 50$). (a) Trapping fraction $f_{\rm tr}$ (right vertical axis) and relative energy spread $\Delta\gamma/\gamma$ (left vertical axis). (b) Bunch length σ_z/λ_p (left vertical axis), rms radius σ_r/λ_p (left vertical axis), and normalized transverse rms emittance $\epsilon_\perp/\lambda_p$ (right vertical axis).

fraction is defined as N_b/N_s where N_b is the number of test electrons in the bunch and N_s the total number of test electrons in the simulation. Unless otherwise noted, the simulations were carried out for the following parameters ranges: $\langle a_0^2\rangle$ from 0.5 to 0.88, $\langle a_1^2\rangle$ from 0 to 0.32, drive pulse length from $L_0 = \lambda_p$ to $9\lambda_p/8$, injection pulse length $L_1 = \lambda_p/2$, drive and injection pulse radii $r_i = \lambda_p$, frequencies $\omega_0 = \omega_1 = 50\ \omega_p$ and propagation length $\omega_p t$ from 50 to 100. The trapping fraction can be related to the number of trapped particles by $N_e = n_0 f_{\rm tr} V_{\rm load}$, where $V_{\rm load} = \lambda_p^3$ is the initial volume of loaded test particles.

Three configurations of the two-pulse colliding pulse injector were simulated: (i) two counterpropagating, collinear laser pulses with equal polarizations, (ii) two pulses colliding at a finite interaction angle with equal polarizations, and (iii) two counter-

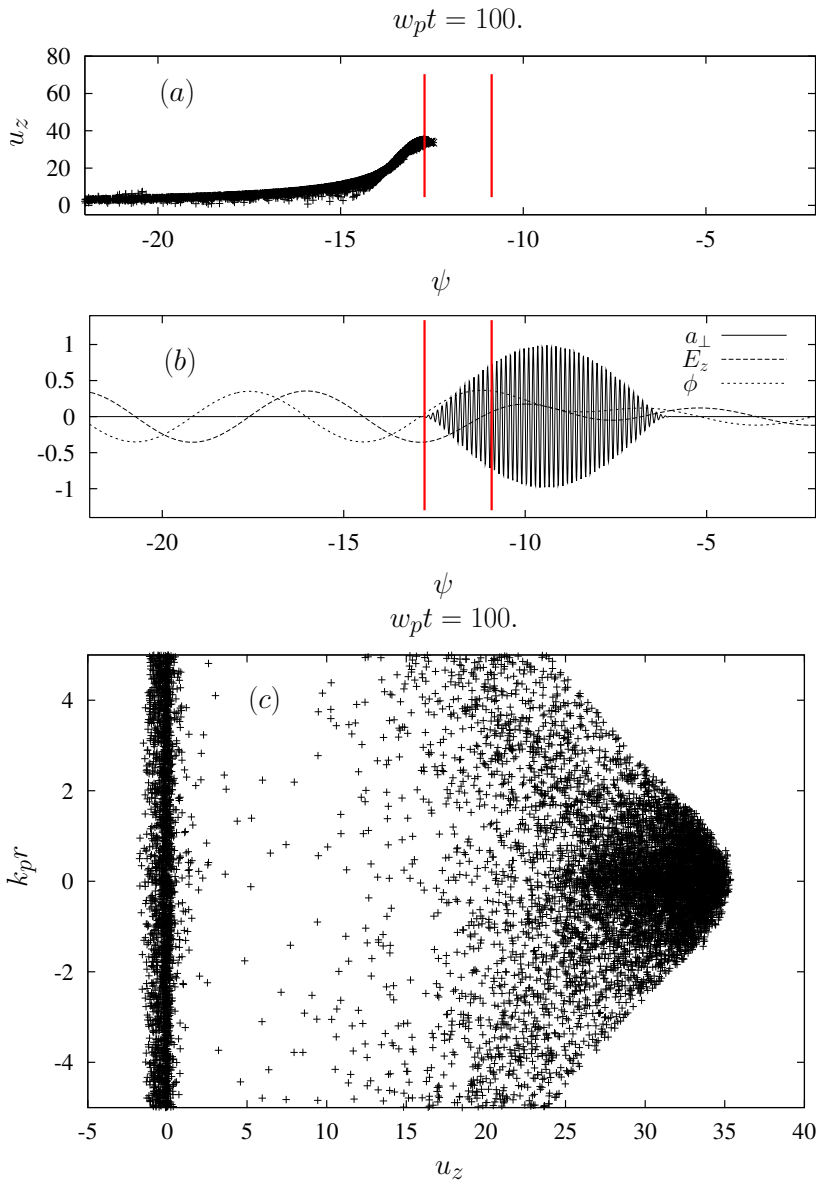

Figure 3.14: (a) Longitudinal electron momentum u_z versus phase $\psi = k_p\zeta$. (b) Normalized laser strength $a_\perp$ (solid curve), longitudinal electric field E_z (dashed curve) and wakefield potential ϕ (dotted curve) versus phase [note that the trapped and focused region is $-4\pi < \psi < -7\pi/2$ (between solid red lines)]. (c) Longitudinal momentum versus normalized beam radius $k_p r$. Laser-plasma parameters: $\langle a_0^2 \rangle = 0.5$, $\omega_0/\omega_p = 50$, $L_0 = 9\lambda_p/8$, $\langle a_1^2 \rangle = 0.18$, $\omega_1/\omega_p = 50$, $L_1 = \lambda_p/2$, parallel polarization, and $\omega_p t = 100$.

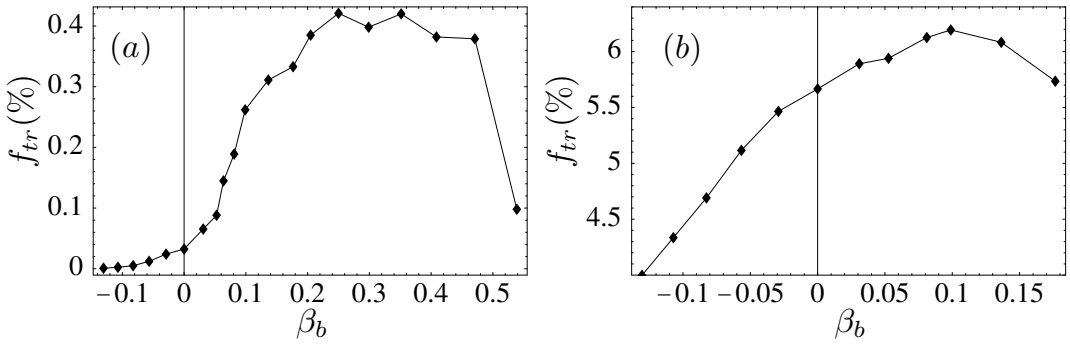

Figure 3.15: Trapping fraction $f_{\rm tr}$ as a function of beat wave phase velocity β_b for two collinear, counterpropagating laser pulses with equal polarization for the parameters: (a) $\langle a_0^2\rangle = 0.5$, $\omega_0 = 50\ \omega_p$, $L_0 = 9\lambda_p/8$, $\langle a_1^2\rangle = 0.125$, $L_1 = \lambda_p/2$, $\omega_p t = 50$ and (b) same parameters except with $\langle a_0^2\rangle = 0.88$ and $\langle a_1^2\rangle = 0.245$.

propagating, collinear laser pulses with orthogonal polarizations.

3.6.1 Two collinear pulses

This section presents results for the basic two-pulse colliding injector geometry in which the pulses are collinear and counterpropagating with equal polarizations. Figure 3.13 shows the trapped fraction $f_{\rm tr}$ of electrons, relative energy spread $\Delta\gamma/\gamma$, rms bunch length σ_z/λ_p, rms radius σ_r/λ_p, and normalized transverse rms emittance $\epsilon_\perp/\lambda_p$ versus counterpropagating laser pulse intensity after a propagation time of $\omega_p t = 50$ for the parameters: $\langle a_0^2\rangle = 0.5$, $\omega_0/\omega_p = 50$, $L_0 = 9\lambda_p/8$, $\omega_1/\omega_p = 50$, and $L_1 = \lambda_p/2$.

Simulations using the 3D particle tracking code point out that typical electron bunches produced by colliding laser pulses have a "head-to-tail" energy correlation as can be seen in Fig. 3.14(a), which shows the normalized longitudinal momentum u_z versus longitudinal phase ψ for the parameters $\langle a_0^2\rangle = 0.5$, $\omega_0/\omega_p = 50$, $L_0 = 9\lambda_p/8$, $\langle a_1^2\rangle = 0.18$, $\omega_1/\omega_p = 50$, $L_1 = \lambda_p/2$, and $\omega_p t = 100$. The corresponding field profiles versus ψ are shown in Fig. 3.14(b). In Fig. 3.14(c), the normalized transverse radial position of the particles $k_p r$ is shown versus normalized longitudinal momentum u_z for the parameters of Fig. 3.14(a). The mean kinetic energy of the electron bunch is found to be $T \simeq 17.3$ MeV. The most energetic electrons that reside at the head of the bunch are on trapped orbits that are both accelerating and focusing and, hence,

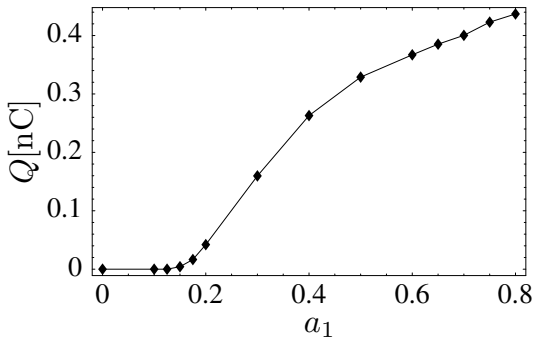

Figure 3.16: Bunch charge Q[nC] versus a_1 with $\lambda_0 = 0.8$ μm, $\lambda_p = 40$ μm ($n_0 = 6.9\ 10^{17}$ cm^{-3}), $L_0 = r_0 = 40$ μm, and $\langle a_0^2 \rangle = 0.88$.

remain close to the axis. Moving back through the bunch, the electrons are on orbits with less acceleration and less focusing. The least energetic electrons at the back of the bunch reside on orbits that are transversely defocusing and are hence scattered transversely.

The bunch emittance is approximated as $\epsilon_\perp = \gamma_0 \beta_0 \sqrt{\langle x^2 \rangle \langle x'^2 \rangle} \simeq \sqrt{\langle x^2 \rangle \langle u_x^2 \rangle}$ where $u_0 = \gamma_0 \beta_0 \simeq \gamma_0$ is the axial momentum of the electron bunch. As a_1 increases, trapping becomes more efficient, with corresponding increases in $f_{\rm tr}$, $\Delta\gamma/\gamma$, σ_z/λ_p, and σ_r/λ_p. This is consistent with the fact that the overlap in phase space area between beat wave and wakefield separatrices increases as a_1 increases, as shown in Fig. 3.5. Maximum acceptance for the electron plasma wave is obtained for $\langle a_1^2 \rangle \simeq 0.125$ and, consequently, emittance reaches an asymptotic value. Figure 3.15 shows the change in trapping fraction $f_{\rm tr}$ as a function of the beat wave phase velocity for the parameters of Fig. 3.13 and for the case $\langle a_0^2 \rangle = 0.88$. The maximum of $f_{\rm tr}$ occurs near $\beta_b \simeq 0.35$ for $\langle a_0^2 \rangle = 0.5$ and $\beta_b \simeq 0.1$ for $\langle a_0^2 \rangle = 0.88$, which is qualitatively similar to theoretical predictions found for circular polarization (cf. Fig. 3.4).

The total charge in the bunch Q can be estimated from the trapping fraction $f_{\rm tr}$ (the fraction of the initial electrons that remain on trapped and focused orbits) by $Q = e n_0 f_{\rm tr} \lambda_p^3$. The bunch density was calculated assuming a square beam profile using the relationships between the length, radius and corresponding RMS quantities, i.e., $L_b = 2\sqrt{3}\sigma_z$ is the full beam length, σ_z the RMS beam length, $r_b = 2\sigma_r$ the beam radius and σ_r the beam RMS radius. A plot of bunch charge Q versus a_1 is shown in Fig. 3.16 for the parameters: $\lambda_0 = 0.8$ μm, $\lambda_p = 40$ μm ($n_0 = 6.9\ 10^{17}$ cm^{-3}),

$L_0 = r_0 = 40$ μm, and $\langle a_0^2 \rangle = 0.88$. Due to the small volume of the trapped bunch $V_{\rm tr}$, the bunch density n_b can be very high, where $n_b = Q/V_{\rm tr}$.

For example, the colliding laser intensities $\langle a_0^2 \rangle = 0.88$ and $\langle a_1^2 \rangle = 0.18$ yield an electron bunch with $\sigma_r/\lambda_p \simeq 0.1$, $\sigma_z/\lambda_p \simeq 0.02$, $Q \simeq 0.28$ nC, and $n_b/n_0 \simeq 3.2$. This raises the question of beam loading.

3.7 Beam loading considerations

Beam loading, whereby the trapped electron bunch significantly alters the accelerating wakefield, can degrade the quality of the electron bunch. Beam loading is neglected in the particle tracking code.

To estimate the effects of beam loading, the wakefield generated by the trapped electron bunch propagating in an initially uniform plasma can be calculated [61, 62] and compared to the wakefield driven by the pump laser pulse. Following a similar procedure as Sec. 2.3, the expression of the electronic density becomes

$$\frac{n_e}{n_0} = 1 - \frac{n_b}{n_0} + k_p^{-2} \nabla \cdot \left(\nabla \sqrt{1+u^2} + \frac{\partial \mathbf{u}}{\partial ct} \right) . \tag{3.63}$$

Using Ampère's law

$$\nabla \times \mathbf{B} = -4\pi e n_e \beta_e - 4\pi e n_b \beta_b + \frac{\partial \mathbf{E}}{\partial ct} , \tag{3.64}$$

along with Eq. (2.22),

$$\frac{e\mathbf{E}}{m_e c^2} = -\nabla \sqrt{1+u^2} - \frac{\partial \mathbf{u}}{\partial ct} , \tag{3.65}$$

Eq. (2.20),

$$\frac{e\mathbf{B}}{m_e c^2} = \nabla \times \mathbf{u} , \tag{3.66}$$

and expressing β_e as a function of $\mathbf{u}$, i.e., $\beta_e = \mathbf{u}/(1+u^2)^{1/2}$, we get a one-fluid equation of motion similar to Eq. (2.26) but including the contribution from an external beam

[63], which is

$$\left[\frac{\partial^2}{\partial c^2 t^2} + \nabla\times\nabla\times + \frac{k_p^2}{\sqrt{1+u^2}}\left(1-\frac{n_b}{n_0}\right)\right]\mathbf{u} = -\frac{\partial}{\partial ct}\nabla\sqrt{1+u^2} \\ -\frac{\mathbf{u}}{\sqrt{1+u^2}}\nabla\cdot\left[\frac{\partial \mathbf{u}}{\partial ct} + \nabla\sqrt{1+u^2}\right] - k_p^2\frac{n_b}{n_0}\beta_b \ , \tag{3.67}$$

where n_b is the density of the drive electron bunch and n_0 is the ambient plasma density. This equation assumes that the ions are immobile and that the electron beam is not evolving, i.e., continuity and equation of motion for the electron beam are not considered. Next $n_b/n_0 \sim O(a_i^2) \sim O(\epsilon^2)$ is assumed. This implies that both the perturbations on the plasma caused by the incoming laser pulses and the electron beam are on the same order of magnitude and consequently can be added linearly. For the investigation of weak nonlinearities, Eq. (3.67) is expanded up to second order in the small parameter ϵ around the equilibrium solution $\mathbf{u}_0 = \mathbf{a}_0 = \psi_0 = 0$ and $n_e = n_0$, i.e., the normalized fluid momentum is written as $\mathbf{u} = \mathbf{u}_1 + \mathbf{u}_2$, where indexes denotes expansion order [$\mathbf{u}_1 \sim O(\epsilon)$ and $\mathbf{u}_2 \sim O(\epsilon^2)$]. To first order, it is found that $\mathbf{u}_1 = \mathbf{a}$ (see Sec. 2.4 for further detail) and to second order Eq. (3.67) becomes

$$\left(\frac{\partial^2}{\partial c^2 t^2} + \nabla\times\nabla\times + k_p^2\right)\mathbf{u} = -\frac{\partial}{\partial ct}\nabla\frac{a^2}{2} - k_p^2\frac{n_b}{n_0}\beta_b \ . \tag{3.68}$$

Equation 3.68 is not separable in term of the vector potential a_i (transverse wave) and the axial electron momentum $\nabla\psi$ due to the form of n_b/n_0. This implies that an equation for the fields must be solved instead. Next we derive a close system of coupled equations for the electric field $\mathbf{E}$ and the background plasma density variation $\delta n/n_0$, where $\delta n = n_e - n_0$. Taking the time derivative of Eq. 3.68 and using the second order relationship between the normalized electron momentum, electric field [from Eq. (3.65)] and electron density [from Eq. (3.63)], given by

$$k_p\frac{\mathbf{E}}{E_0} = -\nabla\frac{a^2}{2} - \frac{\partial \mathbf{u}}{\partial ct} \ , \tag{3.69}$$

$$\frac{\partial}{\partial ct}\left(\nabla\cdot\mathbf{u}\right) = k_p^2\left(\frac{\delta n}{n_0} + \frac{n_b}{n_0}\right) - \nabla^2\frac{a^2}{2} \ , \tag{3.70}$$

along with $\nabla \times \nabla \times \mathbf{u} = \nabla(\nabla \cdot \mathbf{u}) - \nabla^2 \mathbf{u}$, we get

$$\boxed{\left(\nabla^2 - k_p^2 - \frac{\partial^2}{\partial c^2 t^2}\right)\frac{\mathbf{E}}{E_0} = -k_p \nabla\left(\frac{\delta n}{n_0} + \frac{n_b}{n_0}\right) - k_p \beta_b \frac{\partial}{\partial ct}\left(\frac{n_b}{n_0}\right) + k_p \nabla \frac{a^2}{2}}\,. \quad (3.71)$$

where $E_0 = k_p m_e c^2/e$ is the cold fluid wave breaking limit. In order to get the second equation for the electron density, first we calculate the second order solution of the continuity equation, i.e.,

$$\frac{\partial n_e}{\partial ct} + \nabla \cdot \left(\frac{n_e\ \mathbf{u}}{\sqrt{1+u^2}}\right) = 0\ , \quad (3.72)$$

becomes

$$\frac{\partial}{\partial ct}\left(\frac{\delta n}{n_0}\right) \simeq -\nabla \cdot \mathbf{u}\ , \quad (3.73)$$

and insert into Eq. (3.70) which gives

$$\boxed{\left(\frac{\partial^2}{\partial c^2 t^2} + k_p^2\right)\frac{\delta n}{n_0} = \nabla^2 \frac{a^2}{2} - k_p^2 \frac{n_b}{n_0}}\,. \quad (3.74)$$

Eqs. (3.71) and (3.74) can be further simplified by changing variables from (z,t) to $(\zeta = z - ct, \tau)$ and assuming that $\beta_\phi \simeq \beta_g \simeq \beta_b \simeq 1$ where β_ϕ is the laser phase velocity, β_g the laser group velocity and β_b the beam normalized velocity. This gives for the partial derivatives $\partial/\partial ct = \partial/\partial c\tau - \partial/\partial\zeta$ and $\partial/\partial z = \partial/\partial\zeta$. Estimating the beam loading effect, we are mainly interested in comparing the strength of the perturbation with respect to the wakes driven by the laser pulses. Next only the longitudinal wakes will be discussed. The normalized density perturbation $\delta n/n_0 \ll 1$ and normalized axial electric field $E_z/E_0 \ll 1$ driven in an initially uniform plasma by either a short electron bunch (n_b/n_0 drive term) or a short laser pulse (a^2 drive term) are given by

$$\left(\frac{\partial^2}{\partial\zeta^2} + k_p^2\right)\frac{\delta n}{n_0} = \left(\nabla_\perp^2 + \frac{\partial^2}{\partial\zeta^2}\right)\frac{\langle a^2\rangle}{2} - k_p^2 \frac{n_b}{n_0}\ , \quad (3.75)$$

$$\left(\nabla_\perp^2 - k_p^2\right)\frac{E_z}{E_0} = k_p \frac{\partial}{\partial\zeta}\left(\frac{\langle a^2\rangle}{2} - \frac{\delta n}{n_0}\right)\ , \quad (3.76)$$

where the angular brackets denote an average over the fast laser frequency (with

$\omega^2 \gg \omega_p^2$). In deriving the above equations, the quasi-static approximation was assumed, i.e, the drive beams and the resulting wakefields are functions of only the variables $\zeta = z - ct$ and $r_\perp$.

Consider the wakefield generated by the electron bunch in the absence of the laser pulse. Solving Eq. (3.76) with $a^2 = 0$ and a cylindrically-symmetric drive n_b yields

$$\frac{\delta n}{n_0} = k_p \int_0^\zeta d\zeta' \sin[k_p(\zeta - \zeta')] \frac{n_b(\zeta')}{n_0} \ , \tag{3.77}$$

$$\frac{E_z}{E_0} = k_p^3 \int_\infty^\zeta d\zeta' \int_0^\infty dr' r' \cos[k_p(\zeta - \zeta')] I_0\left(k_p r_<\right) K_0\left(k_p r_>\right) \frac{n_b(r', \zeta')}{n_0} \ , \tag{3.78}$$

where I_0 and K_0 are the zeroth-order modified Bessel functions of the second kind, and $r_<$ ($r_>$) denote the smaller (larger) of r and r' respectively. For a uniform beam profile $n_b(r, \zeta) = n_b \Theta(r_b - r)\Theta(-\zeta)\Theta(\zeta + L_b)$ of radius r_b and length L_b, where Θ is a step function, the profile of the perturbed density and the axial wakefield are inside the bunch $-L_b \le \zeta \le 0$

$$\delta n/n_0 = -2(n_b/n_0) \sin^2\left(k_p \zeta/2\right) \ , \tag{3.79}$$

$$E_z/E_0 = -(n_b/n_0) F_R(r) \sin k_p \zeta \ , \tag{3.80}$$

and behind $\zeta < -L_b$

$$\delta n/n_0 = -2(n_b/n_0) \sin\left(k_p L_b/2\right) \sin k_p\left(\zeta + L_b/2\right) \ , \tag{3.81}$$

$$E_z/E_0 = -(n_b/n_0) F_R(r) \left[\sin k_p \zeta - \sin k_p\left(\zeta - L_b\right)\right] \ , \tag{3.82}$$

where the radial profile function is

$$F_R(r) = \begin{cases} 1 - k_p r_b K_1(k_p r_b) I_0(k_p r) \ , & \text{for } r < r_b \\ k_p r_b I_1(k_p r_b) K_0(k_p r) \ , & \text{for } r > r_b \end{cases} \tag{3.83}$$

with I_1 and K_1 the first-order modified bessel functions. Assuming $k_p L \ll 1$ yields

at the back of the bunch,

$$\delta n/n_0 \simeq -\left(k_p L_b\right)^2 \left(n_b/n_0\right)/2 \,, \tag{3.84}$$

$$E_z/E_0 \simeq k_p L_b \left(n_b/n_0\right) F_R(r) \,, \tag{3.85}$$

Consider now the wakefield generated by the laser pulse in the absence of the electron bunch. Solving Eq. (3.76) with $n_b = 0$ yields

$$\frac{\delta n}{n_0} = k_p \int_0^\zeta d\zeta' \sin[k_p(\zeta - \zeta')] \left(\nabla_\perp^2 + \frac{\partial^2}{\partial \zeta'^2}\right) \frac{\langle a^2(\zeta')\rangle}{2} \,, \tag{3.86}$$

$$\frac{E_z}{E_0} = k_p \int_0^\zeta d\zeta' \sin[k_p(\zeta - \zeta')] \frac{\partial}{\partial \zeta'} \frac{\langle a^2(\zeta')\rangle}{2} \,. \tag{3.87}$$

Assuming a laser pulse with a half-sine axial profile and a Gaussian radial profile, similar to Eq. (3.11), with a pulse length $L = \lambda_p$ (the resonant case yielding maximum plasma wave amplitude) gives

$$\frac{\delta n}{n_0} = \frac{\pi}{8} a_0^2 \left[1 + \frac{8}{k_p^2 r_s^2}\left(1 - \frac{2r^2}{r_s^2}\right)\right] \exp\left(-\frac{2r^2}{r_s^2}\right) \,, \tag{3.88}$$

$$\frac{E_z}{E_0} = \frac{\pi}{8} a_0^2 \exp\left(-\frac{2r^2}{r_s^2}\right) . \tag{3.89}$$

Beam loading can be neglected provided that the wakefield generated by the trapped electron bunch is small compared to that generated by the drive laser pulse. Consequently, from Eqs. (3.85) and (3.89), beam loading can be neglected provided

$$\alpha_l = \frac{k_p L_b}{a_0^2} \frac{n_b}{n_0} F_R(0) \ll 1 \,. \tag{3.90}$$

For a narrow beam $k_p^2 r_b^2 \ll 1$ and along the axis $F_R(r = 0) \simeq [0.308 - 0.5 \ln(k_p r_b)] k_p^2 r_b^2$. The bunch charge Q, normalized bunch-induced axial electric field E_z/E_0, and normalized bunch-induced density perturbation $\delta n/n_0$ are plotted in Fig. 3.17 as a function of a_1 for $\langle a_0^2\rangle = 0.88$ and the parameters of Fig. 3.16. In the regime $\langle a_1^2\rangle \gtrsim 0.045$, the density perturbation becomes large, $k_p L_b(n_b/n_0) > 1$, and the effects of nonlinear beam loading can no longer be neglected. Nonlinear beam loading will most likely

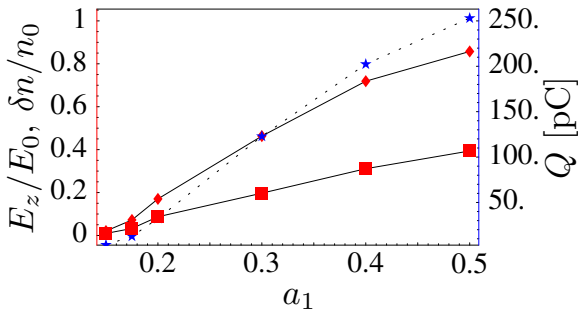

Figure 3.17: Bunch charge Q in pC (right vertical axis, stars), normalized axial electric field E_z/E_0 (left vertical axis, points), and normalized density perturbation $\delta n/n_0$ (left vertical axis, squares) generated by the electron bunch alone (here the laser contribution is not included) versus a_1 with $\lambda_0 = 0.8$ μm, $\lambda_p = L_0 = r_0 = 40$ μm, and $\langle a_0^2 \rangle = 0.88$.

reduce the bunch quality (fraction trapped, average energy, etc.).

To reduce beam loading, the pump laser amplitude and, consequently, the plasma wave amplitude can be reduced, which also reduces the trapping. For example, $\langle a_0^2 \rangle = 0.5$, $\langle a_1^2 \rangle = 0.18$, $k_p \sigma_r \simeq 0.4$, and $k_p \sigma_z \simeq 0.04$ [Fig 3.13(b)] give a trapped bunch density of $n_b/n_0 \simeq 0.57$ and, hence, $\alpha_l \simeq 0.02$, which satisfies Eq. (3.90). The bunch charge Q, normalized bunch-induced axial electric field E_z/E_0, and normalized bunch-induced density perturbation $\delta n/n_0$ are plotted in Fig. 3.18 as a function of a_1 for $\langle a_0^2 \rangle = 0.5$ and the parameters of Fig. 3.17. For the cases shown in Fig. 3.18, the effects of beam loading should be minimal.

3.7.1 Effects of interaction angle and polarization

Non-collinear geometry

Experimentally, the colliding pulse injector geometry can be simplified by using two pulses that intersect in a non-collinear geometry, since this avoids having additional optics in the path of the accelerated electron bunches. The interaction angle θ between the two laser pulses is given by $\cos\theta = (\mathbf{k}_0 \cdot \mathbf{k}_1)/(k_0 k_1)$, where k_0 propagates along the z-axis and k_1 is in the x-z plane ($\theta = \pi$ corresponds to collinear, counterpropagating pulses). Note for non-collinear interactions, the component of the beat wave phase velocity along the z-axis is reduced, i.e., $c\beta_{b_z} = \Delta\omega/(k_0 - |k_1|\cos\theta)$,

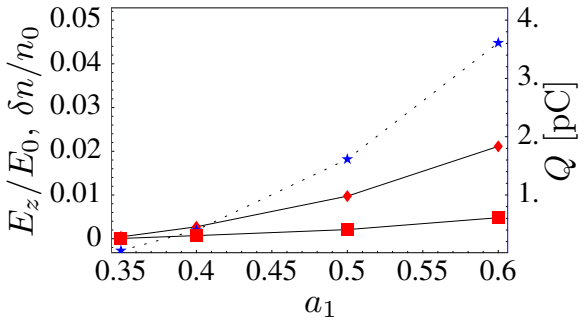

Figure 3.18: Bunch charge Q in pC (right vertical axis, stars), normalized axial electric field (E_z/E_0) (left vertical axis, points), and normalized density perturbation ($\delta n/n_0$) (left vertical axis, squares) generated by the electron bunch alone versus a_1 with $\lambda_0 = 0.8$ μm, $\lambda_p = 40$ μm ($n_0 = 6.9\ 10^{17}$ cm^{-3}), $L_0 = r_0 = 40$ μm, and $\langle a_0^2 \rangle = 0.5$. Note that the parameter regime is well below the beam loading limit.

$c\beta_{b_x} = \Delta\omega/(|k_1|\sin\theta)$, and $c\beta_{b_y} = 0$, for $\theta \in (\pi/2, \pi)$. In addition to the axial (z-axis) component of the beat wave ponderomotive force, proportional to $(k_0 - |k_1|\cos\theta)a_0 a_1$, there is now a transverse component, proportional to $(|k_1|\sin\theta)a_0 a_1$, that pushes electrons off axis. Figure 3.19 shows the trapping fraction versus interaction angle at $\omega_p t = 50$ for $\langle a_0^2 \rangle = 0.5$, $\omega_0/\omega_p = 50$, $L_0 = 9\lambda_p/8$, $\langle a_1^2 \rangle = 0.125$, $\omega_1/\omega_p = 50$, and $L_1 = \lambda_p/2$. As the angle θ decreases from $\theta = \pi$ to $\theta = \pi/2$ (transverse injection), the trapping fraction decreases to zero. Furthermore, for the $\theta = \pi/2$ case, when the delay between the injection and the pump pulses was increased, such that the injection pulse intersects the wakefield and does not overlap with the pump pulse (as in Umstadter *et al.* [18], and Hemker *et al.* [44]), no trapping was observed.

Orthogonal polarization

All of the above examples have assumed parallel polarization, i.e., $\mathbf{a}_0 \cdot \mathbf{a}_1 = a_0 a_1$, and injection is the result of the ponderomotive force associated with the beat wave $\mathbf{F}_{\rm beat} = -(m_e c^2/\gamma)\nabla(\mathbf{a}_0 \cdot \mathbf{a}_1)$. For orthogonal polarizations, $\mathbf{F}_{\rm beat} = \mathbf{0}$ (since $\mathbf{a}_0 \cdot \mathbf{a}_1 = 0$), and the beat wave mechanism can no longer be responsible for electron injection. For orthogonal polarizations, the time-average force on the electrons is given by $\mathbf{F}_{\rm pond} = m_e c^2 \nabla(\phi - \gamma) \simeq m_e c^2 \nabla\phi - (m_e c^2/\gamma)(\nabla \hat{a}_0^2/2 + \nabla \hat{a}_1^2/2)$. Electron injection can still be the result of the ponderomotive force associated with envelope of the injection laser pulse, $\mathbf{F}_{\rm env} \simeq -(m_e c^2/\gamma)\nabla \hat{a}_1^2/2$, but this is relatively small

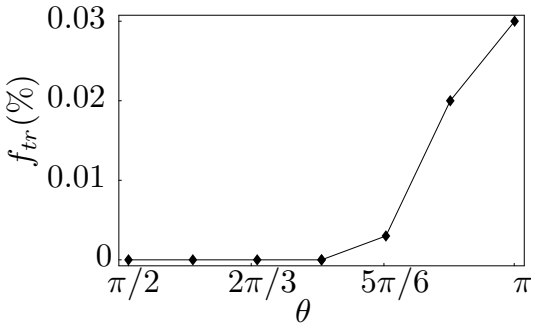

Figure 3.19: Trapping fraction $f_{\rm tr}$ as a function of angle for two laser beams with equal polarization at $\omega_p t = 50$ with $\langle a_0^2 \rangle = 0.5$, $\omega_0/\omega_p = 50$, $L_0 = 9\lambda_p/8$, $\langle a_0^2 \rangle = 0.125$, $\omega_1/\omega_p = 50$, and $L_1 = \lambda_p/2$.

compared to that of the beat wave as discussed in the introduction. As an example, a case was simulated identical to that shown in Fig. 3.14, except with orthogonal polarization. For the orthogonal polarization case, there are no trapped electrons, compared to $f_{\rm tr} \simeq 6.5 \times 10^{-4}$ for the parallel polarization case. For orthogonal polarization, trapping can occur, but for higher laser intensities in which nonlinear effects (not included in the test particle simulation model) become important. The details of trapping using orthogonal polarizations are presently being explored using particle-in-cell simulations [64].

3.8 Effect of polarization on electron motion in beat waves

Test particle simulations of the colliding pulse injection process indicate that trapping occurs more readily for the case of linear polarization compared to that of circular polarization. One reason for this difference is the form of the normalized laser intensity (i.e., the ponderomotive potential) for the two polarizations. Consider the case of two counterpropagating and overlapping laser pulses with uniform profiles (i.e., pulse rise time effects are neglected). For circular polarization $\mathbf{a} = \sum_i \hat{a}_i(\cos\psi_i \mathbf{e}_x + \sin\psi_i \mathbf{e}_y)$, such that $a^2 = \hat{a}_0^2 + \hat{a}_1^2 + 2\hat{a}_0\hat{a}_1 \cos\psi_b$ is independent of the fast laser phase ψ_i and only a function of the beat phase $\psi_b = \psi_0 - \psi_1 \simeq 2k_0 z - \Delta\omega t$. Because $a^2 = a^2(\psi_b)$, the Hamiltonian for the motion of an electron in the combined laser fields is time

independent, $H_b(u_z, \psi_b) = \sqrt{1 + a^2(\psi_b) + u_z^2} - \beta_b u_z$, i.e., the Hamiltonian describes the motion of an electron in a single beat wave characterized by a single phase velocity. In this case the electron motion is regular as describe in Sec. 3.4.2.

For linear polarization $\mathbf{a} = \sum_i \hat{a}_i \cos\psi_i \mathbf{e}_x$, such that $a^2 = \hat{a}_0^2 \cos^2\psi_0 + \hat{a}_1^2 \cos^2\psi_1 + \hat{a}_0\hat{a}_1[\cos\psi_b + \cos(\psi_0 + \psi_1)]$. In this case the ponderomotive potential is, in effect, composed of four waves. In addition to the slow beat wave $\hat{a}_0\hat{a}_1 \cos\psi_b$, there is a forward going wave $\hat{a}_0^2 \cos^2\psi_0$, a backward going wave $\hat{a}_1^2 \cos^2\psi_1$, and a wave at the sum of the laser phases $\hat{a}_0\hat{a}_1 \cos(\psi_0 + \psi_1)$. The end result is that the Hamiltonian is no longer time independent and an analytic solution for the motion of a test electron in the combined laser fields is intractable.

To study the effect of polarization, the motion of test particles is studied numerically for two identical, counterpropagating laser pulses, neglecting the effects of the space charge potential ($\phi = 0$). The first set of simulations, shown in Fig. 3.20, is for two overlapping pulses with uniform profiles, i.e., the effects of the laser envelope profiles are neglected. In this case, a group of electrons is initially loaded at rest over one-half of a beat period (spaced uniformly) within the laser fields. Here, the time-averaged intensities of the circularly and linearly polarized laser pulses are chosen to be equal, $\langle a_0^2 \rangle = \langle a_1^2 \rangle = 0.5$.

Results for circular polarization are shown in Fig. 3.20 (a), which indicates that the orbits are regular and well behaved, as is described by the Hamiltonian theory in Sec. 3.4.2. In this case, the maximum electron momentum in the beat wave is less than or equal to that of the maximum of the beat wave separatrix given by Eq. (3.46).

The corresponding case for linear polarization is shown in Fig. 3.20 (b). For linear polarization, the orbits are irregular and, for sufficiently intense laser pulses, can become chaotic. This is similar to the case of "stochastic heating" in counterpropagating laser fields as studied by Sheng *et al.* [60]. In this case the electrons are not confined to a single beat wave period and the maximum momentum can exceed that of the maximum of the beat wave separatrix as predicted by a Hamiltonian theory for circularly polarized pulses. To study the effect of the finite rise times of the laser pulses, a second set of simulations was performed. In these simulations, the electrons were loaded at rest in the region between the two counterpropagating laser pulses before they overlapped (spaced uniformly over a width equal to half of a beat period).

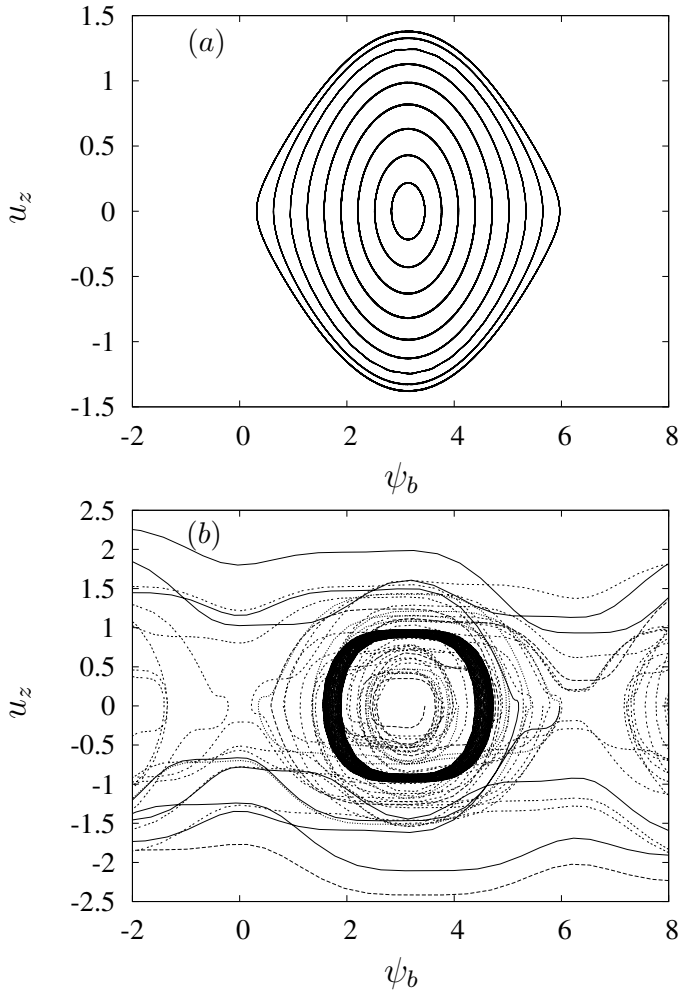

Figure 3.20: Phase space orbits (u_z, ψ_b) of test electrons in two counterpropagating laser pulses with (a) circular polarization and (b) linear polarization. Here both lasers are infinite plane waves with $\langle a_0^2 \rangle = \langle a_1^2 \rangle = 0.5$, i.e., equal time-averaged intensities.

The initial conditions were such that the electrons were first struck by the left-going pulse for a short time (less than a beat period) before being struck by the right-going pulse (at which time the electrons experience the beat wave). Here the laser pulses have a finite length of $L_0 = L_1 = 50\lambda_0$ and a radius of $r_0 = r_1 = 50\lambda_0$ with equal peak time-averaged intensities of $\langle a_0^2 \rangle = \langle a_1^2 \rangle = 0.5$.

The case of circular polarization is shown in Fig. 3.21 (a). Initially, the electrons move to the left due the axial ponderomotive force of the left-going pulse. As the two pulses collide, the electrons begin to execute orbits within the beat wave. As the laser

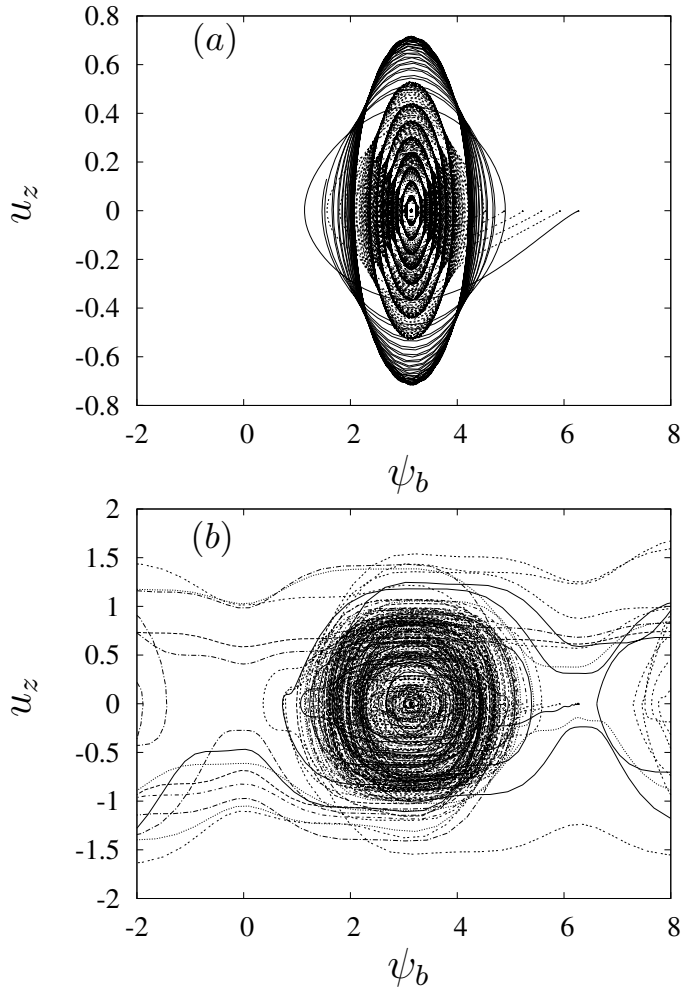

Figure 3.21: Phase space orbits (u_z, ψ_b) of test electrons in two counterpropagating laser pulses with (a) circular polarization and (b) linear polarization. Here the laser pulses have a finite length of $L_0 = L_1 = 50\lambda_0$ and a radius of $r_0 = r_1 = 50\lambda_0$ with equal peak time-averaged intensities of $\langle a_0^2 \rangle = \langle a_1^2 \rangle = 0.5$.

pulses continue to overlap, the size of the ponderomotive beat wave increases, since the local laser intensity of the two pulses is increasing. This leads to larger beat wave orbits. The end result is that the electrons are confined to a single period of the beat wave and, for these initial conditions, the maximum momentum is significantly less than that corresponding to the top of the beat wave separatrix given by Eq. (3.46).

The case of linear polarization is shown in Fig. 3.21 (b). Again, the electron orbits are highly irregular and chaotic. The electrons are not confined to a single beat wave

period and the maximum momentum exceeds that predicted by a simple Hamiltonian theory of the separatrix for circularly polarized pulses.

The above simulations shed insight as to why injection and trapping occurs more readily for linear polarization than it does for circular polarization. For circular polarization, electrons initially loaded at rest within a single beat wave period remain confined to a single period of the beat wave with momenta less than that of the beat wave separatrix. For linear polarization, the electron trajectories become chaotic, no longer confined to a single beat wave period, and obtain momenta exceeding that predicted by the separatrix corresponding to the circular polarization case. The fact that linear polarization results in large phase excursions as well as large momentum gains, in comparison to circular polarization, implies that the use of linear polarization can be more effective than circular polarization in the beat wave injection and trapping of electrons but with bunches having typically a larger energy spread.

3.9 Conclusion

An alternative configuration of the colliding pulse injector that uses a single pump pulse and a single counterpropagating injection pulse has been analyzed and simulated. This single injection pulse configuration has the advantages of simplicity and ease of experimental implementation. Injection is the result of the slow ponderomotive beat wave generated when the backward injection pulse collides with the rear portion of the forward pump pulse. Injection requires high pump laser intensity ($a_0 \simeq 1$) and modest injection pulse intensity ($a_1 \simeq 0.2$). Test particle simulations indicate that significant amounts of charge can be trapped and accelerated ($Q \sim 10$ pC), up to the limits imposed by beam loading. In addition, the accelerated bunches are ultrashort (~ 1 fs) with good beam quality ($\Delta\gamma/\gamma \sim$ few percent at a mean energy of ~ 10 MeV and a normalized rms emittance on the order 0.4 mm.mrad). Reduction of the energy spread can be achieved by including a density taper in the trapping region. The density taper will rephase electrons and consequently reduce the energy spread and increase the bunch charge. Also examined was the effect of interaction angle. For an interaction angle of 150° (where 180° is collinear, counterpropagating), the trapping fraction is only reduced by roughly ten percent, thus allowing efficient non-collinear

interaction geometries for further ease of experimental implementation. When the interaction angle was decreased to 90° (transverse injection geometry), no trapping was observed for the parameters of the simulation. Similarly, no trapping was observed for the parameters of the simulations for the case of orthogonal polarization. This confirms that the mechanism responsible for injection is the result of the slow ponderomotive force associated with the beating of the laser pulses, and not due to ponderomotive force associated with the envelope of the injection pulse.

One limitation of the approach used in this research is that it relies on test particle simulations in which the fields (lasers and wakes) were specified analytically. This model becomes inaccurate as a_0 and a_1 approach and exceed unity, since analytical expressions for nonlinear wakefields in 3D are lacking in the literature. Self-consistent simulations, such as using particle-in-cell codes, are required in this nonlinear regime, and this line of research is currently being pursued. Likewise, experiments on colliding pulse injection are being pursued at LBNL, as well as other laboratories world wide.

Chapter 4

Improvement of electron beam quality in optical injection schemes using negative plasma density gradients

Contents

4.1 Introduction

In this Chapter a negative plasma density gradient is proposed as a method for enhancing the electron beam quality in laser injection schemes [22]. If a laser injection scheme is operated close to threshold, electrons will be injected into the region of the wake that is accelerating but defocusing. To have a trapped electron bunch that is both accelerated and focused, it is necessary to shift the bunch forward in phase. This can be accomplished with a downward density ramp. As the density decreases, the plasma wavelength increases, thus a relativistic electron will be shifted forward in phase relative to the wake. This can shift an electron from the defocusing to the focusing region of the accelerating wake. In addition, if injection occurs on the density down-ramp, the trapping can occur more readily since the phase velocity of the wake is lowered on the down ramp. Numerical examples are given based on a three dimensional (3D) particle tracking code for the specific case of the two-pulse CPI method with density gradients.

4.2 Theory Section

4.2.1 Fields of laser and wake

We begin our considerations with the Maxwell's equations and the hydrodynamics equations for a relativistic cold electron fluid [9, 39]:

$$\nabla \cdot \left(\frac{e\mathbf{E}}{mc^2} \right) = -k_{p0}^2 \left[\frac{n_e - n_0(z)}{n_{00}} \right] , \tag{4.1}$$

$$\nabla \cdot \left(\frac{e\mathbf{B}}{mc^2} \right) = \mathbf{0} , \tag{4.2}$$

$$\nabla \times \left(\frac{e\mathbf{E}}{mc^2} \right) = -\frac{\partial}{\partial ct} \left(\frac{e\mathbf{B}}{mc^2} \right) , \tag{4.3}$$

$$\nabla \times \left(\frac{e\mathbf{B}}{mc^2} \right) = -k_{p0}^2 \frac{n_e}{n_{00}} \frac{\mathbf{u}}{\gamma} + \frac{\partial}{\partial ct} \left(\frac{e\mathbf{E}}{mc^2} \right) , \tag{4.4}$$

and

$$\frac{\partial (\mathbf{u} - \mathbf{a})}{\partial ct} = \nabla (\phi - \gamma) , \tag{4.5}$$

together with the general vorticity

$$\mathbf{\Omega} = \nabla \times (\mathbf{u} - \mathbf{a}) = \mathbf{0} \,, \tag{4.6}$$

and

$$e\mathbf{E}/mc^2 = -\nabla\phi - \frac{\partial \mathbf{a}}{\partial ct} \,, \tag{4.7}$$

$$e\mathbf{B}/mc^2 = \nabla \times \mathbf{a} \,. \tag{4.8}$$

The electromagnetic fields $\mathbf{E}$ and $\mathbf{B}$, vector potential $\mathbf{a}$ and potential ϕ are normalized with respect to e/mc^2, $k_{p0} = \omega_{p0}/c$ is the plasma wave number for the density n_{00} corresponding to the maximum ion background density in the homogeneous region of the plasma, n_e is the electron density, $n_0(z)$ is the background ion density profile, $\mathbf{u} = \mathbf{p}/mc^2$ is the normalized electron fluid momentum, $\gamma = \sqrt{1+u^2}$ is the relativistic factor and lastly the ions are assumed to be fixed.

The fluid-Maxwell's system of equation together is closed. Therefore the full system can be reduced to one equation for the dimensionless electron fluid momentum $\mathbf{u}$ [39],

$$\left[\frac{\partial^2}{\partial c^2 t^2} + \nabla \times \nabla \times + \frac{k_p^2(z)}{\sqrt{1+u^2}}\right]\mathbf{u} = -\frac{\partial}{\partial ct}\nabla\sqrt{1+u^2} - \frac{\mathbf{u}}{\sqrt{1+u^2}}\nabla\cdot\left[\frac{\partial \mathbf{u}}{\partial ct} + \nabla\sqrt{1+u^2}\right] \tag{4.9}$$

where $k_p(z) = (4\pi n_0(z) e^2/m_e c^2)^{1/2}$ has been used. In the mildly relativistic limit ($\mathbf{u} \ll 1$), Eq (4.9) can be further simplified, leading to

$$\left[\frac{\partial^2}{\partial c^2 t^2} + \nabla \times \nabla \times + k_p^2(z)\right]\mathbf{u} = -\frac{\partial}{\partial ct}\nabla\frac{u^2}{2} - \mathbf{u}\nabla\cdot\frac{\partial \mathbf{u}}{\partial ct} + O(\mathbf{u}^3) \tag{4.10}$$

where the approximations $(1+u^2)^{1/2} \simeq 1 + u^2/2$ and $(1-u^2)^{1/2} \simeq 1 - u^2/2$ have been used. We examine the nonlinear equation (4.10) order by order by writing $\mathbf{u} = \mathbf{u_1} + \mathbf{u_2}$ where $\mathbf{u}_1 \ll 1$ and $\mathbf{u}_2 \sim O(u_1^2)$, giving to first order

$$\left[\frac{\partial^2}{\partial c^2 t^2} + \nabla \times \nabla \times + k_p^2(z)\right]\mathbf{u}_1 = \mathbf{0} \tag{4.11}$$

From the general vorticity [Eq (4.6)] one can deduce the relationship $\mathbf{u} = \mathbf{a} + \nabla\psi$,

where $\mathbf{u}_L = \nabla\psi$ correspond to the irrotational part of the momentum. Inserting the first order version of that equation into (4.11) gives

$$\left[\frac{\partial^2}{\partial c^2 t^2} - \nabla^2 + k_p^2(z)\right]\mathbf{a}_1 + \left[\frac{\partial^2}{\partial c^2 t^2} + k_p^2(z)\right]\nabla\psi_1 = \mathbf{0} \tag{4.12}$$

We want to examine, for the case of a plasma density gradient $n_0(z)$, under what conditions the terms $\mathbf{a}_1$ and $\nabla\psi_1$ in Eq (4.12) are separable into two independent equations,

$$\boxed{\left[\frac{\partial^2}{\partial c^2 t^2} - \nabla^2 + k_p^2(z)\right]\mathbf{a}_1 = \mathbf{0}} \tag{4.13}$$

and,

$$\left[\frac{\partial^2}{\partial c^2 t^2} + k_p^2(z)\right]\nabla\psi_1 = \mathbf{0}\,. \tag{4.14}$$

Using the fact that $\mathbf{a}_1$ and $\nabla\psi_1$ represents the rotational and irrotational part of $\mathbf{u}_1$, taking the divergence of Eq (4.13) gives the condition

$$\boxed{a_{1z}k_p k_p' = 0} \tag{4.15}$$

where $k_p' = dk_p/dz$. This is always fullfilled in quasi 1-dimensional geometry (1-D), i.e., for a large laser spot size $k_p r_0 \gg 1$ or for the case of a long density taper $k_p L_t \gg 1$. For convenience Eq (4.14) can be further modified using (4.5) in order to give an equation for the first order plasma wave,

$$\left[\frac{\partial^2}{\partial c^2 t^2} + k_p^2(z)\right]\nabla\phi_1 = \mathbf{0}\,. \tag{4.16}$$

Taking the curl of (4.16) gives similar conditions,

$$\boxed{k_p\nabla_\perp\phi_1 \times \left(k_p'\mathbf{e}_z\right) = \mathbf{0}} \tag{4.17}$$

where $\mathbf{e}_z$ is a unit vector. Under this conditions the first order wake ϕ_1 is negligible while the first order vector potential $\mathbf{a}_1$ corresponds to the propagation of a laser pulse inside a plasma with the dispersion relation $k^2c^2 = \omega^2 - \omega_p^2(z)$.

To second order Eq (4.10) becomes,

$$\left[\frac{\partial^2}{\partial c^2 t^2} + \nabla \times \nabla \times + k_p^2(z)\right] \mathbf{u}_2 = -\frac{\partial}{\partial ct}\nabla \frac{u_1^2}{2} - \mathbf{u}_1 \nabla \cdot \frac{\partial \mathbf{u}_1}{\partial ct} \tag{4.18}$$

Inserting the solution $\mathbf{u_1} = \mathbf{a_1}$ along with the conditions $k_p r_0 \gg 1$ or $k_p L_t \gg 1$ gives

$$\left[\frac{\partial^2}{\partial c^2 t^2} - \nabla^2 + k_p^2(z)\right] \mathbf{a}_2 = \mathbf{0} \ , \tag{4.19}$$

and,

$$\boxed{\left[\frac{\partial^2}{\partial c^2 t^2} + k_p^2(z)\right] \nabla \phi_2 = k_p^2(z) \nabla \frac{a_1^2}{2}} \tag{4.20}$$

Eq (4.19) has no source terms giving $\mathbf{a}_2 = \mathbf{0}$ as a non trivial solution and ϕ_2 represents the nonlinear second order plasma wave solution for the case of a slowly varying background ion density ramp.

4.2.2 Structure of the code

This Section describes modifications to the 3D particle tracking code, introduced in Sec. 3.6, in which the electromagnetic fields for the laser pulses and their corresponding wakefields are specified analytically via linear theory. The laser fields of the pump ($i = 0$) and injection ($i = 1$) laser pulses are described by the normalized vector potentials $\mathbf{a}_i = e\mathbf{A}_i/m_e c^2$. The general solution to Eq (4.13), together with the paraxial approximation [which is equivalent to Eq. (3.9) but using $k_p(z)$ instead], can be found through the W.K.B approximation [65, 66] providing $k_p L_t \gg 1$, where L_t is the length of the density taper. In the following we will further assume that the plasma is underdense $\omega_p/\omega_0 \ll 1$ such that the plasma index of refraction is close to unity. Under these conditions the W.K.B solution is equivalent to solving the paraxial wave equation treating k_p as a constant and neglecting higher order contribution from the slowly varying plasma density gradient. The transverse laser fields (linearly polarized in the x-direction and propagating along the z-axis) are given by [52]

$$a_{xi}(r, \zeta_i) = \hat{a}_i(r, \zeta_i) \cos \psi_i \ , \tag{4.21}$$

with

$$\hat{a}_i(r,\zeta_i) = a_i(r_i/r_{si}) \exp\left(-r^2/r_{si}^2\right) \sin\left(\pi\zeta_i/L_i\right) \ , \tag{4.22}$$

for $-L_i < \zeta_i < 0$ and zero otherwise, where $\zeta_0 = z - \beta_{g0}ct$ (forward comoving coordinate), $\zeta_1 = -z - \beta_{g1}ct$ (backward comoving coordinate), $\beta_{gi} = \eta_i$ is the linear group velocity, $\beta_{\phi i} = \eta_i^{-1}$ is the linear phase velocity, $\eta_i = \sqrt{1 - \omega_p^2/\omega_i^2 - 4/(k_i r_i)^2}$ is the plasma index of refraction, $\psi_i = k_i(z - \beta_{\phi i}ct) + \alpha_i \ r^2/r_{si}^2 + \alpha_i - \tan^{-1}\alpha_i$ is the phase, $k_i = \omega_i/(\beta_{\phi i}c)$ is the wavenumber, ω_i is the frequency in vacuum, $r_{si}(z) = r_i\sqrt{1+\alpha_i(z)}$ is the spot size, r_i is the spot size at waist (here chosen to be $z = Z_{f_i}$), $\alpha_i(z) = (z - Z_{f_i})^2/Z_{R_i}^2$, $Z_{R_i} = k_i\eta_i \ r_i^2/2$ is the Rayleigh length, L_i is the pulse length, and a constant has been omitted in the definition of ψ_i that represents the initial position and phase of the laser pulse. The axial component of the laser field is specified via $\nabla \cdot \mathbf{a_i} = \mathbf{0}$. Keeping only the leading order contributions gives

$$a_{zi}(r,\zeta_i) \simeq 2x[\hat{a}_i(r,\zeta_i)/(k_i r_{si}^2)] \left(\sin\psi_i - \alpha_i \cos\psi_i\right) \ . \tag{4.23}$$

Included in the simulations are the wakefields generated by both the pump and injection laser pulses. For linear polarization and a slowly varying density variation, i.e., $L_t \gg \lambda_p$ the normalized electric field of the wakefield $k_{p0}\mathbf{E}_i/E_0 = -\nabla\phi_{2i}$ is given by Eq. (4.20),

$$\left[\partial^2/\partial\zeta_i^2 + k_p^2(z)\right] k_{p0}\mathbf{E}_i/E_0 \simeq k_p^2(z)\nabla\hat{a}_i^2/4 \ , \tag{4.24}$$

where $k_p = \omega_p/c$, $E_0 = mc^2k_{p0}/e$ is the cold nonrelativistic wavebreaking field normalized to a fixed ion density n_{00}. Note that time-averaging has been performed over the fast laser oscillation (laser frequency), i.e., $\langle\hat{a}_i^2\cos^2\psi_i\rangle = \hat{a}_i^2/2$. Using $\zeta = z - ct$ and $z' = z$ gives $\partial/\partial ct = -\partial/\partial\zeta$ and $\partial/\partial z = \partial/\partial\zeta + \partial/\partial z'$. Furthermore assuming that a_i is a function of ζ_i only, the solution to Eq. (4.24) is

$$\boxed{\mathbf{E}_i(r,\zeta_i)/E_0 = -(k_p(z)/4k_{p0})\int_0^{\zeta_i} d\zeta_i' \sin[k_p(z)(\zeta_i - \zeta_i')](\partial/\partial\zeta_i' + \nabla_\perp)\hat{a}_i^2(r,\zeta_i')} \tag{4.25}$$

Specifically, Eq. (4.24) yields the electric field generated inside the pulse ($-L_i < \zeta_i < 0$),

$$\frac{\mathbf{E}_{ri}}{E_0} = \frac{a_i^2}{2}\frac{r_i^2 r}{k_{p0} r_{si}^4} e^{-2r^2/r_{si}^2}\left[1 + \frac{(4\pi^2/k_p^2 L_i^2)\cos(k_p\zeta_i) - \cos(2\pi\zeta_i/L_i)}{(1 - 4\pi^2/k_p^2 L_i^2)}\right] , \tag{4.26}$$

$$\frac{\mathbf{E}_{zi}}{E_0} = \frac{k_p}{k_{p0}}\frac{a_i^2}{8}\frac{r_i^2}{r_{si}^2} e^{-2r^2/r_{si}^2}\left[\frac{(4\pi^2/k_p^2 L_i^2)\sin(k_p\zeta_i) - \sin(2\pi\zeta_i/L_i)}{(1 - 4\pi^2/k_p^2 L_i^2)}\right] , \tag{4.27}$$

and behind the pulse ($\zeta_i < -L_i$)

$$\frac{\mathbf{E}_{ri}}{E_0} = a_i^2\frac{r_i^2 r}{k_{p0} r_{si}^4} e^{-2r^2/r_{si}^2}\left(\frac{4\pi^2}{k_p^2 L_i^2}\right)\frac{\sin[k_p(\zeta_i + L_i/2)]\sin(k_p L_i/2)}{(1 - 4\pi^2/k_p^2 L_i^2)} , \tag{4.28}$$

$$\frac{\mathbf{E}_{zi}}{E_0} = -\frac{k_p}{k_{p0}}\frac{a_i^2}{4}\frac{r_i^2}{r_{si}^2} e^{-2r^2/r_{si}^2}\left(\frac{4\pi^2}{k_p^2 L_i^2}\right)\frac{\cos[k_p(\zeta_i + L_i/2)]\sin(k_p L_i/2)}{(1 - 4\pi^2/k_p^2 L_i^2)} . \tag{4.29}$$

For the resonant case $L = \lambda_p$, which corresponds to conditions close to maximum wakefield generation, we get inside the pulse

$$\frac{\mathbf{E}_{ri}}{E_0} = \frac{a_i^2}{2}\frac{r_i^2 r}{k_{p0} r_{si}^4} e^{-2r^2/r_{si}^2}\left[1 - \cos(k_p\zeta_i) - (k_p\zeta_i/2)\sin(k_p\zeta_i)\right] , \tag{4.30}$$

$$\frac{\mathbf{E}_{zi}}{E_0} = -\frac{k_p}{k_{p0}}\frac{a_i^2}{8}\frac{r_i^2}{r_{si}^2} e^{-2r^2/r_{si}^2}\left[\sin(k_p\zeta_i)/2 - (k_p\zeta_i/2)\cos(k_p\zeta_i)\right] , \tag{4.31}$$

and behind the pulse,

$$\frac{\mathbf{E}_{ri}}{E_0} = \frac{\pi a_i^2}{2}\frac{r_i^2 r}{k_{p0} r_{si}^4} e^{-2r^2/r_{si}^2}\sin(k_p\zeta_i) , \tag{4.32}$$

$$\frac{\mathbf{E}_{zi}}{E_0} = -\frac{k_p}{k_{p0}}\frac{\pi a_i^2}{8}\frac{r_i^2}{r_{si}^2} e^{-2r^2/r_{si}^2}\cos(k_p\zeta_i) . \tag{4.33}$$

The ion density profile is assumed to be of the form

$$\boxed{\frac{n_0(z)}{n_{00}} = 1 - \frac{\tau_t}{2}\left[1 + \tanh\left(\frac{z - z_t}{L_t}\right)\right]} \tag{4.34}$$

where n_{00} is the ion density before the density drop-off ($z < 0$), z_t the location of the transition and $\tau_t = \Delta n_0/n_{00}$ the relative change of density.

Note that for high laser intensities ($|a_i| > 1$), this model becomes inaccurate. To describe the nonlinear regime in 3D, as well as other nonlinear effects such as beam loading, requires self-consistent simulations such as can be done with particle-in-cell codes, which is beyond the scope of this dissertation.

4.2.3 Density down-ramps

A density down-ramp can enhance the number of trapped and focused electrons by two effects: (1) A decrease in density shifts the position of an electron forward in phase with respect to the wakefield and (2) a decrease in density decreases the phase velocity of the wake, thus providing a lower threshold for injection. Consider a change in density from n_i to n_f ($n_i > n_f$) over a length L_t. The phase of the electron before and after the transition are given by $\psi_i = k_{pi}\zeta$ and $\psi_f = k_{pf}\zeta$, respectively, assuming that the slippage between the electron and the drive laser pulse is small over L_t (ζ is approximately constant), where $\zeta = z - ct$ is the position of the electron behind the drive pulse ($\zeta < 0$ behind the drive pulse), and $k_{pi} = \omega_{pi}/c$ and $k_{pf} = \omega_{pf}/c$ are the plasma wavenumbers evaluated at n_i and n_f, respectively. Hence, the change in phase of the electron after the density transition is $\Delta\psi = \psi_i - \psi_f$, i.e.,

$$\boxed{\Delta\psi = \psi_i \left[1 - (n_f/n_i)^{1/2}\right] \simeq \psi_i \left(\Delta n/2n_i\right)} \tag{4.35}$$

assuming $\Delta n = n_i - n_f \ll n_i$. Hence, the change in density required to shift an electron forward in phase by a small amount (i.e., $\Delta\psi \sim \pi/4$) is $\Delta n/n_i = 2(\Delta\psi/\psi_i) = 2(\Delta\psi/k_{pi}\zeta)$. Note that rephasing becomes easier (a smaller $\Delta n/n_i$ is required) with increasing distance behind the driver (larger $|\zeta|$). Hence, rephasing is more efficient for the three-pulse CPI configuration than for two-pulse CPI, assuming the injection point for three-pulse CPI is behind the first wake period.

If the injection (pulse collision) point was to occur on the down-ramp (as opposed to prior to it), then trapping could be further enhanced due to the decrease in phase velocity of the wake on the down-ramp. The wake phase velocity v_p can be calculated

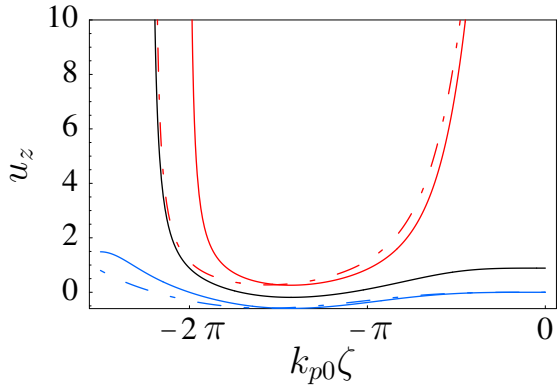

Figure 4.1: (Color) Phase space plot showing cold fluid orbit for $n_0/n_{00} = 1$ (blue solid line), $n_0/n_{00} = 0.7$ (blue dot-dashed line), trapped and focused orbit for $n_0/n_{00} = 1$ (red solid line), $n_0/n_{00} = 0.7$ (red dot-dashed line) and orbit of an electron in a trapped but defocusing region of the wakefield for $n_0/n_{00} = 1$ (black solid line). Laser parameters: $L_0 = \lambda_{p0}$ and $a_0 = 1$.

from the wake phase $\psi = k_p(z)(z - ct)$ via $v_p/c = -(\partial\psi/\partial ct)/(\partial\psi/\partial z)$. This gives

$$v_p/c = 1/(1 + k_p^{-1}k_p'\zeta), \tag{4.36}$$

where primes denote a derivative with respect to the z variable and $k_p' = (k_p/2n)n'$. Since $\zeta < 0$ behind the drive pulse, the phase velocity decreases on a density down-ramp ($dn/dz < 0$). Note that this effect becomes more pronounced the larger the distance behind the driver. Thus, the reduction in phase velocity due to the down-ramp is potentially more effective for three-pulse CPI than for two-pulse CPI. Eventually, even in the absence of an injection pulse, the down-ramp leads to wavebreaking and injection for a sufficiently large distance behind the pump pulse [45], assuming that the wake amplitude does not damp.

4.3 Simulation results

In the following simulations, the plasma was modeled by a group of test electrons initially at rest and loaded randomly in a three dimensional spatial region of length λ_p and transverse radius $\lambda_p/2$, uniformly about the z-axis, corresponding to a volume $V_0 = \pi\lambda_p^3/4$. This spatial region was chosen to be ahead of the pump laser pulse, and

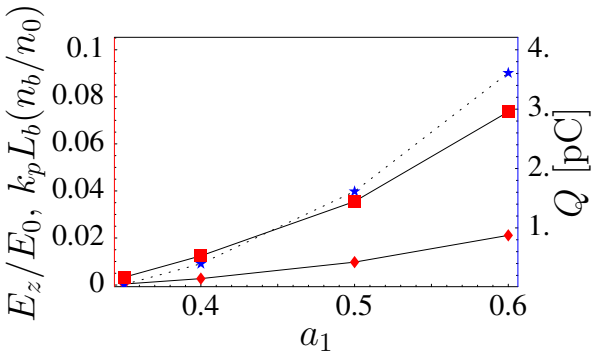

Figure 4.2: (Color) Bunch charge Q in pC (right vertical axis, stars), $k_pL_b(n_b/n_0)$ (left vertical axis, squares) and normalized axial electric field E_z/E_0 (left vertical axis, points) generated by the electron bunch alone (here the laser contribution is not included) versus a_1 with $\lambda_0 = 0.8$ μm, $L_0 = 9\lambda_{p0}/4$, $r_0 = \lambda_{p0} = 40$ μm, $a_0 = 1$, homogeneous plasma, i.e., no density ramp and $ct = 47\ k_{p0}^{-1} \simeq 300$ μm after injection

timed with respect to the initial position of the injection pulse such that when the two pulses collide, the test electrons fill the entire region in which trapping may occur. After the collision, various properties of the trapped electron bunch were monitored as function of propagation time, such as the mean energy, the energy spread, the root-mean square (RMS) bunch length, RMS bunch radius and the trapping fraction. Here, the trapping fraction is defined as N_b/N_s where N_b is the number of test electrons in the bunch and N_s the total number of test electrons in the simulation. A quasi-1D configuration with $r_i \simeq \lambda_p$ was chosen, such that most of the injected electrons, although in a defocusing region of the accelerating wave, will only slowly depart transversely from their initial on-axis location. A density down-ramp will then rephase those electrons onto a trapped and focused orbit. This is shown in Fig. 4.1, where the cold fluid orbit and trapped and focused orbit are both shown for an initial density n_{00} and another density 30% smaller. Note that the focusing region has been extended farther behind the pump pulse. The simulations were carried out for normalized laser-plasma parameters $a_0 = 1$, $\omega_0/\omega_{p0} = 50$, $L_0 = \lambda_{p0}$ or $9\lambda_{p0}/8$, $\omega_1/\omega_{p0} = 50$ and $L_1 = \lambda_{p0}/2$. Parameter scans were performed for the injection pulse normalized vector potential a_1 and for the parameters corresponding to the density ramp such as the length L_t, the center of the transition z_t and the relative change of density τ_t. Figure 4.2 shows the resulting electron beam characteristics produced

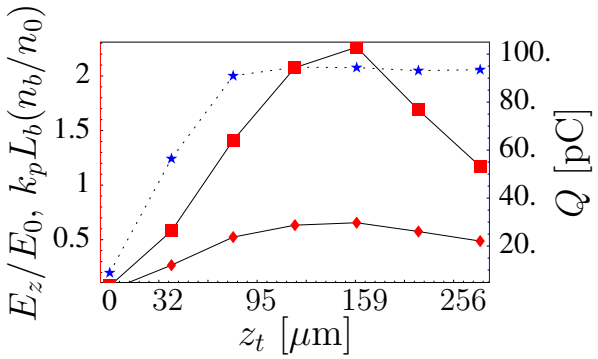

Figure 4.3: (Color) Bunch charge Q in pC (right vertical axis, stars), $k_pL_b(n_b/n_0)$ (left vertical axis, squares) and normalized axial electric field E_z/E_0 (left vertical axis, points) generated by the electron bunch alone versus z_t with $\lambda_0 = 0.8$ μm, $L_0 = 9\lambda_{p0}/4$, $r_0 = \lambda_{p0} = 40$ μm, $a_0 = 1$, $a_1 = 0.5$, $L_t = \lambda_{p0}$, $\tau_t = 30\%$ and $ct = 147\ k_{p0}^{-1} \simeq 935$ μm after injection

in a uniform plasma without the use of a plasma density gradient [21]. The total charge in the bunch Q was estimated from the trapping fraction $f_{\rm tr}$ (the fraction of the initial electrons that remain on trapped and focused orbits) by $Q = en_0 f_{\rm tr} V_0$. The bunch density was calculated assuming a square beam profile using the relationships between the length, radius and corresponding RMS quantities, i.e., $L_b = 2\sqrt{3}\sigma_z$ is the full beam length, σ_z the RMS beam length, $r_b = 2\sigma_r$ the beam radius and σ_r the beam RMS radius. For the configuration shown in Fig. 4.2, the typical value of the charge injected is on the order ~ 4 pC. Note also that for high bunch charge, beam loading may become important [see Sec. 3.7 for further details]. For a uniform beam profile $n_b(r,\zeta) = n_b\Theta(r_b - r)\Theta(-\zeta)\Theta(\zeta + L_b)$ of radius r_b and length L_b, where Θ is a step function, the amplitude of the perturbed density and the axial electric field of the bunch-induced wake is found to be at the back of the bunch [21, 61, 62],

$$\delta n/n_0 \simeq -\left(k_pL_b\right)^2 \left(n_b/n_0\right)/2\ , \tag{4.37}$$

$$E_z/E_0 \simeq k_pL_b\left(n_b/n_0\right) F_R(r)\ , \tag{4.38}$$

assuming $k_pL_b \ll 1$, $\delta n/n_0 \ll 1$, and $E_z/E_0 \ll 1$, where the radial profile function is $F_R(r) = 1 - k_pr_bK_1(k_pr_b)I_0(k_pr)$ for $r < r_b$. Here I_0 and K_1 are modified Bessel functions. For a narrow beam $k_p^2r_b^2 \ll 1$ and along the axis $F_R(r = 0) \simeq$

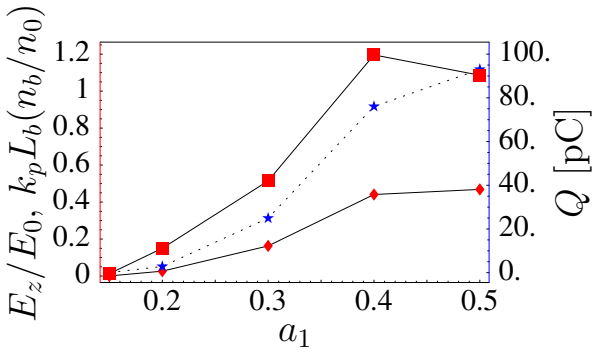

Figure 4.4: (Color) Bunch charge Q in pC (right vertical axis, stars), $k_pL_b(n_b/n_0)$ (left vertical axis, squares) and normalized axial electric field E_z/E_0 (left vertical axis, points) generated by the electron bunch alone versus a_1 with $\lambda_0 = 0.8$ μm, $L_0 = 9\lambda_{p0}/4$, $r_0 = \lambda_{p0} = 40$ μm, $a_0 = 1$, $z_t = 240$ μm, $L_t = \lambda_{p0}$, $\tau_t = 30\%$ and $ct = 147\ k_{p0}^{-1} \simeq 935$ μm after injection

$[0.308 - 0.5\ln(k_pr_b)]k_p^2r_b^2$. Note that this solutions are obtained from the linearized fluid-Maxwell equations included an external beam where the latter is assumed non involving. For $k_pL_b(n_b/n_0) \simeq 1$ the linear approximation becomes inaccurate and higher order methods such as PIC or fluid codes must be used. The other parameter of interest is a comparison of the wakefield intensity produced by the laser pulse with respect to the wake induced by the beam itself. The latter is required to be much smaller. Using Eq. (4.33) together with Eq. (4.38) yield an approximated ratio,

$$\alpha_l = \frac{k_pL_b}{a_0^2}\frac{n_b}{n_0}F_R(0) \ll 1\ , \tag{4.39}$$

which is valid for a laser beam close to the resonnant condition $L \simeq \lambda_p$. For the case of Fig. 4.2 beam loading is a negligible effect.

Figure 4.3 shows the amount of charge in the trapped and focused region of the plasma wave as a function of the density down ramp center z_t for the laser-plasma parameters: $a_0 = 1$, $\omega_0/\omega_{p0} = 50$, $L_0 = 9\lambda_{p0}/8$, $a_1 = 0.5$, $\omega_1/\omega_{p0} = 50$, $L_1 = \lambda_{p0}/2$, $L_t = \lambda_{p0}$, $\tau_t = 30$ % and $\omega_{p0}t = 147$ after injection. λ_{p0} corresponds to the plasma wavelength prior to the density transition. The total charge is increasing temporarily up to a plateau region reached at about $k_{p0}z_t = 4\pi$. As mentioned above, Figure 4.1 shows the phase shift of the trapped and focused region after passing through the density transition [according to Eq. (4.35)] as well as a typical orbit of an electron

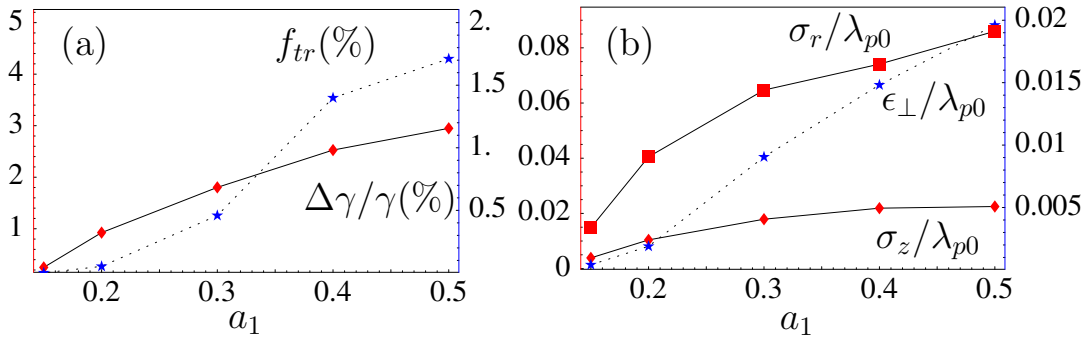

Figure 4.5: (Color) Trapped bunch parameters versus a_1 (for two collinear, counter-propagating laser pulses with equal polarization, $a_0 = 1$, $\omega_0/\omega_{p0} = 50$, $L_0 = 9\lambda_{p0}/8$, $\omega_1/\omega_{p0} = 50$, $L_1 = \lambda_{p0}/2$, $k_{p0}z_t = 12\pi$, $k_{p0}L_t = 2\pi$, $\tau_t = 30\%$ and $ct = 147\ k_{p0}^{-1}$). (a) Trapping fraction $f_{\rm tr}$ (right vertical axis) and relative energy spread $\Delta\gamma/\gamma$ (left vertical axis). (b) Bunch length σ_z/λ_{p0} (left vertical axis), rms radius σ_r/λ_{p0} (left vertical axis), and normalized transverse rms emittance $\epsilon_\perp/\lambda_{p0}$ (right vertical axis).

lying in the defocusing region. The latter electrons will circulate along this path towards the high energy region and will cross the extented focusing region of the plasma wave at some later time after injection. Delaying the density transition until those electrons reach the phase $\psi_f \simeq 2\pi$ will allow for rephasing of maximum amount of charge. In Fig. 4.3, a charge per bunch enhancement by a factor of ~ 50 is shown. In this case beam loading may become important, i.e., the bunch induced wakefield E_z/E_0 becomes comparable to the wake generated by the drive laser pulse alone. Nonlinear beam loading will most likely reduce the bunch quality (fraction trapped, average energy, etc.). Note that the oscillation showns in Fig. 4.3 for the electric field E_z/E_0 as well as for the beam density $k_pL_b(n_b/n_0)$ may be attributed to the extra focusing provided to the rephased electrons by the plasma wave.

Figure 4.4 plots the parameter $k_pL_b(n_b/n_0)$ (which is used as an indicator for the estimation of the validity of the linear regime in the calculation of beam loading), the electric field E_z/E_0 induced by the electron beam alone and the charge trapped as a function of the injection laser strength a_1 for the same laser-plasma parameters as of Fig. 4.3 except for $k_{p0}z_t = 12\pi$. The latter corresponds to the region of Fig. 4.3 were maximum trapping is achieved. Comparing Fig. 4.2 with Fig. 4.4 shows a lower trapping threshold as expected ($a_{1\rm min} \simeq 0.35$ versus 0.15). The electron beam remains very compact as shown in Fig. 4.5. The RMS bunch radius σ_r and RMS

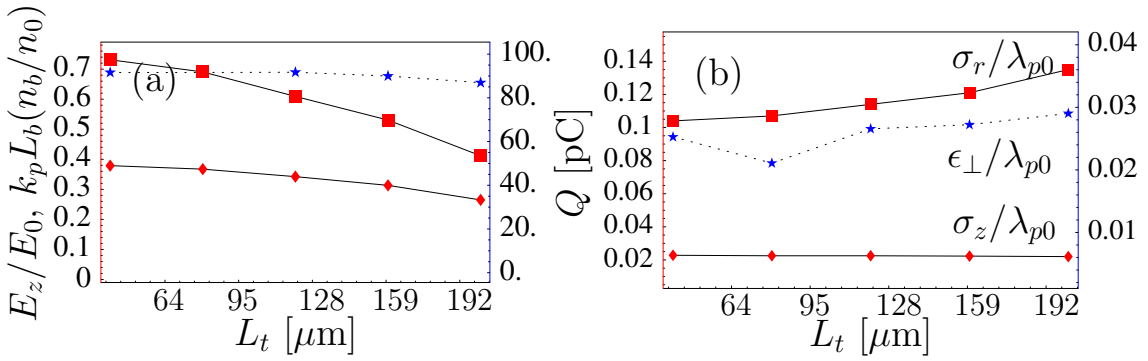

Figure 4.6: (Color) (a) Bunch charge Q in pC (right vertical axis, stars), $k_pL_b(n_b/n_0)$ (left vertical axis, squares) and normalized axial electric field E_z/E_0 (left vertical axis, points) generated by the electron bunch alone. (b) Bunch length σ_z/λ_{p0} (left vertical axis), rms radius σ_r/λ_{p0} (left vertical axis), and normalized transverse rms emittance $\epsilon_\perp/\lambda_{p0}$ (right vertical axis) versus L_t for the laser-plasma parameters: $\lambda_0 = 0.8$ μm, $L_0 = 9\lambda_{p0}/4$, $r_0 = \lambda_{p0} = 40$ μm, $a_0 = 1$, $a_1 = 0.5$, $z_t = 280$ μm, $\tau_t = 30\%$ and $ct = 147\ k_{p0}^{-1} \simeq 935$ μm after injection.

bunch half length σ_z are on the order of a few percent of the plasma wavelength λ_{p0} which corresponds to *attosecond* durations. The bunch normalized emittance is approximated as $\epsilon_\perp = \gamma_0\beta_0\sqrt{\langle x^2\rangle\langle x'^2\rangle} \simeq \sqrt{\langle x^2\rangle\langle u_x^2\rangle}$, where $u_0 = \gamma_0\beta_0 \simeq \gamma_0$ is the axial momentum of the electron bunch. For the case of Fig. 4.5, the emittance is typically small, i.e., for $\lambda_{p0} = 40$ μm ($n_{00} = 6.9 \times 10^{17}$ cm^{-3}), we have $\epsilon_\perp <$ 0.8 mm.mrad for an average kinetic energy of $T \simeq 23$ MeV. The energy spread $\Delta\gamma/\gamma$ is on the order of a few percent. A 1D analysis of the dephasing length [9] (which is the typical length required for a trapped electron to outrun the plasma wave and get a maximum energy gain) gives $L_d \simeq \gamma_p^2\lambda_p$, where $\gamma_p = (1-\beta_p^2)^{1/2}$ is the plasma wave relativistic factor and $\beta_p = \beta_{g0}$ is the plasma wave normalized momentum which is equal to the laser group velocity in the linear regime. For an underdense plasma $\omega_p/\omega_0 \ll 1$, we have $\gamma_p \simeq \omega_0/\omega_p$ corresponding to $L_d \sim 10$ cm for $n_0 \sim 7 \times 10^{17}$ cm^{-3}. Furthermore, in 3D the Rayleigh length $Z_R \simeq k_0 r_0^2/2$ (which is the typical distance beyond which the laser strength a_0 is divided by $\sqrt{2}$) must be compared to the dephasing length and is found to be on the order 4 cm. The beam parameters shown in Fig. 4.5 are evaluated only after a propagation distance on the order 1 mm, we then expect an improvement of beam quality over longer acceleration distances (increase of kinetic energy, lower energy spread, etc.).

Figure 4.6(a) plots the parameter $k_p L_b(n_b/n_0)$, bunch charge Q and bunch-induced axial electric field E_z/E_0 as a function of the density transition length L_t. This shows a very low incidence on the beam quality. Trapping fraction remains mainly unchanged. The small increase in bunch radius together with the emittance [Fig. 4.6(a)] can be explained by the fact that a long density transition implies that the electron beam remains for a longer period of time in a defocusing phase. The requirement on the transition length L_t is to be smaller that the typical distance it takes an electron to outrun the plasma wave. For the laser-plasma parameters used in this paper, we have $Z_R < L_d$, which also implies $1 \ll L_t \ll Z_R$ as a relevant boundary. This demonstrate the feasibility of using negative plasma density gradients in laboratory experiments as a mean for rephasing trapped but unfocused electrons.

Figure 4.7 shows the trapped bunch charge and corresponding beam loading parameters as a function of the relative change of density τ_t for the laser-plasma parameters: $\lambda_0 = 0.8$ μm, $L_0 = r_0 = \lambda_{p0} = 40$ μm, $a_0 = 1$, $a_1 = 0.2$, $z_t = 240$ μm, $L_t = 40$ μm and $ct = 147\ k_{p0}^{-1} \simeq 935$ μm after injection. Note that $a_1 = 0.2$ is found to be close to the trapping threshold for $\tau_t \simeq 25$ % and by increasing τ_t the trapped charge in the bunch become as high as $Q = 20$ pC for $\tau_t = 60$ %. Concequenty for such value of τ_t, the trapping threshold is lower than 0.2, which is order of magnitude smaller that the laser strength required in ponderomotive injection schemes [18]. Another possible interesting regime would be to lower the drive pulse strength instead of the injection pulse. Using $k_p L_0 = k_p r_0 = k_p r_1 = 2\pi$ along with $a_1 = 0.5$ and $k_p L_1 = 4\pi$ (a length far from the resonant condition in order to minimize the injection wake which could interfere with the wake generated by the drive pulse itself for the case of a modest value of a_0) combined with a long taper length, $k_p z_t > 5\pi$ (to allow maximum injection, i.e., see Fig. 4.3) and $\tau_t = 30$ % may provide a threshold as low as $a_0 = 0.8$.

4.4 Conclusion

Plasma density down-ramps have been proposed as a method for improving electron bunch quality in laser injection schemes. A decrease in density implies an increase in plasma wavelength, which can shift a relativistic electron from the defocusing to the

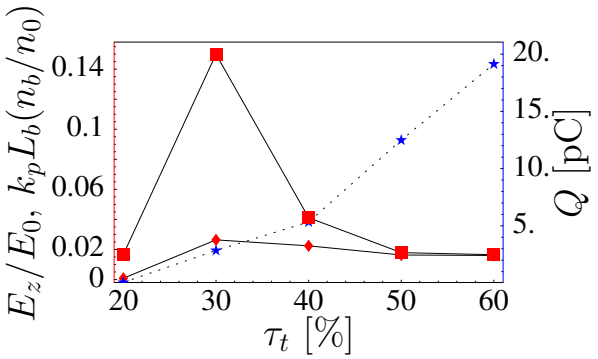

Figure 4.7: (Color) Bunch charge Q in pC (right vertical axis, stars), $k_pL_b(n_b/n_0)$ (left vertical axis, squares) and normalized axial electric field E_z/E_0 (left vertical axis, points) generated by the electron bunch alone versus τ_t with $\lambda_0 = 0.8$ μm, $L_0 = r_0 = \lambda_{p0} = 40$ μm, $a_0 = 1$, $a_1 = 0.2$, $z_t = 240$ μm, $L_t = 40$ μm and $ct = 147\ k_{p0}^{-1} \simeq 935$ μm after injection.

focusing region of the accelerating wakefield. Also, a decrease in density leads to a decrease in wake phase velocity, which can lower the trapping threshold. The specific method of two-pulse CPI was examined using a 3D test particle tracking code. A density down-ramp of 30% led to about ~ 50 times enhancement of trapping fraction of background plasma electrons compared to the standard two-pulses colliding-pulses injection scheme. Furthermore, no degradation of overall bunch parameters was observed compared to the uniform plasma case. A small incidence on the beam quality was also found by using a long density transition which makes it experimentally feasible with available gas jet technology. The overall trapping threshold for electron injection into the plasma wave was also lowered allowing the use of conventional laser systems.

One limitation of the approach used in this research is that it relies on test particle simulations in which the fields (lasers and wakes) were specified analytically. This model becomes inaccurate as a_0 and a_1 approach and exceed unity and self-consistent simulations, such as using particle-in-cell codes, are required in this nonlinear regime.

Chapter 5

Space charge effects in large energy spread e-beams

Contents

5.1 Introduction

The aim of this Chapter is to discuss vacuum propagation of beams produced by plasma based accelerators. Such beams are typically very compact, with a relatively high charge per bunch and energy spread (depending on experimental scheme). An important issue is to understand how these beams evolve as they exit the plasma. What are the changes these bunches undergo and how quickly do they occur? How does the energy spread, emittance, bunch duration change? In this Chapter, we will concentrate on two types of beams:

(i) The first type of beams are produced by the self-modulated laser-wakefield-accelerator (SM-LWFA) [9]. The latter relies on self-trapping to inject electrons into the plasma wakefield. Because the electrons are self-injected, the resulting bunch typically has a large energy spread, characterized by an exponential distribution in energy with a temperature ranging from 1-10's of MeV. The bunch can have high charge $\sim 1-10$ nC, with typical transverse dimensions ~ 10 μm and bunch half length ~ 10 μm, giving a high number density $\sim 2.5\times10^{19}$ cm^{-3}.

(ii) The second type of beams are produced by optical injection, such as in the colliding pulse injector (CPI) scheme [19–22], which allows the production of electron bunches of small relative energy spread. CPI uses two to three short laser pulses of length L comparable to the plasma wavelength λ_p. The drive pulse generates the wake, and the beating of the backward pulse with the drive pulse (or a third pulse) injects electrons with a small phase spread into the wakefield. This scheme offers detailed control of the injection process, and since $L \lesssim \lambda_p$, Raman and self-modulation instabilities will be suppressed. The resulting electron bunches carry a charge $\sim 10-200$ pC, with an average energy > 10 MeV, and a relative energy spread of $1-10$ %. The bunch typical transverse dimensions are ~ 10 μm, and the bunch half length is ~ 2.5 μm, corresponding to a number density of $\sim 2.5\times10^{17}$ cm^{-3}. This is two orders of magnitude smaller than in the self-modulated regime, but the longitudinal quality of the beam is much better because of the small relative energy spread.

Several algorithms for computing space charge forces have been proposed and intensively used over the past years to model electron beam dynamics in linacs and storage

rings [67–69]. Such methods generally assume that the electron beam has a small energy spread. In this case there is a single coordinate system (frame) in which all beam particles are non-relativistic, simplifying considerably the calculation of electromagnetic self fields. This method may not be directly applied to beams with large energy spreads and it is consequently useful to develop new models allowing for fast computation of beam dynamics without the necessary use of fully explicit techniques such as particle-in-cell codes [54, 55] which are known to be computationally costly.

In this Chapter, we consider evolution of the electron beam in vacuum and in the absence of external forces. Its organization is the following: The assumptions and numerical methods (envelope equations, ellipsoidal shell decomposition, Poisson solvers, and point-to-point interactions) are summarized from Sec. 5.2 to Sec. 5.7. These models are compared to each others and their approximations are discussed in great detail. More specifically, Sec. 5.2 and 5.3 derive the electrostatic fields for an heterogeneous ellipsoid and an ellipsoidal shell. The latter both characterize the typical shapes which will be used as our basic assumptions for an analytical description of the electron bunches. From those results, Sec. 5.4 examines a rapid and innovative method for the calculation of space charge effects, assuming paraxial approximation but capable of handling beams with an arbitrary energy distribution [36]. The method is valid for a large parameter regime, making assumptions only about the position space ellipsoidal symmetry properties of the charge distribution. In order to obtain simple analytical expressions for the space charge force, in this Section, we specialize to the case of charge distributions with radial symmetry about the axis of propagation. Section 5.5 gives a comprehensive summary of the envelope model followed by the descriptions, in Sec. 5.6, of a modified electrostatic particle-in-cell code. The latter is an extension of the model discussed in Sec. 5.4 and does not make any assumptions on the spacial symmetries of the electron beam. In Sec. 5.7, a three-dimensional point-to-point interaction (3D-PPI) approach will be discussed. This method applies to large energy spread beams and does not require the paraxial approximation. Section 5.8 examines some electron sources produced by CPI and SM-LWFA experiments, Sec. 5.9 compares PPI and PIC codes for the simulation of space charge dominated beams, and finally, Sec. 5.10 discusses (i) both limitations and possible generalization of the PPI model and (ii) emittance growth for beams with large energy spreads.

5.2 Heterogeneous ellipsoids

In this Section a comprehensive summary on potential theory applied to a charge distribution with ellipsoidal symmetry is provided. An excellent derivation is given in the book *Ellipsoidal Figures of Equilibrium* from S. Chandrasekhar [70] which will not be detailed here. The general formulation for the potential of a heterogeneous ellipsoid can be derived with the combined use of geometry and calculus. Note that for the special case of gaussian charge density the integral representation of the potential,

$$\phi(\mathbf{x}) = \frac{1}{4\pi\epsilon_0}\int_{-\infty}^{\infty}\frac{\rho(\mathbf{x}')}{|\mathbf{x}-\mathbf{x}'|}d^3\mathbf{x}' \,, \tag{5.1}$$

can be directly integrated, this is shown in Appendix F.

For simplicity, we will assume that the charge distribution is at rest and that the ellipsoid is located at the center of the frame of reference, i.e., $\bar{x}_i = 0$. For a solid homogeneous ellipsoid with density distribution $\rho(r^2)$ the potential [70] is

$$\boxed{\phi(x,y,z) = \frac{a_1 a_2 a_3}{4\epsilon_0}\int_0^{\infty}\frac{du}{\Delta(u)}\int_{r^2(u)}^{1} dr^2\rho(r^2)} \tag{5.2}$$

where

$$r^2 = \sum_i \frac{x_i^2}{a_i^2} \,, \tag{5.3}$$

$$r^2(u) = \sum_i \frac{x_i^2}{a_i^2+u} \,, \tag{5.4}$$

and

$$\Delta(u) = \sqrt{(a_1^2+u)(a_2^2+u)(a_3^2+u)} \,. \tag{5.5}$$

The general form for the electric field is

$$E_i = -\frac{\partial\phi}{\partial x_i} = -\int_0^{\infty}\frac{\partial f(x,y,z,u)}{\partial x_i}du \,, \tag{5.6}$$

with

$$f(x,y,z,u) = \frac{1}{4\epsilon_0}\frac{a_1 a_2 a_3}{\Delta(u)}\int_{r^2(u)}^{1} dr^2\rho(r^2) \,, \tag{5.7}$$

and

$$\frac{\partial f(x,y,z,u)}{\partial x_i} = -\frac{1}{4\epsilon_0}\frac{a_1a_2a_3}{\Delta(u)}\rho[r^2(u)]\frac{\partial r^2(u)}{\partial x_i} \ , \tag{5.8}$$

i.e.,

$$\boxed{E_i = \frac{a_1a_2a_3}{2\epsilon_0}x_i\int_0^\infty \frac{du}{(a_i^2+u)\,\Delta(u)}\rho[r^2(u)]} \tag{5.9}$$

For the special case where the density profile has the form

$$\rho(r^2) = \begin{cases} \rho_0, \text{ for } r^2 \leq 1 \ , \\ 0, \text{ otherwise} \ , \end{cases} \tag{5.10}$$

we get *inside* the ellipsoid,

$$E_i = \frac{\rho_0}{2\epsilon_0}a_1a_2a_3x_iA_i(0,\infty) \ , \tag{5.11}$$

and for a point *outside* the ellipsoid, Eq. (5.4) gives $r^2(\lambda) = 1$ where $\lambda > 0$ and the integral may be rewritten as

$$E_i = \frac{\rho_0}{2\epsilon_0}a_1a_2a_3x_iA_i(\lambda,\infty) \ , \tag{5.12}$$

where

$$\boxed{A_i(\lambda,\infty) = \int_\lambda^\infty \frac{du}{(a_i^2+u)\,\Delta(u)}} \tag{5.13}$$

and,

$$\boxed{\begin{aligned} 2\lambda\,(x,y,z) \;&=\; x^2+y^2+z^2-a^2-a_3^2+ \\ &\quad \sqrt{\left(x^2+y^2+z^2-a^2-a_3^2\right)^2+4\left[a_3^2\left(x^2+y^2\right)+a^2\left(z^2-a_3^2\right)\right]} \end{aligned}} \tag{5.14}$$

These results will be used next section for the calculation of the fields of an homogeneous ellipsoidal shell and in Sec. 5.5 for the derivation of the envelope equations.

5.3 Electrostatic field of an homogeneous ellipsoidal shell

The density profile of an homogeneous ellipsoidal shell can be defined in general as

$$\rho(r^2) = \begin{cases} \rho_0, \text{ for } m_0^2 \leq r^2 \leq m_1^2, \\ 0, \text{ otherwise.} \end{cases} \tag{5.15}$$

We again have to transform the limit of integrations $r \rightarrow u$. The new limits of integration for a shell become $u = (u_0, u_1)$ where u_0 is the positive root of the equation $r^2(u_0) = m_0^2$ and u_1 the positive root of $r^2(u_1) = m_1^2$. Three regions can then be defined depending of the point of observation.
Region A: in the *interior* of a shell (inside both ellipsoids), the field is zero

$$E_i = 0 \, . \tag{5.16}$$

Region B: *inside* of a shell (between the ellipsoid boundaries)

$$E_i = \frac{\rho_0}{2\epsilon_0} x_i A_i(0, u_0) \, . \tag{5.17}$$

Region C: *exterior* of a shell (outside both ellipsoid)

$$E_i = \frac{\rho_0}{2\epsilon_0} x_i A_i(u_1, u_0) \, . \tag{5.18}$$

For the special case of a round beam $a_1 = a_2 = a$, we have closed forms

$$\boxed{A_i(u_1, u_0) = \int_{u_1}^{u_0} \frac{du}{(a_i^2 + u)\,(a^2 + u)\,\sqrt{a_3^2 + u}}} \tag{5.19}$$

where $u_i = \lambda_i / m_i^2$ and,

$$\boxed{\begin{aligned} 2\lambda_i \;=\; & x^2 + y^2 + z^2 - m_i^2\,(a^2 + a_3^2) + \\ & \sqrt{\left[x^2 + y^2 + z^2 - m_i^2\,(a^2 + a_3^2)\right]^2 + 4m_i^2\left[a_3^2\,(x^2 + y^2) + a^2\,(z^2 - m_i^2 a_3^2)\right]} \end{aligned}} \tag{5.20}$$

The space charge coefficients are

$$A = A_1 = A_2 = g_0(u_0) - g_0(u_1),\ A_3 = h_0(u_0) - h_0(u_1)\ , \tag{5.21}$$

with

$$g_0(u) = \frac{1}{a^2 - a_3^2}\left\{ \frac{\sqrt{a_3^2+u}}{a^2+u} + \frac{\tan^{-1}\left[\sqrt{a_3^2+u}/\sqrt{a^2+u}\right]}{a^2-a_3^2} \right\}\ , \tag{5.22}$$

and

$$h_0(u) = \frac{2}{a^2 - a_3^2}\left\{ \frac{1}{\sqrt{a_3^2+u}} + \frac{\tan^{-1}\left[\sqrt{a_3^2+u}/\sqrt{a^2+u}\right]}{a^2-a_3^2} \right\}\ . \tag{5.23}$$

These equations give a full description of the electrostatic fields acting on an ellipsoidal shell. Next Section generalizes these results to moving shells and presents the outline of a new approach which will be applied to large energy spread beams through binning of the electron distribution in momentum space, providing a computationally fast and very efficient method to calculate space charge effects for beams in the paraxial limit, that is when transverse blowout is moderate ($|\beta_\perp| \ll \beta_z$).

5.4 Derivation of the basic equations for the shell approach

5.4.1 Structure of the code

The 6D beam distribution function is represented numerically as a collection of macroparticles [36]. The phase space coordinates of these macroparticles evolve under the influence of the collective space charge forces. To compute these space charge forces, we divide the range of longitudinal momenta spanned by the beam into a series of bins. Each bin has a normalized longitudinal momentum width $\Delta u_z = \Delta p_z/(mc) \ll 1$. Consequently, in the rest frame of each bin, the macroparticles within that bin are non-relativistic, and the space charge forces in that frame may be computed from the electrostatic field of the macroparticle charge distribution.

The macroparticle charge distribution is modeled as a series of concentric ellipsoidal shells. The parameters of these ellipsoidal shells, such as the RMS radii, the

density and the average position, are obtained by statistical averages over the selected macroparticles. Analytical expressions are used for the electrostatic field for each ellipsoidal shell [70], which allow for writing a fast computational algorithm. The total electrostatic field due to the macroparticles is given by the sum over the ellipsoidal shells.

To calculate the force on a given macroparticle at each time step, we iterate through each momentum bin, and, from the electrostatic fields of the macroparticles in that bin, calculate the space charge force on the given macroparticle in the rest frame of that bin. We then transform this space charge force into the lab frame. The total force on the macroparticle is the vector sum of the Lorentz-transformed space charge forces due to all the momentum bins. This procedure is repeated for each macroparticle, giving all the forces needed to evolve the macroparticle distribution to the next time step.

Note that the binning by momentum, and the calculation of the ellipsoid parameters characterizing the macroparticle charge distribution associated with each bin, is done at every time step.

5.4.2 Adaptive longitudinal momentum grid

In order to be able to approximate the space charge fields as purely electrostatic, the collection of charges generating these fields must be non-relativistic in their common rest frame. Such an approximation requires that the normalized momentum spread in the rest frame be small, that is $\Delta p_{\rm cm}/(mc) = \Delta u_{\rm cm} = \eta \ll 1$.
This condition is achieved in the code by using an adaptive binning technique to break the longitudinal momentum distribution up into bins (the transverse momentum spread is small because of the small angular spread in the beam). This can be done as follow: Performing a Lorentz transformation on the 4-vector normalized momentum $u^\alpha \equiv (\gamma, \gamma\beta)$ gives the relationship between the momentum spread in the laboratory frame Δu_z and the momentum spread in the rest frame $\Delta u_z^{\rm cm}$ [68], i.e.,

$$\Delta u_z^{\rm cm} \simeq \eta = \gamma \left(\Delta u_z - \beta \Delta\gamma\right) \ . \tag{5.24}$$

Paraxial approximation gives $\gamma^2 \simeq 1+u_z^2$ and $\gamma\Delta\gamma \simeq u_z\Delta u_z$ or $\Delta\gamma \simeq \beta\Delta u_z$. Inserting this results into Eq. (5.24) we get

$$\Delta u_z \simeq \eta\gamma \simeq \eta\sqrt{1+u_z^2}\,. \tag{5.25}$$

Using Eq. (5.25), the bin width requirement in terms of laboratory longitudinal (z) momentum, for a laboratory momentum u_{z_k} in bin k, is found to be

$$\Delta u_z = u_{z_{k+1}} - u_{z_k} \simeq \eta\sqrt{1+u_{z_k}^2}\,, \tag{5.26}$$

and in the limiting case $\eta \ll 1$ one has,

$$\frac{du_z(k)}{dk} \simeq \eta\sqrt{1+u_z^2}\,. \tag{5.27}$$

Hence, the longitudinal momentum bins are defined by

$$u_{z_k} = \sinh\left(\eta + k\ \sinh^{-1} u_{z_0}\right)\ . \tag{5.28}$$

The bin index for a given momentum u_z is

$$\boxed{k = \left\lfloor \frac{\sinh^{-1} u_z - \sinh^{-1} u_{z_0}}{\eta} \right\rfloor} \tag{5.29}$$

Note that u_{z_0} is taken as the lowest momentum of the distribution function: it defines the first bin.

5.4.3 Total force calculations

For the macroparticles in momentum bin k, we compute in the laboratory frame the transverse (a_{1k} and a_{2k} along x and y) and longitudinal (a_{3k} along the coordinate z) RMS sizes of the bunch, and the mean longitudinal position of the bunch ($\bar{z}_k$). As noted above, radial symmetry is assumed , so that $a_{1k} = a_{2k} \equiv a_k$, in order to be able to use a simple analytical solution for the fields.

The quantities a_k and a_{3k} define an ellipsoid which models the shape of the macroparticle distribution. This ellipsoid is decomposed into a number of concen-

tric ellipsoidal shells $s_k = 1, 2, \cdots, N_k$. The inner boundary of shell s_k is designated $m_0(s_k)\, a_k$ radially, and $m_0(s_k)a_{3k}$ longitudinally; the outer boundary is $m_1(s_k)a_k$ radially, and $m_1(s_k)a_{3k}$ longitudinally. The numbers $m_0(s_k)$ and $m_1(s_k)$, which range from 0 to μ_m (maximum ellipsoidal coordinate of the distribution function $\mu^2 = (x^2+y^2)/a_k^2 + (z-\bar{z}_k)^2/a_{3k}^2$), are chosen such that the volume of each of the ellipsoidal shells is the same. The density of macroparticles within shell s_k, $\rho_{0_{s_k}}$, is calculated numerically from the macroparticle distribution. Using the Lorentz transformation

$$\begin{cases} \mathbf{E} = \gamma_0 \mathbf{E}' - \gamma_0^2(\gamma_0+1)^{-1}\beta_0\,(\beta_0 \cdot \mathbf{E}')\,, \\ \mathbf{B} = \gamma_0 \beta_0 \times \mathbf{E}', \end{cases} \tag{5.30}$$

one can calculate the electromagnetic field produced by an ellipsoidal shell, acting at the coordinate $\{x, y, z\}$ in the laboratory frame,

$$E_{s_k}^{(x)}(x,y,z) = \frac{\rho_{0_{s_k}}}{2\epsilon_0} a_k^2 \gamma_k a_{3_k} x A_{s_k}(u_{1_k}(x,y,z)\,, u_{0_k}(x,y,z)), \tag{5.31}$$

$$E_{s_k}^{(y)}(x,y,z) = \frac{\rho_{0_{s_k}}}{2\epsilon_0} a_k^2 \gamma_k a_{3_k} y A_{s_k}(u_{1_k}(x,y,z)\,, u_{0_k}(x,y,z)), \tag{5.32}$$

$$E_{s_k}^{(z)}(x,y,z) = \frac{\rho_{0_{s_k}}}{2\epsilon_0} a_k^2 \gamma_k a_{3_k} (z-\bar{z}_k)\, A_{3_{s_k}}(u_{1_k}(x,y,z)\,, u_{0_k}(x,y,z)), \tag{5.33}$$

and

$$B_{s_k}^{(x)}(x,y,z) = -\beta_k E_{s_k}^{(y)}(x,y,z), \tag{5.34}$$

$$B_{s_k}^{(y)}(x,y,z) = \beta_k E_{s_k}^{(x)}(x,y,z), \tag{5.35}$$

$$B_{s_k}^{(z)}(x,y,z) = 0, \tag{5.36}$$

in which A_{s_k} ($A_{3_{s_k}}$) is the transverse (longitudinal) space charge coefficient, and $\gamma_k = (1-\beta_k^2)^{-1/2}$ is the relativistic factor of the k^{th} bin. The space charge coefficients in the rest frame of a shell were derived in Sec. 5.3 and for the case of a moving electron distribution may be generalized, yielding in the laboratory frame [36]

$$A_{s_k}(u_{1_k}, u_{0_k}) = g_{0_k}(u_{0_k}) - g_{0_k}(u_{1_k})\,, \tag{5.37}$$

$$A_{3_{s_k}}(u_{1_k}, u_{0_k}) = h_{0_k}(u_{0_k}) - h_{0_k}(u_{1_k})\,, \tag{5.38}$$

with

$$g_{0_k}(u) = \left(a_k^2 - \gamma_k^2 a_{3_k}^2\right)^{-1} \left\{ \frac{\sqrt{\gamma_k^2 a_{3_k}^2 + u}}{a_k^2 + u} + \frac{\tan^{-1}\left[\sqrt{\gamma_k^2 a_{3_k}^2 + u}/\sqrt{a_k^2 - \gamma_k^2 a_{3_k}^2}\right]}{\sqrt{a_k^2 - \gamma_k^2 a_{3_k}^2}} \right\}, \tag{5.39}$$

and

$$h_{0_k}(u) = \frac{2}{a_k^2 - \gamma_k^2 a_{3_k}^2} \left\{ \left(\gamma_k^2 a_{3_k}^2 + u\right)^{-1/2} + \frac{\tan^{-1}\left[\sqrt{\gamma_k^2 a_{3_k}^2 + u}/\sqrt{a_k^2 - \gamma_k^2 a_{3_k}^2}\right]}{\sqrt{a_k^2 - \gamma_k^2 a_{3_k}^2}} \right\}. \tag{5.40}$$

We also have $u_{0_k}(x, y, z) = \lambda_k\left(x, y, z, m_0^2(s_k)\right)/m_0^2(s_k)$, and
$u_{1_k}(x, y, z) = \lambda_k\left(x, y, z, m_1^2(s_k)\right)/m_1^2(s_k)$, in which

$$\begin{aligned} 2\lambda_k\left(x, y, z, m^2\right) &= x^2 + y^2 + \gamma_k^2\left(z - \bar{z}_k\right)^2 - m^2 a_k^2 - m^2\gamma_k^2 a_{3k}^2 + \\ &\quad \Big[\left(x^2 + y^2 + \gamma_k^2\left(z - \bar{z}_k\right)^2 - m^2 a_k^2 - m^2\gamma_k^2 a_{3k}^2\right)^2 + \\ &\quad 4m^2\gamma_k^2\left(a_{3k}^2\left(x^2 + y^2\right) + a_k^2\left(\left(z - \bar{z}_k\right)^2 - m^2 a_{3k}^2\right)\right)\Big]^{1/2}. \end{aligned} \tag{5.41}$$

If $\left(x^2 + y^2\right)/a_k^2 + \left(z - \bar{z}_k\right)^2/a_{3k}^2 < m^2$, then $\lambda_k\left(x, y, z, m^2\right) = 0$.

Knowing the electromagnetic field from a single shell, one can easily deduce the resulting total force *per unit charge* acting on a given macroparticle by summing over all ellipsoidal shells s_k, and then over all momentum bins k:

$$\begin{aligned} F_x &= \sum_k \left(1 - \beta_z\beta_k\right) \sum_{s_k} E_{s_k}^{(x)}, \\ F_y &= \sum_k \left(1 - \beta_z\beta_k\right) \sum_{s_k} E_{s_k}^{(y)}, \\ F_z &= \sum_k \sum_{s_k} E_{s_k}^{(z)} + \beta_x \sum_k \beta_k \sum_{s_k} E_{s_k}^{(x)} + \beta_y \sum_k \beta_k \sum_{s_k} E_{s_k}^{(y)}, \end{aligned} \tag{5.42}$$

where $\beta = (\beta_x, \beta_y, \beta_z)$ is the macroparticle normalized velocity.

The shell approach has been compared to several other methods such as the direct integration of the coupled envelope equations [35, 68, 71], a modified Poisson solver and a 3-D point to point interaction code [72]. Each of these methods have their own set of approximations which we are going to review next.

5.5 Envelope equations

This Section gives a comprehensive summary of the envelope equations derived for both ellipsoidal symmetric beams and finite cylinders of charge. Limitations of this approach will be further discussed in Sec. 5.8.

5.5.1 Coupled envelope equations in ellipsoidal geometry

In the following we will assume that the electron bunch has an ellipsoidal symmetry with a circular cross section throughout the interaction. The envelope equations can be defined as (see Appendices I and J for further details)

$$\sigma_\perp'' - \frac{3}{2}\frac{Nr_e}{\gamma_0^2\beta_0^2}\lambda_3\sigma_\perp A(\sigma_\perp,\gamma_0\sigma_z) - \frac{\tilde{\epsilon}_x^2}{\sigma_\perp^3} = 0\,, \tag{5.43}$$

$$\sigma_z'' - \frac{3}{2}\frac{Nr_e}{\gamma_0^2\beta_0^2}\lambda_3\sigma_z A_3(\sigma_\perp,\gamma_0\sigma_z) - \frac{\tilde{\epsilon}_z^2}{\sigma_z^3} = 0\,, \tag{5.44}$$

where N is the number of electrons in the bunch, $r_e = e^2/(4\pi\epsilon_0 m_e c^2)$ the classical electron radius, m_e the electron rest mass, $\beta_0 = v_0/c$ and v_0 the average velocity of the bunch, c the vacuum speed of light, $\gamma_0 = (1-\beta_0^2)^{-1/2}$ the relativistic factor, $\sigma_\perp$ the transverse RMS radius and σ_z the longitudinal RMS half length. $\tilde{\epsilon}_x$ and $\tilde{\epsilon}_z$ are the longitudinal and transverse trace-space RMS emittance given by

$$\tilde{\epsilon}_x = \sqrt{\langle X^2\rangle\langle X'^2\rangle - \langle XX'\rangle^2}\,, \tag{5.45}$$

$$\tilde{\epsilon}_z = \sqrt{\langle Z^2\rangle\langle Z'^2\rangle - \langle ZZ'\rangle^2}\,, \tag{5.46}$$

with $X' = p_x/p_0$, $Z' = \delta/\gamma_0^2$, $\delta = (p_z - p_0)/p_0$, p_x and p_z are the transverse and longitudinal electron momentum, $p_0 = m_e\gamma_0\beta_0 c$ the average momentum of the electron bunch and the RMS energy spread is defined as $\tilde{\eta} = \beta_0^2\gamma_0^2\sqrt{\langle Z'^2\rangle}$. The quantities A_i [Sec. 5.2] and λ_3 can be viewed as geometrical factors related to space charge effects [70, 73, 74],

$$A_i(\sigma_\perp,\sigma_z) = \int_0^\infty \frac{du}{(\sigma_i^2+u)\,\Delta(u)}\,, \tag{5.47}$$

$$\Delta(u) = \left(\sigma_\perp^2+u\right)\left(\sigma_z^2+u\right)^{1/2}\,, \tag{5.48}$$

and

$$A = A_1 = A_2 \; . \tag{5.49}$$

However it was shown by Lapostolle *et al.* [75] and Sacherer *et al.* [73] that for ellipsoidal bunches, where the RMS emittance is either constant or specified in advance, evolution of the RMS beam projections are nearly independent of the density profile. This means that for calculation of the RMS dynamics, the actual distribution can be replaced by an equivalent uniform beam, which has the same RMS values. In this case $\lambda_3 = 1/(5\sqrt{5})$. In the shell approach, we have made use of homogeneous ellipsoidal beams to model dynamics of more general electron distributions under space charge blowout. As a matter of consistency, it is also more convenient for the envelope description to use the radius of the uniform ellipsoid (a, a_3) instead of RMS quantities, where $a_i = \sqrt{5}\ \sigma_i$. The envelope equations for a bunched beam can also be rewritten to underline the transverse-longitudinal coupling through the space charge forces [68]. Further making use of the relation [70] $2A + A_3 = 2/(a^2\gamma_0 a_3)$ and writing A_3 is terms of the aspect ratio $x = a/(\gamma_0 a_3)$,

$$A_3(a, \gamma_0 a_3) = \left(\gamma_0^3 a_3^3\right)^{-1} g_0\left[a/(\gamma_0 a_3)\right] \; , \tag{5.50}$$

$$g_0(x) = \int_0^\infty \left(x^2 + u\right)^{-1} (1+u)^{-3/2}\, du \; , \tag{5.51}$$

we get for the envelope equations,

$$\boxed{a'' - \frac{3}{2}\frac{Nr_e}{\gamma_0^3\beta_0^2}\frac{1}{aa_3}\left[1 - \frac{a^2}{2\gamma_0^2 a_3^2} g_0\left(\frac{a}{\gamma_0 a_3}\right)\right] - \frac{\epsilon_x^2}{a^3} = 0} \tag{5.52}$$

$$\boxed{a_3'' - \frac{3}{2}\frac{Nr_e}{\gamma_0^5\beta_0^2}\frac{1}{a_3^2} g_0\left(\frac{a}{\gamma_0 a_3}\right) - \frac{\epsilon_z^2}{a_3^3} = 0} \tag{5.53}$$

with $\epsilon_x^2 = 5\ \tilde{\epsilon}_x^2$ and $\epsilon_z^2 = 5\ \tilde{\epsilon}_z^2$, the transverse and longitudinal full emittances, respectively.

Sec. 5.8 will compare the envelope model to the other numerical methods introduced in this Chapter and will further define a range of application for the use of the envelope equations in general.

In the next Section, we discuss envelope models but for the specific case of beams

with cylindrical shape. This specific geometry was first introduced by A. Chao *et al.* [71] to describe evolution of beams produced by plasma sources under space charge interaction. The latter approach is more restrictive than using ellipsoids [35] because an approximate analytical derivation of the force may be obtained only for beams with small aspect ratios $a/(\gamma_0 a_3) \ll 1$. Vacuum propagation of space charge dominated beams often leads to aspect ratios which increase and may greatly exceed unity. The requirement of small aspect ratio however may not introduce much error if the space charge interaction is orders of magnitude smaller when $a/(\gamma_0 a_3) \sim 1$. Note also that this method can not be used to describe non-relativistic beams with pancake shape. The derivation of the force is tedious and is shown in Appendix K for the specific configuration discussed by A. Chao *et al.* [71], that is a cylindrical beam with a uniform transverse and quadratic longitudinal density profile. Other configurations are also discussed such as hollow beams, linear longitudinal density profile, etc.

5.5.2 Coupled envelope equations in cylindrical geometry

The use of envelope equations is limited to the assumptions of small energy spread (up to ~ 50 %) and divergence (few tens of mrads) [35, 71]. As mentioned above, the paper by Chao *et al.* [71] studied the limited case of beams with small aspect ratios $a/(\gamma_0 a_3) \ll 1$, assuming a bunch with cylindrical symmetry, a uniform radial and quadratic longitudinal *line-charge* density profile,

$$\lambda(z) = \frac{3N}{4a_3^3}\left(a_3^2 - z^2\right), \text{ for } |z| \leq a_3 \, . \tag{5.54}$$

They define the envelope equations as,

$$a'' - \frac{3}{2}\frac{Nr_e}{\gamma_0^3\beta_0^2}\frac{1}{aa_3} - \frac{\epsilon_x^2}{a^3} = 0 \, , \tag{5.55}$$

$$a_3'' - \frac{3}{2}\frac{Nr_e}{\gamma_0^5\beta_0^2}\frac{1}{a_3^2}g_1\left(\frac{a}{\gamma_0 a_3}\right) - \frac{\epsilon_z^2}{a_3^3} = 0 \, , \tag{5.56}$$

where the transverse envelope equation is simply the KV equation [68]. The longitudinal space charge coefficient $g_1(x)$ assumes a long beam $x = a/(\gamma_0 a_3) \ll 1$ and is

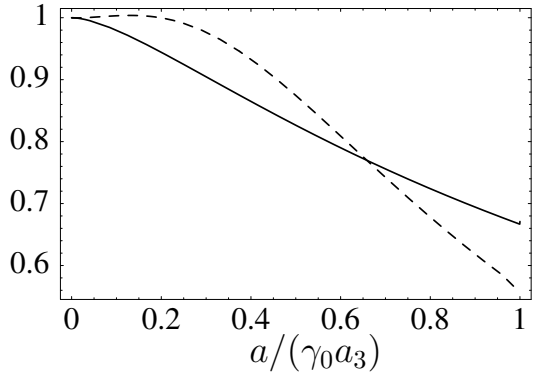

Figure 5.1: Ratio of longitudinal forces $g_0(x)/g_1(x)$ (dashed line) and transverse forces (solid line) are shown as a function of the aspect ratio $a/(\gamma_0 a_3)$.

given by,

$$g_1(x) = 2\left[\ln\left(\frac{\sqrt{5\ x^2+1}}{\sqrt{5}\ x}\right) + \frac{1}{2}\right] \ . \tag{5.57}$$

Figure 5.1 shows the ratio $g_0(x)/g_1(x)$ as a function of the aspect ratio $x = a/(\gamma_0 a_3)$. This two models, beside the fact that the geometry is different (ellipsoids versus cylinders) exhibit similar behaviors. Basically there is a qualitatively good agreement for a range $0 < x < 0.1$ and within 20 % up to $x < 0.5$.

However, further comparing both derivations of the space charge force, in the case of a cylindrical charge distribution, showed a few conceptual differences (which are summarized in Appendix K). The expression we found for the fields in the interior of a cylinder, in the "long beam limit" approximation ($x \ll 1$) and for $|z| < a_3$, using a quadratic density profile [Eq. (5.54)], is

$$E_z(r,\theta,z) = -\frac{\lambda'(z)}{2\pi\epsilon_0\gamma^2}\left[\ln\left(\frac{2\gamma\sqrt{a_3^2-z^2}}{a}\right) - \frac{1}{2}\left(1+\frac{r^2}{a^2}\right)\right] \ , \tag{5.58}$$

i.e.,

$$\boxed{E_z(r,\theta,z) = \frac{3eNz}{4\pi\epsilon_0 a_3^3\gamma^2}\left[\ln\left(\frac{2\gamma\sqrt{a_3^2-z^2}}{a}\right) - \frac{1}{2}\left(1+\frac{r^2}{a^2}\right)\right]} \tag{5.59}$$

and,

$$E_r(r,z) = \frac{\lambda(z)r}{2\pi\epsilon_0 a^2} \ , \tag{5.60}$$

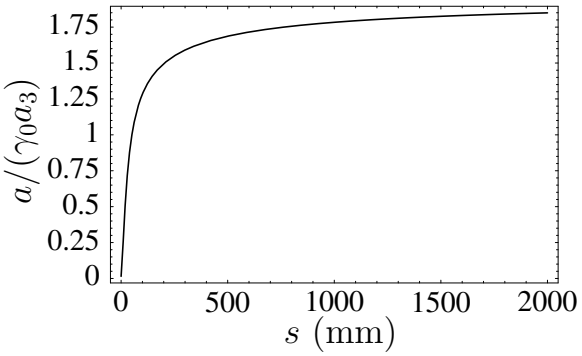

Figure 5.2: Aspect ratio $x = a/(\gamma_0 a_3)$ versus propagation distance s (mm) for an initial transverse radius $a = 19$ μm, longitudinal half-length $a_3 = 77$ μm, divergence $x' = 2.5$ mrad, energy spread $\eta = 42.8$ % and beam relativistic factor $\gamma_0 = 13.7$.

that is,

$$\boxed{E_r(r,z) = \frac{3eNr}{8\pi\epsilon_0 a^2 a_3}\left(1 - \frac{z^2}{a_3^2}\right)} \tag{5.61}$$

leading to a set of coupled envelope equations,

$$\boxed{a'' - \frac{6}{5}\frac{Nr_e}{\gamma_0^3\beta_0^2}\frac{1}{aa_3} - \frac{\epsilon_x^2}{a^3} = 0} \tag{5.62}$$

and,

$$\boxed{a_3'' - \frac{3}{2}\frac{Nr_e}{\gamma_0^5\beta_0^2}\frac{1}{a_3^2}g_2\left(\frac{a}{\gamma_0 a_3}\right) - \frac{\epsilon_z^2}{a_3^3} = 0} \tag{5.63}$$

where

$$g_2(x) = -2\ln\left(\frac{x}{\alpha_3}\right) \ , \tag{5.64}$$

and,

$$\alpha_3 \simeq 0.6723 \ . \tag{5.65}$$

As mentioned in the previous Section, the weaknesses of using cylinders comes from the limiting assumptions that are required for an analytical expression for the fields. Assuming $x \ll 1$ allows only for an accurate description of space charge blow-out over short distances (typically on the order of $25 - 50$ mm from the source for the specific case studied in [71]), as can be seen in Fig. 5.2 for example. A direct comparison of the

two models (constant density ellipsoids and parabolic cylinders) is impossible. While Eq (5.52) converges to the KV equation in the limit $\gamma a_3 \ggg a$, Eq (5.62) does not (a cylinder with constant longitudinal density profile would lead to the KV equation).

5.6 A modified Electrostatic Particle-In-Cell code

In this Section we describe an electrostatic Particle-in-cell (PIC) code that may be used to model large energy spread beams. The latter characterize an extension of the shell model [Sec. 5.4] and does not make any assumptions on the spacial symmetries of the electron beam. The PIC result is obtained from a 3-D Poisson solver [76], that calculates the electrostatic field of an arbitrary charge distribution in its rest frame. The resulting field is then Lorentz transformed to the laboratory frame. The large energy spread beam is handled through binning in momentum following Eq. (5.29). This method is based on the assumption of a rest frame for the beam which neglects transverse currents effects (paraxial approximation) and, hence the longitudinal magnetic field B_z. The total force *per unit charge*, as in Eq. (5.42), can be written in the form

$$F_x = \sum_k (1 - \beta_z \beta_k)\, E_k^{(x)}, \tag{5.66}$$

$$F_y = \sum_k (1 - \beta_z \beta_k)\, E_k^{(y)}, \tag{5.67}$$

$$F_z = \sum_k E_k^{(z)} + \beta_x \sum_k \beta_k E_k^{(x)} + \beta_y \sum_k \beta_k E_k^{(y)}, \tag{5.68}$$

where $\mathbf{E}_k = (E_k^{(x)}, E_k^{(y)}, E_k^{(z)})$ is the electrostatic field in the laboratory frame of the k^{th} bin. This PIC method will be compared to other approaches in Sec. 5.8.

5.7 A 3-D point to point interaction approach

This Section derives the basic set of equations for a 3-D point-to-point interaction model (PPI). This method is very general and allows for the calculation of space

charge dominated electron beam dynamics without the requirement of paraxial approximation, as in the previous models [Sec 5.4 to 5.6]. In the PPI approach, the 6D beam distribution function is also represented numerically as a collection of macroparticles. The electromagnetic fields generated by this method are calculated directly from relativistic particle-particle interaction, outlined in Ref. [72]. Radiation effects are not included and retardation effects are approximated. The fields evaluation is based on a Lorentz transformation and assumes, at each time step, a constant velocity for the electrons. This assumption implies that the velocity spread between two macroparticles must remain small (moderate space charge interaction) during the time interval $\Delta t = t - t_{\mathrm{RET}}$ where t is the *now-time* (i.e, associated with the force evaluation) and t_{RET} the *retarded time*, i.e., the time when the macroparticle j emitted the electromagnetic field seen at t by macroparticle i. The retarded time is defined as follow,

$$\boxed{t_{RET} = t - |\mathbf{r} - \mathbf{r}_j(t_{RET})|/c} \tag{5.69}$$

To calculate the fields generated by particle j at the position of particle i, first both particle coordinates are transformed to the rest frame of particle j,

$$\mathbf{r}'_{ij} = \mathbf{r}_{ij} + \frac{\gamma_j^2}{\gamma_j + 1} \left(\mathbf{r}_{ij} \cdot \beta_j\right) \beta_j \ , \tag{5.70}$$

where $\mathbf{r}_{ij} = \mathbf{r}_i - \mathbf{r}_j$ is the distance measured in the laboratory frame and $\mathbf{r}'_{ij}$ is the distance in the rest frame. Within the rest frame of particle j only an electric field is present. This coulomb field is given by

$$\mathbf{E}'_{j\to i} = \frac{Q_m}{4\pi\epsilon_0} \frac{\mathbf{r}'_{ij}}{|\mathbf{r}'_{ij}|^3} \ , \tag{5.71}$$

where $Q_m = -Ne$ is the charge of the macroparticle. Transforming this electric field back to the laboratory frame and summing over all particles yields the electromagnetic fields at the position of particle i,

$$\mathbf{E}_i = \sum_{j\neq i} \gamma_j \left\{ \mathbf{E}'_{j\to i} - \frac{\gamma_j}{\gamma_j + 1} \left(\mathbf{E}'_{j\to i} \cdot \beta_j\right) \beta_j \right\} \ , \tag{5.72}$$

$$\mathbf{B}_i = \sum_{j\neq i} \gamma_j \beta_j \times \mathbf{E}'_{j\to i} \ . \tag{5.73}$$

Each macroparticle represent a large number N of elementary electrons. In order to reduce the large angle scattering effect, which overestimates the real collision term cross section in PPI models, the macroparticles should be considered as particle clouds of radius r_0. Under this assumption, within the cloud, the Coulomb repulsion force decreases to zero when two clouds completely overlap, that is

$$\mathbf{E}'_{j\to i} = \frac{Q_m}{4\pi\epsilon_0}\frac{\mathbf{r}'_{ij}}{r_0^3}\ ,\ \text{if}\ |\mathbf{r}'_{ij}| < r_0. \tag{5.74}$$

Note that the introduction of r_0 is the primary approximation, and we expect the PPI to yield the most accurate results for large energy spread beams compared to the two other methods (shells or PIC).

5.7.1 Benchmarking

The benchmarking of the PPI algorithm has been done by simulating the blow-up of an initially cold homogeneous spherical electron distribution. This configuration enables exact calculation of the total energy of the system. The *energy conservation* law for a system of N_m macroparticles interacting with an electromagnetic field is given by [77],

$$\frac{\partial}{\partial t}\left[\sum_i^{N_m}(\gamma_i - 1)m_e c^2 + \int_V d^3x\left(\frac{\epsilon_0\mathbf{E}^2}{2} + \frac{\mathbf{B}^2}{2\mu_0}\right)\right] = -\oint_S dS\ \mathbf{n}\cdot\mathbf{S}\ , \tag{5.75}$$

where $\mathbf{S}$ is the Poynting vector, V is a volume containing the entire charged particle system, S the corresponding surface enclosing the volume V and $\mathbf{n}$ a unit vector normal (outward) to the surface S. The electron distribution is taken initially cold, which implies that the total energy at $t = 0$ is purely electrostatic (assuming radiation fields are negligible), that is

$$H_i = \frac{N_m U_0}{N_e}\ , \tag{5.76}$$

together with

$$U_0 = \int_V d^3x\ \frac{\epsilon_0\mathbf{E}^2}{2} = \frac{3Q^2}{20\pi R\epsilon_0}\ , \tag{5.77}$$

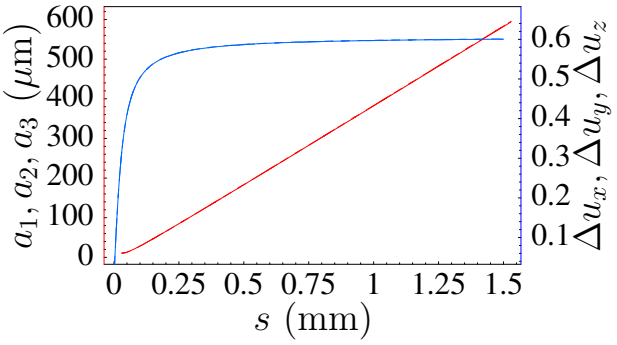

Figure 5.3: (Color) Simulation of the space charge blowout of an initially cold spherical electron distribution with parameters: Charge $Q = 1$ nC, beam energy $E_0 = 0$, radius $a_1 = a_2 = a_3 = 24$ μm, energy spread $\eta = 0$, divergence $x'_{\max} = 0$, average distance between macroparticles $n_0^{-1/3} \simeq 1.74$ μm and cut-off radius $r_0 = 100$ nm. Beam radius and RMS momentum spread along the three coordinate axis is shown as a function of propagation distance s.

where integration is over all space and N_e is the total number of real electrons. In deriving Eq. (5.77), the expression of the electrostatic field of a spherical homogeneous charge distribution $\mathbf{E} = \rho r/(3\epsilon_0)$ has been used along with the charge density $\rho = 3Q/(4\pi R^3)$. With the initial condition of a sphere of charge Q and radius R, the PPI simulation is run until the space charge interaction is negligible and the electron motion is purely ballistic. At the final time step, the expression for the total energy becomes,

$$\boxed{H_f = \sum_i^{N_m} (\gamma_i - 1) m_e c^2} \tag{5.78}$$

Energy conservation obviously requires $\Delta H = |H_f - H_i| = 0$. Figure 5.3 shows the time evolution of the equivalent *uniform-density* bunch length a_1, a_2, a_3 (the equivalent uniform-density quantities are obtained from the RMS values by multiplication by $\sqrt{5}$), and the RMS normalized momentum Δu_x, Δu_y and Δu_z for the initial beam parameters: charge $Q = 1$ nC, radius $R = a_1 = a_2 = a_3 = 24$ μm, average energy $E_0 = 0$, energy spread $\eta = 0$, divergence $x'_{\max} = 0$. An identical time evolution of the beam RMS dynamics along the three axes (Ox, Oy, Oz) is found as expected. The corresponding relative error in the energy conservation is shown in Fig. 5.4(a), for various sizes r_0, where $\Gamma = (H_f - H_i)/(H_f + H_i)$. An estimate of the typical distance

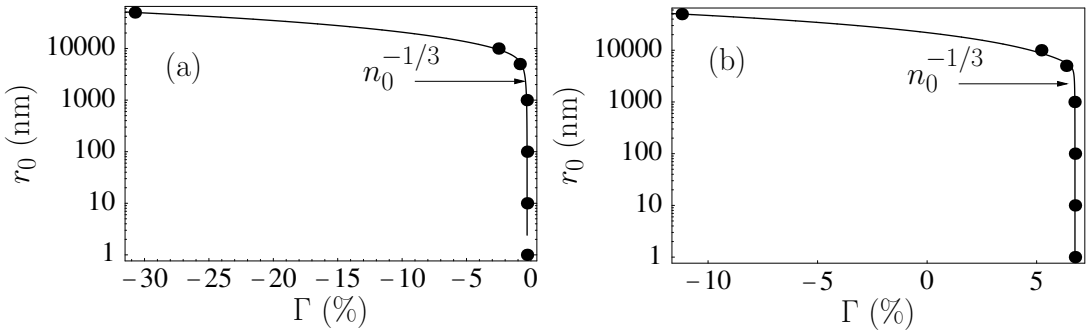

Figure 5.4: Energy conservation relative error Γ versus cut-off parameter r_0 for (a) an initially cold spherical electron distribution with parameters: Charge $Q = 1$ nC, beam energy $E_0 = 0$, radius $a_1 = a_2 = a_3 = 24$ μm, energy spread $\eta = 0$, divergence $x'_{\max} = 0$, typical distance between macroparticles $n_0^{-1/3} \simeq 1.74$ μm and (b) a moving ellipsoidal charge distribution with identical parameters except for $E_0 = 1.12$ MeV and $a_3 = 10.92$ μm, corresponding to a cold spherical electron distribution in its rest frame, i.e., $a'_1 = a'_2 = a'_3 = 24$ μm ($a'_3 = \gamma_0 a_3$). The latter allows for a direct comparison with analytical estimates.

between macroparticles in the system $d = n_0^{-1/3}$ has been introduced through the initial macroparticle density n_0, that is

$$n_0 = \frac{3N_m}{4\pi a^2 a_3}, \tag{5.79}$$

were $N_m = |Q_m/e|$ is the number of macroparticles. As can be seen in Fig. 5.4(a), choosing $r_0 > n_0^{-1/3}$ introduces an excessive smoothing of the electromagnetic fields leading to a deviation from energy conservation. Figure 5.4(b) plots the energy conservation relative error for the case of a moving ellipsoidal charge distribution with identical initial parameters as Fig. 5.4(a) except for $E_0 = 1.12$ MeV and $a_3 = 10.92$ μm, corresponding to a cold spherical electron distribution in its rest frame, i.e., $a'_1 = a'_2 = a'_3 = 24$ μm ($a'_3 = \gamma_0 a_3$). The initial total energy of the system can be calculated analytically, i.e., according to relativistic principles, *any* quantity of rest energy W^0 will be attributed the value $\gamma_0 W^0$ by an observer who sees it being transported with a velocity $v_0 = c(1 - \gamma_0^{-2})^{-1/2}$ [78]. The above calculations for a spherical charge distribution in the beam rest frame may thus be generalized to any arbitrary *inertial*

frame, giving an expression for the total energy (kinetic plus potential),

$$\boxed{H_i = N_m \left(\gamma_0 - 1\right) m_e c^2 + \left(\frac{N_m}{N_e}\right) \gamma_0 U_0} \tag{5.80}$$

In Appendix G, a derivation of a covariant expression for the electromagnetic energy and momentum is given together with a short review of the historical background leading to this result. Figure 5.4(a) and (b) show a similar behavior, that is, for $r_0 < n_0^{-1/3}$ the PPI method reaches convergence. The relative error is found to be less than -5×10^{-2} % for the case of Fig 5.4(a), providing an accurate calculation of beam dynamics, and within 6.75 % for Fig 5.4(b). Those two particular examples are collision-less*, indicating that there is no additional requirement on r_0 beside the condition $r_0 < n_0^{-1/3}$. The difference in the relative error shown in Fig 5.4 may be explained using geometrical arguments and is *mainly* caused by the approximative way retardation effects are handled in the PPI method. Figure 5.5 shows a simplified configuration of two macroparticles, which is sufficient to describe the problem because the PPI method calculates the interaction force between two macroparticles at a time (N-body). Obviously this is not the case for the other methods introduced in this dissertation (the shell approach, for instance, smooths the macroparticle distribution). The PPI method uses the position of the macroparticle and the point of observation at the present time to calculate the fields. As explained earlier, a Lorentz transformation to the frame co-moving with the macroparticle is performed and the distance $r'(t' = 0)$ [Fig. 5.5(b)] is used to evaluate the electrostatic field in the rest frame (the macroparticle is static). At this point, it is necessary to insist on the fact that this approach does not neglect retardation but instead performs an approximative evaluation. Lets assume for a moment that the macroparticle has a constant velocity in the lab. frame. Then, in the rest frame, its location remains at the origin at all times t' (note that it is easier to handle the problem if we choose to locate the macroparticle at the origin). In this particular case, the position $r'(t' = 0)$ remains valid even at the retarded time $t' = t'_{\mathrm{RET}}$, which is the actual time the observer sees the electromagnetic field emitted

*For systems where collisions may play an important role, the relative error in the energy conservation is expected to remain unchanged for $r_0 < n_0^{-1/3}$ because the collisions are purely elastic. To get a correct estimate for the minimum value of r_0, conservation of phase space structure may be considered as an alternate means. For this systems, $r_0 \sim n_0^{-1/3}$ is considered best.

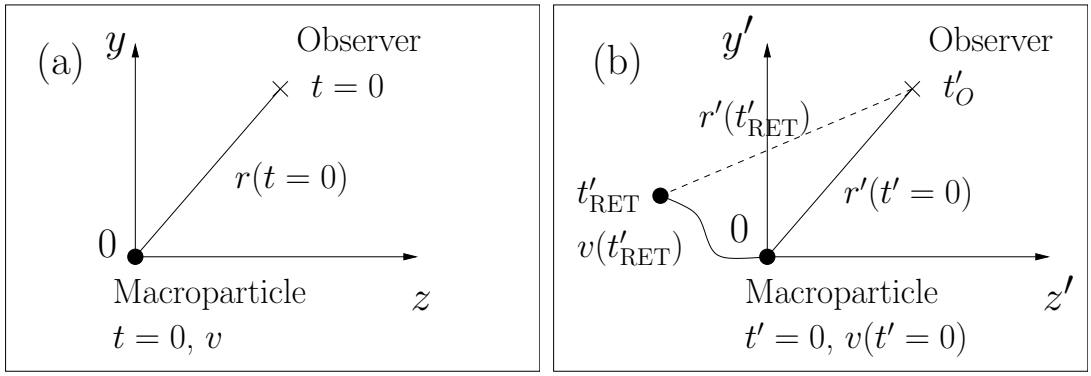

Figure 5.5: (*a*) Two macroparticles in the lab. frame are shown. Their respective positions are shown at the present time; consistent with the assumptions in the PPI method. (*b*) Corresponding two macroparticles in the frame comoving with the macroparticle located at the origin (we discuss the electromagnetic fields emitted by the latter and seen by the observer, assumed to be located at the position of the second macroparticle). $r'(t'=0)$ is the actual distance used to calculate the force in the PPI method; the latter would be exact if the macroparticle had a constant velocity during the time interval it takes the light to travel from the macroparticle to the point of observation. For the case of a velocity spread the macroparticle was located at another position than the origin at $t' = t'_{\mathrm{RET}}$, where t'_{RET} is the retarded time. This is the error introduced in the PPI method, explained using geometrical arguments. Note that retardation effects are not neglected in the PPI method but simply approximated as explained above.

by the macroparticle. In other words, in this case the electromagnetic field calculated in the lab. frame is exact and includes retardation [79]. Radiation is absent because the velocity is constant. We may generalize the discussion by saying that if during the time interval $\Delta t' = t'_0 - t'_{\mathrm{RET}} = |r'(t'_{\mathrm{RET}})|/c$ (in the rest frame), the velocity spread $\Delta v'/v(t'_{\mathrm{RET}}) = [v(t'_{\mathrm{RET}}) - v(t'=0)]/v(t'_{\mathrm{RET}}) \ll 1$ then the retardation effects are correctly calculated, i.e., $\Delta r'/r'(t'_{\mathrm{RET}}) = |r'(t'_{\mathrm{RET}}) - r'(t'=0)|/r'(t'_{\mathrm{RET}}) \ll 1$.

Using the latter argument, the difference in the relative error found in Fig 5.4 between the spherical charge distributions at rest or moving with $\gamma_0 m_e c^2 \simeq 1.12$ MeV may be explained as follows. Comparing two identical events in the beam frame (for example the space charge interaction between two macroparticles at the same time t' in both cases), the distance $\Delta r'$ will artificially change for the moving bunch introducing a greater error $\Delta r'/r'(t'_{\mathrm{RET}})$. For ultra-relativistic beams ($\gamma_0 \gg 1$) however,

$\Delta r'$ will reach an asymptotic value, leading to a constant error in the evaluation of the fields. Note that ignoring radiation is a good approximation, as will be shown in Sec. 5.10.

5.8 Simulation results

In this Section, the different analytical and numerical methods introduced in this Chapter will be compared with each other and a range of application will be defined for each of them. Those methods will be further used for the simulation of vacuum transport of electron beams produced by plasma sources.

5.8.1 Compact electron sources

Small energy spread

The validity of the envelope approach requires small divergence (up to a few tens of mrads), low peak current and low energy spread ($\eta \lesssim 50$ %). In Fig. 5.6, we plot the equivalent *uniform-density* bunch radius and bunch length as a function of propagation distance using respectively the shell approach, the coupled envelope equations Eq. (5.52) and (5.53) and the 3D-PPI code. The bunch charge is $Q = 100$ pC, the initial radius $a = 6$ μm, length $a_3 = 2.5$ μm, divergence $x' = 2$ mrad, energy spread $\eta = 5$ %, average beam energy $E_0 = 5.25$ MeV, aspect ratio $x = a/(\gamma_0 a_3) \simeq 0.23$ and cut-off radius $r_0 = 100$ nm. Good agreement is found between the three models, within an 4.8 % margin. For such beams the coupled envelope equations can be applied accurately [35]. This typical example is also found to be an upper limit for the usability of either the shell or the envelope models and corresponds to a maximum current given by,

$$\bar{I} = \bar{I}_{\max} = \frac{3Q}{4a_3}\beta_0 c \simeq 9 \text{ kA}. \tag{5.81}$$

It is possible to define a general quantity for the beam in order to better characterize the space charge blowout and also the range of applicability of either the shell method or the envelope equations. It can be expressed as the ratio of the beam current

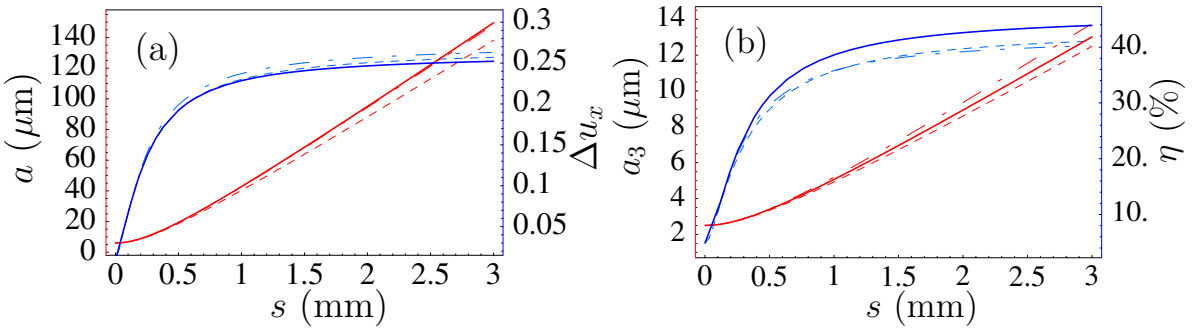

Figure 5.6: (Color) Simulation of the space charge blowout of a small energy spread compact electron bunch with input parameters: Charge $Q = 100$ pC, beam energy $E_0 = 5.25$ MeV, radius $a = 6$ μm, half-length $a_3 = 2.5$ μm, energy spread $\eta = 4.8$ %, divergence $x'_{max} = 2$ mrad, typical distance between macroparticles $n_0^{-1/3} \simeq 266$ nm and cut-off radius $r_0 = 100$ nm. Evolution of (a) transverse radius $a = \sqrt{5}\ \sigma_x$ and transverse momentum spread Δu_x, (b) longitudinal half-length $a_3 = \sqrt{5}\ \sigma_z$ and energy spread $\eta = \sqrt{5}\ \Delta u_z / \langle u_z \rangle$ as a function of propagation distance $s = ct$ is shown using the envelope model (solid), 3D-PPI (dashed) and shell method (dot-dashed).

normalized with respect to the Alfvèn current, that is

$$\boxed{\alpha_b = \frac{\bar{I}}{\gamma_0 I_A} \frac{1.8 \times 10^2}{a^2_{[\mu\mathrm{m}]}}} \tag{5.82}$$

where $I_A = 17 \times 10^3\ \gamma_0 \beta_0$. α_b is an *approximate coefficient* characterizing the initial averaged magnitude of the space charge force assuming a "long" beam under the paraxial approximation, i.e., when transverse current is negligible. For $\bar{I} = \bar{I}_{\max}$, $\alpha_b \simeq 1$ and in general $\alpha_b \leq 1$ is necessary for using the envelope and shell description.

Large energy spread

For beams with large energy spread ($\eta > 50$ %), Eq. (5.52) and (5.53) do not apply anymore but the shell model is found to be a very accurate method. Fig. 5.7 plots the *uniform-density* bunch radius a, bunch length a_3, energy spread η and the RMS transverse normalized momentum Δu_x as a function of propagation distance s and for the three models, i.e., envelope, shell and PPI. The electron bunch energy is $E_0 = 6$ MeV, the initial bunch radius $a = 6$ μm, bunch length $a_3 = 2.5$ μm,

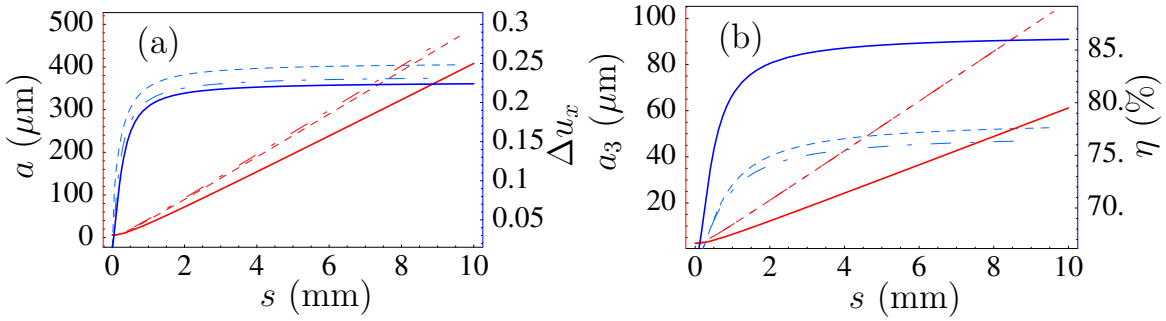

Figure 5.7: (Color) Simulation of the space charge blowout of a large energy spread compact electron bunch with input parameters: charge $Q = 100$ pC, beam energy $E_0 = 6$ MeV, transverse radius $a = 6$ μm, half-length $a_3 = 2.5$ μm, energy spread $\eta = 65$ %, divergence $x'_{max} = 2$ mrad, typical distance between macroparticles $n_0^{-1/3} \simeq 266$ nm and cut-off radius $r_0 = 100$ nm. Evolution of (a) transverse radius a and transverse RMS momentum spread Δu_x, (b) longitudinal half-length a_3 and energy spread η as a function of propagation distance s is shown using the envelope model (solid), 3D-PPI (dashed) and shell method (dot-dashed).

divergence $x' = 2$ mrad, energy spread $\eta = 65$ % and total charge $Q = 100$ pC.

Fig. 5.8 shows the same quantities, i.e., $a(s)$, $a_3(s)$, $\Delta u_x(s)$ and $\eta(s)$ but for a long bunch. The electron energy is $E_0 = 8.5$ MeV, the initial bunch radius $a = 19$ μm, bunch length $a_3 = 76.8$ μm, divergence $x' = 3$ mrad, energy spread $\eta = 74.5$ % and total charge $Q = 1.6$ nC. In this case the energy spread $\eta(s)$ exhibits a typical behavior which is a direct contribution of the terms $\beta_x B_y - \beta_y B_x$ in the longitudinal force. These terms are naturally neglected in the envelope equation, under the paraxial approximation, but included in the shell and PPI. From Figs. 5.7 and 5.8, it is found that the shell and PPI codes provide a similar description of the RMS bunch dynamics within an 4 % margin whereas the difference with respect to the coupled envelope equations is more than 27 % relative error.

5.8.2 Application to plasma sources

Colliding pulse injection

Test particle simulations of the colliding pulse LWFA injector [19–21], in which two counterpropagating laser pulses are used to inject electrons from the background plasma directly into the wake, indicate the production of a trapped bunch $N \sim 10^8$

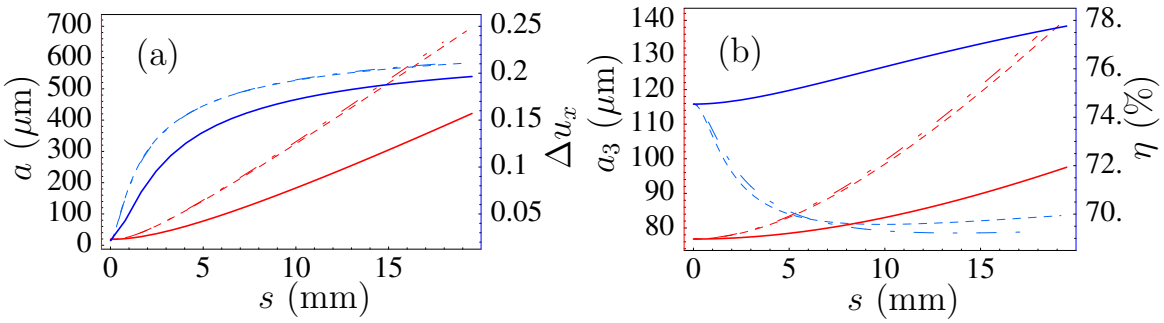

Figure 5.8: (Color) Simulation of the space charge blowout of a large energy spread long electron bunch with input parameters: Charge $Q = 1.6$ nC, beam energy $E_0 = 8.5$ MeV, radius $a = 19$ μm, half-length $a_3 = 76.8$ μm, energy spread $\eta = 74.5$ %, divergence $x'_{max} = 3$ mrad, typical distance between macroparticles $n_0^{-1/3} \simeq 1.8$ μm and cut-off radius $r_0 = 1$ μm. Evolution of (a) transverse radius a and transverse RMS momentum spread Δu_x, (b) longitudinal half-length a_3 and energy spread η as a function of propagation distance s is shown using the envelope model (solid), 3D-PPI (dashed) and shell method (dot-dashed).

electrons with a low energy spread $\eta < 1 - 5$ %, low normalized emittance $\epsilon_x \sim 1$ mm-mrad, a transverse size on the order of the laser spot size $\sigma_\perp \sim 6$ μm and of ultrashort duration, i.e. $\sigma_z \sim 1 - 5$ μm. Such test particle simulations, however, neglected the space charge effects of the accelerated bunch.

Space charge effects can limit the amount of charge that can be transported in an ultrashort, tightly focused electron bunch, i.e., space charge can lead to a increase in both the longitudinal and transverse bunch dimensions. In a LWFA, space charge effects may not be of concern while the bunch is in the plasma wave, since the longitudinal and transverse fields of the wake are typically much greater than the space charge forces of the bunch. This is not the case, however, as the bunch exits the plasma into a vacuum region with no applied fields. In this case, space charge can lead to a rapid blow-up of the bunch.

Fig. 5.9 plots the bunch divergence x' and energy spread η, by solving Eq. (5.52) and (5.53), as a function of charge Q (at $s = 10$ cm) assuming an electron bunch energy $E_0 = 15$ MeV (solid line) and $E_0 = 45$ MeV (dashed line), an initial bunch radius $a = 6$ μm, bunch length $a_3 = 2.5$ μm, divergence $x' = 2$ mrad, energy spread $\eta = 4$ % and a total amount of charge from 0 to 150 pC. The beam was initially assumed to be at focus, i.e., $a'(0) = a'_3(0) = 0$.

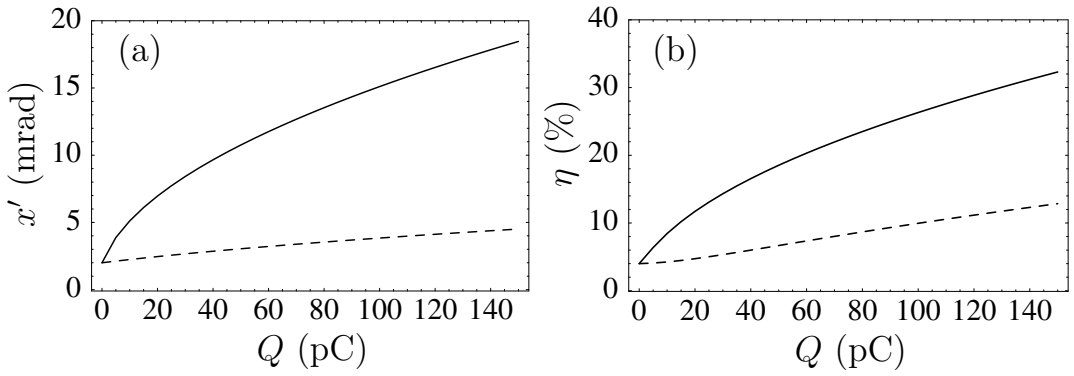

Figure 5.9: Vacuum propagation of a compact electron beam produced by plasma based accelerators using the colliding pulse injection scheme. Input parameters: Beam energy $E_0 = 15$ MeV (solid line) and $E_0 = 45$ MeV (dashed line), radius $a = 6$ μm, half-length $a_3 = 2.5$ μm, energy spread $\eta = 4$ % and divergence $x'_{max} = 2$ mrad. Estimates for (a) the beam divergence and (b) energy spread, as a function of charge, is shown for a beam located in vacuum at $s = 10$ cm from the plasma exit.

Fig. 5.10 plots the ratios a_{sc}/a and a_{3sc}/a_3 at $s = 10$ cm where a_i is the bunch radius obtained by solving Eq. (5.52) and (5.53) for the same parameters as Fig. 5.9 and $a_{sc}(s)$ is the bunch radius assuming the beam is space charge dominated, i.e., in this case the terms ϵ_x^2/a^3 and ϵ_z^2/a_3^3 are removed from Eq. (5.52) and (5.53). Note that Fig. 5.10 allows for a clear separation of the two regimes: (i) emittance dominated $a_{sc}/a_i \ll 1$ and (ii) space charge dominated $a_{sc}/a_i \simeq 1$.

These figures clearly show that a fairly high energy electron bunch with a total amount of charge of several pC produced by colliding pulse injection can rapidly blow-up via space charge due to its very compact size. For this typical bunch, below 5 pC the beam is emittance dominated, i.e., in this case one can neglect the effect of space charge. Above this value space charge must be considered and clearly participates in the beam growth. However, for electron beams in the energy range ~ 40 MeV, space charge effects will be greatly reduced. A plasma based accelerator using the CPI scheme should operate in that regime.

SM-LWFA injector

The development of high intensity short laser pulses has made it possible to study high energy electron production on a tabletop. MeV electrons have been observed

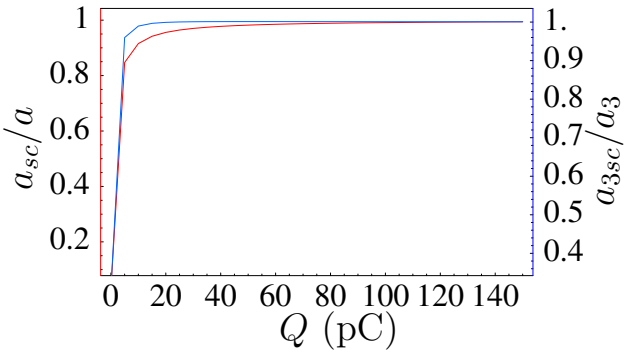

Figure 5.10: Ratio of the radius a_{sc}/a and half-length a_{3sc}/a_3 as a function of charge is shown for a typical beam produced by colliding pulse injection. This calculation has been performed using the envelope model where $a_{sc}(s)$ assumes the beam is space charge dominated. Regimes where $a_{sc}/a \ll 1$ are emittance dominated and $a_{sc}/a \simeq 1$ are space charge dominated, respectively. Input parameters: Bunch energy $E_0 = 15$ MeV, radius $a = 6$ μm, half-length $a_3 = 1.5$ μm, energy spread $\eta = 4$ %, divergence $x'_{max} = 2$ mrad and the beam is taken to be located in vacuum, $s = 10$ cm from the plasma exit.

worldwide in many experiments over the past years [8, 16, 23–31]. The common set-up for these experiments was a single intense incoming laser pulse focused on a supersonic gas jet without a preformed plasma channel. The typical diameter of the gas jets ranged on the order $0.5 - 2$ mm. It was found that the number of electrons versus energy produced in those single-beam experiments fits either a single or a double exponential decay law $dN/dE \propto \exp(-E/T_e)$, where T_e is the electron temperature which was experimentally found to be typically on the order 4 MeV. In Fig. 5.11, we plot the equivalent uniform-density bunch radius, bunch length, divergence, and relative momentum spread, as a function of propagation distance, for the SM-LWFA case. The equivalent uniform-density quantities are obtained from the RMS values by multiplication by $\sqrt{5}$. The initial phase-space density was assumed uniform in all 6 dimensions, with a bunch charge of $Q = 5$ nC. The initial bunch longitudinal momentum ranges from $p_{z0} : 0.1 \rightarrow 23$ MeV/c, corresponding to an exponential distribution with $kT = 4$ MeV [Fig. 5.12]. The initial bunch radius was $a = 6$ μm, initial length $a_3 = 10$ μm, and initial divergence $x'_0 = 2$ mrad. From Fig. 5.11(a) we see a good agreement for the transverse dynamics between the three models: shells (dot-dashed line), PPI (solid line) and PIC (dashed line). However,

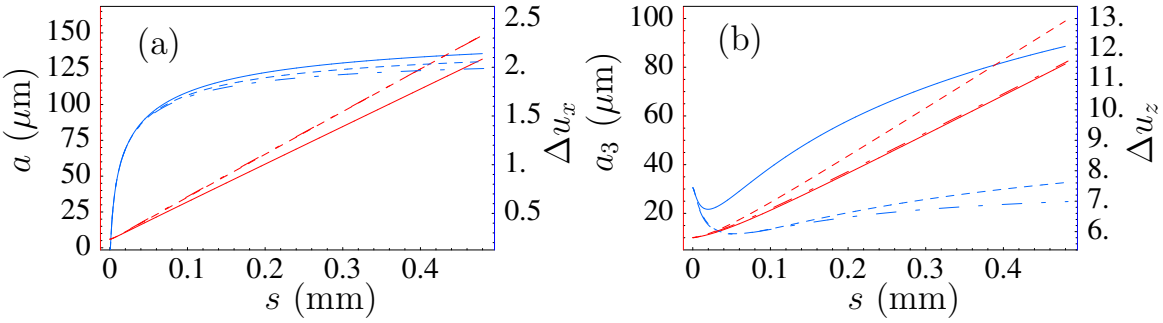

Figure 5.11: (Color) Simulation of the space charge blowout of typical beams produced by plasma accelerators in the self-modulated regime. Input parameters: Charge $Q = 5$ nC, beam temperature $k_BT = 4$ MeV, radius $a = 6$ μm, half-length $a_3 = 10$ μm, divergence $x'_{max} = 2$ mrad, typical distance between macroparticles $n_0^{-1/3} = 422$ nm and cut-off radius $r_0 = 100$ nm. Evolution of (a) transverse radius a and transverse RMS momentum spread Δu_x, (b) longitudinal half-length a_3 and longitudinal RMS momentum spread Δu_z as a function of propagation distance s is shown using the 3D-PPI model (solid), electrostatic PIC (dashed) and shell method (dot-dashed).

the beam distributions exhibit differences and this may be an issue for beams with large energy spread, i.e., RMS quantities may not provide enough information and higher order moments may need to be included.

It is also found, from Fig. 5.11(a), that transverse space charge effects vanish at a very early stage (~ 200 μm) whereas the longitudinal dynamics are more persistent as can be seen in Fig. 5.11(b). This plot shows, on the contrary, disagreement between the three models. This indicates that paraxial approximation is not valid and that more general space charge models such as PPI or fully 3-D electromagnetic PIC codes are needed. Figure 5.11(b) shows clear evidence that neither the shell [Sec. 5.4] nor the electrostatic PIC model [Sec. 5.6] apply anymore. Recall that the main difference between electrostatic PIC and shells comes from the smoothing of the density within an ellipsoidal shell. This explains the incapability of the shell model to describe beam dynamics when the local beam phase space correlations play an important role.

For this particular example of an initial beam distribution with a Boltzmann profile in energy, the low energy high density region will experience both transverse blow-out and longitudinal acceleration. The latter results in a substantial increase of the energy spread over long distances, i.e., at $s = 1.5$ mm [not shown in Fig. 5.11]. The energy spread is a factor of two higher than its initial value. The longitudinal

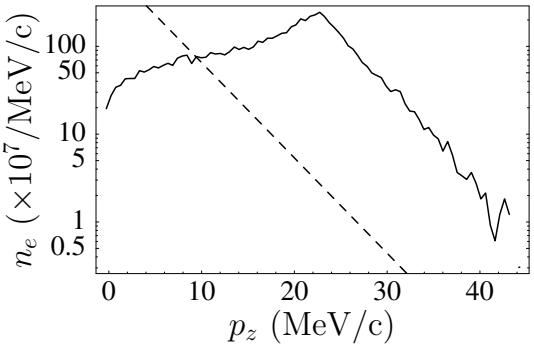

Figure 5.12: Electron bunch energy density for the same initial parameters as Fig. (5.11), that is, total beam charge $Q = 5$ nC, temperature $k_B T = 4$ MeV, radius $a = 6$ μm, half-length $a_3 = 10$ μm, divergence $x'_{max} = 2$ mrad, average distance between macroparticles $n_0^{-1/3} = 422$ nm and cut-off radius $r_0 = 100$ nm. (a) shows the input electron distribution and (b) after a vacuum propagation of $s = 1.5$ mm.

dynamics reaches the ballistic state after a propagation distance of $s \sim 1.5$ mm. Note that the dynamics of the low energy region lead to a general change of the final beam profile, as shown in Fig. 5.12, i.e., the distribution peaks around $u_z \simeq 45$.

In order to investigate the validity of the paraxial approximation, the PPI algorithm is modified so as to include the latter assumption, i.e., the transverse normalized velocities in the field solver are neglected $\beta_{xj} = \beta_{yj} = 0$ and $\beta_j = \beta_{zj}\mathbf{e}_z$ were $\mathbf{e}_z$ is a unit vector. Eqs. (5.72)-(5.73) become

$$\mathbf{E}_{\perp i} = \sum_{j \neq i} \gamma_j \mathbf{E}'_{\perp, j \to i} \, , \tag{5.83}$$

$$\mathbf{E}_{zi} = \sum_{j \neq i} \mathbf{E}'_{z, j \to i} \, , \tag{5.84}$$

$$\mathbf{B}_i = \sum_{j \neq i} \gamma_j \beta_{zj} \, \mathbf{e}_z \times \mathbf{E}_i \, , \tag{5.85}$$

where $\mathbf{E}'_{j \to i}$ is given by Eq. (5.74), and $\gamma_j = (1 + u_{zj}^2)^{1/2}$ is the relativistic factor. Figure 5.13 compares Eqs. (5.83)-(5.85) to the electrostatic PIC method [Sec. 5.6], which is a paraxial code. There is agreement both in the transverse and longitudinal dynamics of the electron bunch. The differences between Fig. 5.13 and Fig. 5.11 for the PPI results show the deviation from the paraxial approximation.

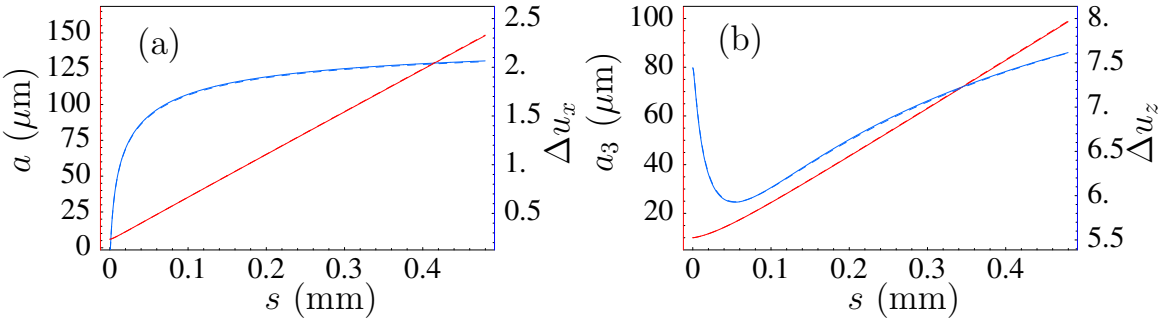

Figure 5.13: Comparison between the reduced 3D-PPI model in the paraxial approximation (solid line) and the electrostatic PIC (dashed line) for the case of a large energy spread beam with an exponential energy profile. Input parameters: Charge $Q = 5$ nC, temperature $k_BT = 4$ MeV, radius $a = 6$ μm, half-length $a_3 = 10$ μm, divergence $x'_{max} = 2$ mrad, typical distance between macroparticles $n_0^{-1/3} = 422$ nm and cut-off radius $r_0 = 100$ nm. Evolution of (a) transverse radius a and transverse RMS momentum spread Δu_x, (b) longitudinal half-length a_3 and longitudinal RMS momentum spread Δu_z as a function of propagation distance s is shown.

Space charge estimate for SM-LWFA injectors using realistic macroparticle distributions

In this Section we will adress the need to use macroparticle distributions containing realistic phase-space correlations as found in SM-LWFA beams, and discuss space charge effets using distributions produced by fully electromagnetic PIC codes.

Experiments using both uniform plasma and channel guided plasmas have observed sub-structures in the beam distribution function. Formation of electron bunches with small energy spread followed by a bulk of low energy electrons was observed [32–34] when the plasma length, after injection of background plasma electrons into the plasma wave through the wave breaking process, was on the order of the dephasing length. This length corresponds to the typical distance for a trapped electron to overcome the accelerated region of the wakefield. Typically those electron beams have a high charge on the order of a few nCs and compact dimensions scaling like the laser pulse size while the small energy spread sub-bunch has a charge $\sim$ 500 pC and a length on the order of a plasma wavelength $\lambda_p = 2\pi c/\omega_p$, where $\omega_p = (4\pi n_0 e^2/m_e)^{1/2}$ is the plasma frequency and n_0 is the plasma density. These beams hence have a very high average density $\bar{n}_b \sim 10^{19}$ cm^{-3} and for electrons with MeV range total

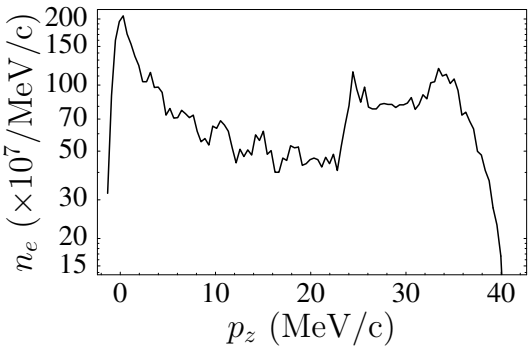

Figure 5.14: Final energy distribution for a beam with an initialy exponential energy decay law and a longitudinal $z-p_z$ linear correlation. Initial parameters: total charge $Q = 5$ nC, temperature $T_e = 4$ MeV, radius $a = 6$ μm, half length $a_3 = 10$ μm and divergence $x'_0 = 2$ mrad

energy, space charge force may play an important role in the beam dynamics while propagating in vacuum.

It has been previously shown [Sec. 5.8.1] that the dynamics of beams with small energy spread and divergence are well described by an envelope equation. Furthermore for moderate space charge interaction and beams in the space charge dominated regime, i.e., where the emittance term in the envelope equation is typically small compared to the space charge term, ellipsoidal symmetric beams with identical initial RMS parameters will exhibit similar growth during propagation. For these beams the effect of initial position space-energy correlation are negligible, whereas for beams with large energy spread, it will strongly affect the changes in time of the distribution function. The full knowledge of the six-dimensional (6D) initial phase space distribution function is then required for accurate description of the beam dynamics. Figure 5.12 shows the beam energy distribution after a propagation distance of 1.5 mm from an initial constant density electron distribution in real and momentum space. Figure 5.14 shows a distribution which initially has a linear correlation in the $z - p_z$ space after a propagation distance of 9 mm. The linear correlation means that electrons at the front of the bunch have the highest energies and proportionally electrons at the back are the slowest. The input beam parameters were assumed to be a total charge $Q = 5$ nC, a temperature $T_e = 4$ MeV, a radius $a = 6$ μm, a halflength $a_3 = 10$ μm and a divergence $x'_0 = 2$ mrad. The space charge simulations were per-

formed using PPI model [Sec. 5.7]. Analysis of the final beam distributions for the two cases of Fig. 5.12 and Fig. 5.14 comfirm the hypothesis that the knowledge of the initial phase space correlations within the beams are crucial for an accurate description of its time evolution. The beam of Fig. 5.12 exhibits a peak at $p_z \simeq 25$ MeV/c, whereas the example of Fig. 5.14 shows formation of two peaks. This obviously does not agree with experimental measurements. Note that both cases experience some structural change and among everything a substantial gain of energy. This strongly suggest that similar beams parameters may be sensitive to space charge effects.

In order to get a correct understanding of experimental results, realistic beam distributions may be obtained from self-consistent simulations such as particle-in-cells (PIC) codes [54, 55]. The mechanism responsible for electron production is the self-modulated laser-wakefield-accelerator (SM-LWFA) regime [9] in which the laser pulse length L is on the order or greater than the plasma wavelength. PIC simulations using the code VORPAL [56] showed the production of a small energy spread electron bunch in front of a bulk of a high density electron beam for both an initially uniform plasma and with a preformed plasma channel [33]. The electron bunch lies in the first bucket of the plasma wave and typically has a higher average energy than the rest of the beam, allowing for extraction using a magnetic spectrometer. For moderate laser strength, this can be explained by the combined effect of beam loading and laser pulse evolution which together turn-off injection and allows for the formation of a bunch with small energy spread while further behind the laser pulse, transverse wavebreaking may increase the amount of charge injected, resulting in a substantially higher energy spread in this sub-region of the beam ($\sim 100\%$) and a higher degree of phase mixing [11, 33]. Figure 5.15(a) shows the axial electron beam phase-space $z - p_z$ for a two-dimensional (2D) slab simulation of a short intense laser pulse propagating through a plasma channel with the laser-plasma parameters: normalized vector potential $a = eA/m_e c^2 = 2.15$ where m_e is the electron rest mass and e the elementary electron charge respectively, carrier frequency $\lambda_0 = 0.8$ μm, laser duration $\tau = L/c = 58$ fs, spot size at waist $r_0 = 7.3$ μm, background plasma density $n_0 = 1.8 \times 10^{19}$ cm^{-3}, 10 particles-per-cell, a grid size $\Delta z = 90/2700 = 0.03$ μm axially, $\Delta x = 80/300 = 0.26$ μm transversally and a parabolic channel of radius $r_c = 40$ μm. The frame shown corresponds to a laser propagation distance of ~ 1360 μm. If the distance exceeds the dephasing length, which in the 1D limit can be defined as $L_d \simeq (\lambda_p/\lambda_0)^2 \lambda_p$, the

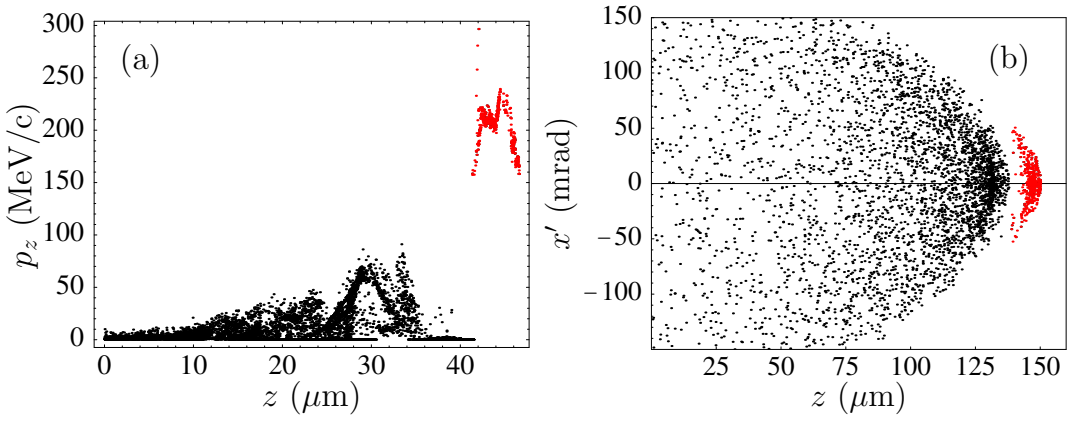

Figure 5.15: (Color) $z - p_z$ phase-space projection of a 3-D electron distribution (a) after a laser propagation distance of ~ 1.36 mm inside a preformed plasma channel and (b) z versus beam divergence x' after a propagation of 4.8 mm in vacuum. The laser-plasma parameters were a laser strength $a = 2.15$, carrier frequency $\lambda_0 = 0.8$ μm, duration $\tau = L/c = 58$ fs, spot size at waist $r_0 = 7.3$ μm, nominal plasma density $n_0 = 1.8 \times 10^{19}$ cm^{-3} and channel radius $r_c = 40$ μm.

beam will strongly evolve to a point where phase mixing smooths the entire bunch. It is crucial to terminate the plasma at a distance on the order of the dephasing length after electron injection into the wakefield to observe experimentally the production of an electron bunch with a small energy spread. Vacuum transport of the beam shown in Fig. 5.15 has been performed using the 3D-PPI method. The PIC simulation is currently a 2D slab, and in order to get a 3D electron distribution, the output of the code has been assumed circular symmetric. The line charge density λ_m associated with a 2D slab macroparticle is defined as,

$$\lambda_m = n_0/(\Delta x \Delta z N_p) \ , \tag{5.86}$$

where N_p is the number of macroparticles per cell. The density is assumed identical between 2D and 3D geometry giving a number of 3D macroparticles $N_{m,i}$ at a radius r_i away from the longitudinal axis,

$$N_{m,i} = 2\pi \lfloor r_i \lambda_m \rfloor \ , \tag{5.87}$$

where $r_i = |y_i|$, y_i is the transverse coordinate of a 2D slab macroparticle and only

half of the slab is considered, i.e., only macroparticles lying in the $y > 0$ plane. The 3D electron distribution is populated following,

$$x_i^* = r_i \cos\theta_i \ , y_i^* = r_i \sin\theta_i \ , z_i^* = z_i \ , \tag{5.88}$$

where $\{x_i^*, y_i^*, z_i^*\}$ stand for the Cartesian coordinate of a 3D macroparticle, θ_i is a random number between 0 and 2π and z_i is the transverse coordinate of a 2D slab macroparticle. The same transformation has been repeated for the momentum domain $\mathbf{p}_i$. The total charge Q in the 3D beam is calculated following

$$Q = -2\pi e \sum_i^{N_{2D}^>} r_i \lambda_m \ , \tag{5.89}$$

where $N_{2D}^>$ is the number of 2D slab macroparticles in the $y > 0$ plane. For the case of Fig. 5.15, $N_p = 10$, $\Delta x = 0.26$ μm and $\Delta z = 0.03$ μm giving $e\lambda_m \simeq 2.5$ nC/m. The total charge may vary depending on the selected energy cut-off from the PIC simulation. Taking electrons above ~ 500 keV within a radius $R = 6$ μm gives a total charge $Q \sim 1.4$ nC whereas energies greater than ~ 100 keV give $Q \sim 3.2$ nC. The small energy spread beam [red color] contains a charge $Q \sim 25$ pC. Note that fully 3D PIC simulations shows an enhancement of the amount of charge trapped for a similar resolution in the simulation parameters [80]. Charge in the trapped beam is then found to be closer to experimental observations [33]. In the following, the 3D electron distribution derived from the 2D slab PIC simulation is used as a model for a typical beam produced by laser-plasma interaction. The charge is varied in the space charge simulation to study its effect on the beam dynamics. Figure 5.16(a) shows the initial beam distribution (blue dashed line), final beam distribution (blue solid line) after a propagation distance of 4.8 mm for a total beam charge of $Q = 2.8$ and $Q = 8.5$ nC (red dashed and solid line) respectively. The latter case clearly exhibits important changes in beam temperature [Fig. 5.16(c)], which strongly suggest that space charge effects must be included. Figures 5.16(b) and (d) show a similar behavior. Note that the overall "two-temperature" profile is unchanged which is in good agreement with experimental observations. The latter example assumed a preformed homogeneous plasma and a higher density $n_0 = 4 \times 10^{19}$ cm^{-3} which will provide a greater ratio

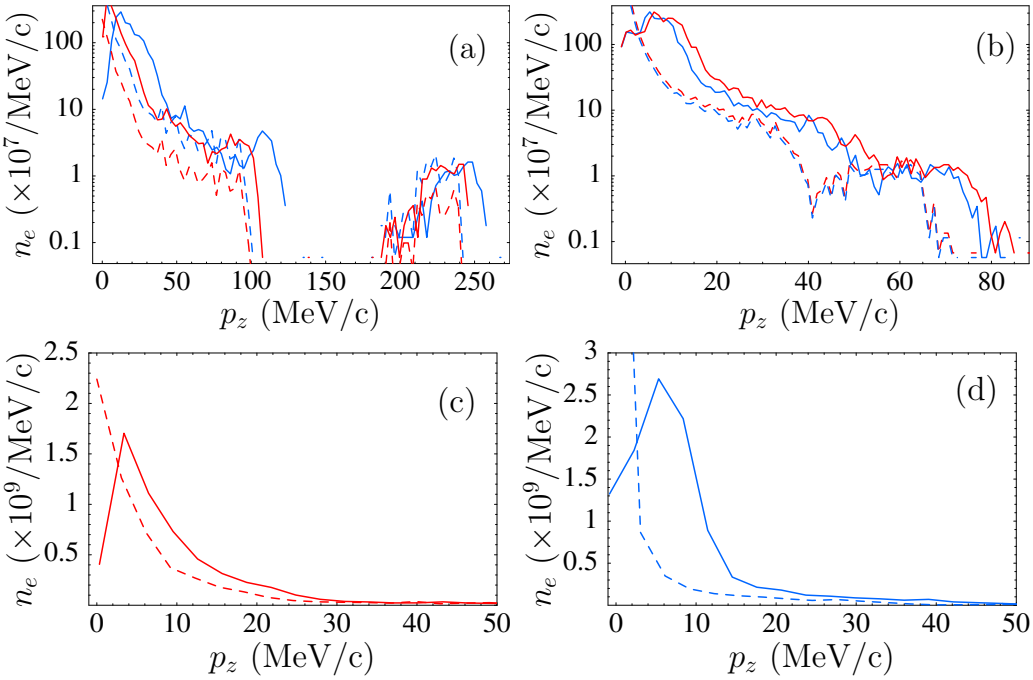

Figure 5.16: (Color) (a) Logarithmic plot of the initial beam energy distribution (dashed-line) and final (solid line) assuming a total beam charge of $Q = 2.8$ nC (blue) and $Q = 8.5$ nC (red) for the parameters of Fig. 5.15. (b) same except for a higher density plasma without a preformed channel, assuming a total beam charge of $Q = 5.1$ nC (blue) and $Q = 6$ nC (red). A zoom of the low energy region, highlighting the changes in beam temperature induced by space charge interaction, is shown in (c) for the channeled case [i.e., same as (a)] and in (d) for the single laser pulse experiment [corresponding to the log. plot (b)]. The laser-plasma parameters for the latter example were $a = 2.2$, $\lambda_0 = 0.8$ μm, $\tau = L/c = 55$ fs, $r_0 = 7.4$ μm, $n_0 = 4 \times 10^{19}$ cm^{-3}.

of charge trapped for a lower energy gain, consequently increasing the effect of space charge. The resolution used in the PIC simulation is $\Delta x = 0.26$ μm, $\Delta z = 0.05$ μm and $N_p = 10$ providing $e\lambda_m = 8.3$ nC/m. Selecting electrons above 500 keV gives $Q \sim 3.8$ nC and $Q \sim 5.1$ nC for $E > 100$ keV. The example of Fig. 5.16(b) is chosen for a charge $Q = 5.2$ nC.

A detailed study of the RMS quantities of the small energy spread electron bunch of Fig. 5.15 [red color] shows significant energy gain during vacuum propagation while beam quality is maintained, i.e., space charge interaction with the remaining

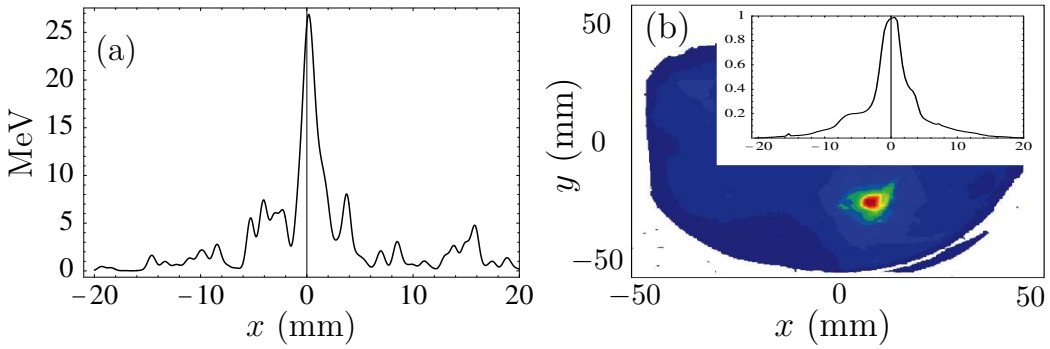

Figure 5.17: (Color) Radiated energy on a phosphor screen 70 cm away from the gas jet, (a) lineout using the electron beam produced by the fully explicit PIC simulation of a channel guided laser pulse [Fig. 5.15] and (b) radiation from a 10×10 cm phosphor screen imaged on a CCD camera which is taken from experimental measurements with similar laser-plasma parameters. Red color highlight the largest energy deposition from the electron beam onto the phosphor and blue the smallest, respectively.

low energy residual charge of the whole beam induce an energy boosting. The total charge in the beam is assumed 3.2 nC. At the plasma exit [Fig. 5.15(a)], the beam has an energy spread $\eta = 9.2\%$, an average energy $T \simeq 204.5$ MeV, a divergence $\sigma_{x'} \simeq 16.3$ mrad and a bunch length $\sigma_z \simeq 1.42$ μm. After $ct = 4.8$ mm, the energy spread and divergence is found to be a few percent lower, the bunch length is $\sigma_z \simeq 2.4$ μm and the average energy is $T \simeq 209.4$ MeV leading to an energy gain of 2.4 % (a total beam charge of 10 nC would induce ~ 10 % energy gain) and consequently a 2.2 % decrease in trace-space emittance $\epsilon_x = \sqrt{\langle x^2\rangle\langle x'^2\rangle - \langle xx'\rangle^2}$. Note that besides the high average energy of the bunch, space charge still has a significant effect. This can be explained in part by the very short dimensions of the whole beam at vaccum-plasma boundary, on the order of the laser size, giving an average beam number density $\bar{n}_b \simeq 3 \times 10^{18}$ cm^{-3}. In addition, Fig. 5.15(b) shows the total beam divergence after 4.8 mm of vacuum propagation, the red beam remains ultra compact. The latter has been confirmed experimentally by measurements of radiated light emitted by the electron beam passing through a phosphor screen. Figure 5.17 compares the simulated radiated energy from the electron beam produced by the PIC simulation in the channel guided case [Fig. 5.15] with respect to experimental data from similar laser-plasma parameters. Both cases exhibit a bright emission spot with a full width half maximum (FWHM) on the order of 3 mm.

Similar effects are observed for the unchanneled case $n_0 = 4{\times}10^{19}$ cm^{-3} [Fig. 5.18(a)] but with a significantly higher energy gain as expected. The high energy electron bunch [red color] contains a charge $Q \simeq 55$ pC (assuming a total charge of 5.2 nC). After a 4.8 mm vacuum propagation distance energy spread reduces from $\eta \simeq 12.6$ % to 11 %, average energy increase from $T \simeq 55.7$ MeV to 65 MeV (energy gain of 16.7 %) leading to a 12.5 % decrease in trace-space emittance together with a divergence lowered by ~ 9.7 %. Besides a more intense space charge interaction than in the channeled case, the electron bunch propagates well in vacuum as shown in Fig. 5.18(b).

Note that in both cases some beam compaction and focusing is observed. The latter can be understood as a pinching effect from the θ-component of the magnetic field generated by the high longitudinal current of the beam as a whole.

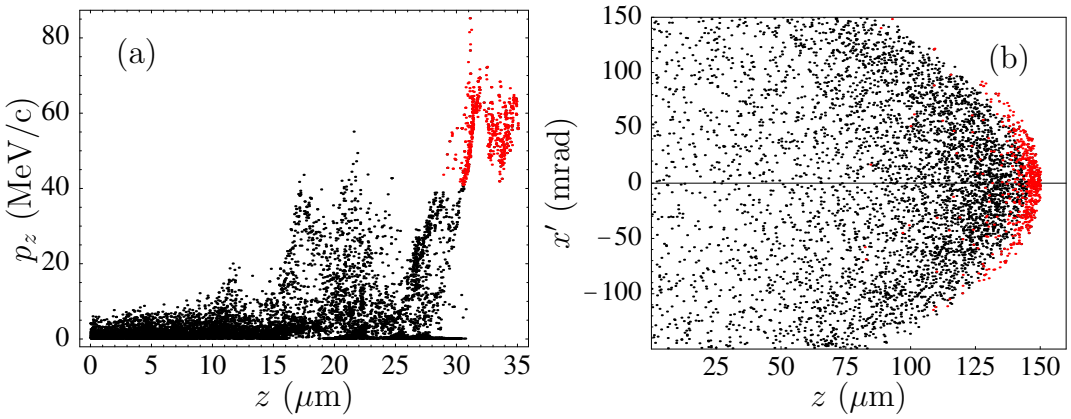

Figure 5.18: (Color) $z - p_z$ phase-space projection of a 3-D electron distribution (a) after a laser propagation distance of ~ 530 μm inside an homogeneous pre-ionised plasma and (b) z versus beam divergence x' after a propagation of 5.3 mm in vacuum. The laser-plasma parameters were a laser strength $a = 2.2$, carrier frequency $\lambda_0 = 0.8$ μm, pulse duration $\tau = L/c = 55$ fs, spot size at waist $r_0 = 7.4$ μm and nominal density $n_0 = 4 \times 10^{19}$ cm^{-3}.

5.9 Comparison between PPI and PIC for the simulation of space charge dominated beams

In this Section, we modify the PPI algorithm in order to perform a direct comparison with respect to a Poisson solver in terms of total CPU time and accuracy of the methods. In Sec. 5.8.2 we pointed out that beams produced by plasma based accelerators in the so-called self-modulated regime will experience drastic changes under space charge interaction. This results in a overall increase of beam sizes up to millimeter scale. A Poisson solver calculates the electric field by a finite-difference scheme from a smoothed density on a grid. This approach requires enough statistics through high numbers of particles per cell (typically greater than 5) and a grid size small enough to resolve internal sub-structures within the beam (typically $\Delta x_i \sim 0.1 - 1\ \mu$m). The Poisson solver used in our simulations has an adaptive grid size, i.e., the grid number is fixed but the grid size is adjusted as the beam evolves. This adaptive technique reduce computing time for the same accuracy goals compared to conventional PIC methods which have a fixed decomposition domain. On the other hand, the main advantage of using the PPI technique is that it does not rely on a grid (although PPI requires the numerical parameter $r_0 \sim n_0^{-1/3}$).

In the following a parameter scan was performed showing parameters needed to solve the beam configuration of Fig. 5.11 using both a Poisson solver and PPI. For this scan, PPI was modified such that a single beam rest frame was assumed. The fields solver in the PPI code is reduced to

$$\mathbf{E}_{\perp i} = \bar{\gamma} \sum_{j \neq i} \mathbf{E}'_{\perp, j \to i} \ , \tag{5.90}$$

$$\mathbf{E}_{z i} = \sum_{j \neq i} \mathbf{E}'_{z, j \to i} \ , \tag{5.91}$$

and,

$$\mathbf{B}_i = \bar{\beta}_z \mathbf{e}_z \times \mathbf{E}_i \ , \tag{5.92}$$

where $\mathbf{E}'_{j \to i}$ is given by Eq. (5.74), $\bar{\beta}_z = \bar{u}_z / (1 + \bar{u}_z^2)^{1/2}$ is the average electron normalized velocity, $\bar{\gamma} = (1 + \bar{u}_z^2)^{1/2}$ the average relativistic factor, $\bar{u}_z$ the average normalized momentum and $\mathbf{e}_z$ a unit vector. Note that no binning was used for the electrostatic

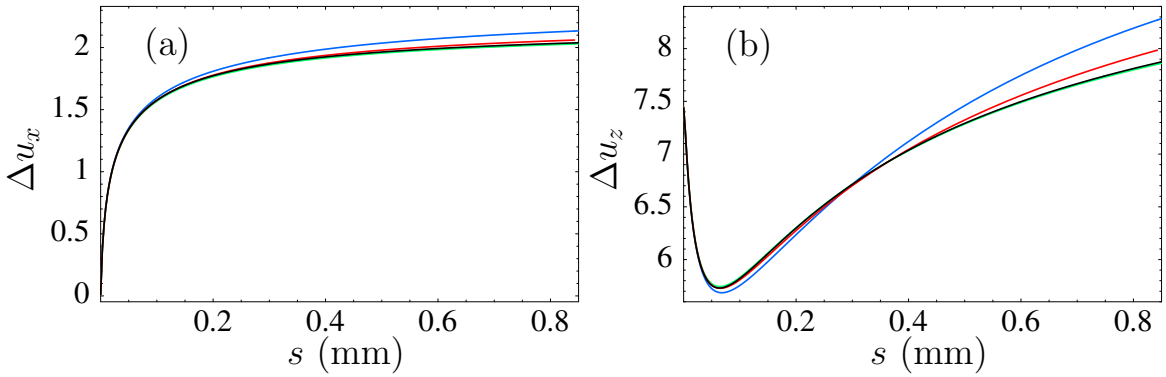

Figure 5.19: Comparison between the reduced 3D-PPI model and the electrostatic PIC for the case of a large energy spread beam with an exponential energy profile. Input parameters: Charge $Q = 5$ nC, temperature $k_BT = 4$ MeV, radius $a = 6$ μm, half-length $a_3 = 10$ μm and divergence $x'_{max} = 2$ mrad. In (black) PPI with $N = 20032$ macroparticles, cut-off radius $r_0 = 100$ nm and averaged macroparticle distance $n_0^{-1/3} = 422$ nm, (green) electrostatic PIC with $N = 10.24 \times 10^6$ macroparticles and grids $128^2 \times 512$, (red) electrostatic PIC with $N = 20.48 \times 10^6$ macroparticles and grids 256^3 and (blue) electrostatic PIC with $N = 2.56 \times 10^6$ macroparticles and grids 128^3. Evolution of (a) transverse RMS momentum spread Δu_x and (b) longitudinal RMS momentum spread Δu_z as a function of propagation distance s is shown.

PIC simulation.

Figure 5.19 shows the comparison between the electrostatic PIC and PPI for the parameters of Fig. 5.11, i.e., for a bunch charge of $Q = 5$ nC, an exponential profile for the longitudinal momentum with a temperature $kT = 4$ MeV, an initial bunch radius of $a = 6$ μm, initial length $a_3 = 10$ μm, and an initial divergence $x'_0 = 2$ mrad. Figures 5.19(a) and (b) plot the transverse and longitudinal RMS momentum spread $\Delta u_{x,(z)}$, respectively, as a function of propagation distance. Figures 5.19 shows the PPI model (black line) with $N = 20032$ macroparticles, $r_0 = 100$ nm, and $n_0^{-1/3} = 422$ nm, the electrostatic PIC with (i) $N = 10.24 \times 10^6$ macroparticles and grids $128^2 \times 512$ (green line), (ii) $N = 20.48 \times 10^6$ macroparticles and grids 256^3 (red line) and (iii) $N = 2.56 \times 10^6$ macroparticles and grids 128^3 (blue line). One can see that 128 adaptive grid points transversally are enough for the Poisson solver to reach convergence whereas a longitudinal grid number greater that 256 is necessary. The example shown in green shows perfect agreement with PPI. For this particular example, it is found that $\tau = 10$ ms/processor/particle is the average PPI's execution

time per time step and $\tau = 2$ ms/processor/particle for the Poisson solver. The small number of particles needed for the PPI run made the simulation significantly faster.

5.10 Discussion

5.10.1 Generalization of the PPI model

The PPI method presented in Sec. 5.7 neglected radiation effects and an approximation was made in the calculation of retardation. The force acting on macroparticle i from macroparticle j was calculated in the laboratory frame using the Lorentz transformed fields from the rest frame of macroparticle j but assuming the event was "instantaneous" in both frames. This assumption implies that the space charge interaction must remain moderate but with a less drastic requirement than for the case of the envelope or shell models [see Sec. 5.7.1 for further details]. Arbitrary large energy spread is permitted, however. A general rule for the applicability of the PPI method may be defined as the potential energy per electron in the *beam frame* must remain lower than the electron rest mass energy itself, that is $\bar{U}'/mc^2 \ll 1$, where $\bar{U}'$ is the total potential energy normalized to the number of electrons in the bunch which can be approximately calculated as

$$\bar{U}' = U_0/N_e \,, \tag{5.93}$$

where N_e is the total number of electrons and U_0 is identical to Eq. (5.77) for beams with initially small energy spreads that is,

$$U_0 \simeq \int_V d^3x' \, \frac{\epsilon_0 \mathbf{E}'^2}{2} \,. \tag{5.94}$$

Beams produced by laser-plasma interactions, particularly in the self-modulated regime have a relatively high charge density giving $\bar{U}'/mc^2 \sim 1$, which sets an upper limit for the use of the PPI model. As was discussed in Sec. 5.8.2, SM-LWFA electron sources have a typical exponential energy density profile, that is the beam is mainly composed of low energy electrons together with a small subset of high energy electrons located at the front of the bunch. The high energy beam dynamics should moderately

be influenced by retardation effects because it mainly interacts with the low energy electrons, assuming the latter do not become relativistic during the time of interaction. This assumption is valid as long as the ballistic spreading is significant between the two populations. The opposite is obviously not true but the charge density of the high energy beam is relatively small and has very little effect on the low energy electrons[†]. Lastly the relative error introduced by the PPI method for the blowout of the low energy electrons may be crudely estimated using the ideal beam distributions of Sec. 5.7.1. The error was found to be on the percent level which is significantly lower than the overall change of the beam temperature [Fig 5.16(c) and (d)] discussed in Sec. 5.8.2.

For the case $\bar{U}'/mc^2 \gtrsim 1$ retardation and radiation effects may play a role in the overall beam dynamics. A generalization of the PPI model may be computed from the Lienard-Wiechert fields which are an exact solution of Maxwell's equations (i.e., including both retardation and radiation), that is [79, 81, 82]

$$\boxed{\mathbf{E}_i(\mathbf{r},t) = \frac{Q_m}{4\pi\epsilon_0}\left\{\left[\frac{\mathbf{n}-\beta_i}{\gamma_i^2\left(1-\mathbf{n}\cdot\beta_i\right)^3 R^2}\right]_{RET} + \left[\frac{\mathbf{n}\times\left\{(\mathbf{n}-\beta_i)\times\dot{\beta}_i\right\}}{c\left(1-\mathbf{n}\cdot\beta_i\right)^3 R}\right]_{RET}\right\}} \tag{5.95}$$

and

$$\boxed{\mathbf{B}_i(\mathbf{r},t) = c^{-1}\left[\mathbf{n}\times\mathbf{E}_i\right]_{RET}} \tag{5.96}$$

where Q_m is the macroparticle charge, $R\mathbf{n} = \mathbf{r}-\mathbf{r}_i$ and the subscript "RET" indicates that the quantities in the brackets are to be evaluated at the retarded time $t_{RET} = t - R/c$. Note that the definition of the retarded time is implicit since R depends on time. More explicitly we have

$$t_{RET} = t - |\mathbf{r} - \mathbf{r}_i(t_{RET})|/c\ . \tag{5.97}$$

For a system of macroparticles interacting via there mutual electromagnetic fields,

[†]Another way of considering the problem would be to assume that the high energy bunch is made of test electrons (neglecting the self interaction inside the bunch and with the rest of the beam). These test particles would get the exact same acceleration from the low energy electrons than in the case of macroparticles (same charge over mass ratio).

the equations of motion are

$$\frac{d\mathbf{p}_i}{dt} = Q_m \sum_{j \neq i} \left[\mathbf{E}_j(\mathbf{r}_i, t) + \mathbf{v}_i \times \mathbf{B}_j(\mathbf{r}_i, t) \right] \ , \tag{5.98}$$

where $\mathbf{E}_j$ and $\mathbf{B}_j$ are the electromagnetic fields due to the motion of macroparticle j. In the Lorentz force, the condition $j \neq i$ is necessary to exclude the self-force. The numerical approach is in principle that used to solve retarded scalar-fields problems [83]: The kinematic information is stored in arrays and retrieved by interpolation when needed later for the retarded quantities.

One of the critical issues with using macroparticles for problems where radiation is present ($\bar{U}'/mc^2 \gtrsim 1$) is the fact that macroparticles exasperate the amount of radiation produced. This may be simply shown by calculating the associated Poynting vector S of an accelerating macroparticle,

$$S = \mu_0^{-1} \left(\sum_i \mathbf{E}_i^m \right) \times \left(\sum_i \mathbf{B}_i^m \right) = N^2 \left(\mathbf{E}_i \times \mathbf{B}_i \right) \ , \tag{5.99}$$

where N is the number of real electrons per macroparticle and $\mathbf{E}^m$ and $\mathbf{B}^m$ are the microscopic radiation fields emitted by the individual electrons [equivalent to Eqs. (5.95)-(5.96) taking $Q_m = -e$]. Equation (5.99) may be interpreted as a coherent sum of radiation emitted by the individual electrons composing the macroparticle (assuming to be all located at the same position). Note that the Larmor formula for the macroparticle may be readily deduced, considering only straight line motion,

$$P = \frac{Q_m^2}{6\pi\epsilon_0 c^3} \left(\frac{dp}{dt} \right)^2 \ . \tag{5.100}$$

In reality, electrons fly apart from each others causing much less radiation through loss of coherence in the emitted radiation fields. This sets an upper limit for using macroparticle models to study 3-D space charge blowout of dense electron beams (both N-body or PIC). In this regime ($\bar{U}'/mc^2 \gtrsim 1$), a small amount of charge per macroparticles would be needed in order to get convergence of the numerical scheme, implying a large number of macroparticles which may not be of practical use with todays computers.

It is possible to derive an approximate expression for the total energy radiated by macroparticles in the case of a spherical charge distribution. Assuming the emission is purely incoherent, i.e., each source is considered independent from the others and the overall radiation is basically N_m times the radiation of one macroparticle, where N_m is the number of macroparticles in the bunch. In reality, there is more energy radiated because of some coherent effects ($\propto N_m^2$) and, consequently, this derivation may be considered as a *lower limit*. Introducing a fluid generalization of Larmor formula, Eq. (5.100), one obtains

$$\frac{dP_T}{dV} = n_m P \ , \tag{5.101}$$

where P_T is the total power radiated and n_m the density of macroparticles. The fields inside the homogeneous spherical charge distribution is given by

$$E_r = \frac{keN_e r}{R^3} \ , \tag{5.102}$$

where N_e is the total number of electrons in the bunch, R the bunch radius and $k = (4\pi\epsilon_0)^{-1}$. The acceleration is readily deduced from the equation of motion (macroparticles have same charge over mass ratio than real electrons),

$$\dot{p}(r) = \frac{e}{m_e} E_r(r) \ , \tag{5.103}$$

providing an expression for the total (normalized) energy radiated by the bunch *of macroparticles*,

$$\boxed{\frac{d\left(E_{\rm rad}/m_e c^2\right)}{cdt} = \frac{2r_e^3 N N_e^3}{5R^4}} \tag{5.104}$$

where the identity $N_e = NN_m$ has been used, N is the total number of electrons *per macroparticle* and r_e is the classical electron radius [$r_e = ke^2/(m_e c^2)$]. The total (normalized) potential energy in the beam, for a spherical charge distribution, is given by Eq. (5.77), that is

$$\frac{U_0}{m_e c^2} = \frac{3r_e N_e^2}{5R} \tag{5.105}$$

and the ratio $E_{\rm rad}/U_0$ by,

$$\boxed{\frac{E_{\rm rad}}{U_0} = \frac{2r_e^2 N N_e (c\Delta t)}{3R^3}} \tag{5.106}$$

For the case of a spherical charge distribution with a radius $R = 24$ μm, charge $Q = 5$ nC, number of macroparticles $N_m = 10^4$ (i.e, containing $N = 3.125 \times 10^6$ electrons) and assuming that the typical scale length for the space charge blow-out is on the order $c\Delta t \simeq 300$ μm, we get $E_{\rm rad}/U_0 \simeq 1.1$ %, i.e, the error introduced in on the percent level. Note that for real electrons (corresponding to $N = 1$), radiation is negligible ($E_{\rm rad}/U_0 \sim 10^{-6}$).

In Appendix L we further discuss energy conservation and benchmarking of N-body codes using Lienard-Wiechert fields. In the next Section, a study of emittance growth for beams with large energy spread is presented.

5.10.2 Emittance growth for beams with large energy spread

Beams with large energy spread can experience emittance growth while propagating in vacuum, even without any space charge interactions [84]. This is relevant to electron sources produced by laser-plasma based accelerators. The expression for the RMS normalized emittance is

$$\epsilon_x = (mc)^{-1}\sqrt{\langle x^2\rangle \langle u_x^2\rangle - \langle x u_x\rangle^2}\,, \tag{5.107}$$

where $\langle x\rangle = \langle u_x\rangle = 0$ was assumed and $\langle x u_x\rangle$ represents the correlations in the $x - u_x$ plane. If the beam can be well fitted by an ellipse in phase-space, then, when beam envelope is at waist, we have $\langle x u_x\rangle = 0$. For purely ballistic motion, the position of an individual particle in a drift space can be written as,

$$x_i = x_{0i} + x'_{0i} z\,, \tag{5.108}$$

where $x'_{0i} = \tan^{-1}(u_{x0i}/u_{z0i})$ with u_{x0i} and u_{z0i} constant. In the following, u_{z0i} will be rewritten as $u_{z0i} = u_{z0}(1+\eta_{0i})$ in order to introduce energy spread $\eta_{0i} = \Delta u_{zi}/u_{z0}$. In general, for beams with large energy spreads, correlations develop in the $x - u_x$ plane,

$$\langle x u_x\rangle = \langle x_0 u_{x0}\rangle + \langle x'_0 u_{x0}\rangle\, z\,, \tag{5.109}$$

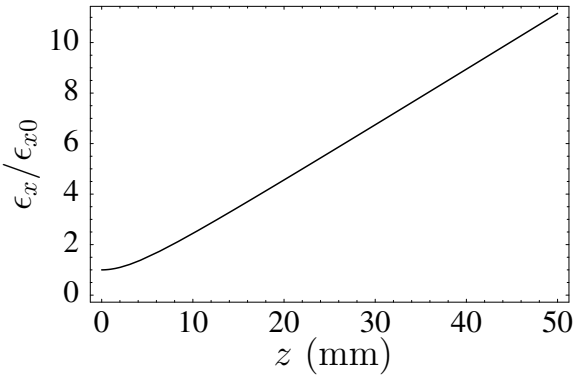

Figure 5.20: Simulation of the normalized emittance growth induced by the large energy spread for a beam with an exponential energy profile. Input parameters: bunch temperature $k_BT = 4$ MeV, radius $a = 6$ μm, half-length $a_3 = 10$ μm, divergence $x'_{max} = 2$ mrad and no space charge effects was assumed throughout this calculation.

i.e., the beam rotates in phase-space. In the same way one can write an analytical expression for transverse emittance growth in a drift space,

$$\epsilon_x = \sqrt{\epsilon_{x0}^2 + 2\alpha_\epsilon z + \beta_\epsilon^2 z^2}\,, \tag{5.110}$$

with,

$$\epsilon_{x0} = \sqrt{\langle x_0^2\rangle \langle u_{x0}^2\rangle - \langle x_0 u_{x0}\rangle^2}\,, \tag{5.111}$$

$$\alpha_\epsilon = \langle x_0 x_0'\rangle \langle u_{x0}^2\rangle - \langle x_0 u_{x0}\rangle \langle x_0' u_{x0}\rangle\ , \tag{5.112}$$

$$\beta_\epsilon = \sqrt{\langle x_0'^2\rangle \langle u_{x0}^2\rangle - \langle x_0' u_{x0}\rangle^2}\,. \tag{5.113}$$

For the case of small divergence ($u_{x0i}/u_{z0i} \ll 1$) and energy spread ($\eta_{0i} \ll 1$), we have $x'_{0i} \simeq u_{x0i}/u_{z0i}$ and $u_{z0i} \simeq u_{z0}$, which leads to conservation of emittance, $\epsilon_x(z) = \epsilon_{x0}$, over large propagation distances. This approximation is valid up to first order in energy spread, i.e.,

$$\alpha_\epsilon = u_{z0}^2 \left[\langle x_0 x_0'\rangle \left\langle x_0'^2 \eta_0 \left(1+\eta_0\right)\right\rangle - \langle x_0 x_0' \eta_0\rangle \left\langle x_0'^2 \left(1+\eta_0\right)\right\rangle\right]\ , \tag{5.114}$$

$$\beta_\epsilon = u_{z0}\sqrt{\langle x_0'^2\rangle \langle x_0'^2 \eta_0^2\rangle - \langle x_0'^2 \eta_0\rangle^2}\,. \tag{5.115}$$

Note that, if $x'_0 \sim \eta_0 \ll 1$ then $\alpha_\epsilon \ll \beta_\epsilon$, and also that a beam with initially no correlations between particle position and energy will have $\alpha_\epsilon = 0$. Figure 5.20 shows transverse emittance growth for the parameters of Fig. 5.11. For this particular example only a distance of $z \simeq 5$ mm is necessary to double emittance. On the other hand, inserting Eq. (5.108) into the expression of the trace space emittance,

$$\tilde{\epsilon}_x = \sqrt{\langle x^2 \rangle \langle x'^2 \rangle - \langle x x' \rangle^2}\,, \tag{5.116}$$

it can be shown that the latter is conserved for arbitrary energy spreads. This suggests that emittance considerations for beams with large energy spread must be handled carefully. Note that conventional pepper-pot techniques actually measure the beam trace-space emittance [85].

5.11 Conclusion

Plasma-based accelerators offer the possibility of providing compact, high energy electron accelerators and are also capable of producing ultrashort electron bunches in which the longitudinal size is much smaller than the transverse size. Space charge effects are not of concern while the bunch is in the plasma wave, since the longitudinal and transverse fields of the wake are typically much greater than the space charge forces of the bunch, but space charge cannot be neglected when an electron bunch propagates in vacuum with no external fields, because of its very compact dimensions, high charge density, relatively low energy (up to few tens of MeVs) and a possibly large energy spread. Conventional space-charge approaches, restricted to small energy spread beams, are not applicable in this case.

In this Chapter, we provided a comprehensive summary of the analytical methods (including their limitations) available for the simulation of such a wide variety of beams: (i) the coupled envelope equations, which assume that the beam shape remains ellipsoidal with a small divergence (paraxial approximation) and small energy spread (typically on the order of a few %) has been discussed. This model can be applied to most sources produced by optical injection such as colliding pulse (CPI). (ii) A novel technique which uses ellipsoidal symmetric beam distribution functions and allows the treatment of arbitrarily large energy spreads has also been

introduced. It assumes the paraxial approximation and allows an extension of the envelope model to beams with large energy spreads. This method has the advantage of being computationaly fast compared to standart technics such as PIC. (iii) A modified electrostatic PIC, allowing for the binning in momentum of the beams with large energy spread has also been presented along with (iv) a 3-D point-to-point interaction method (PPI). The PPI and PIC codes have been compared and applied to the simulations of high density and compact electrons beams where the paraxial approximation is violated. This is relevant to the electron sources produced by the self-modulated laser wakefield accelerator (SM-LWFA). The number density for these beams is typicaly $n_e \sim 10^{19}$ cm^{-3} which results in significant space charge blow-out while propagating in vaccum.

Studying in detail the SM-LWFA regime, we have shown the global effect of correlations on the time evolution of the beam distribution function when energy spread is large. Furthermore, numerical examples using an electromagnetic PIC code has given us the opportunity to describe in great detail the effect of space charge on the sub-structures of these beams. Their features are typically a high charge density and an ensemble of large energy spread sub-bunches with the highest energies in the first beamlet[‡] (this is true provided the beam is extracted after a propagation distance within the plasma on the order of the dephasing length [33]). It was found that space charge plays a major role and can induce electron self-acceleration with a global change of beam energy spectrum while keeping an overall "two-temperature" profile at detector's location. This is consistent with experimental observations. Furthermore, it has been shown that the high energy electron bunch characteristics are preserved during vacuum propagation with an additional energy gain up to $\sim 16\%$, for the examples considered, leading to a significant decrease in trace-space emittance.

In the next Chapter, we will give a summary and conclusions for the work presented in the dissertation along with directions for future work.

[‡]The latter effect may be explained from beam loading which turns-off injection and diminish the wakefield amplitude behind the first bucket.

Chapter 6

Conclusions

Contents

This thesis has analyzed in detail two different but linked topics in laser-plasma interactions for the generation of electron beams. The first is the controlled injection of electrons in laser excited wakes by using one or two additional laser pulses. The second is a study of how dense electron beams propagate in vacuum.

We have shown that the use of colliding laser pulses, as a controlled injection and acceleration scheme of background plasma electrons, leads to formation of ultra-short, high energy compact electron bunches. The calculation has been further extended to the problem of vacuum transport of high brightness electron beams and associated space charge effects, work which can be applied in general to large energy spread beams such as produced by plasma based accelerators.

In this chapter, the theoretical results presented in this dissertation are summarized. Possible future theoretical and computational work is discussed along with experimental applications.

6.1 Summary

In Chap. 2, we have derived the basic set of equations for the generation of a plasma wave by an intense ($a \sim 1$), ultra short ($\tau \sim 50$ fs) laser pulse. These equations were used throughout the dissertation to describe in detail the injection of background plasma electrons using the slow beatwave (interference term) of two counter-propagating colliding laser pulses (CPI).

Chapter 3 was devoted in particular to the case of two linearly polarized laser pulses in an homogeneous plasma [21]. The advantage of using the CPI method to inject electrons into the plasma wave compared to standard single-beam methods is that it offers a better control of the injection process. Injection schemes relying on a single drive beam (such as, for instance, the self-modulated laser-wakefield-accelerator [SM-LWFA] [9], the bubble regime [17, 80], etc.) rely on an instability to drive a plasma wave to the wave breaking limit, which induce self-trapping of plasma electrons. These regimes have succeeded in producing electron beams containing multi-nCs of charge with energies in excess of 10's of MeVs. Furthermore, a careful control of the acceleration length, laser and plasma parameters has produced electron beams with %-level

energy spread sub-structures (the latter may be extracted using a magnetic spectrometer) leading to production of single quasi-monoenergetic dense electron bunches [32–34]. The weakness of the single-beam method, used as a compact electron source, is due to the nonlinear process of driving the wake to the self-injection threshold (i.e, an instability). A small variation in laser-plasma parameters may greatly modify the characteristics of the electron bunch [11].

CPI operates in the linear regime (which makes it much less sensitive to laser-plasma fluctuations), that is, the drive laser pulse is resonant ($L_0 \simeq \lambda_p$ where L_0 is the laser pulse length and λ_p is the plasma wavelength) and requires modest drive and injection laser intensities ($a_0 \simeq 1$ and $a_1 \simeq 0.5$, respectively). Colliding pulse injection allows for injection into a single wakefield "bucket" and electrons are injected always at the same location in the plasma wake improving the electron source stability. In Chap. 3, for the case of linearly polarized laser pulses with equal frequency (which characterize the easiest experimental implementation), we have shown that the production of ultra-short electron beams is possible. These bunches typically have a high energy $\sim 10 - 100$ MeV and above (depending on accelerator characteristics, that is, plasma length, nominal density, etc.), charge on the order $\sim 10 - 100$ pC (up to 300 pC has been observed but for such beam densities beam loading may be of concern), small normalized emittance < 1 mm.mrad and a small energy spread (typically a few percent). The bunch duration was found to be typically on the order of a few percent of the plasma wavelength, which implies formation of attosecond electron bunches for short plasma wavelengths.

One limitation of the approach used in this research is that it relies on test particle simulations in which the fields (lasers and wakes) were specified analytically. Specifically, analytical expressions were used for the wakefield valid to second order in the normalized laser field a_i^2. This model becomes inaccurate as a_i^2 approaches and exceeds unity and self-consistent simulations, such as using particle-in-cell (PIC) or fluids codes, are required in this nonlinear regime. A second approximation used in the test particle simulations is the neglection of the wake generated by the trapped bunch, i.e., neglection of beam loading. These test particle simulations indicate that the colliding pulse trapping mechanism is rather robust, i.e., it is easy to trap electrons up to beam loading limit. Again, to fully assess the utility of the colliding pulse injection in the high-charge limit, self-consistent simulations are required.

A combined method using colliding laser pulses together with a negative plasma density gradient has been introduced in Chap. 4. A decrease in density implies an increase in plasma wavelength, which can shift a relativistic electron from the defocusing to the focusing region of the accelerating wakefield. Simulations showed the possibility of enhancing charge by more than an order of magnitude (~ 50) while keeping overall beam brightness the same. The trapped bunch quality was found to depend only weakly on the length of the ramp (L_t), indicating that the use of experimentally feasible ramps with $L_t \gg \lambda_p$ can be effective in enhancing the trapped bunch. Since the use of down ramps increases the number of trapped and focused electrons, the overall trapping threshold for electron injection into the plasma wave is lowered, which allows the production of trapped bunches with lower intensity laser pulses.

Compact electrons beams which are produced by single-beam or CPI methods may be subject to deterioration of their brightness du to space charge interaction. Simulation of the transport of beams with a large energy spread may be done using fully explicit PIC codes but require important computer resources such as large super-computers. Consequently, the development of alternative method is really important. In Chap. 5 we have proposed and reviewed fast analytical and semi-analytical methods which allow for studying dynamics of space charge dominated electron beams on much faster time scales for obtaining results and physical insight. The major finding are:

- Coupled envelope equations (Sec. 5.5) may be used to describe dynamics of beams with modest energy spreads (up to ~ 50 %) and divergences (few tens of mrads) [35, 71]. An upper limit for the usability of the envelope model may be characterized using the approximate coefficient $\alpha_b \leq 1$ where

$$\alpha_b = \frac{\bar{I}}{\gamma_0 I_A} \frac{1.8 \times 10^2}{R^2_{[\mu\mathrm{m}]}} \ , \tag{6.1}$$

  I is the average beam current, $I_A = 17 \times 10^3 \ u_0$ the Alfvèn current, $u_0 = \gamma_0 \beta_0$ the beam normalized momentum and R the beam radius.

- The shells approach (Sec. 5.4) can be summarized as a generalization of the

envelope equations model but applied to beams with *arbitrary* energy spread [36]. Small beam divergence is still required however to satisfy the paraxial approximation ($\beta_\perp/\beta_z \ll 1$) together with the condition $\alpha_b \leq 1$.

- Another alternative method based on a 3-D point-to-point interaction scheme (PPI) has also been introduced (Sec. 5.7) which may be applied to arbitrary electron distributions (including large energy spread and divergence). The code was compared to PIC and found to reach convergence using a relatively modest amount of macroparticles, providing a seemingly faster method for the examples described in this dissertation. The PPI method neglects radiation effects and an approximation is made in the calculation of retardation (Chap. 5, Sec. 5.7.1 and 5.10). A general rule for the applicability of the PPI model may be defined as follow: the potential energy per electron in the *beam frame* must remain lower than the electron rest mass energy itself, that is $\bar{U}'/mc^2 < 1$, where $\bar{U}'$ is the total potential energy normalized to the number of electrons in the bunch which can be approximately calculated as

$$\bar{U}' = U_0/N_e \ , \tag{6.2}$$

where N_e is the total number of electrons and

$$U_0 \simeq (\epsilon_0/2) \int d^3x' \ \mathbf{E}'^2 \ . \tag{6.3}$$

This definition of U_0 is strictly valid for beams with an initially small energy spread.

Simulation of vacuum transport for typical beams produced by CPI injectors (Sec. 5.8.2) shows no significant effects of space charge for average beam energies beyond $\sim$ 40 MeV [Fig 5.9]. SM-LWFA based electron sources, on the contrary, will experience space charge blowout (Sec. 5.8.2) due to the higher charge density (typically two order of magnitude more than CPI based sources). These bunches typically have a multi-beam structure provided by the injection over multi plasma wave "buckets" during wavebreaking process. If the acceleration length after injection is on the order

the dephasing length, a quasi-monoenergetic bunch with an average energy typically higher than the rest of the beam may be extracted. The overall space charge interaction in vacuum leads to a global change in beam temperature but conserving a "two-temperature" profile, which is consistent with experimental observations, whereas the quasi-monoenergetic bunch may benefit from the additional acceleration, due to the longitudinal space charge forces, while keeping overall high brightness.

We next discuss future directions for the work presented in this dissertation.

6.2 Future directions

6.2.1 Colliding pulse injection

Numerical predictions for the CPI method have been studied in this dissertation through test particle simulations. The latter uses prescribed electromagnetic fields which are valid up to second order in the laser strength a_i (the next order correction to the plasma wave is proportional to $a_i^4/16$ for linearly polarized laser pulses). Methods combining fluid-simulations (for more accurate wakefield calculation) with test particles may be a direction to explore. The other limitation of test particle simulations is the inability to cope with self-consistent space charge interaction between the compact injected electron beam and the plasma [beam loading]. Beam loading may be simulated accurately through the use of PIC codes. However to describe the injection process, a very fine grid is necessary, typically longitudinally $\Delta z < \lambda_0/40$ to resolve correctly the fast laser time scale. Transversally the grid size should be chosen to give an electron temperature on the grid close to the real experimental plasmas*, that is a few tens of eVs. This constraint on the simulation parameters may require important computer resources. An approximate scaling law for the time required by a PIC simulation may be defined as follow [11, 86]: the total CPU time per processor,

*Non-physical heating of the simulated plasma may be observed (i) if the grid does not resolve sufficiently the laser carrier frequency (error introduced in the particle pusher) and (ii) if the ratio of the Debye length to the grid size $\lambda_D/\Delta z$ is less than 0.3 (in 1D) [54].

per second and per time step is given by

$$\Delta t = N_G \left(N_{ppc} + 1\right) \tau_p \ , \tag{6.4}$$

where τ_p is the particle push time which is typically $\tau_p \simeq 6$ μs on Seaborg (NERSC super-computer) for the PIC code VORPAL [56], N_{ppc} is the number of particle per cell, and $N_G = \Pi_i N_{Gi}$ the number of grid points.

A high resolution PIC simulation with $N_{ppc} = 10$ particle/cell, a plasma size of 80 μm $\times$ 120 μm corresponding to 4000×6000 grids in 2D slab geometry assuming a grid size $\Delta z = \Delta x = \lambda_0/40$, where $\lambda_0 = 0.8$ μm is the laser carrier frequency, would take $\Delta t \simeq 0.44$ hours per time step, per processor. One time step in the simulation is related to the Courant condition [11, 54, 55] which is on the order of $\tau_{\rm step} \simeq 0.1$ fs (or $c\tau_{\rm step} \simeq 0.03$ μm) for the case considered. A plasma length of $L = 1$ mm (using a moving window) would take $N_t \simeq 34000$ time steps, giving a total simulation time of $N_t \Delta t / N_{pr} \simeq 58$ hours in 2D slab using $N_{pr} = 256$ processors. A 3D simulation with the same resolution would take $N_{Gy} = 6000$ times more.

A set of new experiments devoted in particular to the understanding of the physics of optical injection using two linearly polarized laser pulses in underway at LBNL [87]. The experiments are based on a 10 Hz Ti : Al_2O_3 CPA laser system. Low energy laser pulses from the oscillator (of wavelength $\lambda_0 \simeq 800$ nm) are first temporally stretched, and split into two pulses. The drive pulse is amplified up to 0.4 J/pulse for seeding a plasma wave and the injection pulse is amplified to ~ 0.1 J/pulse. Table 6.1 summa-

Table 6.1: Parameters of the two-pulse colliding-pulse experiment at LBNL.

	Drive pulse	Colliding pulse
Energy (J/pulse)	0.4	0.1
τ (fs)	$40 - 150$	$40 - 150$
r_0 (μm)	7.5	14.5
Power (TW)	$1 - 10$	$0.6 - 2.5$
a_0	$1 - 2.8$	$0.3 - 0.6$

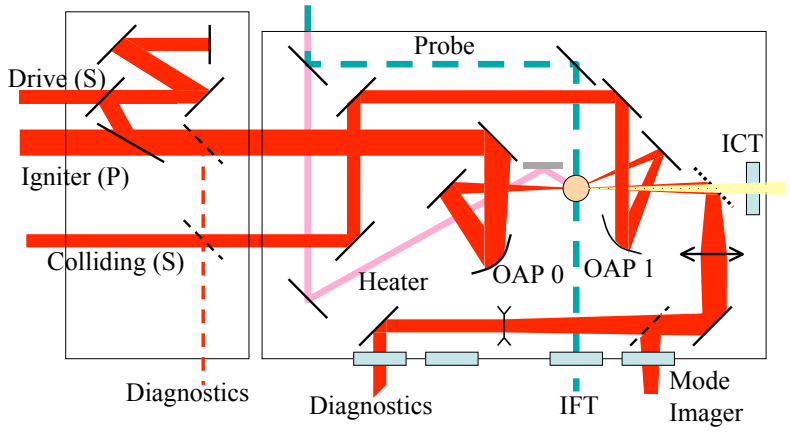

Figure 6.1: Schematic of the experimental setup. The high power laser beams are focused using an off-axis parabolic mirror (OAP) onto a high pressure pulsed gas jet operating with about 70 bar helium backing pressure, respectively. An integrating current transformer (ICT) is used to measure the charge pr bunch of the electron beam and plasma densities are measured with the interferometer (IFT).

rizes the experimental parameters[†]. The colliding beam intersect the drive beam from the downstream direction at a 19 degree angle, which should still trap ~ 40 % of the nominal charge compared to head-on collisions (according to Fig. 3.19 in Chap. 3). The schematic of the experiment is shown in Fig. 6.1.

The CPI experiment is based on the standard laser wakefield regime. Extended interaction length requires a preformed plasma channel [11, 33]. A guiding channel is formed using a variation of the igniter-heater method [Fig. 6.1]. By adjusting the energy and the timing of the guide formation pulses, the channel profile may be matched to guide the drive pulse without distortion over 10 Rayleigh lengths (Z_R). Using a preformed plasma channel, the resonant drive pulse is expected to generate a wakefield inside the plasma channel without trapping significant amounts of background electrons (dark current) [11, 33]. Note that long injection pulse may be

[†]Note that the relationship $a_0 = 5.489\sqrt{P[\mathrm{TW}]}/r_0[\mu\mathrm{m}]$ has been used

useful as non-resonant beams produce very little wake and in addition an increased overlapping time produces higher charge per bunch.

Another means of increasing the charge, while conserving the overall high brightness of the beam, is to use a negative density plasma gradient, as previously discussed. It has been demonstrated that long transition length, i.e. over many plasma wavelengths [see for example Chap. 4 and Fig. 4.6] does not affect the total amount of charge that may be rephased. This can be done experimentally using two gas jets with different backing pressures.

6.2.2 Space charge simulations

Continuing the previous discussion on PIC requirements, in Chap. 5 the electron distributions used to model plasma based electron sources in the SM-LWFA regime were obtained from self-consistent 2D slab PIC simulations. The 3D electron beams were deduced from the PIC simulations assuming circular symmetry. However the charge in the quasi-monoenergetic bunches seemed to be systematically lower (up to an order of magnitude) than the experimental observations. This may be explained in part because of the large differences in the wake structure between 2D slab and 3D geometry in the blowout regime [11]. Note that a higher charge per bunch will increase the intensity of the space charge interaction. Accurate electron beam distributions may be obtained through simulations using 3D PIC codes but a converging answer will again require a great amount of hours of CPU time with todays computers.

Appendix A

The mathematical framework of plasma physics

Contents

A plasma is composed of charged particles interacting with respect to each others via the Lorentz force. This implies, in principle, to solve the full N-body problem is order to understand the dynamics of each particle within the plasma. This is both analytically and computationally impossible even with present days computers. The full N-body problem in its usual description is said to be in "Lagrangian coordinates", which are the coordinates following the particle's motion. They can be stated as follow,

$$\dot{\mathbf{P}}_i = \sum_j^N \mathbf{F}_{ji} \tag{A.1}$$

$$\dot{\mathbf{X}}_i = \mathbf{P}_i/(m_0\gamma) \tag{A.2}$$

where $\gamma = \sqrt{1+\mathbf{P}_i^2/(m_0c^2)}$, m_0 is the particle rest mass and $\mathbf{F}_{ji}$ is the interaction force between particle i and the j-th particle in the plasma. The full force calculation for the whole plasma involves $\sim N^2$ coupled terms. This shows the importance of using reduced models for equations driving the plasma, keeping in minds that experiments only measure *average* parameters. This leads to our next topic, the derivation of the Klimontovitch equation.

A.1 Klimontovitch equation

A better approach for building the equations describing the time evolution of a plasma is the so-called use of "Eulerian coordinates". Particle position and momentum in Eqs (A.1)-(A.2) is represented as a function of time, the Eulerian coordinates (x, p) define the particle position in phase space as a continuous function of x and p. The relation between $\mathbf{x}$, $\mathbf{X}_i$, $\mathbf{p}$, $\mathbf{P}_i$ can be linked through the use of the delta function [88]

$$\delta[\mathbf{x}-\mathbf{X}_i(t)]\delta[\mathbf{p}-\mathbf{P}_i(t)] \tag{A.3}$$

where $\delta[\mathbf{x}-\mathbf{X}_1] = \delta[x-X_1]\delta[y-Y_1]\delta[z-Z_1]$, etc. Note that δ-function has units of density.

For the whole plasma, the total density can be stated as follow

$$N_s(\mathbf{x},\mathbf{p},t) = \sum_{i=1}^{N_0}\delta[\mathbf{x}-\mathbf{X}_i(t)]\delta[\mathbf{p}-\mathbf{P}_i(t)] \tag{A.4}$$

$$N(\mathbf{x},\mathbf{p},t) = \sum_{e,i} N_s(\mathbf{x},\mathbf{p},t) \tag{A.5}$$

with N_0 the number of particles in the specie N_s and N the total density of particles in the plasma, i.e., after summation over the ions and electrons. An exact equation for the time evolution of the plasma is obtained by taking the time derivative of the density N_s, from Eq (A.4), this is

$$\begin{aligned}\frac{\partial N_s(\mathbf{x},\mathbf{p},t)}{\partial t} = & -\sum_{i=1}^{N_0}\dot{\mathbf{X}}_i\cdot\nabla_{\mathbf{x}}\,\delta[\mathbf{x}-\mathbf{X}_i(t)]\delta[\mathbf{p}-\mathbf{P}_i(t)] \\ & -\sum_{i=1}^{N_0}\dot{\mathbf{P}}_i\cdot\nabla_{\mathbf{p}}\,\delta[\mathbf{x}-\mathbf{X}_i(t)]\delta[\mathbf{p}-\mathbf{P}_i(t)]\end{aligned} \tag{A.6}$$

with $\nabla_x \equiv (\partial_x,\partial_y,\partial_z)$ and $\nabla_p \equiv (\partial_{p_x},\partial_{p_y},\partial_{p_z})$ where we have used the relations

$$\frac{\partial f(a-b)}{\partial a} = -\frac{\partial f(a-b)}{\partial b} \tag{A.7}$$

and

$$\frac{df[g(t)]}{dt} = \dot{g}\frac{df}{dg} \tag{A.8}$$

We can write $\dot{\mathbf{X}}_i$ and $\dot{\mathbf{P}}_i$ in terms of $\mathbf{P}_i$ and the microscopic electromagnetic fields $\mathbf{E}^m$ and $\mathbf{B}^m$, whereupon Eq (A.6) becomes

$$\begin{aligned}\frac{\partial N_s(\mathbf{x},\mathbf{p},t)}{\partial t} = & -\sum_{i=1}^{N_0}\mathbf{V}_i\cdot\nabla_{\mathbf{x}}\,\delta[\mathbf{x}-\mathbf{X}_i(t)]\delta[\mathbf{p}-\mathbf{P}_i(t)] \\ & -\sum_{i=1}^{N_0} q_s\Big\{\mathbf{E}^m(\mathbf{X}_i(t),t)+\mathbf{V}_i/c\times\mathbf{B}^m(\mathbf{X}_i(t),t)\Big\} \\ & \cdot\nabla_{\mathbf{p}}\,\delta[\mathbf{x}-\mathbf{X}_i(t)]\delta[\mathbf{p}-\mathbf{P}_i(t)]\end{aligned} \tag{A.9}$$

Using the property of the Dirac delta function

$$a\delta(a-b) = b\delta(a-b) \tag{A.10}$$

we can replace $\mathbf{V}_i$ with $\mathbf{v}$ and $\mathbf{X}_i$ with $\mathbf{x}$ leading to

$$\frac{\partial N_s(\mathbf{x},\mathbf{p},t)}{\partial t} = -\mathbf{v}\cdot\nabla_{\mathbf{x}} \sum_{i=1}^{N_0} \delta[\mathbf{x}-\mathbf{X}_i]\delta[\mathbf{p}-\mathbf{P}_i]$$
$$-q_s\left\{\mathbf{E}^m(\mathbf{x},t) + \mathbf{v}/c \times \mathbf{B}^m(\mathbf{x},t)\right\}\cdot\nabla_{\mathbf{p}} \sum_{i=1}^{N_0} \delta[\mathbf{x}-\mathbf{X}_i]\delta[\mathbf{p}-\mathbf{P}_i] \tag{A.11}$$

The two summations on the right of Eq (A.11) are just the density (A.5); therefore

$$\boxed{\left[\frac{\partial}{\partial t} + \mathbf{v}\cdot\nabla_{\mathbf{x}} + q_s\left(\mathbf{E}^m(\mathbf{x},t) + \frac{\mathbf{v}}{c}\times\mathbf{B}^m(\mathbf{x},t)\right)\cdot\nabla_{\mathbf{p}}\right] N_s(\mathbf{x},\mathbf{p},t) = 0} \tag{A.12}$$

Which is the exact Klimontovitch equation. The macroscopic electromagnetic fields are determined self-consistently from Maxwell's equations (in Gaussian units)

$$\nabla\cdot\mathbf{E}^m = 4\pi\sum_s q_s \int d^3p\ N_s(\mathbf{x},\mathbf{p},t) \tag{A.13}$$

$$\nabla\cdot\mathbf{B}^m = 0 \tag{A.14}$$

$$\nabla\times\mathbf{E}^m = -\frac{1}{c}\frac{\partial\mathbf{B}^m}{\partial t} \tag{A.15}$$

and

$$\nabla\times\mathbf{B}^m = \frac{4\pi}{c}\sum_s q_s\int d^3p\ \mathbf{v}\ N_s(\mathbf{x},\mathbf{p},t) + \frac{1}{c}\frac{\partial\mathbf{E}^m}{\partial t} \tag{A.16}$$

The Klimontovitch equation, together with Maxwell's equations, constitute an exact description of a plasma. Given the initial positions and velocities of the particles, the initial densities $N_e(\mathbf{x},\mathbf{p},t=0)$ and $N_i(\mathbf{x},\mathbf{p},t=0)$ are given exactly by Eq. (A.4). The initial fields are then chosen to be consistent with Maxwell's equations. With these initial conditions the problem is completely deterministic, and the densities are

exactly determined for all time.

In practice we never carry out this procedure. The Klimontovitch equation contains everyone of the exact particle orbits. This is far more information than we want or need. What is needed is information about certain average properties of the plasma. The usefulness of the Klimontovitch equation comes from its role as a starting point in the derivation of equations that describe the average properties of the plasma. Before deriving the plasma kinetic equation, a few points can be made concerning the Klimontovitch equation. It is equivalent to a continuity equation in 6-D phase-space. The vectors $\mathbf{X}_i(t)$ and $\mathbf{P}_i(t)$ are simply characteristics of Eq (A.12). This can be shown as follow. Assume we want to follow a trajectory in phase-space, i.e., a characteristics solution of Eq (A.12), then

$$\frac{d}{dt}N_s(\mathbf{X}_i(t),\mathbf{P}_i(t),t) = \left(\frac{\partial}{\partial t} + \dot{\mathbf{X}}_i \cdot \nabla_{\mathbf{X}} + \dot{\mathbf{P}}_i \cdot \nabla_{\mathbf{P}}\right) N_s(\mathbf{X}_i(t),\mathbf{P}_i(t),t) = 0 \quad \text{(A.17)}$$

which says that the density is constant along an electron trajectory. d/dt is called a *convective derivative*.

A.2 Plasma kinetic equation

As we have argued in Section A.1, the Klimontovitch equation is a rewriting of the microscopic equations of motion for the particles, and is thereby concerned with the microscopic information in matching details. A correspondence to the macroscopic world in which we observe the plasma through a set of macroscopic variables may be provided by the averaging process in Gibbs' sense as follows [89]: the angular brackets $\langle \cdots \rangle$ denote an ensemble average over replicas of the system with the same "macroscopic realizations", represented by e.g., thermodynamic, hydrodynamic, electromagnetic variables and the single-particle distribution functions. In many cases, we may alternatively interpret $\langle A \rangle$ as the space-time average of a physical quantity A over scales substantially greater than those associated with the fluctuations.

The general procedure for calculating the modification of the smoothed (or coarse-grained) single-particle distribution function $f_s(\mathbf{x},\mathbf{p},t)$ due to discrete particle collisions can be summarized as follow [77]. The microscopic phase-space density N_s and

electromagnetic fields $\mathbf{E}^m$ and $\mathbf{B}^m$ are expressed as

$$N_s(\mathbf{x},\mathbf{p},t) = \langle N_s(\mathbf{x},\mathbf{p},t)\rangle + \delta N_s(\mathbf{x},\mathbf{p},t) \tag{A.18}$$

$$\mathbf{E}^m(\mathbf{x},t) = \langle \mathbf{E}^m(\mathbf{x},t)\rangle + \delta \mathbf{E}^m(\mathbf{x},t) \tag{A.19}$$

and

$$\mathbf{B}^m(\mathbf{x},t) = \langle \mathbf{B}^m(\mathbf{x},t)\rangle + \delta \mathbf{B}^m(\mathbf{x},t) \tag{A.20}$$

where $\langle N_s(\mathbf{x},\mathbf{p},t)\rangle = f_s(\mathbf{x},\mathbf{p},t)$, $\langle \mathbf{E}^m(\mathbf{x},t)\rangle = \mathbf{E}(\mathbf{x},t)$ and $\langle \mathbf{B}^m(\mathbf{x},t)\rangle = \mathbf{B}(\mathbf{x},t)$, denotes ensemble averaged values and δN_s, $\delta\mathbf{E}$, and $\delta\mathbf{B}$ denote fluctuations about the mean induced by discrete particle effects. Taking the ensemble average of the Klimontovitch-Maxwell equations (A.12), (A.13) and (A.16), and making use of $\langle \delta N_s\rangle = \langle \delta \mathbf{E}^m\rangle = \langle \delta \mathbf{B}^m\rangle = 0$, we obtain

$$\left[\frac{\partial}{\partial t} + \mathbf{v}\cdot\nabla_{\mathbf{x}} + q_s\left(\mathbf{E}(\mathbf{x},t) + \frac{\mathbf{v}}{c}\times\mathbf{B}(\mathbf{x},t)\right)\cdot\nabla_{\mathbf{p}}\right] f_s(\mathbf{x},\mathbf{p},t) = \left(\frac{\partial f_s}{\partial t}\right)_{\text{coll}} \tag{A.21}$$

$$\nabla\cdot\mathbf{E} = 4\pi\sum_s q_s\int d^3p\ f_s(\mathbf{x},\mathbf{p},t) \tag{A.22}$$

$$\nabla\cdot\mathbf{B} = 0 \tag{A.23}$$

$$\nabla\times\mathbf{E} = -\frac{1}{c}\frac{\partial\mathbf{B}}{\partial t} \tag{A.24}$$

and

$$\nabla\times\mathbf{B} = \frac{4\pi}{c}\sum_s q_s\int d^3p\ \mathbf{v}\ f_s(\mathbf{x},\mathbf{p},t) + \frac{1}{c}\frac{\partial\mathbf{E}}{\partial t} \tag{A.25}$$

where $(\partial f_s/\partial t)_{\text{coll}}$ is defined by

$$\left(\frac{\partial f_s}{\partial t}\right)_{\text{coll}} = -q_s\left\langle\left(\delta\mathbf{E} + \frac{\mathbf{v}}{c}\times\delta\mathbf{B}\right)\cdot\nabla_{\mathbf{p}}\ \delta N_s\right\rangle \tag{A.26}$$

The left side of Eq. (A.21) contains smoothly varying functions representing collective effects, while the right side represents the collisional effects. Note that the collision term scales on the order of the inverse of the plasma parameter, i.e., $(\partial f_s/\partial t)_{\text{coll}} \sim$

$O(\Lambda_s^{-1})$, where $\Lambda_s = n_0 \lambda_{D_s}^3$, n_0 is the background plasma density and λ_{D_s} the debye length for specie s, which is given by

$$\lambda_{D_s} = \sqrt{\frac{T_s}{4\pi n_0 e^2}} \tag{A.27}$$

or in engineering units

$$\Lambda_s \simeq 4 \times 10^8 T_s^{3/2}[\text{eV}]/n_0^{1/2}[\text{cm}^{-3}] \tag{A.28}$$

and

$$\lambda_{D_s}[\text{cm}] \simeq 720\sqrt{T_s[\text{eV}]/n_0[\text{cm}^{-3}]} \tag{A.29}$$

For the typical parameters relevant to plasma based accelerators which is $n_0 \sim 10^{19}$ cm^{-3} and $T_e \sim 10 - 50$ eV we get $\Lambda_e \sim 4 - 40$. Note than for those experiments ions are immobile on the time scale of interest, only electron motion is considered. For such plasmas, collisions become relevant after many plasma oscillations ω_p, which is the (collective) plasma frequency given by

$$\omega_p = \sqrt{4\pi n_0 e^2/m_0} \tag{A.30}$$

with m_0 the electron rest mass. In engineering units we get $\omega_p[\text{s}^{-1}] = 2\pi\ 9000\ n_0[\text{cm}^{-3}]$. For times scales $\tau \sim \omega_p^{-1} \ll \nu_{ei}^{-1} \sim \nu_{ee}^{-1}$, we can safely neglect (large angle) collisions and Eq. (A.21) becomes

$$\boxed{\left[\frac{\partial}{\partial t} + \mathbf{v}\cdot\nabla_{\mathbf{x}} + q_s\left(\mathbf{E}(\mathbf{x},t) + \frac{\mathbf{v}}{c}\times\mathbf{B}(\mathbf{x},t)\right)\cdot\nabla_{\mathbf{p}}\right] f_s(\mathbf{x},\mathbf{p},t) = 0} \tag{A.31}$$

where ν_{ei} (ν_{ee}) is the electron-ion (electron-electron) collision frequency, respectively. They are the most relevant collision terms. The ion-ion and ion-electron collisions typically occurs in a much greater time scale (in other words electrons termilize first).

Eq. (A.31) is the Vlasov equation (sometimes referred as the collisionless Boltzmann equation). Note that, in addition to the Klimontovitch equation, there is another equation, the Liouville equation, which also provides an exact description of a plasma. Like the Klimontovitch equation, the Liouville equation is of no direct use,

but provides a starting point for the construction of approximate theories (BBGKY hierarchy). One of the most useful practical results of this approach is to provide us with an approximate form of the collision term $(\partial f_s/\partial t)_{\text{coll}}$. Discussion on that matter can be found in [88–91] and references therein.

A.3 Conservation relations for the Vlasov equation

The nonlinear Vlasov-Maxwell equations can be used to derive conservation relations [77]. The most relevant relation which will be used later in the text for discussing some numerical methods, is the energy conservation law. Writing Eq. (A.31) in the form of a continuity equation, which is

$$\frac{\partial}{\partial t} f_s + \nabla_{\mathbf{x}} \cdot (\mathbf{v} f_s) + \nabla_{\mathbf{p}} \cdot \left[q_s \left(\mathbf{E}(\mathbf{x}, t) + \frac{\mathbf{v}}{c} \times \mathbf{B}(\mathbf{x}, t) \right) f_s \right] = 0 \tag{A.32}$$

We operate on Eq. (A.32) with $\sum_s \int d^3p(\gamma - 1)m_s c^2$, where $\gamma = \sqrt{1 + \mathbf{p}^2/(m_s c^2)}$ and m_s the rest mass of species s. Making use of Eqs. (A.22)-(A.25), one obtain the energy balance equation

$$\begin{aligned} &\frac{\partial}{\partial t} \left(\sum_s \int d^3p(\gamma - 1)m_s c^2 f_s + \frac{|\mathbf{E}|^2 + |\mathbf{B}|^2}{8\pi} \right) \\ &\quad + \nabla_{\mathbf{x}} \cdot \left(\sum_s \int d^3p(\gamma - 1)m_s c^2 \mathbf{v} f_s + \frac{c}{4\pi} \mathbf{E} \times \mathbf{B} \right) = 0 \end{aligned} \tag{A.33}$$

Equation (A.33) relates the local rate of change of the total (particle plus field) energy to the divergence of the flux of particles energy plus field energy. Integrating that equation over a Volume V containing the entire charge particle system * yields,

$$\boxed{\frac{\partial}{\partial t} \left[\int_V d^3x \left(\sum_s \int d^3p(\gamma - 1)m_s c^2 f_s + \frac{|\mathbf{E}|^2 + |\mathbf{B}|^2}{8\pi} \right) \right] = - \oint_S dS \; \mathbf{n} \cdot \mathbf{S}} \tag{A.34}$$

*Note that integrals over the divergence terms can be converted to integrals over the surface S enclosing the volume V (Green-Ostrogradsky relation).

Here $\mathbf{n}$ is the unit vector normal (outward) to the surface S. The pointing vector S in Eq. (A.34) is defined by

$$\mathbf{S} = \frac{c}{4\pi}\mathbf{E} \times \mathbf{B} \tag{A.35}$$

Note that $\mathbf{n} \cdot \mathbf{S}$ is the normal flux of electromagnetic energy flowing out of the volume V through the surface S

A.4 Macroscopic fluid description

In this dissertation all analytical and numerical calculations will aim to find approximate expressions for the smoothed distribution function $f_s(\mathbf{x}, \mathbf{p}, t)$. Plasma with temperature $T_e \sim 10$ eV can be considered cold, meaning the pressure (in a fluid point of view) can be neglected and in this special case the fluid equations will actually provide an exact solution of the Vlasov equation (A.31). This will be shown next. In the cold fluid theory, we follow the evolution of the particle number density n_s, mean velocity $\mathbf{V}_s(\mathbf{x}, t)$ and mean momentum $\mathbf{P}_s(\mathbf{x}, t)$ define by,

$$n_s(\mathbf{x}, t) = \int d^3p \; f_s(\mathbf{x}, \mathbf{p}, t) \tag{A.36}$$

$$n_s(\mathbf{x}, t)\mathbf{V}_s(\mathbf{x}, t) = \int d^3p \; \mathbf{v} f_s(\mathbf{x}, \mathbf{p}, t) \tag{A.37}$$

$$n_s(\mathbf{x}, t)\mathbf{P}_s(\mathbf{x}, t) = \int d^3p \; \mathbf{p} f_s(\mathbf{x}, \mathbf{p}, t) \tag{A.38}$$

where $\mathbf{v} = (\mathbf{p}/m_s)\left(1 + \mathbf{p}^2/m_s^2c^2\right)^{-1/2}$

The continuity equation is obtained by integrating Eq. (A.31) over the momentum space $\int d^3p \cdots$, i.e.,

$$\frac{\partial}{\partial t} n_s + \nabla \cdot (n_s \mathbf{V}_s) = 0 \tag{A.39}$$

and the force balance equation from $\int d^3p \; \mathbf{p} \cdots$,

$$\left(\frac{\partial}{\partial t} + \mathbf{V}_s \cdot \nabla\right) \mathbf{P}_s = q_s \left(\mathbf{E} + \frac{\mathbf{v}}{c} \times \mathbf{B}\right) - \frac{1}{n_s} \nabla \cdot \mathcal{P}_s \tag{A.40}$$

where $\mathcal{P}_s$ is the pressure tensor.

$$\mathcal{P}_s = \int d^3p \ (\mathbf{p} - \mathbf{P}_s)(\mathbf{v} - \mathbf{V}_s) f_s(\mathbf{x}, \mathbf{p}, t) \tag{A.41}$$

No manipulation of the moment equations can fix their most serious defect: lack of closure [91]. Since each moment is coupled to the next higher one (evolution of density depends on velocity, evolution of velocity depends on pressure and so on), any finite set of exact equations will have more unknowns than equations. Therefore some additional information (a small parameter, a limiting assumption or some additional physics input) is always needed to determine the evolution of the system and close the fluid system of equations. However, as stated above, it is important to note that a cold fluid description of a plasma is equivalent to a kinetic description based on the Vlasov-Maxwell equations provided the distribution function $f_s(\mathbf{x}, \mathbf{p}, t)$ is on the form

$$f_s(\mathbf{x}, \mathbf{p}, t) = n_s(\mathbf{x}, t)\delta\left[\mathbf{p} - \mathbf{P}_s(\mathbf{x}, t)\right] \tag{A.42}$$

Integration of Eq. (A.41) readily gives $\mathcal{P}_s = 0$, and Eq. (A.38)

$$\int d^3p \ \mathbf{v} f_s(\mathbf{x}, \mathbf{p}, t) = n_s(\mathbf{x}, t)\mathbf{V}_s(\mathbf{x}, t) = n_s(\mathbf{x}, t)\mathbf{P}_s(\mathbf{x}, t)/\gamma_s(\mathbf{x}, t)m_s \tag{A.43}$$

Here for a cold fluid element, the flow velocity $\mathbf{V}_s$, momentum $\mathbf{P}_s$ and relativistic mass factor $\gamma_s(\mathbf{x}, t)$ are related by $\mathbf{P}_s = \gamma_s(\mathbf{x}, t)m_s\mathbf{V}_s$, where

$$\gamma_s(\mathbf{x}, t) = \sqrt{1 + \mathbf{P}_s^2(\mathbf{x}, t)/m_s c^2} \tag{A.44}$$

Appendix B

Nonlinear three-dimensional averaged fluid model

In this Appendix a multiple-scale analysis is performed on the Maxwell-fluid system of equations. The plasma is underdense, i.e., $\omega_p/\omega_0 \ll 1$ where ω_p is the plasma frequency and ω_0 the laser frequency. Clearly the laser and plasma operate at very different temporal time and spacial scales, therefore performing a multiple-scale perturbation analysis will allow for a clear separation in the Maxwell-fluid equations between the "fast" equations related to laser evolution and "slow" equations associated with plasma effects. We start with the Maxwell and fluid equations transformed to the frame comoving with the laser pulse and normalized with respect to the vaccum laser wave number $k_0 = \omega_0/c$. This yields the transformed Poisson equation,

$$\left(\nabla_\perp^2 + \frac{\partial^2}{\partial\zeta^2}\right)\phi = \epsilon^2\left(\frac{n_e}{n_0} - 1\right) , \tag{B.1}$$

where $\zeta \equiv k_0\zeta$, $\tau \equiv \omega_0\tau$, $\epsilon = k_p/k_0$ and the normalized vector potential,

$$\left(\frac{\partial^2}{\partial c^2\tau^2} - 2\frac{\partial^2}{\partial c\tau\partial\zeta} - \nabla_\perp^2\right)\mathbf{a} = -\epsilon^2\frac{n_e\mathbf{u}}{n_0\gamma} - \left(\nabla_\perp + \frac{\partial}{\partial\zeta}\mathbf{e}_z\right)\left(\frac{\partial}{\partial c\tau} - \frac{\partial}{\partial\zeta}\right)\phi , \tag{B.2}$$

followed by the Coulomb gauge,

$$\nabla_\perp \cdot \mathbf{a}_\perp + \frac{\partial a_z}{\partial\zeta} = 0 , \tag{B.3}$$

equation of motion for a fluid electron,

$$\left(\frac{\partial}{\partial c\tau}-\frac{\partial}{\partial\zeta}\right)(\mathbf{u}-\mathbf{a})=\left(\nabla_\perp+\frac{\partial}{\partial\zeta}\mathbf{e}_z\right)(\phi-\gamma)\ , \tag{B.4}$$

and continuity equation,

$$\frac{\partial n_e}{\partial c\tau}+\frac{\partial}{\partial\zeta}(u_z-\gamma)\frac{n_e}{\gamma}+\nabla_\perp\cdot\left(\mathbf{u}_\perp\frac{n_e}{\gamma}\right)=0\ . \tag{B.5}$$

In a multiple-scale perturbation analysis the smallness parameter is obviously ϵ. The laser-plasma parameters (electron density n_e, potential ϕ, vector potential $\mathbf{a}$, etc ...) are expressed as follow,

$$Q(\zeta,\tau)=Q_0(\zeta_0,\zeta_1,\cdots,\zeta_n,\tau_2)+\epsilon Q_1(\zeta_0,\zeta_1,\cdots,\zeta_n,\tau_2)+\cdots+\epsilon^n Q_n(\zeta_0,\zeta_1,\cdots,\zeta_n,\tau_2)\ , \tag{B.6}$$

where $\zeta_n=\epsilon^n(k_0\zeta)$. Operationally we treat $\zeta_0,\zeta_1,\ \cdots$ as *independent variables*, and expand the time derivatives in Eq. (B.6) according to,

$$\frac{\partial}{\partial\zeta}\equiv\frac{\partial}{\partial\zeta_0}+\epsilon\frac{\partial}{\partial\zeta_1}+\epsilon^2\frac{\partial}{\partial\zeta_2}+O(\epsilon^3)\ . \tag{B.7}$$

It follows from Eq. (B.7) that

$$\frac{\partial^2}{\partial\zeta^2}\equiv\frac{\partial^2}{\partial\zeta_0^2}+2\epsilon\frac{\partial}{\partial\zeta_0\partial\zeta_1}+\epsilon^2\left(\frac{\partial^2}{\partial\zeta_1^2}+2\frac{\partial}{\partial\zeta_0\partial\zeta_2}\right)+O(\epsilon^3)\ . \tag{B.8}$$

The additional assumption is that transverse evolution is typically slow, i.e., a space (time) scale on the order of the plasma wavelength (frequency) $\nabla_\perp\equiv\epsilon\nabla_\perp$ and $\partial/\partial\tau\equiv\epsilon^2\partial/\partial\tau_2$ which is equivalent to the so-called quasi-static approximation [9, 43] (slow time evolution is the frame comoving with the drive laser pulse). Substituting Eqs. (B.6)-B.8 into (B.1), and equating to zero the coefficients of successive powers

of ϵ, we find for Poisson's equation

$$\begin{aligned}&\frac{\partial^2\phi_0}{\partial\zeta_0^2}+\epsilon\left(2\frac{\partial\phi_0}{\partial\zeta_0\partial\zeta_1}+\frac{\partial^2\phi_1}{\partial\zeta_0^2}\right)+\\&\epsilon^2\left(\frac{\partial^2\phi_0}{\partial\zeta_1^2}+2\frac{\partial\phi_1}{\partial\zeta_0\partial\zeta_1}+\frac{\partial^2\phi_2}{\partial\zeta_0^2}+2\frac{\partial\phi_0}{\partial\zeta_0\partial\zeta_2}+\nabla_\perp^2\phi_0\right)\\&=\epsilon^2\left(\frac{n_e}{n_0}-1\right)\ .\end{aligned}\tag{B.9}$$

Order ϵ^0 gives $\partial^2\phi_0/\partial\zeta_0^2=0$ which gives $\phi_0\equiv\phi_0\left(\zeta_1,\cdots,\tau_2\right)$, i.e., ϕ_0 is a slowly varying quantity. The same conclusion can be derived from the first order equation which is $\partial^2\phi_1/\partial\zeta_0^2=0$. Lastly, The second order equation yields

$$\left(\nabla_\perp^2+\frac{\partial^2}{\partial\zeta_1^2}\right)\phi_0+\frac{\partial^2\phi_2}{\partial\zeta_0^2}=\left(\frac{n_e}{n_0}-1\right)\ .\tag{B.10}$$

Averaging over the fast time scale ζ_0

$$\left\langle\left(\nabla_\perp^2+\frac{\partial^2}{\partial\zeta_1^2}\right)\phi_0+\frac{\partial^2\phi_2}{\partial\zeta_0^2}\right\rangle_{\zeta_0}=\left\langle\frac{n_e}{n_0}-1\right\rangle_{\zeta_0}\ ,\tag{B.11}$$

gives

$$\boxed{\left(\nabla_\perp^2+\frac{\partial^2}{\partial\zeta_1^2}\right)\phi_s=\left\langle\frac{n_e}{n_0}\right\rangle_{\zeta_0}-1}\tag{B.12}$$

where the subscript "0" has been replaced by "s" for "slow". The wave equation [Eq. (B.2)] becomes

$$\begin{aligned}&\left[\epsilon^4\frac{\partial^2}{\partial c^2\tau_2^2}-\epsilon^2\left(2\frac{\partial^2}{\partial c\tau_2\partial\zeta_0}+\nabla_\perp^2\right)-2\epsilon^3\frac{\partial^2}{\partial c\tau_2\partial\zeta_1}\right]\mathbf{a}=-\epsilon^2\frac{n_e\mathbf{u}}{n_0\gamma}\\&-\left[\epsilon\nabla_\perp+\left(\frac{\partial}{\partial\zeta_0}+\epsilon\frac{\partial}{\partial\zeta_1}\right)\mathbf{e}_z\right]\left[\epsilon^2\frac{\partial}{\partial c\tau_2}-\frac{\partial}{\partial\zeta_0}-\epsilon\frac{\partial}{\partial\zeta_1}\right]\left(\phi_s+\epsilon^2\phi_{2f}\right)\ ,\end{aligned}\tag{B.13}$$

which gives

$$-\left(\frac{2}{c}\frac{\partial^2}{\partial\tau_2\partial\zeta_0}+\nabla_\perp^2\right)\mathbf{a}=-\frac{n_e\mathbf{u}}{n_0\gamma}+\left(\nabla_\perp+\frac{\partial}{\partial\zeta_1}\mathbf{e}_z\right)\frac{\partial\phi_s}{\partial\zeta_1}+\frac{\partial^2\phi_{2f}}{\partial\zeta_0^2}\mathbf{e}_z+O(\epsilon)\ .\tag{B.14}$$

Following a procedure similar to Section A.2, we express the vector potential as a slow quantity $\mathbf{a}_s(\zeta_1, \cdots, \tau_2)$ and a fast quantity $\mathbf{a}_f(\zeta_0, \zeta_1, \cdots, \tau_2)$ such that

$$\langle \mathbf{a} \rangle_{\zeta_0} = \langle \mathbf{a}_s + \mathbf{a}_f \rangle_{\zeta_0} = \mathbf{a}_s \ , \tag{B.15}$$

and,

$$\mathbf{a}_f = \mathbf{a} - \langle \mathbf{a} \rangle_{\zeta_0} \ , \tag{B.16}$$

where $\mathbf{a}_s$ correspond to the averaged value of $\mathbf{a}$ over the fast oscillation $k_0\zeta$. Averaging Eq. (B.14) gives

$$\boxed{-\nabla_\perp^2 \mathbf{a}_s = -\left\langle \frac{n_e \mathbf{u}}{n_0 \gamma} \right\rangle_{\zeta_0} + \left(\nabla_\perp + \frac{\partial}{\partial \zeta_1} \mathbf{e}_z \right) \frac{\partial \phi_s}{\partial \zeta_1} + O(\epsilon)} \tag{B.17}$$

and substracting Eq. (B.17) from (B.14) provides an equation for $\mathbf{a}_f$, i.e.,

$$\boxed{-\left(\frac{2}{c} \frac{\partial^2}{\partial \tau_2 \partial \zeta_0} + \nabla_\perp^2 \right) \mathbf{a}_{f\perp} = -\frac{n_e \mathbf{u}_\perp}{n_0 \gamma} + \left\langle \frac{n_e \mathbf{u}_\perp}{n_0 \gamma} \right\rangle_{\zeta_0} + O(\epsilon)} \tag{B.18}$$

The RHS of Eq. (B.18) will be rearranged later. In order to do so one must find the magnitude of the slow and fast component of $\mathbf{u}$, n_e and γ. Note that in (B.18) only $\mathbf{a}_{f\perp}$ has been kept. It can be shown from the Coulomb gauge that a_{zf} is typically a first order quantity. Applying a multiple-scale expansion to Eq (B.3) we get

$$\epsilon \nabla_\perp \cdot \mathbf{a}_\perp + \left(\frac{\partial}{\partial \zeta_0} + \epsilon \frac{\partial}{\partial \zeta_1} \right) a_z \mathbf{e}_z = \mathbf{0} \ . \tag{B.19}$$

From $\partial a_z / \partial \zeta_0 = 0$ we may conclude that $a_{zs} \equiv O(1)$ and $a_{zf} \equiv O(\epsilon)$ giving to order $O(\epsilon)$

$$\boxed{\nabla \cdot \mathbf{a}_s = \mathbf{0}} \tag{B.20}$$

and

$$\boxed{\nabla_\perp \cdot \mathbf{a}_{f\perp} + \frac{\partial a_{z1f}}{\partial \zeta_0} \mathbf{e}_z = \mathbf{0}} \tag{B.21}$$

after replacing $\mathbf{a}$ in Eq (B.19) by $\mathbf{a}_s + \mathbf{a}_f$ and averaging. Next we derive the fast and slow component of the normalized momentum $\mathbf{u}$. Starting from the equation of

motion (B.4),

$$\left(\frac{\partial}{\partial c\tau} - \frac{\partial}{\partial \zeta}\right)(\mathbf{u} - \mathbf{a}) = \left(\nabla_\perp + \frac{\partial}{\partial \zeta}\mathbf{e}_z\right)(\phi - \gamma) \ , \tag{B.22}$$

we get,

$$\left(\epsilon^2\frac{\partial}{\partial c\tau} - \frac{\partial}{\partial \zeta_0} - \epsilon\frac{\partial}{\partial \zeta_1}\right)(\mathbf{u} - \mathbf{a}) = \left[\epsilon\nabla_\perp + \left(\frac{\partial}{\partial \zeta_0} + \epsilon\frac{\partial}{\partial \zeta_1}\right)\mathbf{e}_z\right](\phi - \gamma) \ . \tag{B.23}$$

Making use again of the expansions $\mathbf{u} = \mathbf{u}_s + \mathbf{u}_f$ and $\mathbf{a} = \mathbf{a}_s + \mathbf{a}_f$, Eq. (B.23) yields to order $O(1)$,

$$\frac{\partial}{\partial \zeta_0}(\mathbf{u}_{f\perp} - \mathbf{a}_{f\perp}) = \mathbf{0} \ , \tag{B.24}$$

giving

$$\boxed{\mathbf{u}_{f\perp} = \mathbf{a}_{f\perp}} \tag{B.25}$$

and lastly

$$\frac{\partial}{\partial \zeta_0}(u_{zf} - a_{zf} - \gamma_f) = 0 \ . \tag{B.26}$$

i.e., using $a_{zf} \equiv O(\epsilon)$ we deduce the relationship $(u_{zf} - \gamma_f) \equiv O(\epsilon)$. The first order expansion of Eq. (B.23) provides, after averaging, an equation for $\mathbf{u}_s$ which is,

$$\boxed{-\frac{\partial}{\partial \zeta_1}(\mathbf{u}_s - \mathbf{a}_s) = \left(\nabla_\perp + \frac{\partial}{\partial \zeta_1}\mathbf{e}_z\right)(\phi_s - \gamma_s)} \tag{B.27}$$

An expression for γ_s may also be derived from the longitudinal projection of Eq. (B.22) neglecting the $\partial/\partial\tau$ terms [quasi-static approximation valid to order $0(\epsilon^2)$],

$$-\frac{\partial}{\partial \zeta}(u_z - a_z) = \frac{\partial}{\partial \zeta}(\phi - \gamma) \ . \tag{B.28}$$

Further integrating over ζ yields

$$-(u_z - a_z) = \phi - \gamma + 1 \ , \tag{B.29}$$

and

$$\gamma = \frac{1 + u_\perp^2 + (1 + \Psi)^2}{2(1 + \Psi)} \tag{B.30}$$

where $\Psi = \phi - a_z$. Expanding into fast and slow component gives to order $O(1)$ [recall that $a_z = a_{zs} + O(\epsilon)$ and $\phi = \phi_s + O(\epsilon^2)$],

$$\gamma_s + \gamma_f = \frac{1 + (\mathbf{a}_{f\perp} + \mathbf{u}_{s\perp})^2 + (1 + \Psi_s)^2}{2\,(1 + \Psi_s)} , \tag{B.31}$$

$$= \frac{1 + a_{f\perp}^2 + u_{s\perp}^2 + 2\,\mathbf{a}_{f\perp} \cdot \mathbf{u}_{s\perp} + (1 + \Psi_s)^2}{2\,(1 + \Psi_s)} . \tag{B.32}$$

Averaging over ζ_0 yield

$$\boxed{\gamma_s = \frac{1 + \left\langle a_{f\perp}^2 \right\rangle + u_{s\perp}^2 + (1 + \Psi_s)^2}{2\,(1 + \Psi_s)}} \tag{B.33}$$

and

$$\boxed{\gamma_f = \gamma - \gamma_s = \frac{a_{f\perp}^2 - \left\langle a_{f\perp}^2 \right\rangle_{\zeta_0} + 2\mathbf{a}_{f\perp} \cdot \mathbf{u}_{s\perp}}{2\,(1 + \Psi_s)}} \tag{B.34}$$

which is typically a small quantity. Lastly, Eq. (B.5) is the remaining of the Maxwell-fluid equation's system to be perturbed

$$\epsilon^2 \frac{\partial n_e}{\partial c\tau} + \left(\frac{\partial}{\partial \zeta_0} + \epsilon \frac{\partial}{\partial \zeta_1} \right) (u_z - \gamma) \frac{n_e}{\gamma} + \epsilon \nabla_\perp \cdot \left(\mathbf{u}_\perp \frac{n_e}{\gamma} \right) = 0 , \tag{B.35}$$

giving to order $O(1)$,

$$\frac{\partial}{\partial \zeta_0} (u_z - \gamma) \frac{n_e}{\gamma} = 0 . \tag{B.36}$$

We know from Eq. (B.26) that $(u_{zf} - \gamma_f) \equiv O(\epsilon)$ providing,

$$(u_{zs} - \gamma_s) \frac{\partial}{\partial \zeta_0} \left(\frac{n_e}{\gamma} \right) = 0 , \tag{B.37}$$

and,

$$\frac{n_e}{\gamma} = \left. \frac{n_e}{\gamma} \right|_s + O(\epsilon) . \tag{B.38}$$

After expanding into slow and fast component, to first order Eq (B.35) becomes

$$\frac{\partial}{\partial\zeta_1}\left(u_{zs}-\gamma_s\right)\frac{n_s}{\gamma_s}+\frac{\partial}{\partial\zeta_0}\left[\left(u_{zf}-\gamma_f\right)\frac{n_s}{\gamma_s}+\left(u_{zs}-\gamma_s\right)\frac{n_f}{\gamma_s}+\cdots\right]+\nabla_\perp\cdot\left(\mathbf{u}_{s\perp}\frac{n_s}{\gamma_s}\right)=0\,, \tag{B.39}$$

where the relationship $n_s/\gamma_s = n_e/\gamma|_s$ has been used, which is straightforward to show. Taking the average of (B.39) over the fast scale ζ_0 provides a continuity equation for the components in the plasma varying on the order of the slow scale ζ_1 .

$$\boxed{\nabla_\perp\cdot\left(\mathbf{u}_{s\perp}\frac{n_s}{\gamma_s}\right)+\frac{\partial}{\partial\zeta_1}\left(u_{zs}-\gamma_s\right)\frac{n_s}{\gamma_s}=0} \tag{B.40}$$

We can now simplify the source terms in the PDE describing the slow and fast component of the normalized vector potential [Eq. (B.17)-(B.18)], i.e.,

$$\left\langle\frac{n_e}{n_0}\frac{\mathbf{u}}{\gamma}\right\rangle_{\zeta_0}=\frac{n_s}{n_0\gamma_s}\left\langle\mathbf{a}_{f\perp}+\mathbf{u}_s\right\rangle_{\zeta_0}=\frac{n_s}{n_0}\frac{\mathbf{u}_s}{\gamma_s} \tag{B.41}$$

and,

$$\frac{n_e}{n_0}\frac{\mathbf{u}}{\gamma}-\left\langle\frac{n_e}{n_0}\frac{\mathbf{u}}{\gamma}\right\rangle_{\zeta_0}=\frac{n_s}{n_0}\frac{\mathbf{a}_{f\perp}}{\gamma_s} \tag{B.42}$$

giving

$$\boxed{-\nabla_\perp^2\mathbf{a}_s=-\frac{n_s}{n_0}\frac{\mathbf{u}_s}{\gamma_s}+\left(\nabla_\perp+\frac{\partial}{\partial\zeta_1}\mathbf{e}_z\right)\frac{\partial\phi_s}{\partial\zeta_1}} \tag{B.43}$$

and finally

$$\boxed{\left(\frac{2}{c}\frac{\partial^2}{\partial\tau_2\partial\zeta_0}+\nabla_\perp^2\right)\mathbf{a}_{f\perp}=\frac{n_s}{n_0}\frac{\mathbf{a}_{f\perp}}{\gamma_s}} \tag{B.44}$$

At this stage we may return to the physical variables ζ and τ, and substitute $\zeta_0=\zeta$, $\zeta_1=\epsilon\zeta$, etc ... in the perturbation solutions. In summary the [closed] averaged Maxwell-fluid system of equations allow for a clear separation between the equations describing the slow time scale plasma quantities such as the density n_s, normalized vector potential $\mathbf{a}_s$ fluid velocity $\mathbf{u}_s$ and the fast laser time scale $\mathbf{a}_f$. For convenience, the set of equations is summarized below. The perturbed equations yields an equation

for the [fast] laser evolution in the plasma,

$$\boxed{\left(\frac{2}{c}\frac{\partial^2}{\partial\tau\partial\zeta}+\nabla_\perp^2\right)\mathbf{a}_{f\perp}=k_p^2\frac{n_s}{n_0}\frac{\mathbf{a}_{f\perp}}{\gamma_s}} \tag{B.45}$$

along with the fast Coulomb gauge,

$$\boxed{\nabla\cdot\mathbf{a}_f=\mathbf{0}} \tag{B.46}$$

an equation for the slow normalized vector potential associated with the plasma response to the perturbation created by the fast laser pulse,

$$\boxed{\nabla_\perp^2\mathbf{a}_s=k_p^2\frac{n_s}{n_0}\frac{\mathbf{u}_s}{\gamma_s}-\nabla\frac{\partial\phi_s}{\partial\zeta}} \tag{B.47}$$

together with the slow Coulomb gauge,

$$\boxed{\nabla\cdot\mathbf{a}_s=\mathbf{0}} \tag{B.48}$$

the slow potential

$$\boxed{\nabla^2\phi_s=k_p^2\left(\frac{n_s}{n_0}-1\right)} \tag{B.49}$$

the slow continuity equation

$$\boxed{\nabla_\perp\cdot\left(\mathbf{u}_{s\perp}\frac{n_s}{\gamma_s}\right)+\frac{\partial}{\partial\zeta}\left(u_{zs}-\gamma_s\right)\frac{n_s}{\gamma_s}=0} \tag{B.50}$$

and lastly a slow fluid momentum equation for the plasma electron

$$\boxed{-\frac{\partial}{\partial\zeta}\left(\mathbf{u}_s-\mathbf{a}_s\right)=\nabla\left(\phi_s-\gamma_s\right)} \tag{B.51}$$

An envelope equation for the laser pulse may be derived from Eq. (B.45). For a linearly polarized laser pulse, assuming $\mathbf{a}_{f\perp}=\hat{a}_\perp\exp(ik_0\zeta)\ \mathbf{e}_\perp$+c.c, where "c.c" stands for

complex conjugate, we find,

$$\boxed{\left[2\frac{\partial}{\partial c\tau}\left(ik_0+\frac{\partial}{\partial\zeta}\right)+\nabla_\perp^2\right]\hat{a}_\perp=k_p^2\frac{n_s}{n_0}\frac{\hat{a}_\perp}{\gamma_s}} \tag{B.52}$$

The paraxial approximation consist of neglecting the ζ derivative in comparison with the lowest order wave number k_0. Finite laser pulse length effects are represented by the operator $2\partial^2/\partial\tau\partial\zeta$, which is the leading-order correction to the paraxial wave equation. The latter term is needed to describe group velocity dispersion, direct forward scattering and self-modulational type instabilities. Note that the quasi-static approximation preclude the correct description of Raman backscatter (RBS) and sidescatter (SRS) because RBS and SRS waves are "fast" in the frame comoving with the drive laser pulse and consequently $\partial^2/\partial\tau^2$ must be retained in the wave operator. The reduced set of equations (B.52), (B.46)-(B.51) have been used extensively in the literature [9, 42, 92–94]. They are averaged over the laser fast scale $k_0\zeta$ offering a computationally time efficient fluid-like description of laser-plasma interactions without having to resolve the fast laser oscillations on a grid.

Note that a careful perturbation analysis where $\hat{a}_\perp$ is the small parameter [$\hat{a}_\perp \ll 1$ is assumed] shows that the wakefield ϕ_s is typically on the order $O(\hat{a}_\perp^2/4)$, the slow vector potential $a_s \sim O(\hat{a}_\perp^4/16)$ where the latter corresponds to slow magnetic field generation and the evolution equation for the fast laser pulse may be reduced to

$$\boxed{\left[2\frac{\partial}{\partial c\tau}\left(ik_0+\frac{\partial}{\partial\zeta}\right)+\nabla_\perp^2\right]\hat{a}_\perp=k_p^2\left(1+\frac{\delta n_s}{n_0}-\frac{\hat{a}_\perp^2}{4}\right)\hat{a}_\perp+O(\hat{a}_\perp^4/16)} \tag{B.53}$$

where $\delta n_s/n_0$ corresponds to the second order density perturbation and $1/\gamma_s = 1-\hat{a}_\perp^2/4+O(\hat{a}_\perp^4/16)$. Eq. (B.53) is found to be equivalent to Eq. (2.56).

The derivation of the averaged laser-plasma equations has been carried out in the frame ($\zeta = z-ct,\ \tau = t$) which corresponds to a "snapshot" at each time step. It is possible to derive the same set of equation in a frame ($\zeta = z-ct,\ z' = z$) corresponding to the "lab" frame [95]. The quasi static approximation in this frame is characterized by the assumption $\partial/\partial z' \equiv \epsilon^2\partial/\partial z'$, i.e. $k_pZ_R \gg 1$ where Z_R is the laser Rayleigh length. The equivalent laser-plasma equations in the ($\zeta,\ z'$) frame are

obtained simply by substituting $c\tau$ by z'. For instance, in "detectors" coordinates Eq. (B.53) becomes

$$\boxed{\left[2\frac{\partial}{\partial z'}\left(ik_0+\frac{\partial}{\partial\zeta}\right)+\nabla_\perp^2\right]\hat{a}_\perp = k_p^2\left(1+\frac{\delta n_s}{n_0}-\frac{\hat{a}_\perp^2}{4}\right)\hat{a}_\perp + O(\hat{a}_\perp^4/16)} \qquad \text{(B.54)}$$

Equation (B.53) or (B.54) may be solved analytically through the Source Dependent Expansion method (SDE) [9, 10] to calculate laser propagation and evolution inside the plasma, i.e., relativistic self-focusing, nonlinear coupling of the laser envelope to a plasma wave, instabilities (forward Raman and self-modulational), betatron oscillations, etc.

Appendix C

Wakefield calculation for a half-sine laser pulse

Contents

In this Appendix we will derive solutions of Eq. (2.44) within the quasi-static approximation,

$$\phi(\mathbf{r},\zeta) = k_p \int_0^\zeta d\zeta' \sin k_p(\zeta-\zeta')\ a^2(\mathbf{r},\zeta')/2\ , \tag{C.1}$$

for the special case of Gaussian laser pulse with a half-sine longitudinal profile, solution of the paraxial wave equation (3.10)

$$a_x(r,\zeta) = \hat{a}(r,\zeta)\cos(k_0\zeta+\psi_0)\ , \tag{C.2}$$

with

$$\hat{a}(r,\zeta) = a_0(r_0/r_s)\exp\left(-r^2/r_s^2\right)\sin\left(\pi\zeta/L\right)\ , \tag{C.3}$$

for $-L<\zeta<0$ and zero otherwise, where $\zeta\simeq z-ct$ (underdense plasma), $k_0=\omega_0/(\beta_\phi c)$ is the wavenumber, ω_0 is the frequency in vacuum, $\psi_0=\alpha\, r^2/r_s^2+\alpha-\tan^{-1}\alpha$ is the phase, $r_s(z)=r_0\sqrt{1+\alpha(z)}$ is the spot size, r_0 is the spot size at waist (here chosen to be at $z=0$), $\alpha(z)=z^2/Z_R^2$, $Z_R=k_0\eta\, r_0^2/2$ is the Rayleigh length, L_0 is the pulse length and a_0 is the maximum amplitude of the normalized vector potential. Inserting (C.2) into (C.1) gives

$$\phi = k_p\int_0^\zeta d\zeta' \sin k_p(\zeta-\zeta')\ \hat{a}^2/4\left[1+\cos\left(2k_0\zeta'+2\psi_0\right)\right]\ . \tag{C.4}$$

The second part of the integral is small providing $\epsilon=k_p/k_0\ll 1$, this can be shown as follow: after repeated integration by parts, it is possible to express the resultant fast component of the wakefield ϕ_f in the form of a power series in ϵ. To first approximation we have

$$\phi_f \simeq -\left(\frac{k_p}{2k_0}\right)^2\frac{\hat{a}(\mathbf{r},\zeta)}{4}\cos(2k_0\zeta+2\psi_0)\ , \tag{C.5}$$

giving $\phi_f\sim O(\epsilon^2)\ll 1$ for an underdense plasma. The slow component of the wakefield

$$\phi_s = k_p\int_0^\zeta d\zeta' \sin k_p(\zeta-\zeta')\ \hat{a}^2/4\ , \tag{C.6}$$

will be studied next (i) for the resonant case $L=\lambda_p$ and (ii) for an arbitrary laser

length. The only term ζ-dependent of (C.3) is $\sin(\pi\zeta/L)$, the rest can be treated as a constant. For clarity we recast (C.3) in the form

$$\hat{a}(\mathbf{r},\zeta) = \tilde{a}(\mathbf{r})\sin(\pi\zeta/L) \ , \tag{C.7}$$

with

$$\tilde{a}(r,\zeta) = a_0(r_0/r_s)\exp\left(-r^2/r_s^2\right) \ . \tag{C.8}$$

C.1 Standard regime

In the standard regime we have $k_pL = 2\pi$ and (C.6) becomes

$$\phi_s = \tilde{a}^2/8 \int_0^\zeta d\zeta' \sin(\zeta-\zeta')\,(1-\cos\zeta') \ . \tag{C.9}$$

where the normalization $\zeta \to k_p\zeta$ has been introduced. Using the expression

$$\cos\zeta' \sin(\zeta-\zeta') = 1/2\left[\sin\zeta + \sin(\zeta-2\zeta')\right] \ , \tag{C.10}$$

we have inside the laser pulse ($-2\pi \leqslant \zeta \leqslant 0$)

$$\begin{aligned} \int_0^\zeta \sin(\zeta-\zeta')\ d\zeta' &= -\int_\zeta^0 \sin u\, du \ , \\ &= 1-\cos\zeta \ , \end{aligned} \tag{C.11}$$

$$\int_0^\zeta \frac{\sin\zeta}{2}\, d\zeta' = \frac{\zeta}{2}\sin\zeta \ , \tag{C.12}$$

and,

$$\int_0^\zeta \frac{\sin(\zeta-2\zeta')}{2}\, d\zeta' = \frac{1}{4}\int_{-\zeta}^{\zeta} \sin u\, du = 0 \ , \tag{C.13}$$

which gives

$$\boxed{\phi_s = \frac{\tilde{a}^2}{8}\left(1-\cos\zeta-\frac{\zeta}{2}\sin\zeta\right)} \tag{C.14}$$

and behind the pulse ($\zeta < -2\pi$)

$$\phi_s = \frac{\tilde{a}^2}{8} \int_0^{-2\pi} d\zeta' \sin(\zeta - \zeta') \, (1 - \cos\zeta') \, , \tag{C.15}$$

becomes

$$\boxed{\phi_s = \frac{\tilde{a}^2}{8} \pi \sin\zeta} \tag{C.16}$$

Note that $\phi_s \sim O(1)$ and consequently $\phi_s \gg \phi_f$ for an underdense plasma ($\epsilon \ll 1$).

C.2 General case

Starting from

$$\phi_s = \frac{\tilde{a}^2}{8} \int_0^{\zeta} \left(1 - \cos\frac{2\pi}{L}\zeta'\right) \sin\left(\zeta - \zeta'\right) \, d\zeta' \, , \tag{C.17}$$

and using the expression

$$\cos\frac{2\pi}{L}\zeta' \sin\left(\zeta - \zeta'\right) = \frac{1}{2}\left\{\sin\left[\zeta + \left(\frac{2\pi}{L} - 1\right)\zeta'\right] + \sin\left[\zeta - \left(\frac{2\pi}{L} + 1\right)\zeta'\right]\right\} \, , \tag{C.18}$$

we get inside the laser pulse ($-k_p L \leqslant \zeta \leqslant 0$)

$$\begin{aligned} \int_0^{\zeta} \sin\left(\zeta - \zeta'\right) \, d\zeta' &= -\int_{\zeta}^{0} \sin u \, du \, , \\ &= 1 - \cos\zeta \, , \end{aligned} \tag{C.19}$$

together with,

$$\begin{aligned} \frac{1}{2}\int_0^{\zeta} \sin\left[\zeta + \left(\frac{2\pi}{L} - 1\right)\zeta'\right] \, d\zeta' &= \frac{1}{2}\left(\frac{2\pi}{L} - 1\right)^{-1} \int_{\zeta}^{2\pi\zeta/L} \sin u \, du \, , \\ &= \frac{1}{2}\left(\frac{2\pi}{L} - 1\right)^{-1} \left(\cos\zeta - \cos\frac{2\pi}{L}\zeta\right) \, , \end{aligned} \tag{C.20}$$

and

$$\begin{aligned}\frac{1}{2}\int_0^{\zeta}\sin\left[\zeta-\left(\frac{2\pi}{L}+1\right)\zeta'\right]\,d\zeta' &= \frac{1}{2}\left(\frac{2\pi}{L}+1\right)^{-1}\int_{-2\pi\zeta/L}^{\zeta}\sin u\,du\ ,\\ &= -\frac{1}{2}\left(\frac{2\pi}{L}+1\right)^{-1}\left(\cos\zeta-\cos\frac{2\pi}{L}\zeta\right)\ ,\end{aligned} \tag{C.21}$$

which gives

$$\phi_s=\frac{\tilde{a}^2}{8}\left\{1-\cos\zeta-\frac{1}{2}\left[\frac{\cos\zeta-\cos(2\pi\zeta/L)}{2\pi/L-1}-\frac{\cos\zeta-\cos(2\pi\zeta/L)}{2\pi/L+1}\right]\right\}\ , \tag{C.22}$$

and finally after further simplifications

$$\boxed{\phi_s=\frac{\tilde{a}^2}{8}\left[1+\frac{(2\pi/L)^2\cos\zeta-\cos(2\pi\zeta/L)}{1-(2\pi/L)^2}\right]} \tag{C.23}$$

Behind the laser pulse ($\zeta<-k_pL$) we have,

$$\phi_s=\frac{\tilde{a}^2}{8}\int_0^{-k_pL}\left(1-\cos\frac{2\pi}{L}\zeta'\right)\sin\left(\zeta-\zeta'\right)\,d\zeta'\ , \tag{C.24}$$

giving

$$\boxed{\phi_s=\frac{\tilde{a}^2}{4}\left[\left(\frac{2\pi}{L}\right)^2\frac{\sin\left(\zeta+L/2\right)\sin(L/2)}{1-(2\pi/L)^2}\right]} \tag{C.25}$$

Appendix D

One-dimensional equation of motion in the beat wave rest frame

The axial (1D) equation of motion for an electron moving in the combined fields of two *counter-propagating* circularly polarized laser pulses with square profile of the form

$$\mathbf{a}_{\perp i} = a_i \ (\cos\psi_i \ \mathbf{e}_x \pm \sin\psi_i \ \mathbf{e}_y)$$

and a wakefield of the form $\phi = \phi_0 \sin k_p\zeta$ can be expressed as follow

$$\mathbf{u}_\perp = \mathbf{a}_\perp \tag{D.1}$$

$$\frac{1}{c}\frac{du_z}{dt} = \frac{\partial\phi}{\partial z} - \frac{u_\perp}{\gamma}\frac{\partial a_\perp}{\partial z} \tag{D.2}$$

where $\psi_i = k_i(z - \beta_{\phi i}ct)$, $\zeta = z - \beta_{g0}ct$, $|\beta_{\phi i}| = \eta_i^{-1}$, $|\beta_{gi}| = \eta_i$ is the phase and group velocity of the laser pulse inside the plasma, $\eta_i = (1 - \omega_p^2/\omega_i^2)^{1/2}$ the index of refraction, $\mathbf{a}_\perp = \mathbf{a}_{\perp 0} + \mathbf{a}_{\perp 1}$ and the wakefield from the injection pulse $\mathbf{a}_{\perp 1}$ has been neglected, i.e., only the wake of the drive pulse is retained. Using the expression for $\mathbf{a}_\perp$ and ϕ, we get

$$\frac{1}{c}\frac{du_z}{dt} = \phi_0 k_p \cos k_p\zeta + \Delta k \frac{a_0 a_1}{\gamma}\sin\psi_b \tag{D.3}$$

along with

$$\gamma = \sqrt{1 + a_0^2 + a_1^2 + 2a_0a_1\cos\psi_b + u_z^2} \tag{D.4}$$

where $\psi_b = \psi_0 - \psi_1 = \Delta k(z - \beta_b ct)$, $c\beta_b = \Delta\omega/\Delta k$ is the beat wave phase velocity. Using $d\psi_b/dt = \Delta kz - \Delta\omega$ and expressing

$$u_z = \frac{\gamma}{c}\dot{z} = \frac{\gamma}{c\Delta k}\left(\dot{\psi}_b + \Delta\omega\right) \tag{D.5}$$

along with

$$\gamma^2 = \frac{1 + a_0^2 + a_1^2 + 2a_0a_1\cos\psi_b}{1 - c^{-2}(\Delta k)^{-2}\left(\dot{\psi}_b + \Delta\omega\right)^2} \tag{D.6}$$

then Eq. (D.3) can be rewritten in the equivalent form

$$\ddot{\psi}_b + \frac{\dot{\gamma}}{\gamma}\left(\dot{\psi}_b + \Delta\omega\right) = \phi_0 k_p \frac{\Delta kc^2}{\gamma}\cos\frac{k_p}{\Delta k}\left[\psi_b + (\Delta\omega - \Delta k\beta_\phi c)\,t\right] + \frac{c^2(\Delta k)^2}{\gamma^2}a_0a_1\sin\psi_b \tag{D.7}$$

where $\beta_\phi = \beta_{g0}$ is the phase velocity of the plasma wave. The expression for γ in Eq. (D.6) is used to eliminate $\dot{\gamma}$ in favor of $(\psi_b, \dot{\psi}_b, \ddot{\psi}_b)$. After some straightforward algebra that makes twofold use of Eq. (D.6), we find

$$\frac{\dot{\gamma}}{\gamma} = \left[\frac{1}{c^2\left(\Delta k\right)^2}\left(\dot{\psi}_b + \Delta\omega\right)\ddot{\psi}_b - \frac{a_0a_1}{\gamma^2}\dot{\psi}_b\sin\psi_b\right]\left[1 - \frac{1}{c^2\left(\Delta k\right)^2}\left(\dot{\psi}_b + \Delta\omega\right)\right]^{-1} \tag{D.8}$$

Making use of Eq. (D.8) to eliminate $(\dot{\gamma}/\gamma)(\dot{\psi}_b + \Delta\omega)$ in Eq. (D.7) gives

$$\begin{aligned}\ddot{\psi}_b \;=\; & \frac{c^2(\Delta k)^2}{\gamma^2}a_0a_1\sin\psi_b\;\left[1 - \frac{\Delta\omega}{c^2\left(\Delta k\right)^2}\left(\dot{\psi}_b + \Delta\omega\right)\right] \\ & + \phi_0 k_p\frac{\Delta kc^2}{\gamma}\left[1 - \frac{1}{c^2\left(\Delta k\right)^2}\left(\dot{\psi}_b + \Delta\omega\right)^2\right]\cos\frac{k_p}{\Delta k}\left[\psi_b + c\Delta k(\beta_b - \beta_\phi)t\right]\end{aligned} \tag{D.9}$$

where the expression $\Delta\omega - c\Delta k\beta_\phi = c\Delta k(\beta_b - \beta_\phi)$ has been used. Introducing the dimensionless parameter defined by

$$\epsilon_T = \frac{a_0a_1}{1 + a_0^2 + a_1^2} \tag{D.10}$$

the expression for γ in Eq. (D.6) readily reduce to

$$\frac{1}{\gamma^2} = \left[1 - \frac{1}{c^2\left(\Delta k\right)^2}\left(\dot{\psi}_b + \Delta\omega\right)^2\right](1 + 2\epsilon_T\cos\psi_b)^{-1}\left(1 + a_0^2 + a_1^2\right)^{-1} \tag{D.11}$$

The (small) dimensionless parameter ϵ_T defined in Eq. (D.10) is clearly a measure of the strength of the combined transverse electromagnetic fields of the two counter-propagating laser pulses. It is also useful to introduce the dimensionless parameter ϵ_L defined by,

$$\epsilon_L = \frac{\phi_0}{\left(1 + a_0^2 + a_1^2\right)^{1/2}} \frac{k_p}{\Delta k} \tag{D.12}$$

Next inserting Eq. (D.11) into Eq. (D.9), making use of Eq. (D.10)-(D.12) and furthermore normalizing Eq. (D.9) with respect to the bounce frequency of an electron deeply trapped in the slow beat wave $\tau \rightarrow \hat{\omega}_T t$, which is defined as $\hat{\omega}_T = c\Delta k(1-\beta_b^2)\epsilon_T^{1/2}$ gives

$$\boxed{\frac{d^2\psi_b}{d\tau^2} - \omega_T^2\left(\psi_b, \frac{d\psi_b}{d\tau}\right)\sin\psi_b = \delta_L\omega_L^2\left(\psi_b, \frac{d\psi_b}{d\tau}\right)\cos\frac{k_p}{\Delta k}\left[\psi_b + \frac{\left(\beta_b - \beta_\phi\right)\tau}{\left(1-\beta_b^2\right)\sqrt{\epsilon_T}}\right]} \tag{D.13}$$

where,

$$\begin{aligned}
\omega_T^2 &= \left(1 + 2\epsilon_T\cos\psi_b\right)^{-1}\left[1 - \left(1-\beta_b^2\right)\epsilon_T\left(\frac{d\psi_b}{d\tau}\right)^2 - 2\beta_b\epsilon_T^{1/2}\frac{d\psi_b}{d\tau}\right]\left[1 - \beta_b\epsilon_T^{1/2}\frac{d\psi_b}{d\tau}\right] \\
\omega_L^2 &= \left(1 + \epsilon_T\cos\psi_b\right)^{-1/2}\left[1 - \left(1-\beta_b^2\right)\epsilon_T\left(\frac{d\psi_b}{d\tau}\right)^2 - 2\beta_b\epsilon_T^{1/2}\frac{d\psi_b}{d\tau}\right]^{3/2} \\
\delta_L &= \frac{\epsilon_L}{\left(1-\beta_b^2\right)^{1/2}\epsilon_T}
\end{aligned} \tag{D.14}$$

Eq. (D.13) together with Eqs. (D.14) characterize a coupled harmonic oscillator. δ_L is typically small for the parameters of interest related to optical injection using two counterpropagation laser pulses of strength $a_i \sim 1$ and in an underdense plasma $k_p/k_i \ll 1$. Note that the bounce frequency of an electron trapped in the wakefield and in the non-relativistic limit, i.e., when $\phi_0 \ll 1$ is given by $\hat{\omega}_L = \omega_p\phi_0^{1/2}$. Considering an electron interacting with the wakefield alone, it can be shown (following the same procedure discussed above) that the relativistic axial equation of motion in the wakefield rest frame can be expressed as

$$\boxed{\frac{d^2\psi}{d\tau^2} - \left[1 - \left(\phi_0^{1/2}\frac{d\psi}{d\tau} + \beta_\phi\right)^2\right]^{3/2}\cos\psi = 0} \tag{D.15}$$

where again $\psi = k_p(z - \beta_\phi t)$ and the change of variable $\tau \to \hat{\omega}_L t$ has been used.

Appendix E

One-dimensional nonlinear wakefield equation including an external beam

Starting from Eq. (3.67),

$$\left[\frac{\partial^2}{\partial c^2 t^2} + \nabla\times\nabla\times + \frac{k_p^2}{\sqrt{1+u^2}}\left(1-\frac{n_b}{n_0}\right)\right]\mathbf{u} = -\frac{\partial}{\partial ct}\nabla\sqrt{1+u^2} \\ -\frac{\mathbf{u}}{\sqrt{1+u^2}}\nabla\cdot\left[\frac{\partial \mathbf{u}}{\partial ct} + \nabla\sqrt{1+u^2}\right] - k_p^2\frac{n_b}{n_0}\beta_b \,, \tag{E.1}$$

the longitudinal projection gives,

$$\frac{\partial^2 u_z}{\partial c^2 t^2} + k_p^2\frac{u_z}{\gamma}\left(1-\frac{n_b}{n_0}\right) = -\frac{\partial}{\partial ct}\frac{\partial\gamma}{\partial z} - \frac{u_z}{\gamma}\frac{\partial}{\partial z}\left(\frac{\partial u_z}{\partial ct} + \frac{\partial\gamma}{\partial z}\right) - k_p^2\frac{n_b}{n_0}\beta_b \,, \tag{E.2}$$

where $\gamma = \sqrt{1+u_\perp^2+u_z^2}$ and $u_\perp = a_\perp$ in 1-D. Equation (E.2) may be rewritten as,

$$k_p^{-2}\left(\frac{\partial}{\partial ct} + \frac{u_z}{\gamma}\frac{\partial}{\partial z}\right)\left(\frac{\partial u_z}{\partial ct} + \frac{\partial\gamma}{\partial z}\right) = -\left(1-\frac{n_b}{n_0}\right)\frac{u_z}{\gamma} - \frac{n_b}{n_0}\beta_b \,. \tag{E.3}$$

Transforming (E.3) to the frame comoving with the laser pulse $\zeta = z - ct$, $\tau = t$ and furthermore assuming for simplicity that the group velocity of the laser pulse and the velocity of the electron beam is equal to the speed of light (very underdense

plasma $k_p/k_0 \ll 1$), i.e., $\beta_{gl} = \beta_b = 1$. Equation (E.3) becomes under the quasi-static approximation (laser pulse and electron beam assumed function of ζ only),

$$k_p^{-2}\left(-\frac{\partial}{\partial\zeta}+\beta_z\frac{\partial}{\partial\zeta}\right)\left(-\frac{\partial u_z}{\partial\zeta}+\frac{\partial\gamma}{\partial\zeta}\right) = -\left(1-\frac{n_b}{n_0}\right)\beta_z - \frac{n_b}{n_0}\,. \tag{E.4}$$

The 1-D equation of motion, readily gives,

$$\mathbf{u}_\perp = \mathbf{a}_\perp\,, \tag{E.5}$$

$$\frac{\partial}{\partial\zeta}\left(u_z-\gamma+\phi\right) = 0\,, \tag{E.6}$$

i.e.,

$$\gamma - u_z = 1+\phi\,, \tag{E.7}$$

which yields,

$$k_p^{-2}\left(-\frac{\partial}{\partial\zeta}+\beta_z\frac{\partial}{\partial\zeta}\right)\frac{\partial}{\partial\zeta}\left(1+\phi\right) = -\left(1-\frac{n_b}{n_0}\right)\beta_z - \frac{n_b}{n_0}\,, \tag{E.8}$$

and,

$$k_p^{-2}\left(1-\beta_z\right)\frac{\partial^2\phi}{\partial\zeta^2} = \left(1-\frac{n_b}{n_0}\right)\beta_z + \frac{n_b}{n_0}\,, \tag{E.9}$$

and after further simplifications,

$$\boxed{k_p^{-2}\frac{\partial^2\phi}{\partial\zeta^2} = \frac{\beta_z}{1-\beta_z}+\frac{n_b}{n_0}} \tag{E.10}$$

From Eq. (E.7) along with $u_\perp = a_\perp$ and $u_z = \gamma\beta_z$, it is straightforward to show that,

$$\beta_z = \frac{1+a_\perp^2-\left(1+\phi\right)^2}{1+a_\perp^2+\left(1+\phi\right)^2}\,, \tag{E.11}$$

giving,

$$\boxed{k_p^{-2}\frac{\partial^2\phi}{\partial\zeta^2} = \frac{1}{2}\left[\frac{1+a_\perp^2}{\left(1+\phi\right)^2}-1\right]+\frac{n_b}{n_0}} \tag{E.12}$$

along with,

$$\boxed{\frac{\delta n}{n_0} = \frac{1}{2}\left[\frac{1+a_\perp^2}{(1+\phi)^2} - 1\right]} \tag{E.13}$$

where $\delta n = n_e - n_0$ and n_0 is the background ion density.

Appendix F

Direct calculation of the potential for a 3-D Gaussian charge distribution

Starting from the general expression for the potential in integral form [Eq. (5.1)],

$$\phi(\mathbf{x}) = \frac{1}{4\pi\epsilon_0}\int_{-\infty}^{\infty}\frac{\rho(\mathbf{x}')}{|\mathbf{x}-\mathbf{x}'|}d^3\mathbf{x}' \ , \tag{F.1}$$

and using the definition (J.1) for $\rho(\mathbf{x})$,

$$\rho(x,y,z) = \frac{Q}{4\pi a_1 a_2 a_3}h\left(\frac{x^2}{a_1^2}+\frac{y^2}{a_2^2}+\frac{z^2}{a_3^2}\right) \ , \tag{F.2}$$

together with the normalization (J.6), that is,

$$\int_0^{\infty} r^2 h(r^2)dr = 1 \ , \tag{F.3}$$

applied to the special case of a Gaussian charge distribution $h(r) = h_0\exp(-r^2/2)$, where

$$r^2 = \frac{x^2}{a_1^2}+\frac{y^2}{a_2^2}+\frac{z^2}{a_3^2} \ , \tag{F.4}$$

gives $h_0 = \sqrt{2/\pi}$ and,

$$\rho(r) = \frac{Q}{(2\pi)^{3/2} a_1 a_2 a_3} \exp(-r^2/2) \; . \tag{F.5}$$

Equation (F.1) becomes*,

$$\phi(\mathbf{x}) = \frac{Q}{2a_1 a_2 a_3 (2\pi)^{5/2} \epsilon_0} \int_{-\infty}^{\infty} \frac{\exp(-r'^2/2)}{|\mathbf{x} - \mathbf{x}'|} d^3\mathbf{x}' \; , \tag{F.6}$$

with,

$$r'^2 = \frac{x'^2}{a_1^2} + \frac{y'^2}{a_2^2} + \frac{z'^2}{a_3^2} \; , \tag{F.7}$$

and using the Fourier transform of,

$$\frac{1}{|\mathbf{x} - \mathbf{x}'|} = \frac{1}{2\pi^2} \int_{-\infty}^{+\infty} d^3\mathbf{k} \frac{\exp(i\mathbf{k} \cdot (\mathbf{x} - \mathbf{x}'))}{k^2} \; , \tag{F.8}$$

Eq. (F.6) reduces to,

$$\phi(\mathbf{x}) = \frac{Q}{a_1 a_2 a_3 (2\pi)^{9/2} \epsilon_0} \int_{-\infty}^{\infty} d^3\mathbf{k} \frac{\exp(i\mathbf{k} \cdot \mathbf{x})}{k^2} \int_{-\infty}^{\infty} d^3\mathbf{x}' \exp(-i\mathbf{k} \cdot \mathbf{x}') \exp(-r'^2/2) \; . \tag{F.9}$$

Next define $\mathbf{r}'$ such that $r'_x = x'/a_1$, $r'_y = y'/a_2$, $r'_z = z'/a_3$, and κ such that $\kappa_x = a_1 k_x$, $\kappa_y = a_2 k_y$, $\kappa_z = a_3 k_z$ which gives,

$$\phi(\mathbf{x}) = \frac{Q}{(2\pi)^{9/2} \epsilon_0} \int_{-\infty}^{\infty} d^3\mathbf{k} \frac{\exp(i\mathbf{k} \cdot \mathbf{x})}{k^2} \int_{-\infty}^{\infty} d^3\mathbf{r}' \exp(-i\kappa \cdot \mathbf{r}') \exp(-r'^2/2) \; . \tag{F.10}$$

Further transforming the second integral in Eq. (F.10) and choosing the z-axis to line-up with κ such that $\kappa \cdot \mathbf{r} = \kappa r \cos\theta$ in order to simplify the integral, we get

$$\begin{aligned} &\int_{-\infty}^{\infty} d^3\mathbf{r}' \exp(-i\kappa \cdot \mathbf{r}') \exp(-r'^2/2) = \\ &\int_0^{\infty} r'^2 dr' \int_0^{2\pi} d\phi \int_0^{\pi} d\theta \sin\theta \exp(-i\kappa r' \cos\theta) \exp(-r'^2/2) \; . \end{aligned} \tag{F.11}$$

*David Bruhwiler, Tech-X Corporation, private communication.

After the change of variable $\alpha = \cos\theta$ and $d\alpha = -\sin\theta d\theta$, we find

$$\begin{aligned}\int_{-\infty}^{\infty} d^3\mathbf{r}' \exp(-i\kappa\cdot\mathbf{r}')\exp(-r'^2/2) &= 2\pi\int_0^{\infty} r'^2\exp(-r'^2/2)dr'\times \\ &\quad \int_{-1}^{1} d\alpha\left[\cos(\kappa r'\alpha) - i\sin(\kappa r'\alpha)\right] , \\ &= 2\pi\int_0^{\infty} dr' r'^2\exp(-r'^2/2)\left.\frac{\sin(\kappa r'\alpha)}{\kappa r'}\right|_{-1}^{1} , \\ &= \frac{4\pi}{\kappa}\int_0^{\infty} dr' r\sin(\kappa r')\exp(-r'^2/2) , \\ &= (2\pi)^{3/2}\exp(-\kappa^2/2) ,\end{aligned} \tag{F.12}$$

and introducing the latter result into Eq. (F.10) gives,

$$\phi(\mathbf{x}) = \frac{Q}{(2\pi)^3\epsilon_0}\int_{-\infty}^{\infty}\frac{d^3\mathbf{k}}{k^2}\exp(i\mathbf{k}\cdot\mathbf{x})\exp(-\kappa^2/2) , \tag{F.13}$$

i.e.,

$$\begin{aligned}\phi(\mathbf{x}) &= \frac{Q}{(2\pi)^3\epsilon_0}\int_{-\infty}^{\infty}\frac{d^3\mathbf{k}}{k^2}\exp(ik_x x)\exp(ik_y y)\exp(ik_z z)\times \\ &\quad \exp(-a_1^2k_x^2/2)\exp(-a_2^2k_y^2/2)\exp(-a_3^2k_z^2/2) .\end{aligned} \tag{F.14}$$

Introducing the relationship,

$$\frac{1}{k^2} = \int_0^{+\infty} du\exp(-uk^2) , \tag{F.15}$$

inserting into (F.14) and changing the order of integration gives,

$$\begin{aligned}\phi(\mathbf{x}) &= \frac{Q}{(2\pi)^3\epsilon_0}\int_0^{+\infty} du\int_{-\infty}^{\infty} dk_x\exp[ik_x x - \left(u + a_1^2/2\right)k_x^2]\times \\ &\quad \int_{-\infty}^{\infty} dk_y\exp[ik_y y - \left(u + a_2^2/2\right)k_y^2]\times \\ &\quad \int_{-\infty}^{\infty} dk_z\exp[ik_z z - \left(u + a_3^2/2\right)k_z^2] .\end{aligned} \tag{F.16}$$

Finally using the general solution,

$$\int_{-\infty}^{+\infty} ds \exp\left[-p^2 s^2 + iqs\right] = \frac{\sqrt{\pi}}{p} \exp\left(-q^2/4p^2\right) \ , \tag{F.17}$$

yields

$$\phi = \frac{Q}{2^3 \pi^{3/2} \epsilon_0} \int_0^{+\infty} du \frac{\exp\{-x^2/\left[4\left(u + a_1^2/2\right)\right] - y^2/\left[4\left(u + a_2^2/2\right)\right] - z^2/\left[4\left(u + a_3^2/2\right)\right]\}}{\sqrt{\left(u + a_1^2/2\right)\left(u + a_2^2/2\right)\left(u + a_3^2/2\right)}} \ , \tag{F.18}$$

which is identical to

$$\boxed{\phi(\mathbf{x}) = \frac{a_1 a_2 a_3}{2\epsilon_0} \int_0^{+\infty} \frac{du}{\Delta(u)} \rho_0 \exp\left[-r^2(u)/2\right]} \tag{F.19}$$

where,

$$\Delta(u) = \sqrt{\left(u + a_1^2\right)\left(u + a_2^2\right)\left(u + a_3^2\right)} \ , \tag{F.20}$$

$$r^2(u) = \frac{x^2}{\left(u + a_1^2\right)} + \frac{y^2}{\left(u + a_2^2\right)} + \frac{z^2}{\left(u + a_3^2\right)} \ , \tag{F.21}$$

and

$$\rho_0 = \frac{Q}{(2\pi)^{3/2} a_1 a_2 a_3} \ . \tag{F.22}$$

Equation (F.19) is very similar to (5.2), that is,

$$\phi(\mathbf{x}) = \frac{a_1 a_2 a_3}{4\epsilon_0} \int_0^{\infty} \frac{du}{\Delta(u)} \int_{r^2(u)}^{1} dr^2 \rho(r^2) \ , \tag{F.23}$$

except for a constant which appears in solving (5.2) [(F.23)] using the expression (F.5) for the density. However, the potential is obviously defined up to an arbitrary constant and this has no consequences on the calculation of the electrostatic field,

$$\mathbf{E}_i = -\frac{\partial \phi}{\partial x_i} \ . \tag{F.24}$$

Appendix G

Covariant definition of electromagnetic energy and momentum

A covariant definition of the electromagnetic energy and momentum is necessary in order to ensure their invariance in form when changing inertial frames. This underlies the more general rule that physics laws must remain invariant under a Lorentz transformation and, consequently, the electromagnetic energy and momentum must transform as a 4-vector. In this Appendix, we give a comprehensive summary for the derivation of the 4-vector electromagnetic energy-momentum together with some of the historical background associated to it.

For a long time, a great deal of confusion prevailed in connexion with the energy and momentum of the self-field of an electron (historically the discussions for the electromagnetic energy and momentum were related to the self-energy of the electron, it is obviously equivalent to studying a more general electron charge distribution characterizing a beam). According to Abraham and Lorentz, the total energy of the field (at t =const) were to be calculated from (in Gaussian units)[96]

$$E_{AL} = \frac{1}{8\pi} \int_V d^3x \left(\mathbf{E}^2 + \mathbf{B}^2 \right) \ . \tag{G.1}$$

If one commits the further mistake of using on one hand the expressions for the field

in the rest frame of the electron (i.e., using the covariant Lorentz transformation of the Maxwell stress tensor [97]),

$$E_{AL} = \gamma(1+\beta^2)U_0 - \frac{\gamma\beta^2}{4\pi}\int_{V'} d^3x'\ E_z'^2\ , \tag{G.2}$$

where $E_z = E_z'$, $E_x = \gamma E_x'$, $E_y = \gamma E_y'$, $B_x = -\gamma\beta E_y'/c$, $B_y = \gamma\beta E_x'/c$,

$$U_0 = \frac{1}{8\pi}\int_{V'} d^3x'\ \mathbf{E}'^2\ , \tag{G.3}$$

and on the other hand the Lorentz contraction $d^3x = d^3x'/\gamma$ which does not represent a covariant transformation at all (under such a relation d^3x is neither a scalar nor a component of a vector), one gets the following result

$$E_{AL} = \gamma\left(1+\frac{\beta^2}{3}\right)U_0\ , \tag{G.4}$$

where for the specific case of a spherical charge distribution in the rest frame, we have used the identity

$$\frac{1}{8\pi}\int_{V'} d^3x'\ E_z'^2 = \frac{U_0}{3}\ . \tag{G.5}$$

A similar derivation for the 3-momentum (at t =const) using the *definition*

$$\mathbf{P}_{AL} = \frac{1}{4\pi c}\int_V d^3x\ \mathbf{E}\times\mathbf{B}\ , \tag{G.6}$$

gives,

$$\mathbf{P}_{AL} = \frac{4}{3}\gamma\frac{\beta}{c}U_0\ . \tag{G.7}$$

Writting E^{AL} and $\mathbf{P}^{AL}$ as a 4-vector $\mathbf{P}^\mu_{AL} = (E_{AL}/c, \mathbf{P}_{AL})$ we have in *any* inertial frame

$$\mathbf{P}^\mu_{AL} = \left[\gamma\left(1+\frac{\beta^2}{3}\right)\frac{U_0}{c}, \frac{4}{3}\gamma\frac{\beta}{c}U_0\right]\ , \tag{G.8}$$

and in the rest frame

$$\mathbf{P}^\mu_{AL} = \left(\frac{U_0}{c}, \mathbf{0}\right)\ . \tag{G.9}$$

Obviously Eq. (G.8) is not obtainable from Eq. (G.9) by a 4-vector transformation;

$\mathbf{P}_{\mu}^{AL}$ is not covariant. The correct 4-vector character for the electromagnetic energy and momentum (even in the presence of sources) can be assured by some care. The expressions (G.1) and (G.6) can still be considered to define the energy and momentum but in some particular inertial frame K',

$$E' = \frac{1}{8\pi}\int d^3x' \left(\mathbf{E}'^2 + \mathbf{B}'^2\right) \ , \tag{G.10}$$

and

$$\mathbf{P}' = \frac{1}{4\pi c}\int d^3x' \ \mathbf{E}' \times \mathbf{B}' \ , \tag{G.11}$$

where the integrands in (G.10)-(G.11) are elements of the second rank tensor $\Theta^{\mu\nu}$ (Maxwell stress tensor)[82, 96, 97]. Evidently we must contract one of the tensor indices with a 4-vector, and the 4-vector must be such as to reduce to d^3x' in the inertial frame K' [97]. We define the time-like 4-vector,

$$\boxed{d\sigma^{\mu} = n^{\mu} d^3\sigma} \tag{G.12}$$

where $d^3\sigma$ is an invariant element of three-dimensional "area" on a spacelike hyperplane in four dimensions. The equation of the spacelike plane σ associated with $d\sigma^{\mu}$ may be written as [82],

$$\boxed{n_{\mu}x^{\mu} + c\tau = 0} \tag{G.13}$$

where the invariant τ may be identified with the proper time if K' is taken as the rest frame of the electron. The normal to the hyperplane n^{μ} has components $(1, 0, 0, 0)$ in K'. The invariant $d^3\sigma$ is evidently $d^3\sigma = n_{\mu}d^3\sigma^{\mu} = d^3x'$. If the inertial frame K' moves with the velocity $c\beta$ with respect to the inertial frame K, then in K the 4-vector n^{μ} is

$$\boxed{n^{\mu} = (\gamma, \gamma\beta)} \tag{G.14}$$

The general definition of the electromagnetic 4-momentum in *any* frame is therefore

$$c\mathbf{P}^{\mu} = \int \Theta^{\mu\nu} d\sigma_{\nu} = \int \Theta^{\mu\nu} n_{\nu} d^3\sigma \ . \tag{G.15}$$

In K', n_{μ} has only a time component and, with $d^3\sigma = d^3x'$, this covariant expression reduces to Eqs (G.10) and (G.11). In the frame K, we have $n_{\mu} = (\gamma, -\gamma\beta)$ and the

covariant definition has now time and space components [97],

$$\boxed{cP^0 = \gamma \int (u - \mathbf{v}\cdot\mathbf{g})\, d^3\sigma} \tag{G.16}$$

$$\boxed{c\mathbf{P}^i = \gamma \int \left(cg^i - T_{ij}\beta^j\right) d^3\sigma} \tag{G.17}$$

where the energy density is defined as

$$u = \frac{\mathbf{E}^2 + \mathbf{B}^2}{8\pi} \ , \tag{G.18}$$

together with the 3-momentum density

$$\mathbf{g} = \frac{1}{4\pi c}\left(\mathbf{E}\times\mathbf{B}\right) \ , \tag{G.19}$$

and the space part of the Maxwell stress tensor

$$T_{ij} = \frac{1}{4\pi}\left[E_iE_j + B_iB_j - \frac{1}{2}\left(\mathbf{E}^2 + \mathbf{B}^2\right)\delta_{ij}\right] \ . \tag{G.20}$$

If K' is taken as the *rest frame* of the electron (or beam) then the expression for the magnetic field in K (following a Lorentz transformation) is simply given by

$$\mathbf{B} = \beta \times \mathbf{E} \ , \tag{G.21}$$

and the integrand in Eq. (G.16) is thus [97]

$$\begin{aligned} u - \mathbf{v}\cdot\mathbf{g} &= (8\pi)^{-1}\left(\mathbf{E}^2 + \mathbf{B}^2\right) - (4\pi)^{-1}\,\beta\cdot(\mathbf{E}\times\mathbf{B}) \\ &= (8\pi)^{-1}\left(\mathbf{E}^2 + \mathbf{B}^2\right) - (4\pi)^{-1}\,(\beta\times\mathbf{E})\cdot\mathbf{B} \\ &= (8\pi)^{-1}\left(\mathbf{E}^2 - \mathbf{B}^2\right) \end{aligned} \tag{G.22}$$

which is a Lorentz invariant. Consequently, the energy in K is given by

$$cP^0 = \gamma \int \frac{(\mathbf{E}^2 - \mathbf{B}^2)}{8\pi} d^3\sigma \ , \tag{G.23}$$

and further transforming $d^3\sigma$ using the identity $d^3\sigma = n_\mu d^3\sigma^\mu$, we get in K

$$d^3\sigma = \gamma d^3x - \gamma\beta_j \; d\sigma_j \; , \tag{G.24}$$

where the vector $d\sigma_j = dt \; dx_k \; dx_i$, i.e., integration over the two spatial dimensions and time. In K, the integration is over a space-like "surface" that can be chosen to be 3-space at fixed time ($dt = 0$) [98] giving

$$\boxed{cP^0 = \gamma^2 \int \frac{(\mathbf{E}^2 - \mathbf{B}^2)}{8\pi} d^3x} \tag{G.25}$$

Similarly, the equation for the 3-momentum [Eq. (G.17)] becomes

$$\boxed{c\mathbf{P} = \gamma^2\beta \int \frac{(\mathbf{E}^2 - \mathbf{B}^2)}{8\pi} d^3x} \tag{G.26}$$

With the (Lorentz) invariant integrand $(\mathbf{E}^2 - \mathbf{B}^2)$ it is clear that we have a 4-vector

$$P^\mu = \left(P^0/c, \mathbf{P}\right) \; . \tag{G.27}$$

For the special case of an electron distribution with energy $E' = U_0$ and momentum $\mathbf{P'} = 0$ in K' (rest frame) where U_0 is defined as [Eq (G.3)]

$$U_0 = \frac{1}{8\pi} \int d^3x' \; \mathbf{E}'^2 \; , \tag{G.28}$$

we have

$$\boxed{P^0 = \gamma U_0} \tag{G.29}$$

and

$$\boxed{c\mathbf{P} = \gamma\beta U_0} \tag{G.30}$$

where the identity $\mathbf{B} = \beta \times \mathbf{E}$ has been used [78, 96, 97].

Appendix H

Potential theory applied to ellipsoids with arbitrary charge distributions

Contents

It is possible to derive an expression for the potential of an ellipsoid with an arbitrary charge distribution, that is a distribution which is not ellipsoidal symmetric, in the special case where

$$\lim_{\mathbf{x}\to\pm\infty} \rho(\mathbf{x}) = 0 \ , \tag{H.1}$$

and

$$\lim_{\mathbf{x}\to\pm\infty} \frac{\partial^n \rho(\mathbf{x})}{\partial \mathbf{x}^n} = 0 \ , \tag{H.2}$$

where n is an integer. This is the aim of this appendix. This technique may be used as a mean, through a moment expansion, to calculate correction to the fields for ellipsoidal charge distribution that slightly deviate from ellipsoidal symmetry.

H.1 Theorem

For a general charge distribution, the potential is

$$\phi(\mathbf{x}) = \frac{1}{4\pi\epsilon_0} \int_V \frac{\rho(\mathbf{x}')}{|\mathbf{x}-\mathbf{x}'|} d^3x' \ . \tag{H.3}$$

The derivative of the potential is

$$\begin{aligned} \frac{\partial \phi(\mathbf{x})}{\partial x_i} &= \frac{1}{4\pi\epsilon_0} \int_V \rho(\mathbf{x}') \frac{\partial}{\partial x_i} \left\{ \frac{1}{|\mathbf{x}-\mathbf{x}'|} \right\} d^3x' \ , \\ &= -\frac{1}{4\pi\epsilon_0} \int_V \rho(\mathbf{x}') \frac{\partial}{\partial x'_i} \left\{ \frac{1}{|\mathbf{x}-\mathbf{x}'|} \right\} d^3x' \ . \end{aligned} \tag{H.4}$$

We can integrate by part using

$$\frac{\partial}{\partial x'_i} \left\{ \frac{\rho(\mathbf{x}')}{|\mathbf{x}-\mathbf{x}'|} \right\} = \frac{1}{|\mathbf{x}-\mathbf{x}'|} \frac{\partial \rho(\mathbf{x}')}{\partial x'_i} + \rho(\mathbf{x}') \frac{\partial}{\partial x'_i} \left\{ \frac{1}{|\mathbf{x}-\mathbf{x}'|} \right\} \ , \tag{H.5}$$

to get

$$\frac{\partial \phi(\mathbf{x})}{\partial x_i} = \frac{1}{4\pi\epsilon_0} \int_V \frac{1}{|\mathbf{x}-\mathbf{x}'|} \frac{\partial \rho(\mathbf{x}')}{\partial x'_i} d^3x' - \frac{1}{4\pi\epsilon_0} \int_V \frac{\partial}{\partial x'_i} \left\{ \frac{\rho(\mathbf{x}')}{|\mathbf{x}-\mathbf{x}'|} \right\} d^3x' \ . \tag{H.6}$$

The last term can be converted to a surface integral

$$\int_V \nabla \left\{ \frac{\rho(\mathbf{x}')}{|\mathbf{x}-\mathbf{x}'|} \right\} d^3x' = \int_S \frac{\rho(\mathbf{x}')}{|\mathbf{x}-\mathbf{x}'|} d\mathbf{S}' = 0 \,, \tag{H.7}$$

which is zero if the density distribution *goes to zero* on the bounding surface. Then

$$\boxed{\frac{\partial\phi(\mathbf{x})}{\partial x_i} = \frac{1}{4\pi\epsilon_0} \int_V \frac{1}{|\mathbf{x}-\mathbf{x}'|} \frac{\partial\rho(\mathbf{x}')}{\partial x_i'} d^3x'} \tag{H.8}$$

The gradient of the charge density generates a potential which is the gradient of the original potential. From this follow the generalization to the calculation of the fields of an arbitrary distribution. If $\rho(\mathbf{x})$ and $\nabla\rho(\mathbf{x})$ both vanish on the boundary of the configuration, then the potential induced by the "density" distribution $\partial^2\rho/\partial x_i\partial x_j$ is given by $\partial^2\phi/\partial x_i\partial x_j$ where ϕ is the potential due to $\rho(\mathbf{x})$. It is clear that this can be extented to still higher partial derivatives of ρ provided ρ and all necessary lower-order derivatives *vanish* on the boundary.

H.2 Derivation of the fields for ellipsoids with a linear density profile

Let's assume a charge density in the electron beam *rest frame* of the form,

$$\rho(m^2) = -\frac{1}{2}\rho_1 a_i^2 (1-m^2) = -\frac{1}{2}\rho_1 a_i^2 \left(1 - \sum_{i=1}^{3} \frac{x_i^2}{a_i^2} \right) \,, \tag{H.9}$$

such that

$$\frac{\partial\rho(m^2)}{\partial x_i} = -\frac{1}{2}\rho_1 a_i^2 (1-m^2) = \rho_1 x_i \,, \tag{H.10}$$

and one can deduce $\partial\phi/\partial x_i$ from Eq. (5.9)

$$\phi_i = \frac{\partial\phi}{\partial x_i} = \frac{a_1 a_2 a_3}{2\epsilon_0} x_i \int_\lambda^\infty \frac{du}{(a_i^2+u)\,\Delta(u)} \rho[m^2(u)] \,, \tag{H.11}$$

that is,

$$\boxed{\phi_i = -\rho_1 a_i^2 \frac{a_1 a_2 a_3}{4\epsilon_0} x_i \int_\lambda^\infty \frac{du}{(a_i^2+u)\,\Delta(u)} \left(1 - \sum_{k=1}^{3} \frac{x_k^2}{a_k^2+u}\right)} \tag{H.12}$$

where $\lambda(\mathbf{x})$ is given by (5.14) for a point lying outside the ellipsoid and $\lambda = 0$ inside. Equation (H.12) provide an expression for the potential ϕ_i of an ellipsoidal charge density which varies linearly with x_i across the ellipsoid. Again defining $f(x, y, z, u)$ as

$$f(x, y, z, u) = -\rho_1 a_i^2 \frac{a_1 a_2 a_3}{4\epsilon_0} \frac{x_i}{(a_i^2+u)\,\Delta(u)} \left(1 - \sum_{k=1}^{3} \frac{x_k^2}{a_k^2+u}\right). \tag{H.13}$$

The j component of the electrostatic fields with a density varying along i is then given by

$$E_{ij} = -\frac{\partial \phi_i}{\partial x_j} = -\int_\lambda^\infty \frac{\partial f(x, y, z, u)}{\partial x_j} du\ , \tag{H.14}$$

i.e.,

$$\boxed{\begin{aligned} E_{ij} = \quad & \rho_1 a_i^2 \frac{a_1 a_2 a_3}{2\epsilon_0} \Big\{ x_i x_j \int_\lambda^\infty \frac{du}{(a_i^2+u)\left(a_j^2+u\right)\Delta(u)} - \\ & \frac{\delta_{ij}}{2} \int_\lambda^\infty \frac{du}{(a_i^2+u)\,\Delta(u)} Q(x, y, z, u, 1) \Big\} \end{aligned}} \tag{H.15}$$

where

$$Q(x, y, z, u, m^2) = m^2 - \sum_{k=1}^{3} \frac{x_k^2}{a_k^2+u}. \tag{H.16}$$

The potential of a shell with a density which varies linearly with z (i.e, $i = 3$) is constructed by a superposition of a solid ellipsoid of dimension $m_0 a_i$, charge $-\rho_1$ and an ellipsoid of dimensions $m_1 a_i$ and charge ρ_1. We further assume a charge density with a circular symmetry ($a_1 = a_2 = a$). Making use of the integral identity*:

$$\begin{aligned} & -\frac{\rho_0}{4\epsilon_0} m^3 a_1 a_2 a_3 \int_\lambda^\infty \frac{\left[1 - x^2/\left(m^2 a_1^2+u\right) - y^2/\left(m^2 a_2^2+u\right) - z^2/\left(m^2 a_3^2+u\right)\right]}{\sqrt{\left(m^2 a_1^2+u\right)\left(m^2 a_2^2+u\right)\left(m^2 a_3^2+u\right)}}\, du = \\ & -\frac{\rho}{4\epsilon_0} a_1 a_2 a_3 \int_{\lambda/m^2}^\infty \frac{du}{\Delta(u)} Q(x, y, z, u, m^2)\ , \end{aligned} \tag{H.17}$$

*this particular example corresponds to the potential of a solid ellipsoid with dimensions $m a_i$ and constant charge ρ_0 deduced from Eq. (5.2).

the expression for the electrostatic fields acting on a shell with a linear charge density profile may be simplified as follow,

Region A: inside both ellipsoids the field is constant in the z direction.

$$\begin{aligned} E_{3j} &= \frac{\rho_1}{2\epsilon_0} a^2 a_3^3 \left\{ \left[z x_j B_i(0,\infty) - \frac{\delta_{3j}}{2} \int_0^\infty \frac{du}{(a_3^2+u)\,\Delta(u)} Q(x,y,z,u,m_1^2) \right] - \right. \\ &\left. \left[z x_j B_i(0,\infty) - \frac{\delta_{3j}}{2} \int_0^\infty \frac{du}{(a_3^2+u)\,\Delta(u)} Q(x,y,z,u,m_0^2) \right] \right\} , \end{aligned} \tag{H.18}$$

i.e.,

$$\boxed{E_{3j} = -\frac{\rho_1 \,(m_1^2 - m_0^2)}{2\epsilon_0} a^2 a_3^3 \delta_{3j} A_3(0,\infty)} \tag{H.19}$$

where

$$B_j(u_1,u_0) = \int_{u_1}^{u_0} \frac{du}{(a_3^2+u)\left(a_j^2+u\right)\Delta(u)} , \tag{H.20}$$

and

$$A_3(u_1,u_0) = \int_{u_1}^{u_0} \frac{du}{(a_3^2+u)\,\Delta(u)} . \tag{H.21}$$

Region B: between the ellipsoid boundaries

$$\begin{aligned} E_{3j} &= \frac{\rho_1}{2\epsilon_0} a^2 a_3^3 \left\{ \left[z x_j B_j(0,\infty) - \frac{\delta_{3j}}{2} \int_0^\infty \frac{du}{(a_3^2+u)\,\Delta(u)} Q(x,y,z,u,m_1^2) \right] - \right. \\ &\left. \left[z x_j B_j(\lambda_0/m_0^2,\infty) - \frac{\delta_{3j}}{2} \int_{\lambda_0/m_0^2}^\infty \frac{du}{(a_3^2+u)\,\Delta(u)} Q(x,y,z,u,m_0^2) \right] \right\} , \end{aligned} \tag{H.22}$$

and further using the expression,

$$\begin{aligned} I &= \int_{\lambda/m^2}^\infty \frac{du}{(a_3^2+u)\,\Delta(u)} Q(x,y,z,u,m^2) , \\ &= m^2 A_3(\lambda/m^2,\infty) - \sum_{k=1}^3 x_k^2 B_k(\lambda/m^2,\infty) , \end{aligned} \tag{H.23}$$

e.g,

$$B_j(0,\lambda/m^2) = B_j(0,\infty) - B_j(\lambda/m^2,\infty) , \tag{H.24}$$

then

$$\boxed{\begin{aligned} E_{3j} &= -\frac{\rho_1}{4\epsilon_0}a^2a_3^3\delta_{3j}\left\{m_1^2A_3(0,\infty)-m_0^2A_3(\lambda_0/m_0^2,\infty)-\sum_{k=1}^{3}x_k^2B_k(0,\lambda_0/m_0^2)\right\} \\ &\quad +\frac{\rho_1}{2\epsilon_0}a^2a_3^3zx_jB_j(0,\lambda_0/m_0^2) \end{aligned}} \tag{H.25}$$

Region C: outside both ellipsoids

$$\boxed{\begin{aligned} E_{3j} &= -\frac{\rho_1}{4\epsilon_0}a^2a_3^3\delta_{3j}\Big\{m_1^2A_3(\lambda_1/m_1^2,\infty)-m_0^2A_3(\lambda_0/m_0^2,\infty) \\ &\quad -\sum_{k=1}^{3}x_k^2B_k(\lambda_1/m_1^2,\lambda_0/m_0^2)\Big\} \\ &\quad +\frac{\rho_1}{2\epsilon_0}a^2a_3^3zx_jB_j(\lambda_1/m_1^2,\lambda_0/m_0^2) \end{aligned}} \tag{H.26}$$

H.3 Total electric field for a linear charge density profile with an offset

The electric field acting on ellipsoidal shells with a charge density profile of the form,

$$\rho_s = \rho_{0s} + \rho_{1s}z \ , \tag{H.27}$$

is given by,

$$\boxed{\begin{aligned} E_j &= \frac{\rho_{0s}}{2\epsilon_0}a^2a_3x_jA_j(u_1,u_0) \\ &\quad -\frac{\rho_{1s}}{4\epsilon_0}a^2a_3^3\delta_{3j}\left\{m_1^2A_3(u_1,\infty)-m_0^2A_3(u_0,\infty)-\sum_{k=1}^{3}x_k^2B_k(u_1,u_0)\right\} \\ &\quad +\frac{\rho_{1s}}{2\epsilon_0}a^2a_3^3zx_jB_j(u_1,u_0) \end{aligned}} \tag{H.28}$$

where inside the shell (region A) $u_0 = u_1 = 0$, between the shell boundaries (region B) $u_0 = \lambda_0/m_0^2$ and $u_1 = 0$ and finally outside the boudaries (region C) $u_0 = \lambda_0/m_0^2$ and $u_1 = \lambda_1/m_1^2$. The integrals A_i and B_i are known. The A_i's have been defined in Sec. 5.2 and we derive as well an analytical expression for the B_i's, which is necessary

for fast computation purposes.

$$B = B_1 = B_2 = g_1(u_0) - g_1(u_1),\ B_3 = h_1(u_0) - h_1(u_1), \tag{H.29}$$

with

$$g_1(u) = \frac{1}{(a^2 - a_3^2)^2}\left\{ -\frac{2a^2 + a_3^2 + 3u}{(a^2+u)\sqrt{a_3^2+u}} - \frac{3\tan^{-1}\left(\sqrt{a_3^2+u}/\sqrt{a^2-a_3^2}\right)}{\sqrt{a^2-a_3^2}} \right\}, \tag{H.30}$$

and

$$h_1(u) = \frac{2}{(a^2 - a_3^2)^2}\left\{ \frac{4a_3^2 - a^2 + 3u}{3(a_3^2+u)^{3/2}} + \frac{\tan^{-1}\left(\sqrt{a_3^2+u}/\sqrt{a^2-a_3^2}\right)}{\sqrt{a^2-a_3^2}} \right\}. \tag{H.31}$$

H.4 First order correction to the shell approach

One consequence of space charge blowout is the buildup of a head to tail correlation which appears within the bunch. It is a natural effect caused by the relativistic factor γ in the force. Constant shell density was previously assumed in Sec. 5.4 but the results derived in this appendix may be used as a mean through a moment expansion to provide corrections for charge distributions that slowly depart from pure ellipsoidal symmetry. In the following we will restrain to linear corrections but in principle other orders can be easily derived. To first order the shell charge density is written as

$$\rho_{s_k}(x,y,z) = \rho_{0_{s_k}} + \rho_{1_{s_k}}\left(z - \bar{z}_k\right) + O(z^2)\ , \tag{H.32}$$

which is again defined between the shell boundaries

$$m_0^2(s_k) \le \frac{x^2+y^2}{a_k^2} + \frac{(z-\bar{z})^2}{a_{3_k}^2} \le m_1^2(s_k)\ . \tag{H.33}$$

The zeroth order moment calculation provide a way to calculate the coefficient ρ_{0s},

$$Q_{s_k} = \iiint_D \rho_{s_k}(\mathbf{x})\ d^3x = \frac{4\pi}{3}\left(m_1^3(s_k) - m_0^3(s_k)\right)\rho_{0_{s_k}} a_k^2 a_{3_k} \tag{H.34}$$

i.e.,

$$\boxed{\rho_{0_{s_k}} = \frac{3Q_{s_k}}{4\pi\left(m_1^3(s_k) - m_0^3(s_k)\right) a_k^2 a_{3_k}}} \tag{H.35}$$

where Q_{s_k} is the total charge in the shell s_k [i.e., sum over all macroparticles]. Meanwhile first order gives an expression for ρ_{1s} through,

$$\begin{aligned} \bar{z}_{s_k} &= \iiint_D z\rho_{s_k}(\mathbf{x})\, d^3x\ , \\ &= \bar{z}_k + \frac{m_1^5(s_k) - m_0^5(s_k)}{m_1^3(s_k) - m_0^3(s_k)} \frac{a_{3_k}^2}{5} \frac{\rho_{0_{s_k}}}{\rho_{1_{s_k}}}\ , \end{aligned} \tag{H.36}$$

which is

$$\boxed{\rho_{1_{s_k}} = \frac{5}{a_{3_k}^2} \frac{m_1^3(s_k) - m_0^3(s_k)}{m_1^5(s_k) - m_0^5(s_k)} \left(\bar{z}_{s_k} - \bar{z}_k\right) \rho_{0_{s_k}}} \tag{H.37}$$

where $\bar{z}_k$ is the average position of macroparticles inside ellipsoid k and $\bar{z}_{s_k}$ within shell s_k (of ellipsoid k). Note that moment expansion is used here to provide a numerical fit of the electron distribution. Adding this correction to the fields, the electromagnetic field produced by an ellipsoidal shell with a density varying linearly with z, acting at the coordinate $\{x, y, z\}$ in the *laboratory frame* is given by

$$\boxed{\begin{aligned} E_{s_k}^{(x)} &= \frac{a_k^2\gamma_k a_{3_k}}{2\epsilon_0} x \left[\rho_{0_{s_k}} A_{s_k}(u_{1_k}, u_{0_k}) + \rho_{1_{s_k}} a_{3_k}^2 \left(z - \bar{z}_k\right) \gamma_k^2 B_{s_k}(u_{1_k}, u_{0_k})\right]\ , \\ E_{s_k}^{(y)} &= \frac{a_k^2\gamma_k a_{3_k}}{2\epsilon_0} y \left[\rho_{0_{s_k}} A_{s_k}(u_{1_k}, u_{0_k}) + \rho_{1_{s_k}} a_{3_k}^2 \left(z - \bar{z}_k\right) \gamma_k^2 B_{s_k}(u_{1_k}, u_{0_k})\right] \end{aligned}} \tag{H.38}$$

and

$$\boxed{\begin{aligned} E_{s_k}^{(z)} &= \frac{a_k^2\gamma_k a_{3_k}}{4\epsilon_0} \Big\{ 2\rho_{0_{s_k}} \left(z - \bar{z}_k\right) A_{3_{s_k}}(u_{1_k}, u_{0_k}) \\ &\quad - \rho_{1_{s_k}} a_{3_k}^2 \left[m_1^2(s_k) A_{3_{s_k}}(u_{1_k}, \infty) - m_0^2(s_k) A_{3_{s_k}}(u_{0_k}, \infty) - \right. \\ &\quad \left. \left(x^2 + y^2\right) B_{s_k}(u_{1_k}, u_{0_k}) - 3\gamma_k^2 \left(z - \bar{z}_k\right)^2 B_{3_{s_k}}(u_{1_k}, u_{0_k})\right] \Big\} \end{aligned}} \tag{H.39}$$

where again we have $u_{0_k}(\mathbf{x}) = \lambda_k(\mathbf{x}, m_0^2(s_k))/m_0^2(s_k)$, and $u_{1_k}(\mathbf{x}) = \lambda_k(\mathbf{x}, m_1^2(s_k))/m_1^2(s_k)$. $\lambda_k(\mathbf{x}, m^2)$ is given by Eq. (5.41) except if $\left(x^2 + y^2\right)/a_k^2 + \left(z - \bar{z}_k\right)^2/a_{3k}^2 < m^2$ which is

zero in this case. The new set of space charge coefficients are,

$$B_{s_k}(u_{1_k}, u_{0_k}) = g_{1_k}(u_{0_k}) - g_{1_k}(u_{1_k}) \,, \tag{H.40}$$

$$B_{3_{s_k}}(u_{1_k}, u_{0_k}) = h_{1_k}(u_{0_k}) - h_{1_k}(u_{1_k}) \,, \tag{H.41}$$

where

$$g_{1_k}(u) = (a_k^2 - \gamma_k^2 a_{3_k}^2)^{-2} \left\{ -\frac{2a_k^2 + \gamma_k^2 a_{3_k}^2 + 3u}{(a_k^2 + u)\sqrt{\gamma_k^2 a_{3_k}^2 + u}} - \frac{3\tan^{-1}\left(\sqrt{\gamma_k^2 a_{3_k}^2 + u}/\sqrt{a_k^2 - \gamma_k^2 a_{3_k}^2}\right)}{\sqrt{a_k^2 - \gamma_k^2 a_{3_k}^2}} \right\} \,, \tag{H.42}$$

and

$$h_{1_k}(u) = \frac{2}{(a_k^2 - \gamma_k^2 a_{3_k}^2)^2} \left\{ \frac{4\gamma_k^2 a_{3_k}^2 - a_k^2 + 3u}{3(\gamma_k^2 a_{3_k}^2 + u)^{3/2}} + \frac{\tan^{-1}\left(\sqrt{\gamma_k^2 a_{3_k}^2 + u}/\sqrt{a_k^2 - \gamma_k^2 a_{3_k}^2}\right)}{\sqrt{a_k^2 - \gamma_k^2 a_{3_k}^2}} \right\} \,. \tag{H.43}$$

The expression for the total force *per unit charge* is given by Eq. (5.42).

H.5 Discussion

It has been demonstrated in Sec. 5.4 that the shell approach provide a computationally fast and accurate way to calculate space charge effects on beams with large energy spreads. The only requirement is that the space charge blowout is moderate such that paraxial approximation may be assumed throughout the calculation. Adding a first order correction to cope for slight deviations from ellipsoidal symmetry may add the constrain of needing more macroparticles per shell in order to get a precise numerical fit of the charge distribution.

Appendix I

Derivation of the coupled envelope equations

Contents

This Appendix presents a general derivation of the RMS envelope equations using a Hamiltonian approach. This results are valid for an arbitrary electron distribution function. Appendix J will further specialize to ellipsoidal symmetric bunches and Appendix K to the special case of finite cylinder of charge.

I.1 Single particle equation of motion

This Section closely follows the work of R. Ryne *et al* [74]. Starting from the usual definition linking the Lagrangian to the Hamiltonian,

$$L = p\dot{q} - H \ , \tag{I.1}$$

and using the definition of the action,

$$A = \int \left(p\dot{q} - H\right) dt \ , \tag{I.2}$$

one can derive an expression for the Lagrangian in a coordinate system where z is the *independent variable*, i.e.,

$$\begin{aligned} dA &= \left(p\dot{q} - H\right) dt \ , & \text{(I.3)} \\ &= \left(p_x x' + p_y y' + p_z - H t'\right) dz \ , & \text{(I.4)} \end{aligned}$$

with $p_i = \gamma m v_i + q A_i$. Defining $p_t = -H$ yield,

$$\begin{aligned} A &= \int \left(p_x x' + p_y y' + p_t t' + p_z\right) dz \ , & \text{(I.5)} \\ &= \int \hat{L} dz \ , & \text{(I.6)} \end{aligned}$$

where $\hat{L} = p_x x' + p_y y' + p_t t' - K$ and $K = -p_z$. From the expression of the Hamiltonian in terms of the independent variable t,

$$\begin{aligned} H\left(x, p_x, y, p_y, z, p_z; t\right) &= \sqrt{m^2c^4 + c^2\left[\left(p_x - qA_x\right)^2 + \left(p_y - qA_y\right)^2 + \left(p_z - qA_z\right)^2\right]} + q\Phi \ , \\ &= -p_t \ , & \text{(I.7)} \end{aligned}$$

together with

$$\mathbf{B}(x,y,z,t) = \nabla \times \mathbf{A}(x,y,z,t) \; , \tag{I.8}$$

$$\mathbf{E}(x,y,z,t) = -\nabla\Phi(x,y,z,t) - \frac{\partial \mathbf{A}(x,y,z,t)}{\partial t} \; , \tag{I.9}$$

it is readily found a similar expression where z is now the independent variable, i.e.,

$$\begin{aligned} &K\left(x, p_x, y, p_y, t, p_t; z\right) = -p_z \; , \\ &= -\sqrt{\left(p_t + q\Phi\right)^2/c^2 - m^2c^2 - \left(p_x - qA_x\right)^2 - \left(p_y - qA_y\right)^2} - qA_z \; . \end{aligned} \tag{I.10}$$

For the case of space charge, i.e., no external applied fields, $A_x^{\text{self}} = A_y^{\text{self}} = 0$ and $A_z^{\text{self}} = v_0\Phi^{\text{self}}/c^2$, we get

$$K = -\sqrt{\left(p_t + q\Phi^{\text{self}}\right)^2/c^2 - m^2c^2 - p_x^2 - p_y^2} - qA_z^{\text{self}} \; , \tag{I.11}$$

and using variational principles,

$$p_t = -\frac{\partial K}{\partial t} \; , \tag{I.12}$$

$$t = \frac{\partial K}{\partial p_t} \; , \tag{I.13}$$

$$\cdots$$

we can deduce the new expression for the equations of motion [74, 99, 100].

I.2 Reference orbit

In a general manner the reference orbit is identical to the trajectory of a reference particle which evolve in the fields of the beam transport system (quadrupole magnets, rf accelerating cavities, ...) from some initial conditions carefully chosen in order to simplify the form of the overall equations that describe the evolution of any particles in the system. Let (t_0, p_{t0}) denote the trajectory of the reference particle (along with $x = p_x = y = p_y = 0$ to simplify). Using the above Hamiltonian, it follows that the

equations of motion for the reference particle are given by

$$t_0' = \frac{-p_{t0}}{\sqrt{p_{t0}^2 - m^2c^4}} = \frac{1}{v_0} \,, \tag{I.14}$$

and,

$$p_{t0}' = -\frac{\partial K}{\partial t_0} \,, \tag{I.15}$$

where primes stand for d/dz and K is the general Hamiltonian [Eq. (I.11)] containing the external fields as well as the self fields. Φ has been neglected in (I.15) because for a beam evolving in vacuum under space charge blowout alone, the reference particle may simply be chosen as located at the center of the bunch (the center of force) such that $p_{t0}' = 0$, i.e., $p_{t0} = -H = -\gamma_0 mc^2$ and $t_0(z) = z/v_0$, where v_0 is the average beam velocity. This assumption is valid as long as the beam energy spread $\eta = \Delta E/E_0$ remains small.

I.3 Equations in the frame comoving with the reference orbit

Next define variables that are deviations from the reference orbit,

$$\begin{aligned} X &= x \,, \\ P_x &= p_x \,, \\ Y &= y \,, \\ P_y &= p_y \,, \end{aligned} \tag{I.16}$$

and,

$$\begin{aligned} T &= t - t_0(z) \,, \\ P_t &= p_t - p_{t0}(z) \,. \end{aligned} \tag{I.17}$$

The Hamiltonian governing this variables is obtained from the generating function [74, 101]

$$F_2(q, P) = xP_x + yP_y + [t - t_0(z)]\,[P_t + p_{t0}(z)] \,, \tag{I.18}$$

according to

$$Q = \frac{\partial F_2}{\partial P} , \tag{I.19}$$

$$p = \frac{\partial F_2}{\partial q} , \tag{I.20}$$

and

$$K^{\rm new} = K + \frac{\partial F_2}{\partial z} . \tag{I.21}$$

The new Hamiltonian is given by

$$\begin{aligned} &K\left(X, P_x, Y, P_y, T, P_t; z\right) = \\ &-\sqrt{\left[\left(P_t + p_{t0}\right) + q\Phi^{\rm self}\right]^2 / c^2 - m^2c^2 - P_x^2 - P_y^2} - qA_z^{\rm self} + \\ &T\frac{dp_{t0}}{dz} - \left(P_t + p_{t0}\right)\frac{dt_0}{dz} , \end{aligned} \tag{I.22}$$

where

$$\mathbf{A}^{\rm self} = \mathbf{A}^{\rm self}(X, Y, z, T + t_0) , \tag{I.23}$$

$$\Phi^{\rm self} = \Phi^{\rm self}(X, Y, z, T + t_0) . \tag{I.24}$$

Next we will substitute the potentials into the Hamiltonian and drop terms of order 3 and higher in (X, P_x, P_y, Y, T, P_t). Also, since $\Phi^{\rm self}$ is of order 2 and higher, we will keep $\Phi^{\rm self}$ but drop $(\Phi^{\rm self})^2$ and higher powers. It follows that the Hamiltonian is given by

$$\begin{aligned} K &= -mc\left\{\frac{p_{t0}^2 + 2p_{t0}\left(P_t + q\Phi^{\rm self}\right) + P_t^2}{m^2c^4} - 1 - \frac{P_x^2}{m^2c^2} - \frac{P_y^2}{m^2c^2}\right\}^{1/2} - \\ &\quad \frac{v_0}{c^2}q\Phi^{\rm self} - \frac{P_t}{v_0} + \gamma_0 mc^2/v_0 , \end{aligned} \tag{I.25}$$

$$\begin{aligned} &= -mc\left\{\left(\gamma_0^2 - 1\right) - 2\gamma_0\frac{P_t + q\Phi^{\rm self}}{mc^2} + \frac{P_t^2}{m^2c^4} - \frac{P_x^2}{m^2c^2} - \frac{P_y^2}{m^2c^2}\right\}^{1/2} - \\ &\quad \frac{v_0}{c^2}q\Phi^{\rm self} - \frac{P_t}{v_0} + \gamma_0 mc^2/v_0 , \end{aligned} \tag{I.26}$$

i.e.,

$$K = -p_0\left\{1-\frac{2\left(P_t+q\Phi^{\rm self}\right)}{p_0v_0}+\frac{P_t^2}{p_0^2c^2}-\frac{P_x^2}{p_0^2}-\frac{P_y^2}{p_0^2}\right\}^{1/2}- \frac{v_0}{c^2}q\Phi^{\rm self}-\frac{P_t}{v_0}+\gamma_0mc^2/v_0\ , \tag{I.27}$$

where $p_0=\gamma_0mv_0$ has been used along with $A_z^{\rm self}=v_0\Phi^{\rm self}/c^2$. To second order in (X,P_x,Y,P_y,T,P_t), Eq. (I.27) becomes,

$$K \simeq -p_0\left\{1-\frac{\left(P_t+q\Phi^{\rm self}\right)}{p_0v_0}-\frac{4}{p_0^2v_0^2}\frac{P_t^2}{8}+\frac{P_t^2}{2p_0^2c^2}-\frac{P_x^2}{2p_0^2}-\frac{P_y^2}{2p_0^2}\right\}- \frac{v_0}{c^2}q\Phi^{\rm self}-\frac{P_t}{v_0}+\gamma_0mc^2/v_0\ , \tag{I.28}$$

giving,

$$K\simeq\frac{m^2P_t^2}{2p_0^3}+\frac{P_x^2+P_y^2}{2p_0}-\frac{q\Phi^{\rm self}}{\gamma_0^2v_0}-p_0\left(1-\beta_0^{-2}\right)\ . \tag{I.29}$$

Note that $\beta_0^{-2}=1+p_0^{-2}m^2c^2$. The last term in the Hamiltonian is not a function of the canonical variables and consequently does not contribute to the dynamics of the electrons. Therefore, it will not be considered in the calculation. The new expression for the Hamiltonian is,

$$\boxed{K\left(X,P_x,Y,P_y,T,P_t;z\right)=\frac{m^2P_t^2}{2p_0^3}+\frac{P_x^2+P_y^2}{2p_0}-\frac{q\Phi^{\rm self}}{\gamma_0^2v_0}} \tag{I.30}$$

It follows from Hamilton's equations [74, 99, 100] that the equations of motion are given by:

$$X' = \frac{P_x}{p_0}\ , \tag{I.31}$$

$$P_x' = -\frac{q}{\gamma_0^2v_0}\frac{\partial}{\partial X}\Phi^{\rm self}\ , \tag{I.32}$$

$$Y' = \frac{P_y}{p_0}\ , \tag{I.33}$$

$$P_y' = -\frac{q}{\gamma_0^2v_0}\frac{\partial}{\partial Y}\Phi^{\rm self}\ , \tag{I.34}$$

and,

$$T' = \frac{m^2 P_t}{p_0^3} , \tag{I.35}$$

$$P_t' = -\frac{q}{\gamma_0^2 v_0}\frac{\partial}{\partial T}\Phi^{\text{self}} . \tag{I.36}$$

These can be combined in pairs to yield the following three equations

$$\boxed{\begin{aligned} X'' + \frac{q}{\gamma_0^2 p_0 v_0}\frac{\partial}{\partial X}\Phi^{\text{self}} &= 0 \\ Y'' + \frac{q}{\gamma_0^2 p_0 v_0}\frac{\partial}{\partial Y}\Phi^{\text{self}} &= 0 \\ T'' + \frac{q}{\gamma_0^4 p_0 v_0^3}\frac{\partial}{\partial T}\Phi^{\text{self}} &= 0 \end{aligned}} \tag{I.37}$$

Recall that $p_0(z)$ was assumed to be constant, i.e., $p_0' = 0$.

I.4 RMS envelope equations

Evolution equations for the RMS moments of the beam can be obtained using standard techniques. Consider for example, the calculation of $\langle X^2 \rangle$. First, let

$$\sigma_x = \sqrt{\langle X^2 \rangle} , \tag{I.38}$$

giving,

$$\sigma_x' = \frac{\langle XX' \rangle}{\sigma_x} = \frac{1}{p_0}\frac{\langle XP_x \rangle}{\sigma_x} , \tag{I.39}$$

and,

$$\begin{aligned} \sigma_x'' &= \frac{\sigma_x \left(\langle X'P_x \rangle + \langle X'P_x' \rangle \right) - \sigma_x' \langle XP_x \rangle}{p_0 \sigma_x^2} , \\ &= \frac{\langle XP_x' \rangle}{p_0 \sigma_x} + \frac{\epsilon_x^2}{p_0^2 \sigma_x^3} , \end{aligned} \tag{I.40}$$

where the normalized emittance was introduced as,

$$\epsilon_x = \sqrt{\langle X^2 \rangle \langle P_x^2 \rangle - \langle XP_x \rangle^2} . \tag{I.41}$$

The RMS envelope in the x direction is then,

$$\boxed{\sigma_x'' + \frac{q}{p_0 v_0 \gamma_0^2}\frac{1}{\sigma_x}\left\langle X\frac{\partial}{\partial X}\Phi^{\text{self}}\right\rangle - \frac{\epsilon_x^2}{p_0^2\sigma_x^3} = 0} \tag{I.42}$$

Similarly, the equations for the other second moments are given by

$$\boxed{\sigma_y'' + \frac{q}{p_0 v_0 \gamma_0^2}\frac{1}{\sigma_y}\left\langle Y\frac{\partial}{\partial Y}\Phi^{\text{self}}\right\rangle - \frac{\epsilon_y^2}{p_0^2\sigma_y^3} = 0} \tag{I.43}$$

$$\boxed{\sigma_t'' + \frac{q}{p_0 v_0^3 \gamma_0^4}\frac{1}{\sigma_t}\left\langle T\frac{\partial}{\partial T}\Phi^{\text{self}}\right\rangle - \frac{\epsilon_t^2}{p_0^2\gamma_0^4 v_0^4\sigma_t^3} = 0} \tag{I.44}$$

and,

$$\epsilon_y = \sqrt{\langle Y^2\rangle\left\langle P_y^2\right\rangle - \langle YP_y\rangle^2}\,, \tag{I.45}$$

$$\epsilon_t = \sqrt{\langle T^2\rangle\left\langle P_t^2\right\rangle - \langle TP_t\rangle^2}\,. \tag{I.46}$$

Note that it is easy to show that, if Φ^{self} is a quadratic function of X, Y and T (or equivalently, if we simply neglect higher order terms), then the normalized RMS emittances are constants.

I.5 The longitudinal envelope equation

Define Z as the distance between the particle and the reference particle (or design trajectory)

$$Z(z) = v_0 T(z)\,, \tag{I.47}$$

where $T = t - t_0$ is the time difference between the two particles at position z. Recall that

$$P_t = p_t - p_{t0}\,, \tag{I.48}$$

$$= mc^2\left(\Delta\gamma + q\Phi^{\text{self}}/mc^2\right)\,, \tag{I.49}$$

$$\simeq mc^2\Delta\gamma\,, \tag{I.50}$$

where $\Delta\gamma \gg q\Phi^{\rm self}/mc^2$ was assumed, and we get

$$Z' = \frac{m^2 v_0}{p_0^3} P_t = \frac{\Delta\gamma}{\beta_0^2\gamma_0^3} = \frac{\eta}{\beta_0^2\gamma_0^2} \; , \tag{I.51}$$

where $\eta = \Delta E/E_0$ is the beam energy spread, $\Delta E = mc^2\Delta\gamma$ and $E_0 = \gamma_0 mc^2$. Next we will derive the relation between energy spread η and momentum spread $\delta = \Delta p/p_0$ using the definition of the total energy of a free particle [100, 102],

$$E^2 = p^2c^2 + m^2c^4 \; , \tag{I.52}$$

$$E_0^2\,(1+\eta)^2 = p_0^2c^2\,(1+\delta)^2 + m^2c^4 \; , \tag{I.53}$$

and,

$$p_0 c\,(1+\delta) = E_0\sqrt{(1+\eta)^2 - m^2c^4/E_0^2} \; , \tag{I.54}$$

i.e.,

$$\delta(\eta) = \beta_0^{-1}\sqrt{(1+\eta)^2 - m^2c^4/E_0^2} - 1 \; . \tag{I.55}$$

The quantity $\delta(\eta)$ can be developed in a power series in η:

$$\delta(\eta) = \delta(0) + \delta'(0)\eta + \delta''(0)\eta^2/2 + \cdots \; , \tag{I.56}$$

with

$$\delta'(\eta) = \beta_0^{-1}\,(1+\eta)\left[(1+\eta)^2 - m^2c^4/E_0^2\right]^{-1/2} \; , \tag{I.57}$$

$$\delta''(\eta) = \beta_0^{-1}\left[(1+\eta)^2 - m^2c^4/E_0^2\right]^{-1/2} - \beta_0^{-1}\,(1+\eta)^2\left[(1+\eta)^2 - m^2c^4/E_0^2\right]^{-3/2} \; , \tag{I.58}$$

and,

$$\delta'(0) = \beta_0^{-2} \; , \tag{I.59}$$

$$\delta''(0) = -\beta_0^{-4}\gamma_0^{-2} \; , \tag{I.60}$$

i.e., to second order

$$\delta = \beta_0^{-2}\eta + O(\eta^2) \; , \tag{I.61}$$

which gives

$$Z'(z) \simeq \frac{\delta(z)}{\gamma_0^2} \ . \tag{I.62}$$

In a similar manner one can derive the equation for $\delta'(z)$ using Eq. (I.50),

$$P_t = \delta\gamma_0\beta_0^2 mc^2 \ , \tag{I.63}$$

i.e.,

$$\delta = \frac{P_t}{\beta_0^2 E_0} \ , \tag{I.64}$$

and,

$$\delta'(z) = \frac{P_t'(z)}{\beta_0^2 E_0} = \frac{-q}{\gamma_0^3\beta_0^2 mc^2}\frac{\partial\Phi^{\text{self}}}{\partial Z} \ , \tag{I.65}$$

where Eq. (I.36) as been used along with the relation $Z = v_0 T$. Multiplying Eq. (I.44) by v_0, we can now deduce an expression for the longitudinal envelope equation,

$$\boxed{\sigma_z'' + \frac{q}{p_0 v_0 \gamma_0^4}\frac{1}{\sigma_z}\left\langle Z\frac{\partial}{\partial Z}\Phi^{\text{self}}\right\rangle - \frac{\epsilon_z^2}{\gamma_0^4\sigma_z^3} = 0} \tag{I.66}$$

along with,

$$\epsilon_z = \sqrt{\langle Z^2\rangle\langle\delta^2\rangle - \langle Z\delta\rangle^2} \ . \tag{I.67}$$

Appendix J

Coupled envelope equations in ellipsoidal geometry

For the space charge force calculation, the approximation $Z = v_0 T \simeq z - z_0(t)$ is strictly valid only if the beam energy spread is small. Recall that the space charge forces can only be calculated in a frame where t is the independent variable. Next we will consider the calculation of the terms $\left\langle X\partial\Phi^{\text{self}}/\partial X\right\rangle$, $\left\langle Y\partial\Phi^{\text{self}}/\partial Y\right\rangle$ and $\left\langle Z\partial\Phi^{\text{self}}/\partial Z\right\rangle$ in the envelope equations. Assume that the charge density of a single bunch is given by

$$\rho(X,Y,Z) = \frac{Q}{4\pi a_1 a_2 a_3} h\left(\frac{X^2}{a_1^2} + \frac{Y^2}{a_2^2} + \frac{Z^2}{a_3^2}\right) . \tag{J.1}$$

The charge per bunch is equal to Q. By making the substitutions

$$X = a_1 r \sin\theta\cos\phi \, , \tag{J.2}$$

$$Y = a_2 r \sin\theta\sin\phi \, , \tag{J.3}$$

$$Z = a_3 r \cos\theta \, . \tag{J.4}$$

It follows that

$$Q = \iiint_V \rho d^3\mathbf{X} = \frac{Q}{4\pi}\int_0^\infty r^2 h(r^2) dr \int_0^\pi \sin\theta d\theta \int_0^{2\pi} d\phi \, , \tag{J.5}$$

i.e., $h(r^2)$ is normalized according to

$$\int_0^\infty r^2 h(r^2) dr = 1 \; . \tag{J.6}$$

It is also straightforward to show that the second order moments are related to a_1, a_2 and a_3 as shown below,

$$\left\langle X^2 \right\rangle = \frac{a_1^2}{3} \int_0^\infty r^4 h(r^2) dr \; , \tag{J.7}$$

$$\left\langle Y^2 \right\rangle = \frac{a_2^2}{3} \int_0^\infty r^4 h(r^2) dr \; , \tag{J.8}$$

$$\left\langle Z^2 \right\rangle = \frac{a_3^2}{3} \int_0^\infty r^4 h(r^2) dr \; . \tag{J.9}$$

As an example let assume a constant ellipsoid. The boundary is defined by the ellipsoidal coordinate

$$r_{\max}^2 = \frac{X^2}{a_1^2} + \frac{Y^2}{a_2^2} + \frac{Z^2}{a_1^3} = 1 \; , \tag{J.10}$$

we get

$$h(r^2) = 3 \; , \tag{J.11}$$

and,

$$\left\langle X^2 \right\rangle = a_1^2/5 \; , \tag{J.12}$$

$$\left\langle Y^2 \right\rangle = a_2^2/5 \; , \tag{J.13}$$

$$\left\langle Z^2 \right\rangle = a_3^2/5 \; . \tag{J.14}$$

The scalar potential in the *laboratory frame* [Eq. (5.2)] is given by

$$\Phi^{\text{self}}(X,Y,Z) = \frac{\gamma_0 Q}{16\pi\epsilon_0} \int_0^\infty \frac{ds}{\Delta(s)} \int_{m^2(s)}^1 h(m^2) dm^2 \; , \tag{J.15}$$

where,

$$\Delta(s) = \sqrt{\left(a_1^2 + s\right)\left(a_2^2 + s\right)\left(\gamma_0^2 a_3^2 + s\right)} \; , \tag{J.16}$$

and,

$$m^2(s) = \frac{X^2}{a_1^2+s} + \frac{Y^2}{a_2^2+s} + \frac{\gamma_0^2 Z^2}{\gamma_0^2 a_3^2+s} \; . \tag{J.17}$$

It is easy to verify that this potential satisfies the Lorentz gauge

$$\nabla^2 \Phi^{\rm self} - \frac{1}{c^2}\frac{\partial^2}{\partial t^2}\Phi^{\rm self} = \frac{\rho}{\epsilon_0} \; . \tag{J.18}$$

The calculation of $\mathbf{E}$ [Eq. 5.9] is also straightforward,

$$E_x(X,Y,Z) = -\frac{\partial}{\partial X}\Phi^{\rm self} = \frac{\gamma_0 Q}{8\pi\epsilon_0} X \int_0^\infty \frac{ds}{(a_1^2+s)\,\Delta(s)} h[m^2(s)] \; , \tag{J.19}$$

$$E_y(X,Y,Z) = -\frac{\partial}{\partial Y}\Phi^{\rm self} = \frac{\gamma_0 Q}{8\pi\epsilon_0} Y \int_0^\infty \frac{ds}{(a_2^2+s)\,\Delta(s)} h[m^2(s)] \; , \tag{J.20}$$

and,

$$\begin{aligned} E_z(X,Y,Z) &= -\frac{\partial}{\partial z}\Phi^{\rm self} - \frac{\partial}{\partial t}A_z^{\rm self} = -\frac{1}{\gamma_0^2}\frac{\partial}{\partial Z}\Phi^{\rm self} \; , \\ &= \frac{\gamma_0 Q}{8\pi\epsilon_0} Z \int_0^\infty \frac{ds}{(\gamma_0^2 a_3^2+s)\,\Delta(s)} h[m^2(s)] \; . \end{aligned} \tag{J.21}$$

The term $\left\langle X \partial\Phi^{\rm self}/\partial X \right\rangle$ is therefore

$$\left\langle X \frac{\partial}{\partial X}\Phi^{\rm self} \right\rangle = -\frac{\gamma_0 Q}{8\pi\epsilon_0} \iiint_V \frac{\rho[m^2(0)]}{Q} d^3\mathbf{X} \int_0^\infty \frac{X^2 h[m^2(s)] ds}{(a_1^2+s)\,\Delta(s)} \; , \tag{J.22}$$

which suggests the change of variables

$$X = \sqrt{a_1^2+s}\; r\sin\theta\cos\phi \; , \tag{J.23}$$

$$Y = \sqrt{a_2^2+s}\; r\sin\theta\sin\phi \; , \tag{J.24}$$

$$\gamma_0 Z = \sqrt{\gamma_0^2 a_3^2+s}\; r\cos\theta \; , \tag{J.25}$$

and deducing from the Jacobian determinant the relationship between $d^3\mathbf{X}$ and $dr d\theta d\phi$, that is

$$\gamma_0 d^3\mathbf{X} = \Delta(s)\; r^2 dr \sin\theta d\theta d\phi \; , \tag{J.26}$$

we have

$$\left\langle X\frac{\partial}{\partial X}\Phi^{\text{self}}\right\rangle = \frac{-Q}{32\pi^2\epsilon_0 a_1 a_2 a_3}\int_0^\infty r^2 h(r^2)dr\int_0^\pi d\theta\int_0^{2\pi}d\phi\int_0^\infty r^2\sin^3\theta\cos^2\phi \\ h\left[r^2+sr^2\left(\frac{\sin^2\theta\cos^2\phi}{a_1^2}+\frac{\sin^2\theta\sin^2\phi}{a_2^2}+\frac{\cos^2\theta}{\gamma_0^2 a_3^2}\right)\right]ds\ . \tag{J.27}$$

After performing the change of variables

$$\mu^2(s) = r^2+sr^2\left(\frac{\sin^2\theta\cos^2\phi}{a_1^2}+\frac{\sin^2\theta\sin^2\phi}{a_2^2}+\frac{\cos^2\theta}{\gamma_0^2 a_3^2}\right)\ , \tag{J.28}$$

one gets

$$\left\langle X\frac{\partial}{\partial X}\Phi^{\text{self}}\right\rangle = \frac{-Q}{16\pi^2\epsilon_0 a_1 a_2 a_3}\int_0^\infty r^2 h(r^2)dr\int_r^\infty \mu h(\mu^2)d\mu \\ \int_0^\pi d\theta\int_0^{2\pi}\frac{\sin^3\theta\cos^2\phi\ d\phi}{\sin^2\theta\cos^2\phi/a_1^2+\sin^2\theta\sin^2\phi/a_2^2+\cos^2\theta/(\gamma_0^2 a_3^2)}\ , \tag{J.29}$$

and further making use of the integral identity [70]

$$\begin{aligned} I &= \int_0^\pi\sin\theta d\theta\int_0^{2\pi}\frac{\sin^2\theta\cos^2\phi\ d\phi}{\sin^2\theta\cos^2\phi/a_1^2+\sin^2\theta\sin^2\phi/a_2^2+\cos^2\theta/(\gamma_0^2 a_3^2)}\ , \\ &= 2\pi a_1^3 a_2\gamma_0 a_3 A_1(a_1,a_2,\gamma_0 a_3)\ , \end{aligned} \tag{J.30}$$

where

$$A_i(u_1,u_2,u_3) = \int_0^\infty\frac{ds}{(u_i^2+s)\,\Delta(s)}\ , \tag{J.31}$$

and,

$$\Delta(s) = \sqrt{(u_1^2+s)\,(u_2^2+s)\,(u_3^2+s)}\ , \tag{J.32}$$

we obtain a simplified expression for the average space charge term in the envelope equation, i.e.,

$$\left\langle X\frac{\partial}{\partial X}\Phi^{\text{self}}\right\rangle = \frac{-\gamma_0 Q}{8\pi\epsilon_0}a_1^2 A_1(a_1,a_2,\gamma_0 a_3)\int_0^\infty r^2 h(r^2)dr\int_r^\infty\mu h(\mu^2)d\mu\ . \tag{J.33}$$

Now introduce the notation [73]

$$\lambda_3 = \frac{1}{3\sqrt{3}} \left[\int_0^\infty r^2 h(r^2) dr \int_r^\infty \mu h(\mu^2) d\mu \right] \left\{ \int_0^\infty r^4 h(r^2) dr \right\}^{1/2} , \tag{J.34}$$

and noting that

$$a_1^2 A_1(\sigma_x, \sigma_y, \gamma_0 \sigma_z) = \frac{1}{3\sqrt{3}} \left\{ \int_0^\infty r^4 h(r^2) dr \right\}^{1/2} 3\sigma_x^2 \int_0^\infty \frac{ds}{(\sigma_x^2 + s)\, \Delta(s)} , \tag{J.35}$$

we get

$$\boxed{\left\langle X \frac{\partial}{\partial X} \Phi^{\text{self}} \right\rangle = \frac{-3\gamma_0 Q \lambda_3}{8\pi\epsilon_0} \sigma_x^2 A_1(\sigma_x, \sigma_y, \gamma_0 \sigma_z)} \tag{J.36}$$

Sacherer [73] also showed that the value of λ_3 is insensitive to the functional form of h and is approximately equal to $1/(5\sqrt{5})$. Putting all together, we obtain the RMS envelope equation

$$\boxed{\sigma_x'' - \frac{3}{2} \frac{N r_e}{\gamma_0^2 \beta_0^2} \lambda_3 \sigma_x A_1(\sigma_x, \sigma_y, \gamma_0 \sigma_z) - \frac{\tilde{\epsilon}_x^2}{\sigma_x^3} = 0} \tag{J.37}$$

where the number of electrons N and the classical electron radius $r_e = e^2/(4\pi\epsilon_0 mc^2)$ has been introduced. Note also that the quantities A_i and λ_3 can be viewed as geometrical factors related to space charge effects. Similarly it follows that

$$\boxed{\begin{array}{rcl} \left\langle Y \dfrac{\partial}{\partial Y} \Phi^{\text{self}} \right\rangle & = & \dfrac{-3\gamma_0 Q \lambda_3}{8\pi\epsilon_0} \sigma_y^2 A_2(\sigma_x, \sigma_y, \gamma_0 \sigma_z) \\ \left\langle Z \dfrac{\partial}{\partial Z} \Phi^{\text{self}} \right\rangle & = & \dfrac{-3\gamma_0^3 Q \lambda_3}{8\pi\epsilon_0} \sigma_z^2 A_3(\sigma_x, \sigma_y, \gamma_0 \sigma_z) \end{array}} \tag{J.38}$$

and,

$$\boxed{\begin{array}{rcl} \sigma_y'' - \dfrac{3}{2} \dfrac{N r_e}{\gamma_0^2 \beta_0^2} \lambda_3 \sigma_y A_2(\sigma_x, \sigma_y, \gamma_0 \sigma_z) - \dfrac{\tilde{\epsilon}_y^2}{\sigma_y^3} & = & 0 \\ \sigma_z'' - \dfrac{3}{2} \dfrac{N r_e}{\gamma_0^2 \beta_0^2} \lambda_3 \sigma_z A_3(\sigma_x, \sigma_y, \gamma_0 \sigma_z) - \dfrac{\tilde{\epsilon}_z^2}{\sigma_z^3} & = & 0 \end{array}} \tag{J.39}$$

where $\tilde{\epsilon}_x = \epsilon_x/p_0$, $\tilde{\epsilon}_y = \epsilon_y/p_0$ and $\tilde{\epsilon}_z = \epsilon_z/\gamma_0^2$ are the RMS trace-space emittances defined as

$$\tilde{\epsilon}_x = \sqrt{\langle X^2\rangle \langle X'^2\rangle - \langle XX'\rangle^2}\,, \tag{J.40}$$

$$\tilde{\epsilon}_y = \sqrt{\langle Y^2\rangle \langle Y'^2\rangle - \langle YY'\rangle^2}\,, \tag{J.41}$$

$$\tilde{\epsilon}_z = \sqrt{\langle Z^2\rangle \langle Z'^2\rangle - \langle ZZ'\rangle^2}\,. \tag{J.42}$$

Appendix K

Fields acting on a finite cylinder of charge

Contents

A derivation of the electromagnetic fields acting on a finite cylinder of charge, in the long beam limit approximation, is performed in this Appendix. The long beam limit corresponds to the case $a/(\gamma a_3) \ll 1$ where a is the transverse radius, γ the beam relativistic factor and a_3 the beam half-length, respectively. Section K.1 introduce the general expression for the potential of a finite cylinder in integral form. The latter result will be applied to the calculation of the fields [Sec. K.2] and to the derivation of an envelope equation [Sec. K.2.2], for the specific case of a beam with a longitudinal quadratic density profile and uniform radial profile.

K.1 General results

The potential of a static charge distribution $\tilde{\rho}(\tilde{\mathbf{r}})$, in cylindrical coordinates is given by

$$\tilde{V}(\tilde{r},\tilde{\theta},\tilde{z}) = k\int_{-\infty}^{\infty} d\tilde{z}' \int_0^{\infty} d\tilde{r}' \int_0^{2\pi} d\tilde{\theta}' \frac{\tilde{\rho}(\tilde{\mathbf{r}}')}{\sqrt{(\tilde{z}-\tilde{z}')^2 + |\tilde{\mathbf{r}}-\tilde{\mathbf{r}}'|^2}} \,, \tag{K.1}$$

where,

$$k = \frac{1}{4\pi\epsilon_0} \,. \tag{K.2}$$

This is the potential in a system at rest with respect to the charge distribution (rest frame potentials, fields and coordinates are designated with tildes). If the charge distribution is moving along z axis with velocity βc, then to transform to the laboratory, we use

$$\begin{aligned} z - z' &= (\tilde{z}-\tilde{z}')/\gamma \,, \\ \rho &= \tilde{\rho}\gamma \,, \\ \mathbf{r} &= \tilde{\mathbf{r}} \,, \end{aligned} \tag{K.3}$$

so that the potential in the *rest frame*, in terms of lab. coordinates, is

$$\tilde{V}(r,\theta,z) = \frac{k}{\gamma}\int_{-\infty}^{\infty} dz' \int_0^{\infty} dr' \int_0^{2\pi} d\theta' \frac{\rho(\mathbf{r}')}{\sqrt{(z-z')^2 + |\mathbf{r}-\mathbf{r}'|^2/\gamma^2}} \,. \tag{K.4}$$

Let us suppose that the charge density $\rho(\mathbf{r})$ is cylindrically symmetric and separable in the product form

$$\rho(\mathbf{r}) = \sigma(r)\lambda(z) \,, \tag{K.5}$$

with the normalization

$$\iiint_V \rho(\mathbf{r}) d^3\mathbf{r} = eN \ , \tag{K.6}$$

giving

$$\int_{-\infty}^{\infty} \lambda(z) dz = eN \ , \tag{K.7}$$

and,

$$2\pi \int_0^{\infty} \sigma(r) r dr = 1 \ , \tag{K.8}$$

where N is the number of electrons.

Then, with $\mathbf{u} = \mathbf{r}/\gamma$, and letting $z' \to z' - z$, we have

$$\tilde{V}(r,\theta,z) = k\gamma \int_0^{\infty} u'\sigma\left(u'\gamma\right) du' \int_0^{2\pi} d\theta' \int_{-\infty}^{\infty} dz' \frac{\lambda(z'+z)}{\sqrt{z'^2 + |\mathbf{u}-\mathbf{u}'|^2}} \ . \tag{K.9}$$

We will consider in this Appendix only charge densities $\lambda(z)$ which vanish for $|z| > a_3$. In this case , we have

$$\boxed{\tilde{V}(r,\theta,z) = k\gamma \int_0^{\infty} u'\sigma\left(u'\gamma\right) du' \int_0^{2\pi} d\theta' \int_{-a_3-z}^{a_3-z} dz' \frac{\lambda(z'+z)}{\sqrt{z'^2 + |\mathbf{u}-\mathbf{u}'|^2}}} \tag{K.10}$$

K.2 Quadratic longitudinal density profile

For a parabolic charge density profile in the z direction,

$$\lambda(z) = \frac{3eN}{4a_3}\left(1 - \frac{z^2}{a_3^2}\right) \ , \tag{K.11}$$

using

$$\int_{-a_3-z}^{a_3-z} dz' \frac{\lambda(z'+z)}{\sqrt{z'^2+|\mathbf{u}-\mathbf{u}'|^2}} = \frac{3eN}{8a_3^3}\Big\{ -(a_3+3z)\sqrt{(a_3-z)^2+|\mathbf{u}-\mathbf{u}'|^2} - (a_3-3z)\sqrt{(a_3+z)^2+|\mathbf{u}-\mathbf{u}'|^2} + \left(2a_3^2-2z^2+|\mathbf{u}-\mathbf{u}'|^2\right)\ln\left[\frac{a_3-z+\sqrt{(a_3-z)^2+|\mathbf{u}-\mathbf{u}'|^2}}{-a_3-z+\sqrt{(a_3+z)^2+|\mathbf{u}-\mathbf{u}'|^2}}\right]\Big\}, \tag{K.12}$$

we now let $\delta = \mathbf{u}/a_3$, $\delta' = \mathbf{u}'/a_3$ and we further make the approximation $|\delta| = r/(\gamma a_3) \ll 1$. Expanding in powers of $|\delta - \delta'|$ and keeping only the leading order terms gives,

$$-(a_3+3z)\sqrt{(a_3-z)^2+|\mathbf{u}-\mathbf{u}'|^2} - (a_3-3z)\sqrt{(a_3+z)^2+|\mathbf{u}-\mathbf{u}'|^2} \simeq -2a_3^2+6z^2\,, \tag{K.13}$$

and

$$\frac{a_3-z+\sqrt{(a_3-z)^2+|\mathbf{u}-\mathbf{u}'|^2}}{-a_3-z+\sqrt{(a_3+z)^2+|\mathbf{u}-\mathbf{u}'|^2}} \simeq \frac{4\left(a_3^2-z^2\right)}{|\mathbf{u}-\mathbf{u}'|^2}\,. \tag{K.14}$$

Note that such approximation is only valid for $|z| < a_3$. The fields at the edge of the cylinder are not properly defined. We get,

$$\begin{aligned}\tilde{V}(r,\theta,z) \;&\simeq\; \frac{3keN\gamma}{4a_3^3}\int_0^\infty u'\sigma\left(u'\gamma\right)du'\int_0^{2\pi} d\theta'\Big\{ -a_3^2+3z^2+ \\ &\quad \left(a_3^2-z^2\right)\left[\ln 4\left(a_3^2-z^2\right)-\ln|\mathbf{u}-\mathbf{u}'|^2\right]\Big\}\,,\end{aligned} \tag{K.15}$$

i.e.,

$$\begin{aligned}\tilde{V}(r,\theta,z) \;&\simeq\; \frac{3k\pi eN\gamma}{2a_3^3}\int_0^\infty u'\sigma\left(u'\gamma\right)du'\left[-a_3^2+3z^2+\left(a_3^2-z^2\right)\ln 4\left(a_3^2-z^2\right)\right] \\ &\quad -\frac{3keN\gamma}{4a_3^3}\left(a_3^2-z^2\right)\int_0^\infty u'\sigma\left(u'\gamma\right)du'\int_0^{2\pi} d\theta'\ln|\mathbf{u}-\mathbf{u}'|^2\,.\end{aligned} \tag{K.16}$$

There is only one term which is difficult to integrate in this expression:

$$\int_0^\infty u'\sigma\left(u'\gamma\right)du' \int_0^{2\pi} d\theta' \ln\left|\mathbf{u}-\mathbf{u}'\right|^2 , \tag{K.17}$$

in which

$$\left|\mathbf{u}-\mathbf{u}'\right|^2 = u^2+u'^2-2uu'\cos\left(\theta-\theta'\right) . \tag{K.18}$$

To do the θ' integration, we observe that due to *cylindrical symmetry* the result must be independent of θ and concequently we can choose the location $\theta = 0$. Using the identity (for $b<1$)

$$\int_0^{2\pi} \ln\left(1-b\cos x\right)dx = 2\pi \ln\frac{1+\sqrt{1-b^2}}{2} , \tag{K.19}$$

and writing,

$$\left|\mathbf{u}-\mathbf{u}'\right|^2 = \left(u^2+u'^2\right)\left(1-\frac{2uu'}{u^2+u'^2}\cos\theta'\right) , \tag{K.20}$$

we see that

$$b = \frac{2uu'}{u^2+u'^2} , \tag{K.21}$$

and,

$$\frac{1+\sqrt{1-b^2}}{2} = \frac{u^2+u'^2+\left|u^2-u'^2\right|}{2(u^2+u'^2)} , \tag{K.22}$$

that is,

$$\begin{aligned}
\int_0^{2\pi} d\theta \ln\left|\mathbf{u}-\mathbf{u}'\right|^2 &= \int_0^{2\pi} d\theta \left[\ln\left(u^2+u'^2\right)+\ln\left(1-\frac{2uu'}{u^2+u'^2}\cos\theta'\right)\right] , \\
&= 2\pi\left[\ln\left(u^2+u'^2\right)+\ln\left(\frac{u^2+u'^2+\left|u^2-u'^2\right|}{2(u^2+u'^2)}\right)\right] , \\
&= 2\pi\ln\left(\frac{u^2+u'^2+\left|u^2-u'^2\right|}{2}\right) .
\end{aligned} \tag{K.23}$$

Thus if $u'<u$,

$$\int_0^{2\pi} d\theta \ln\left|\mathbf{u}-\mathbf{u}'\right|^2 = 2\pi\ln u^2 , \tag{K.24}$$

while if $u < u'$,

$$\int_0^{2\pi} d\theta \ln |\mathbf{u} - \mathbf{u}'|^2 = 2\pi \ln u'^2 \ , \tag{K.25}$$

and Eq. (K.17) becomes,

$$\begin{aligned} \int_0^\infty u'\sigma\left(u'\gamma\right) du' \int_0^{2\pi} d\theta' \ln |\mathbf{u} - \mathbf{u}'|^2 &= 2\pi\Bigg(\ln u^2 \int_0^u u'\sigma\left(u'\gamma\right) du' + \\ &\qquad \int_u^\infty u' \ln u'^2 \sigma\left(u'\gamma\right) du' \Bigg) \ , \end{aligned} \tag{K.26}$$

providing a new expression for the potential

$$\boxed{\begin{aligned} \tilde{V}(r,\theta,z) \simeq \frac{3k\pi eN\gamma}{2a_3^3} \Bigg\{ & \int_0^\infty u'\sigma\left(u'\gamma\right) du' \left[-a_3^2 + 3z^2 + (a_3^2 - z^2)\ln 4\left(a_3^2 - z^2\right)\right] \\ & -(a_3^2 - z^2)\left(\ln u^2 \int_0^u u'\sigma\left(u'\gamma\right) du' + \int_u^\infty u' \ln u'^2 \sigma\left(u'\gamma\right) du' \right) \Bigg\} \end{aligned}} \tag{K.27}$$

K.2.1 Uniform radial density profile

Fields inside the beam

For a uniform beam of radius a, we have, for $r < a$,

$$\sigma(r) = \frac{1}{\pi a^2} \ . \tag{K.28}$$

Then for $u < a/\gamma$, we have

$$\begin{aligned} \ln u^2 \int_0^u u'\sigma\left(u'\gamma\right) du' &= (\pi a^2)^{-1} \ln u^2 \int_0^u u' du' \ , \\ &= (2\pi a^2)^{-1} u^2 \ln u^2 \ , \end{aligned} \tag{K.29}$$

and,

$$\begin{aligned} \int_u^\infty u' \ln u'^2 \sigma\left(u'\gamma\right) du' &= (\pi a^2)^{-1} \int_u^{a/\gamma} u' \ln u'^2 du' \ , \\ &= (2\pi a^2\gamma^2)^{-1} \left[u^2\left(1 - \ln\frac{u^2}{\gamma^2}\right) - a^2\left(1 - \ln\frac{a^2}{\gamma^2}\right)\right] \ , \end{aligned} \tag{K.30}$$

giving,

$$\tilde{V}(r,\theta,z) \simeq \frac{3keN}{4\gamma a_3^3}\left\{-a_3^2+3z^2+(a_3^2-z^2)\left[\ln 4\left(a_3^2-z^2\right)-\ln\frac{a^2}{\gamma^2}-\frac{u^2\gamma^2}{a^2}+1\right]\right\} . \tag{K.31}$$

The longitudinal electric field is

$$\tilde{E}_z(r,\theta,z) = -\frac{\partial\tilde{V}}{\partial\tilde{z}} = -\frac{1}{\gamma}\frac{\partial\tilde{V}}{\partial z} \simeq -\frac{3keNz}{\gamma^2 a_3^3}\left[1-\ln\left(\frac{2\gamma\sqrt{a_3^2-z^2}}{a}\right)-\frac{1}{2}\left(1-\frac{r^2}{a^2}\right)\right] , \tag{K.32}$$

i.e.,

$$\boxed{\tilde{E}_z(r,\theta,z) \simeq -\frac{2k\lambda'(z)}{\gamma^2}\left[\ln\left(\frac{2\gamma\sqrt{a_3^2-z^2}}{a}\right)-\frac{1}{2}\left(1+\frac{r^2}{a^2}\right)\right]} \tag{K.33}$$

The transverse electric field is

$$\tilde{E}_r(r,\theta,z) = -\frac{\partial\tilde{V}}{\partial\tilde{r}} = -\frac{1}{\gamma}\frac{\partial\tilde{V}}{\partial u} \simeq \frac{3keN}{2\gamma a^2 a_3^3} r(a_3^2-z^2) , \tag{K.34}$$

i.e.,

$$\boxed{\tilde{E}_r(r,\theta,z) \simeq \frac{2k\lambda(z)r}{\gamma a^2}} \tag{K.35}$$

Figure K.1 plots the ratio E_z^*/E_z on axis, for a quadratic density profile [Eq. (K.11)]. E_z^* casts for the longitudinal electric field obtained from direct integration of Eq. (K.1). One can see an excellent agreement with the approximate expression Eq. (K.33) up to the limit $z \simeq a_3$, with,

$$\lim_{z\to a_3} E_z(0,\theta,z) = -\infty . \tag{K.36}$$

The fields at the edge of the cylinder are not properly defined because of the assumptions made in Eq. (K.13)-(K.14) which allow for an analytical solution to be found. E_z is strictly valid for $|z| < a_3$, $a/(\gamma a_3) \ll 1$ (long beam) and $r/(\gamma a_3) \ll 1$.

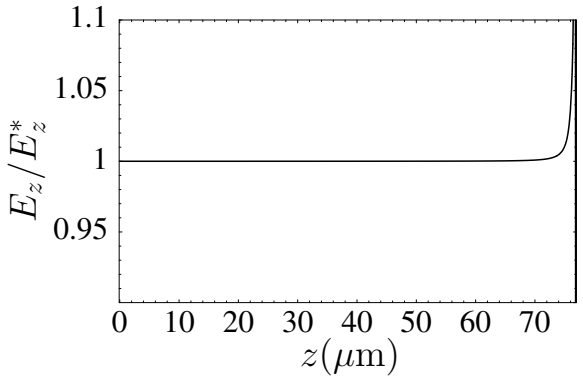

Figure K.1: $E_z^*(0,\theta,z)/E_z(0,\theta,z)$ using a parabolic density profile [Eq. (K.11)] and for $a = 19$ μm, $a_3 = 77$ μm and $\gamma = 13.7$. E_z^* corresponds to the longitudinal electric field obtained from direct integration of Eq. (K.1). Recall that $z = 0$ is the center of the bunch.

Fields outside the beam

For $u > a/\gamma$

$$\int_u^\infty u' \ln u'^2 \sigma\left(u'\gamma\right) du' = 0 \,, \tag{K.37}$$

$$\ln u^2 \int_0^u u' \sigma\left(u'\gamma\right) du' = \left(\pi a^2\right)^{-1} \ln u^2 \int_0^{a/\gamma} u' du' \,, \tag{K.38}$$

$$= \left(2\pi\gamma^2\right)^{-1} \ln u^2 \,, \tag{K.39}$$

and,

$$\tilde{V}(r,\theta,z) \simeq \frac{3keN}{4\gamma a_3^3} \left\{ -a_3^2 + 3z^2 + \left(a_3^2 - z^2\right) \left[\ln 4 \left(a_3^2 - z^2\right) - \ln u^2 \right] \right\} \,. \tag{K.40}$$

The longitudinal electric field is

$$\tilde{E}_z(r,\theta,z) = -\frac{1}{\gamma}\frac{\partial \tilde{V}}{\partial z} \simeq -\frac{3keNz}{\gamma^2 a_3^3} \left(1 - \ln 2\sqrt{a_3^2 - z^2} - \ln u \right) \,, \tag{K.41}$$

$$\simeq -\frac{3keN}{\gamma^2 a_3^3} \left[1 - \ln\left(\frac{2\gamma\sqrt{a_3^2 - z^2}}{r} \right) \right] \,, \tag{K.42}$$

i.e.,

$$\boxed{\tilde{E}_z(r,\theta,z) \simeq -\frac{2k\lambda'(z)}{\gamma^2}\left[\ln\left(\frac{2\gamma\sqrt{a_3^2-z^2}}{r}\right)-1\right]} \tag{K.43}$$

The transverse electric field is

$$\begin{aligned}\tilde{E}_r(r,\theta,z) &= -\frac{\partial\tilde{V}}{\partial\tilde{r}} = -\frac{1}{\gamma}\frac{\partial\tilde{V}}{\partial u} \simeq \frac{3keN}{2\gamma^2 a_3^3}\frac{a_3+z}{u}\,, &\text{(K.44)}\\ &\simeq \frac{3keN}{2\gamma a_3^3}\frac{a_3+z}{r}\,, &\text{(K.45)}\end{aligned}$$

i.e.,

$$\boxed{\tilde{E}_r(r,\theta,z) \simeq \frac{2k\lambda(z)}{\gamma r}} \tag{K.46}$$

K.2.2 Coupled envelope equations

From Sec. I.4 and I.5 we found that the general expression for the coupled RMS equations is given by,

$$\begin{aligned}\sigma_x'' - \frac{e}{p_0 v_0 \gamma_0^2}\frac{1}{\sigma_x}\langle xE_x\rangle - \frac{\tilde{\epsilon}_x^2}{\sigma_x^3} &= 0\,, &\text{(K.47)}\\ \sigma_y'' - \frac{e}{p_0 v_0 \gamma_0^2}\frac{1}{\sigma_y}\langle yE_y\rangle - \frac{\tilde{\epsilon}_y^2}{\sigma_y^3} &= 0\,, &\text{(K.48)}\\ \sigma_z'' - \frac{e}{p_0 v_0 \gamma_0^2}\frac{1}{\sigma_z}\langle zE_z\rangle - \frac{\tilde{\epsilon}_z^2}{\sigma_z^3} &= 0\,, &\text{(K.49)}\end{aligned}$$

where $\tilde{\epsilon}_x = \epsilon_x/p_0$, $\tilde{\epsilon}_y = \epsilon_y/p_0$ and $\tilde{\epsilon}_z = \epsilon_z/\gamma_0^2$ are the RMS trace-space emittances defined as

$$\begin{aligned}\tilde{\epsilon}_x &= \sqrt{\langle x^2\rangle\langle x'^2\rangle - \langle xx'\rangle^2}\,, &\text{(K.50)}\\ \tilde{\epsilon}_y &= \sqrt{\langle y^2\rangle\langle y'^2\rangle - \langle yy'\rangle^2}\,, &\text{(K.51)}\\ \tilde{\epsilon}_z &= \sqrt{\langle z^2\rangle\langle z'^2\rangle - \langle zz'\rangle^2}\,. &\text{(K.52)}\end{aligned}$$

The electric fields in the lab. are non-linear in x,y and z. In the "long beam" limit, that is, for $a \ll \gamma_0 a_3$, inside the cylinder, the transverse electric field in the lab. frame

is found to be

$$E_r(r,z) = \gamma_0 \tilde{E}_r(r,z) = \frac{\lambda(z) r}{2\pi\epsilon_0 a^2} , \tag{K.53}$$

$$= \frac{3eNr}{8\pi\epsilon_0 a^2 a_3}\left(1 - \frac{z^2}{a_3^2}\right) . \tag{K.54}$$

The longitudinal field inside the cylinder is

$$E_z(r,\theta,z) = \tilde{E}_z(r,\theta,z) = -\frac{\lambda'(z)}{2\pi\epsilon_0\gamma_0^2}\left[\ln\left(\frac{2\gamma_0\sqrt{a_3^2 - z^2}}{a}\right) - \frac{1}{2}\left(1 + \frac{r^2}{a^2}\right)\right] ,$$

$$= \frac{3eNz}{4\pi\epsilon_0 a_3^3\gamma_0^2}\left[\ln\left(\frac{2\gamma_0\sqrt{a_3^2 - z^2}}{a}\right) - \frac{1}{2}\left(1 + \frac{r^2}{a^2}\right)\right] . \tag{K.55}$$

Note that since the fields are non-linear functions of the coordinates, the RMS emittances will not be preserved. In the following we will ignore emittance growth is the envelope equation, and the emittances are set equal to their initial values. For the transverse axis we have,

$$\langle xE_x\rangle = \langle yE_y\rangle = \frac{3eN\langle x^2\rangle}{8\pi\epsilon_0 a^2 a_3}\left(1 - \frac{\langle z^2\rangle}{a_3^2}\right) , \tag{K.56}$$

Using $\sigma_z^2 = \langle z^2\rangle = a_3^2/5$ and $\sigma_x^2 = \langle x^2\rangle = \langle r^2\rangle/2 = a^2/4$, where in general $\langle A\rangle$ is defined as,

$$\langle A\rangle = \frac{1}{\pi a^2 eN}\int_0^{2\pi} d\theta \int_0^a r dr \int_{-a_3}^{-a_3} A(r,z)\lambda(z) dz , \tag{K.57}$$

we get

$$\langle xE_x\rangle = \frac{3eN}{40\pi\epsilon_0 a_3} , \tag{K.58}$$

For the longitudinal axis, we have

$$\langle zE_z\rangle = -\frac{3eN\langle z^2\rangle}{8\pi\epsilon_0 a_3^3\gamma_0^2}\left(1 + \frac{\langle r^2\rangle}{a^2}\right) + \frac{3eN}{4\pi\epsilon_0 a_3^3\gamma_0^2}\left\langle z^2 \ln\left(\frac{2\gamma_0\sqrt{a_3^2 - z^2}}{a}\right)\right\rangle , \tag{K.59}$$

where

$$\left\langle z^2 \ln\left(\frac{2\gamma_0\sqrt{a_3^2-z^2}}{a}\right)\right\rangle = \frac{a_3^2}{5}\left[\ln\left(\frac{\gamma_0 a_3}{a}\right) + 2\ln 2 - 1 - \frac{1}{30}\right] , \tag{K.60}$$

and,

$$\langle zE_z\rangle = \frac{3eN}{20\pi\epsilon_0 a_3\gamma_0^2}\ln\left(\frac{\gamma_0\alpha_3 a_3}{a}\right) , \tag{K.61}$$

with $\alpha_3 \simeq 0.6723$. Including $\langle xE_x\rangle$, $\langle yE_y\rangle$ and $\langle zE_z\rangle$ in the envelope equations, we get

$$\boxed{\begin{aligned} \sigma_x'' - \frac{3}{2}\frac{Nr_e}{\gamma_0^3\beta_0^2}\frac{\lambda_3}{\sigma_x\sigma_z} - \frac{\tilde{\epsilon}_x^2}{\sigma_x^3} &= 0 \\ \sigma_y'' - \frac{3}{2}\frac{Nr_e}{\gamma_0^3\beta_0^2}\frac{\lambda_3}{\sigma_y\sigma_z} - \frac{\tilde{\epsilon}_y^2}{\sigma_y^3} &= 0 \\ \sigma_z'' - \frac{3}{2}\frac{Nr_e}{\gamma_0^5\beta_0^2}\frac{\lambda_3}{\sigma_z^2}g_2(\sigma_x,\gamma_0\sigma_z) - \frac{\tilde{\epsilon}_z^2}{\sigma_z^3} &= 0 \end{aligned}} \tag{K.62}$$

where the classical electron radius $r_e = e^2/(4\pi\epsilon_0 mc^2)$ has been introduced and,

$$g_2(\sigma_x,\gamma_0\sigma_z) \simeq 2\ln\left(\frac{\gamma_0\alpha_3'\sigma_z}{\sigma_x}\right) , \tag{K.63}$$

$$\alpha_3' \simeq 0.6 , \tag{K.64}$$

$$\lambda_3 = 1/(5\sqrt{5}) . \tag{K.65}$$

K.2.3 Hollow radial density profile

Starting from Eq. (K.27), that is,

$$\begin{aligned} \tilde{V}(r,\theta,z) \simeq \frac{3k\pi eN\gamma}{2a_3^3}\Bigg\{ &\int_0^\infty u'\sigma\left(u'\gamma\right)du'\left[-a_3^2+3z^2+(a_3^2-z^2)\ln 4\left(a_3^2-z^2\right)\right] \\ &-(a_3^2-z^2)\left(\ln u^2\int_0^u u'\sigma\left(u'\gamma\right)du' + \int_u^\infty u'\ln u'^2\sigma\left(u'\gamma\right)du'\right)\Bigg\} , \end{aligned} \tag{K.66}$$

we are going to calculate in this section the electrostatic field of a ring beam with radius a using the expression for the transverse charge density,

$$\sigma(r) = \frac{\delta(r-a)}{2\pi a} . \tag{K.67}$$

Fields inside the beam

For $u < a/\gamma$,

$$\ln u^2 \int_0^u u'\sigma\left(u'\gamma\right) du' = 0 \,, \tag{K.68}$$

$$\int_u^\infty u' \ln u'^2 \sigma\left(u'\gamma\right) du' \equiv (2\pi a)^{-1} \int_0^\infty \delta(u'\gamma - a) u' \ln u'^2 du' \,, \tag{K.69}$$

$$= (2\pi\gamma^2)^{-1} \ln \frac{a^2}{\gamma^2} \,, \tag{K.70}$$

which gives,

$$\tilde{V}(r,\theta,z) \simeq \frac{3keN}{4\gamma a_3^3} \left\{ -a_3^2 + 3z^2 + (a_3^2 - z^2) \left[\ln 4 \left(a_3^2 - z^2\right) - \ln a^2 + \ln \gamma^2 \right] \right\} \,. \tag{K.71}$$

The longitudinal electric field in the *rest frame* and in terms of lab. coordinates is

$$\tilde{E}_z(r,\theta,z) = -\frac{\partial \tilde{V}}{\partial \tilde{z}} = -\frac{1}{\gamma}\frac{\partial \tilde{V}}{\partial z} \,, \tag{K.72}$$

$$\simeq -\frac{3keNz}{\gamma^2 a_3^3} \left(1 - \ln 2\sqrt{a_3^2 - z^2} + \ln a - \ln \gamma \right) \,, \tag{K.73}$$

$$\simeq -\frac{3keNz}{\gamma^2 a_3^3} \left[1 - \ln \left(\frac{2\gamma\sqrt{a_3^2 - z^2}}{a} \right) \right] \,, \tag{K.74}$$

that is,

$$\boxed{\tilde{E}_z(r,\theta,z) \simeq -\frac{2k\lambda'(z)}{\gamma^2} \left[\ln \left(\frac{2\gamma\sqrt{a_3^2 - z^2}}{a} \right) - 1 \right]} \tag{K.75}$$

The transverse electric field $\tilde{E}_r(r,\theta,z)$ is zero.

Fields outside the beam

For $u > a/\gamma$

$$\int_u^\infty u' \ln u'^2 \sigma\left(u'\gamma\right) du' = 0 \,, \tag{K.76}$$

and,

$$\ln u^2 \int_0^u u'\sigma\left(u'\gamma\right) du' \equiv (2\pi a)^{-1} \ln u^2 \int_0^\infty \delta(u'\gamma - a) u' du' \,, \tag{K.77}$$

$$= (2\pi\gamma^2)^{-1} \ln u^2 \,, \tag{K.78}$$

giving,

$$\tilde{V}(r,\theta,z) \simeq \frac{3keN}{4\gamma a_3^3} \left\{ -a_3^2 + 3z^2 + (a_3^2 - z^2) \left[\ln 4 \left(a_3^2 - z^2 \right) - \ln u^2 \right] \right\} \,. \tag{K.79}$$

The longitudinal electric field is

$$\tilde{E}_z(r,\theta,z) = -\frac{1}{\gamma}\frac{\partial \tilde{V}}{\partial z} \simeq -\frac{3keNz}{\gamma^2 a_3^3} \left(1 - \ln 2\sqrt{a_3^2 - z^2} - \ln u \right) \,, \tag{K.80}$$

$$\simeq -\frac{3keNz}{\gamma^2 a_3^3} \left[1 - \ln\left(\frac{2\gamma\sqrt{a_3^2 - z^2}}{r} \right) \right] \,, \tag{K.81}$$

i.e.,

$$\boxed{\tilde{E}_z(r,\theta,z) \simeq -\frac{2k\lambda'(z)}{\gamma^2} \left[\ln\left(\frac{2\gamma\sqrt{a_3^2 - z^2}}{r} \right) - 1 \right]} \tag{K.82}$$

The transverse electric field is given by

$$\tilde{E}_r(r,\theta,z) = -\frac{\partial \tilde{V}}{\partial \tilde{r}} = -\frac{1}{\gamma}\frac{\partial \tilde{V}}{\partial u} \simeq \frac{3keN}{2\gamma^2 a_3^3} \frac{a_3^2 - z^2}{u} \,, \tag{K.83}$$

$$\simeq \frac{3keN}{2\gamma a_3^3} \frac{a_3^2 - z^2}{r} \,, \tag{K.84}$$

which is,

$$\boxed{\tilde{E}_r(r,\theta,z) \simeq \frac{2k\lambda(z)}{\gamma r}} \tag{K.85}$$

K.3 Linear charge density profile

Starting from Eq. (K.10), for a charge density linear in z,

$$\lambda(z) = \frac{eN}{2a_3}\left(1 + \frac{z}{a_3}\right) , \tag{K.86}$$

using

$$\int_{-a_3-z}^{a_3-z} dz' \frac{\lambda(z'+z)}{\sqrt{z'^2 + |\mathbf{u}-\mathbf{u}'|^2}} = \frac{eN}{2a_3^2}\Bigg\{ \sqrt{(a_3-z)^2 + |\mathbf{u}-\mathbf{u}'|^2} - \sqrt{(a_3+z)^2 + |\mathbf{u}-\mathbf{u}'|^2} + (a_3+z)\ln\left[\frac{a_3 - z + \sqrt{(a_3+z)^2 + |\mathbf{u}-\mathbf{u}'|^2}}{-a_3 - z + \sqrt{(a_3+z)^2 + |\mathbf{u}-\mathbf{u}'|^2}}\right]\Bigg\} . \tag{K.87}$$

We now let $\delta = \mathbf{u}/a_3$, and $\delta' = \mathbf{u}'/a_3$. We make the approximation $|\delta| = r/(\gamma a_3) \ll 1$, and expand in powers of $|\delta - \delta'|$. Keeping only the leading order terms gives,

$$\sqrt{(a_3-z)^2 + |\mathbf{u}-\mathbf{u}'|^2} - \sqrt{(a_3+z)^2 + |\mathbf{u}-\mathbf{u}'|^2} \simeq -2z , \tag{K.88}$$

and

$$\frac{a_3 - z + \sqrt{(a_3+z)^2 + |\mathbf{u}-\mathbf{u}'|^2}}{-a_3 - z + \sqrt{(a_3+z)^2 + |\mathbf{u}-\mathbf{u}'|^2}} \simeq \frac{4\left(a_3^2 - z^2\right)}{|\mathbf{u}-\mathbf{u}'|^2} . \tag{K.89}$$

Note that such approximation is only valid for $|z| < a_3$. The fields at the edge of the cylinder are not properly define. We get,

$$\begin{aligned} \tilde{V}(r,\theta,z) \;\simeq\; & \frac{keN\gamma}{2a_3^2}\int_0^\infty u'\sigma\left(u'\gamma\right) du' \int_0^{2\pi} d\theta' \Big\{ -2z + \\ & (a_3+z)\left[\ln 4\left(a_3^2 - z^2\right) - \ln|\mathbf{u}-\mathbf{u}'|^2\right]\Big\} , \end{aligned} \tag{K.90}$$

thus,

$$\begin{aligned} \tilde{V}(r,\theta,z) \;\simeq\; & \frac{k\pi eN\gamma}{a_3^2}\int_0^\infty u'\sigma\left(u'\gamma\right) du' \left[-2z + (a_3+z)\ln 4\left(a_3^2 - z^2\right)\right] \\ & -\frac{keN\gamma}{2a_3^2}(a_3+z)\int_0^\infty u'\sigma\left(u'\gamma\right) du' \int_0^{2\pi} d\theta' \ln|\mathbf{u}-\mathbf{u}'|^2 . \end{aligned} \tag{K.91}$$

There is only one term which is difficult to integrate in this expression:

$$\int_0^\infty u'\sigma\left(u'\gamma\right)du' \int_0^{2\pi} d\theta' \ln|\mathbf{u}-\mathbf{u}'|^2 \ , \tag{K.92}$$

in which

$$|\mathbf{u}-\mathbf{u}'|^2 = u^2+u'^2-2uu'\cos\left(\theta-\theta'\right) \ , \tag{K.93}$$

To do the θ' integration, we observe that due to *cylindrical symmetry* the result must be independant of θ. So we can choose the location $\theta = 0$. Then we use (for $b<1$)

$$\int_0^{2\pi} \ln\left(1-b\cos x\right)dx = 2\pi \ln\frac{1+\sqrt{1-b^2}}{2} \ . \tag{K.94}$$

Writing,

$$|\mathbf{u}-\mathbf{u}'|^2 = \left(u^2+u'^2\right)\left(1-\frac{2uu'}{u^2+u'^2}\cos\theta'\right) \ , \tag{K.95}$$

we see that

$$b = \frac{2uu'}{u^2+u'^2} \ , \tag{K.96}$$

and,

$$\frac{1+\sqrt{1-b^2}}{2} = \frac{u^2+u'^2+|u^2-u'^2|}{2(u^2+u'^2)} \ , \tag{K.97}$$

$$\begin{aligned}
\int_0^{2\pi} d\theta \ln|\mathbf{u}-\mathbf{u}'|^2 &= \int_0^{2\pi} d\theta \left[\ln\left(u^2+u'^2\right)+\ln\left(1-\frac{2uu'}{u^2+u'^2}\cos\theta'\right)\right] \ , \\
&= 2\pi\left[\ln\left(u^2+u'^2\right)+\ln\left(\frac{u^2+u'^2+|u^2-u'^2|}{2(u^2+u'^2)}\right)\right] \ , \\
&= 2\pi\ln\left(\frac{u^2+u'^2+|u^2-u'^2|}{2}\right) \ ,
\end{aligned} \tag{K.98}$$

Thus if $u'<u$,

$$\int_0^{2\pi} d\theta \ln|\mathbf{u}-\mathbf{u}'|^2 = 2\pi\ln u^2, \tag{K.99}$$

while if $u<u'$,

$$\int_0^{2\pi} d\theta \ln|\mathbf{u}-\mathbf{u}'|^2 = 2\pi\ln u'^2 \ , \tag{K.100}$$

Then

$$\int_0^\infty u'\sigma\left(u'\gamma\right)du' \int_0^{2\pi} d\theta' \ln\left|\mathbf{u}-\mathbf{u}'\right|^2 = 2\pi\Bigg(\ln u^2 \int_0^u u'\sigma\left(u'\gamma\right)du' + \int_u^\infty u' \ln u'^2 \sigma\left(u'\gamma\right)du'\Bigg) , \quad \text{(K.101)}$$

and

$$\boxed{\begin{aligned}\tilde{V}(r,\theta,z) \simeq \frac{k\pi eN\gamma}{a_3^2}\Bigg\{ &\int_0^\infty u'\sigma\left(u'\gamma\right)du' \left[-2z+(a_3+z)\ln 4\left(a_3^2-z^2\right)\right] \\ &-(a_3+z)\left(\ln u^2 \int_0^u u'\sigma\left(u'\gamma\right)du' + \int_u^\infty u' \ln u'^2 \sigma\left(u'\gamma\right)du'\right)\Bigg\}\end{aligned}} \quad \text{(K.102)}$$

K.3.1 Hollow radial density profile

For a ring beam of radius a, we have

$$\sigma(r) = \frac{\delta(r-a)}{2\pi a} , \quad \text{(K.103)}$$

Fields inside the beam

For $u < a/\gamma$,

$$\ln u^2 \int_0^u u'\sigma\left(u'\gamma\right)du' = 0 , \quad \text{(K.104)}$$

$$\int_u^\infty u' \ln u'^2 \sigma\left(u'\gamma\right)du' \equiv (2\pi a)^{-1} \int_0^\infty \delta(u'\gamma - a) u' \ln u'^2 du' , \quad \text{(K.105)}$$

$$= (2\pi\gamma^2)^{-1} \ln\frac{a^2}{\gamma^2} , \quad \text{(K.106)}$$

which gives,

$$\tilde{V}(r,\theta,z) \simeq \frac{keN}{2\gamma a_3^2}\left\{-2z+(a_3+z)\left[\ln 4\left(a_3^2-z^2\right) - \ln a^2 + \ln\gamma^2\right]\right\} . \quad \text{(K.107)}$$

The longitudinal electric field in the *rest frame* and in terms of lab. coordinates is

$$\tilde{E}_z(r,\theta,z) = -\frac{\partial\tilde{V}}{\partial\tilde{z}} = -\frac{1}{\gamma}\frac{\partial\tilde{V}}{\partial z} , \tag{K.108}$$

$$\simeq \frac{keN}{\gamma^2 a_3^2}\left(\frac{a_3}{a_3-z} - \ln 2\sqrt{a_3^2-z^2} + \ln a - \ln\gamma\right) , \tag{K.109}$$

$$\simeq \frac{keN}{\gamma^2 a_3^2}\left[\frac{a_3}{a_3-z} - \ln\left(\frac{2\gamma\sqrt{a_3^2-z^2}}{a}\right)\right] , \tag{K.110}$$

that is,

$$\boxed{\tilde{E}_z(r,\theta,z) \simeq -\frac{2k\lambda'(z)}{\gamma^2}\left[\ln\left(\frac{2\gamma\sqrt{a_3^2-z^2}}{a}\right) - \frac{a_3}{a_3-z}\right]} \tag{K.111}$$

The transverse electric field $\tilde{E}_r(r,\theta,z)$ is zero. On axis, and at the center of the bunch, $z=0$, we have,

$$\tilde{E}_z(0,\theta,0) \simeq -\frac{2k\lambda'(0)}{\gamma^2}\left[\ln\left(\frac{2\gamma a_3}{a}\right) - 1\right] . \tag{K.112}$$

Fields outside the beam

For $u > a/\gamma$

$$\int_u^\infty u' \ln u'^2 \sigma\left(u'\gamma\right) du' = 0 , \tag{K.113}$$

and,

$$\ln u^2 \int_0^u u'\sigma\left(u'\gamma\right) du' \equiv (2\pi a)^{-1} \ln u^2 \int_0^\infty \delta(u'\gamma - a) u' du' , \tag{K.114}$$

$$= (2\pi\gamma^2)^{-1} \ln u^2 , \tag{K.115}$$

giving,

$$\tilde{V}(r,\theta,z) \simeq \frac{keN}{2\gamma a_3^2}\left\{-2z + (a_3+z)\left[\ln 4\left(a_3^2-z^2\right) - \ln u^2\right]\right\} . \tag{K.116}$$

The longitudinal electric field is

$$\tilde{E}_z(r,\theta,z) = -\frac{1}{\gamma}\frac{\partial \tilde{V}}{\partial z} \simeq \frac{keN}{\gamma^2 a_3^2}\left(\frac{a_3}{a_3-z} - \ln 2\sqrt{a_3^2-z^2} - \ln u\right) , \quad \text{(K.117)}$$

$$\simeq \frac{keN}{\gamma^2 a_3^2}\left[\frac{a_3}{a_3-z} - \ln\left(\frac{2\gamma\sqrt{a_3^2-z^2}}{r}\right)\right] , \quad \text{(K.118)}$$

i.e.,

$$\boxed{\tilde{E}_z(r,\theta,z) \simeq -\frac{2k\lambda'(z)}{\gamma^2}\left[\ln\left(\frac{2\gamma\sqrt{a_3^2-z^2}}{r}\right) - \frac{a_3}{a_3-z}\right]} \quad \text{(K.119)}$$

The transverse electric field is

$$\tilde{E}_r(r,\theta,z) = -\frac{\partial \tilde{V}}{\partial \tilde{r}} = -\frac{1}{\gamma}\frac{\partial \tilde{V}}{\partial u} \simeq \frac{keN}{\gamma^2 a_3^2}\frac{a_3+z}{u} , \quad \text{(K.120)}$$

$$\simeq \frac{keN}{\gamma a_3^2}\frac{a_3+z}{r} , \quad \text{(K.121)}$$

which is,

$$\boxed{\tilde{E}_r(r,\theta,z) \simeq \frac{2k\lambda(z)}{\gamma r}} \quad \text{(K.122)}$$

K.3.2 Uniform radial density profile

For a uniform beam of radius a, we have, for $r < a$,

$$\sigma(r) = \frac{1}{\pi a^2} . \quad \text{(K.123)}$$

Fields inside the beam

For $u < a/\gamma$,

$$\ln u^2 \int_0^u u'\sigma\left(u'\gamma\right) du' = (\pi a^2)^{-1} \ln u^2 \int_0^u u' du' , \quad \text{(K.124)}$$

$$= (2\pi a^2)^{-1} u^2 \ln u^2 ,$$

and,

$$\begin{aligned}\int_u^\infty u' \ln u'^2 \sigma\left(u'\gamma\right) du' &= (\pi a^2)^{-1} \int_u^{a/\gamma} u' \ln u'^2 du' \,, \\ &= (2\pi a^2\gamma^2)^{-1} \left[u^2\left(1 - \ln\frac{u^2}{\gamma^2}\right) - a^2\left(1 - \ln\frac{a^2}{\gamma^2}\right)\right] \,,\end{aligned} \tag{K.125}$$

giving,

$$\tilde{V}(r,\theta,z) \simeq \frac{keN}{2\gamma a_3^2}\left\{-2z + (a_3+z)\left[\ln 4\left(a_3^2 - z^2\right) - \ln\frac{a^2}{\gamma^2} - \frac{u^2\gamma^2}{a^2} + 1\right]\right\} \,, \tag{K.126}$$

which allows us to deduce the expression for the longitudinal electric field,

$$\tilde{E}_z(r,\theta,z) = -\frac{1}{\gamma}\frac{\partial\tilde{V}}{\partial z} \simeq \frac{keN}{\gamma^2 a_3^2}\left[\frac{a_3}{a_3 - z} - \ln\left(\frac{2\gamma\sqrt{a_3^2 - z^2}}{a}\right) - \frac{1}{2}\left(1 - \frac{r^2}{a^2}\right)\right] \,, \tag{K.127}$$

i.e.,

$$\boxed{\tilde{E}_z(r,\theta,z) \simeq -\frac{2k\lambda'(z)}{\gamma^2}\left[\ln\left(\frac{2\gamma\sqrt{a_3^2 - z^2}}{a}\right) - \frac{a_3}{a_3 - z} + \frac{1}{2}\left(1 - \frac{r^2}{a^2}\right)\right]} \tag{K.128}$$

The transverse electric field is

$$\tilde{E}_r(r,\theta,z) = -\frac{1}{\gamma}\frac{\partial\tilde{V}}{\partial u} \simeq \frac{keN}{\gamma^2 a^2 a_3^2} r(a_3 + z) \,, \tag{K.129}$$

which is equivalent to,

$$\boxed{\tilde{E}_r(r,\theta,z) \simeq \frac{2k\lambda(z)r}{\gamma a^2}} \tag{K.130}$$

On axis at $r = 0$, and at the center of the bunch, $z = 0$, we have

$$\tilde{E}_z(0,\theta,0) \simeq -\frac{2k\lambda'(0)}{\gamma^2}\left[\ln\left(\frac{2\gamma a_3}{a}\right) - \frac{1}{2}\right] \,. \tag{K.131}$$

Fields outside the beam

For $u > a/\gamma$

$$\int_u^\infty u' \ln u'^2 \sigma\left(u'\gamma\right) du' = 0 \,, \tag{K.132}$$

$$\begin{aligned} \ln u^2 \int_0^u u' \sigma\left(u'\gamma\right) du' &= \left(\pi a^2\right)^{-1} \ln u^2 \int_0^{a/\gamma} u' du' \\ &= \frac{1}{2\pi\gamma^2} \ln u^2 \,, \end{aligned} \tag{K.133}$$

and,

$$\tilde{V}(r,\theta,z) \simeq \frac{keN}{2\gamma a_3^2} \left\{-2z + (a_3+z)\left[\ln 4\left(a_3^2 - z^2\right) - \ln u^2\right]\right\} \,. \tag{K.134}$$

The longitudinal electric field is

$$\tilde{E}_z(r,\theta,z) = -\frac{1}{\gamma}\frac{\partial \tilde{V}}{\partial z} \simeq \frac{keN}{\gamma^2 a_3^2}\left(\frac{a_3}{a_3 - z} - \ln 2\sqrt{a_3^2 - z^2} - \ln u\right) \,, \tag{K.135}$$

$$\simeq \frac{keN}{\gamma^2 a_3^2}\left[\frac{a_3}{a_3 - z} - \ln\left(\frac{2\gamma\sqrt{a_3^2 - z^2}}{r}\right)\right] \,, \tag{K.136}$$

that is,

$$\boxed{\tilde{E}_z(r,\theta,z) \simeq -\frac{2k\lambda'(z)}{\gamma^2}\left[\ln\left(\frac{2\gamma\sqrt{a_3^2 - z^2}}{r}\right) - \frac{a_3}{a_3 - z}\right]} \tag{K.137}$$

The transverse electric field is

$$\tilde{E}_r(r,\theta,z) = -\frac{\partial \tilde{V}}{\partial \tilde{r}} = -\frac{1}{\gamma}\frac{\partial \tilde{V}}{\partial u} \simeq \frac{keN}{\gamma^2 a_3^2}\frac{a_3 + z}{u} \,, \tag{K.138}$$

$$\simeq \frac{keN}{\gamma a_3^2}\frac{a_3 + z}{r} \,, \tag{K.139}$$

i.e.,

$$\boxed{\tilde{E}_r(r,\theta,z) \simeq \frac{2k\lambda(z)}{\gamma r}} \tag{K.140}$$

Appendix L

Relativistic N-body dynamics

Contents

L.1 Equation of motion

For systems of point-particles interacting *via* there mutual electromagnetic fields, the equations of motion are

$$\frac{d\mathbf{p}_i}{dt} = q \sum_{j \neq i} \left[\mathbf{E}_j(\mathbf{r}_i, t) + \frac{\mathbf{v}_i}{c} \times \mathbf{B}_j(\mathbf{r}_i, t) \right] \ , \tag{L.1}$$

where $\mathbf{E}_j$ and $\mathbf{B}_j$ are the electromagnetic fields due to the motion of macroparticle j. In the Lorentz force, the condition $j \neq i$ is necessary to exclude the self-force. The fields satisfy the Maxwell's equations (in CGS units):

$$\frac{\partial \mathbf{E}_i}{\partial t} \ = \ c\nabla \times \mathbf{B}_i - 4\pi \mathbf{j}_i \ , \tag{L.2}$$

and,

$$\frac{\partial \mathbf{B}_i}{\partial t} \ = \ -c\nabla \times \mathbf{E}_i \ , \tag{L.3}$$

where the current $\mathbf{j}_i$ is given by

$$\mathbf{j}_i(\mathbf{r}, t) = q\mathbf{v}_i \delta^3 \left(\mathbf{r} - \mathbf{r}_i(t) \right) \ . \tag{L.4}$$

The solution of Maxwell's equations is well known [79, 81, 82]:

$$\mathbf{E}_i(\mathbf{r}) \ = \ q \left[\frac{\mathbf{n} - \beta_i}{\gamma_i^2 \left(1 - \mathbf{n} \cdot \beta_i\right)^3 R^2} \right]_{RET} + \frac{q}{c} \left[\frac{\mathbf{n} \times \left\{ (\mathbf{n} - \beta_i) \times \dot{\beta}_i \right\}}{\left(1 - \mathbf{n} \cdot \beta_i\right)^3 R} \right]_{RET} \ , \tag{L.5}$$

and,

$$\mathbf{B}_i(\mathbf{r}) \ = \ \left[\mathbf{n} \times \mathbf{E}_i \right]_{RET} \ , \tag{L.6}$$

where $R\mathbf{n} = \mathbf{r} - \mathbf{r}_i$ and the subscript "RET" indicates that the quantities in the brackets are to be evaluated at the retarded time $t_{RET} = t - R/c$. Note that the definition of the retarded time is implicit since R depends on time; more explicitly

we have

$$t_{RET} = t - |\mathbf{r} - \mathbf{r}_i(t_{RET})|/c \tag{L.7}$$

L.2 Energy conservation

The expression for the system energy is what one would expect with except that energy of the self-field must be excluded:

$$\mathcal{E} = \sum_i mc^2\gamma_i + \frac{1}{8\pi}\sum_{i,j\neq i}\int_V d^3\mathbf{r}\,(\mathbf{E}_i\cdot\mathbf{E}_j + \mathbf{B}_i\cdot\mathbf{B}_j)\ . \tag{L.8}$$

It is straighforward calculation to show that energy is conserved. To begin, note

$$mc^2\frac{d\gamma_i}{dt} = \frac{\mathbf{p}_i}{m\gamma_i}\cdot\frac{d\mathbf{p}_i}{dt} = q\sum_{j\neq i}\mathbf{v}_i\cdot\left[\mathbf{E}_j(\mathbf{r}_i) + \frac{\mathbf{v}_i}{c}\times\mathbf{B}_j(\mathbf{r}_i)\right] = q\sum_{j\neq i}\mathbf{v}_i\cdot\mathbf{E}_j(\mathbf{r}_i)\ . \tag{L.9}$$

Thus

$$\begin{aligned}
\frac{d\mathcal{E}}{dt} &= q\sum_{i,j\neq i}\mathbf{v}_i\cdot\mathbf{E}_j(\mathbf{r}_i) + \frac{1}{4\pi}\sum_{i,j\neq i}\int_V d^3\mathbf{r}\left(\mathbf{E}_j\cdot\frac{\partial\mathbf{E}_i}{\partial t} + \mathbf{B}_j\cdot\frac{\partial\mathbf{B}_i}{\partial t}\right)\ , \\
&= q\sum_{i,j\neq i}\mathbf{v}_i\cdot\mathbf{E}_j(\mathbf{r}_i) + \frac{c}{4\pi}\sum_{i,j\neq i}\int_V d^3\mathbf{r}\left[\mathbf{E}_j\cdot(\nabla\times\mathbf{B}_i - 4\pi\mathbf{j}_i) + \mathbf{B}_j\cdot(-\nabla\times\mathbf{E}_i)\right]\ , \\
&= q\sum_{i,j\neq i}\mathbf{v}_i\cdot\mathbf{E}_j(\mathbf{r}_i) - \sum_{i,j\neq i}\int d^3\mathbf{r}\ \mathbf{E}_j\cdot\mathbf{j}_i - \frac{c}{4\pi}\sum_{i,j\neq i}\int_V d^3\mathbf{r}\ \nabla\cdot(\mathbf{E}_j\times\mathbf{B}_i)\ ,
\end{aligned} \tag{L.10}$$

and,

$$\begin{aligned}
\frac{d\mathcal{E}}{dt} &= q\sum_{i,j\neq i}\mathbf{v}_i\cdot\mathbf{E}_j(\mathbf{r}_i) - \sum_{i,j\neq i}\int d^3\mathbf{r}\ \delta\left(\mathbf{r}-\mathbf{r}_i(t)\right)\mathbf{E}_j\cdot\mathbf{v}_i - \frac{c}{4\pi}\sum_{i,j\neq i}\oint_S d\mathbf{A}\cdot(\mathbf{E}_j\times\mathbf{B}_i)\ , \\
&= q\sum_{i,j\neq i}\mathbf{v}_i\cdot\mathbf{E}_j(\mathbf{r}_i) - \sum_{i,j\neq i}\mathbf{E}_j(\mathbf{r}_i)\cdot\mathbf{v}_i - \frac{c}{4\pi}\sum_{i,j\neq i}\oint_S d\mathbf{A}\cdot(\mathbf{E}_j\times\mathbf{B}_i)\ , \\
&= -\frac{c}{4\pi}\sum_{i,j\neq i}\oint d\mathbf{A}\cdot(\mathbf{E}_j\times\mathbf{B}_i)\ .
\end{aligned} \tag{L.11}$$

This is equivalent to a continuity equation for the energy, i.e., the variation over time of the energy inside the volume V is equal to the energy which went thought the

surface S enclosing the volume V. The latter corresponds to radiation energy. The energy conservation law may be recasted in the following way which is suitable for code benchmarking,

$$\boxed{\mathcal{E}' = \mathcal{E} + \frac{c}{4\pi} \sum_{i,j\neq i} \int_0^t dt \oint_S d\mathbf{A} \cdot (\mathbf{E}_j \times \mathbf{B}_i) = \text{cste}} \tag{L.12}$$

L.3 Relativistic two-body problem

The relativistic two-body problem is an interesting example with may be used as a mean to benchmark N-body code using Lienard-Wiechert fields [83]. Assuming initially ($t = 0$) two macroparticles of equal charge, mass and velocity following a straight line path and heading toward each others, the two macroparticles are going to rapidly decelerate up to a minimum distance of approach where they will turn around and go back to infinite separation. During the deceleration-acceleration process they will emit radiation. At $t = 0$ the energy is simply the sum of kinetic energies

$$\mathcal{E}'/(mc^2) = 2\gamma_0 \ , \tag{L.13}$$

where $m = Nm_e$ is the rest mass of the macroparticle and m_e the electron rest mass. At $t \to \infty$ we have kinetic plus radiation field, i.e., the energy conservation law yields

$$\gamma_f = \gamma_0 + \frac{1}{8\pi N m_e c} \left| \int_0^\infty dt \oint_S d\mathbf{A} \cdot (\mathbf{E}_1 \times \mathbf{B}_2 + \mathbf{E}_2 \times \mathbf{B}_1) \right| \ , \tag{L.14}$$

where $\gamma_f \equiv \gamma(t \to \infty)$. The interesting feature about this problem is that after the collision ($t \to \infty$), the macroparticles may gain a substantial amount of kinetic energy, even though the total (field plus particle) energy is conserved. This is due to the fact that the (radiation) fields $\mathbf{E}_1$ and $\mathbf{E}_2$ (identically $\mathbf{B}_1$ and $\mathbf{B}_2$) are in opposite directions leading to a negative interaction energy (time integrated Poynting flux).

Note that Eq. (L.12) characterize an exact (mathematical) conservation law but make very little sense physically when radiation is a significant effect, i.e., in this case a correct treatment of the problem using macroparticles would require inclusion of *radiation reaction* [82, 97] (a simpler derivation may be found in Ref. [81]).

Figure L.1(a) shows the burst of radiation emitted after the collision of two

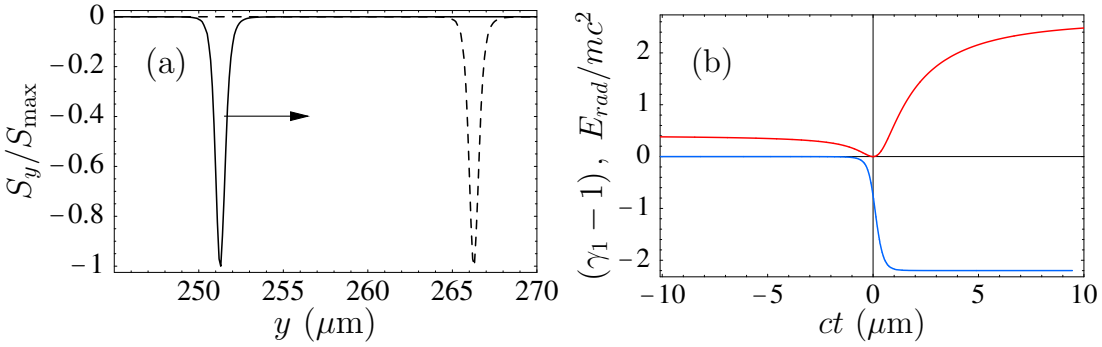

Figure L.1: (a) y-component of the interaction Poynting vector [Eq. L.15] is plotted at $ct = 251.5$ μm (dark solid line) and $ct = 266.5$ μm (dashed line) after the collision, showing that the radiation burst propagates outward with a negative magnitude. (b) Normalized kinetic energy $(\gamma_1 - 1)$ of macroparticle 1 (red solid line) and the corresponding time integrated [interaction] Poynting flux [Eq. L.16] across a sphere encompassing the interaction region (blue solid line).

macroparticles of charge $Q = 100$ pC and initial relativistic factor $\gamma_0 = \sqrt{2}$. The normalized Poynting vector $\mathbf{S}/S_{max}$ is plotted, where

$$\mathbf{S} = \frac{c}{4\pi} \left(\mathbf{E}_1 \times \mathbf{B}_2 + \mathbf{E}_2 \times \mathbf{B}_1 \right) \ , \tag{L.15}$$

for the times $ct = 251.5$ μm (dark solid line) and $ct = 266.5$ μm (dashed line) after the collision, i.e, when the particles reach the distance of closest approach, which is found to be $d_{\min} \simeq 1.36$ μm. The radiation propagates at the speed of light, as expected, outward and with a *negative* magnitude. In this example, the macroparticles propagate along the x-axis which implies that the Poynting vector is maximum along the y-axis.

Figure L.1(b) shows the change in the normalized kinetic energy $(\gamma_i - 1)$ of the macroparticles as a function of time (red solid line) and the corresponding time integrated interaction Poynting flux *per macroparticle* (blue solid line),

$$E_{\rm rad} = \frac{1}{2} \int_0^\infty dt \oint_S d\mathbf{A} \cdot \mathbf{S} \ . \tag{L.16}$$

The numerical integration shown in Fig. L.1 for both the equations of motion Eq. (L.1) together with Eqs (L.5)-(L.6) and the calculation of the radiated interaction energy,

Eq. (L.16), provided an estimate for the value of γ_f with a relative error on the order 10^{-4}.

References

[**1**] T.H. Maiman. Stimulated optical radiation in ruby. *Nature*, 187:493, 1960.

[**2**] http://www.nuc.berkeley.edu/fusion.

[**3**] W.J. Hogan. *Energy from Inertial Fusion*. International Atomic Energy Agency, Vienna, Austria, 1995.

[**4**] A. Yariv. *Quantum Electronics*. Wiley, 1989.

[**5**] E. Esarey, A. Ting, P. Sprangle, D. Umstadter, and X. Liu. Nonlinear analysis of relativistic harmonic generation by intense lasers in plasmas. *IEEE Trans. Plasma Sci.*, 21(1):95–104, 1993.

[**6**] E. Esarey, B. A. Shadwick, P. Catravas, and W. P. Leemans. Synchrotron radiation from electron beams in plasma-focusing channels. *Phys. Rev. E*, 65:056505, 2002.

[**7**] W. P. Leemans, C. G. R. Geddes, J. Faure, Cs. Tóth, J. van Tilborg, C.B. Schroeder, E. Esarey, G. Fubiani, D. Auerbach, B. Marcelis, M. A. Carnahan, R. A. Kaindl, J. Byrd, and M. C. Marin. Observation of terahertz emission from a laser-plasma accelerated electron bunch crossing a plasma-vaccum boundary. *Phys. Rev. Lett.*, 91(7):074802, 2003.

[**8**] W. P. Leemans, J. van Tilborg, J. Faure, C. G. R. Geddes, Cs. Tóth, C. B. Schroeder, E. Esarey, and G. Fubiani. Terahertz radiation from laser accelerated electron bunches. *Phys. Plasmas*, 11(5):2899–2906, May 2004.

[**9**] E. Esarey, P. Sprangle, J. Krall, and A. Ting. Overview of plasma-based accelerator concepts. *IEEE Trans. Plasma Sci.*, 24(2):252–288, 1996.

[**10**] C.B. Schroeder. *Plasma-Based Accelerator Structures*. PhD thesis, University of California at Berkeley, 1999. LBNL report # 44779.

[**11**] C. G. R. Geddes. *Plasma Channel Guided Laser Wakefield Accelerator*. PhD thesis, University of California at Berkeley, 2005.

[**12**] S. Eliezer. *The interaction of high-power lasers with plasmas*. Institute of Physics Publishing, 2002.

[**13**] S.-W. Bahk, P. Rousseau, T. A. Planchon, V. Chvykov, G. Kalintchenko, A. Maksimchuk, G. A. Mourou, and V. Yanovsky. Generation and characterization of the highest laser intensities (10^{22} w/cm^2). *Opt. Lett.*, 29(24):2837–2839, December 2004.

[**14**] D. Strickland and G. Mourou. Compression of amplified chirped optical pulses. *Opt. Comm.*, 56:219–221, 1985.

[**15**] T. Tajima and J. M. Dawson. Laser electron accelerator. *Phys. Rev. Lett.*, 43(4):267, 1979.

[**16**] V. Malka, S. Fritzler, E. Lefebvre, M.-M. Aleonard, F. Burgy, J.-P. Chambaret, J.-F. Chemin, K. Krushelnick, G. Malka, S. P. D. Mangles, Z. Najmudin, M. Pittman, J.-P. Rousseau, J.-N. Scheurer, B. Walton, and A. E. Dangor. Electron acceleration by a wake field forced by an intense ultrashort laser pulse. *Science*, 298:1596–1600, November 2002.

[**17**] A. Pukhov and J. Meyer ter vehn. Laser wake field acceleration: the highly non-linear broken-wave regime. *Appl. Phys. B*, 74:355–361, 2002.

[**18**] D. Umstadter, J. K. Kim, and E. Dodd. Laser injection of ultrashort electron pulses into wakefield plasma waves. *Phys. Rev. Lett.*, 76(12):2073–2076, 1996.

[**19**] E. Esarey, R. F. Hubbard, W. P. Leemans, A. Ting, and P. Sprangle. Electron injection into plasma wake fields by colliding laser pulses. *Phys. Rev. Lett.*, 79(14):2682–2685, 1997.

[**20**] C. B. Schroeder, P. B. Lee, J. S. Wurtele, E. Esarey, and W. P. Leemans. Generation of ultrashort electron bunches by colliding laser pulses. *Phys. Rev. E*, 59(5):6037–6047, 1999.

[**21**] G. Fubiani, E. Esarey, C. B. Schroeder, and W. P. Leemans. Beat wave injection of electrons into plasma waves using two interfering laser pulses. *Phys. Rev. E*, 70(1):016402, 2004.

[**22**] G. Fubiani, E. Esarey, K. Nakamura, C.B. Schroeder, and W. P. Leemans. Enhancement of laser injection methods by plasma density gradients. In *Advanced Accelerator Concepts*, volume 737, pages 887–893. AIP Conf. Proc, 2004.

[**23**] C. Gahn, G. D. Tsakiris, A. Pukhov, J. Meyer-ter-Vehn, G. Pretzler, P. Thirolf, D. Habs, and K.J. Witte. Multi-mev electron beam generation by direct laser

acceleration in high-density plasma channels. *Phys. Rev. Lett.*, 83(23):4772–4775, December 1999.

[**24**] W. P. Leemans, D. Rodgers, P. E. Catravas, C. G. R. Geddes, G. Fubiani, E. Esarey, B. A. Shadwick, R. Donahue, and A. Smith. Gamma-neutron activation experiments using laser wakefield accelerators. *Phys. Plasmas*, 8(5):2510–2516, May 2001.

[**25**] T. Hosokai, K. Kinoshita, A. Zhidkov, K. Nakamura, T. Watanabe, H. Kotaki, M. Kando, K. Nakajima, and M. Uesaka. Effect of a laser prepulse on a narrow-cone ejection of mev electrons from a gas jet irradiated by an ultrashort laser pulse. *Phys. Rev. E*, 67:036407, 2003.

[**26**] T. Hosokai, K. Kinoshita, A. Zhidkov, K. Nakamura, H. Kotaki, M. Kando, K. Nakajima, and M. Uesaka. Refraction effects on the cavity formation and interaction of an intense ultra-short laser pulse with a gas jet. *Phys. Plasmas*, 11(10):L57–L60, October 2004.

[**27**] C. I. Moore, A. Ting, K. Krushelnick, E. Esarey, R. F. Hubbard, B. Hafizi, H. R. Burris, C. Manka, and P. Sprangle. Electron trapping in self-modulated laser wakefields by raman backscatter. *Phys. Rev. Lett.*, 79(20):3909–3912, November 1997.

[**28**] A. Ting, C. I. Moore, K. Krushelnick, C. Manka, E. Esarey, P. Sprangle, R. F. Hubbard, H. R. Burris, R. Fisher, and M. Baine. Plasma wakefield generation and elecron acceleration in a self-modulated laser wakefield accelerator experiment. *Phys. Plasmas*, 4(5):1889–1899, May 1997.

[**29**] A. Modena, Z. Najmudin, A. E. Dangor, C. E. Clayton, K. A. Marsh, C. Joshi, V. Malka, C. B. Darrow, C. Danson, D. Neely, and F. N. Walsh. Electron acceleration from the breaking of relativistic plasma waves. *Nature*, 377:606–608, 1995.

[**30**] R. Wagner, S.-Y. Chen, A. Maksimchuk, and D. Umstadter. Electron acceleration by a laser wakefield in a relativistically self-guided channel. *Phys. Rev. Lett.*, 78(16):3125–3128, April 1997.

[**31**] X. Wang, M. Krishnan, N. Saleh, H. Wang, and D. Umstadter. Electron acceleration and the propagation of ultrashort high-intensity laser pulses in plasmas. *Phys. Rev. Lett.*, 84(23):5324–5327, June 2000.

[**32**] S. P. D. Mangles, C. D. Murphy, Z. Najmudin, A. G. R. Thomas, J. L. Collier, A. E. Dangor, E. J. Divall, P. S. Fosterand J. G. Gallacher, C. J. Hooker, D. A. Jaroszynski, A. J. Langley, W. B. Mori, P. A. Norreys, F. S. Tsung, R. Viskup,

B. R. Walton, and K. Krushelnick. Monoenergetic beams of relativistic electrons from intense laser-plasma interactions. *Nature*, 431:538–541, 2004.

[**33**] C.G.R. Geddes, Cs. Toth, J. van Tilborg, E. Esarey, C.B. Schroeder, D. Bruhwiler, C. Nieter, J. Cary, and W.P. Leemans. High quality electron beams from a laser wakefield accelerator using plasma channel guiding. *Nature*, 431:538–541, 2004.

[**34**] J. Faure, Y. Glinec, A. Pukhov, S. Kiselev, S. Gordienko, E. Lefebvre, J.P. Rousseau, F. Burgy, and V. Malka. A laser-plasma accelerator producing monoenergetic electron beams. *Nature*, 431:541–544, 2004.

[**35**] G. Fubiani, E. Esarey, and W. P. Leemans. Studies of space-charge effects in ultrashort electron bunches. In P. Colestock and S. Kelly, editors, *Advanced Accelerator Concepts*, volume 569, pages 423–435. AIP Conf. Proc, 2001.

[**36**] G. Fubiani, G. Dugan, W. P. Leemans, E. Esarey, and J. L. Bobin. Semi-analytical 6d space charge model for dense electron bunches with large energy spreads. In C. E. Clayton and P. Muggli, editors, *Advanced Accelerator Concepts*, volume 647, pages 203–212. AIP Conf. Proc, 2002.

[**37**] H. Ruhl. Collective super-intense laser-plasma interaction. Habilitation thesis, Technischen Universität Darmstadt, Germany, 2000.

[**38**] L. Gorbunov, P. Mora, and T. M. Antonsen. Magnetic field of a plasma wake driven by a laser pulse. *Phys. Rev. Lett.*, 76:2495, 1996.

[**39**] L. Gorbunov, P. Mora, and T. M. Antonsen. Quasistatic magnetic field generated by a short laser pulse in an underdense plasma. *Phys. Plasmas*, 4(12):4358–4368, December 1997.

[**40**] N. E. Andreev, L. M. Gorbunov, V.I. Kirsanov, A. A. Pogosova, and R. R. Ramazashvili. The theory of laser self-resonant wake field excitation. *Phys. Scripta*, 49:101–109, 1994.

[**41**] A. H. Nayheh. *Perturbation methods*. John Wiley & Sons, 2000.

[**42**] V.I. Berezhiani, S. M. Mahajan, and N. L. Shatashvili. Theory of magnetic field generation by relativistic strong laser radiation. *Phys. Rev. E*, 55:1082–1095, 1997.

[**43**] P. Sprangle, E. Esarey, and A. Ting. Nonlinear interaction of intense laser pulses in plasmas. *Phys. Rev. A*, 41(8):4463–4469, 1990.

[**44**] R. G. Hemker, K.-C. Tzeng, W. B. Mori, C. E. Clayton, and T. Katsouleas. Computer simulations of cathodeless, high-brightness electron-beam production by multiple laser beams in plasmas. *Phys. Rev. E*, 57(5):5920–5928, 1998.

[**45**] S. Bulanov, N. Naumova, F. Pegoraro, and J. Sakai. Particle injection into the wave acceleration phase due to nonlinear wake wave breaking. *Phys. Rev. E*, 58(5):R5257–R5260, 1998.

[**46**] E. Esarey, C. B. Schroeder, W. P. Leemans, and B. Hafizi. Laser-induced electron trapping in plasma-based accelerators. *Phys. Plasmas*, 6(5):2262–2268, May 1999.

[**47**] J. Krall, E. Esarey, P. Sprangle, and G. Joyce. Propagation of radius-tailored laser pulses over extended distances in a uniform plasma. *Phys. Plasmas*, 1(5):1738–1743, 1994.

[**48**] W. P. Leemans, P. Catravas, E. Esarey, C. G. R. Geddes, C. Toth, R. Trines, C. B. Schroeder, B. A. Shadwick, J. van Tilborg, and J. Faure. Electron-yield enhancement in a laser-wakefield accelerator driven by asymmetric laser pulses accelerator driven by asymmetric laser pulses. *Phys. Rev. Lett.*, 89:174802, 2002.

[**49**] D. Gordon, K.-C. Tzeng, C. E. Clayton, A. E. Dangor, V. Malka, K. A. Marsh, A. Modena, W. B. Mori, P. Muggli, Z. Najmudin, D. Neely, C. Danson, and C. Joshi. Observation of electron energies beyond the linear dephasing limit from a laser-excited relativistic plasma wave. *Phys. Rev. Lett.*, 80(10):2133–2136, March 1998.

[**50**] E. Esarey, B. Hafizi, R. Hubbard, and A. Ting. Trapping and acceleration in self-modulated laser wakefields. *Phys. Rev. Lett.*, 80(25):5552–5555, 1998.

[**51**] M. Uesaka. *Femtosecond Beam Science*. Imperial College Press, 2005.

[**52**] E. Esarey and W. P. Leemans. Non-paraxial propagation of ultrashort laser pulses in plasma channels. *Phys. Rev. E*, 59:1082–1095, 1999.

[**53**] E. Esarey, P. Sprangle, J. Krall, and A. Ting. Self-focusing and guiding of short laser pulses in ionizing gases and plasmas. *IEEE J. of Quantum Electronics*, 33(11):1879–1914, 1997.

[**54**] C. K. Birdsall and A. B. Langdon. *Plasma Physics Via Computer Simulation*. IOP Publishing, 1998.

[**55**] R. W. Hockney and J. W. Eastwood. *Computer Simulation Using Particles*. McGraw-Hill, 1981.

[**56**] C. Nieter and J.R. Cary. Vorpal: a versatile plasma simulation code. *J. Comp. Phys.*, 196:448, 2004.

[**57**] R. C. Davidson and W. A. McMullin. Stochastic particle instability for an electron motion in combined helical wiggler, radiation, and longitudinal wave fields. *Phys. Rev. A*, 26(1):410–422, 1982.

[**58**] B. V. Chirikov. A universal instability of many-dimensional oscillator systems. *Phys. Rep.*, 52(5):265–379, 1979.

[**59**] A. J. Lichtenberg and M. A. Lieberman. *Regular and Stochastic Motion.* Springer-Verlag, New York, 1983.

[**60**] Z.-M. Sheng, K. Mima, Y. Sentoku, M.S Jovanović, T. Taguchi, J. Zhang, and J. Meyer-ter-Vehn. Stochastic heating and acceleration of electrons in colliding laser fields in plasma. *Phys. Rev. Lett.*, 88(5):055004–1–055004–4, February 2002.

[**61**] R. Keinings and M. E. Jones. Two-dimensional dynamics of the plasma wakefield accelerator. *Phys. Fluids*, 30:252–263, 1987.

[**62**] T. Katsouleas, S. Wilks, P. Chen, J. M. Dawson, and J. J. Su. Beam loading in plasma accelerators. In *Part. Accel. Conf.*, volume 22, pages 81–99, 1987.

[**63**] A.J.W. Reitsma, V.V. Goloviznin, L.P.J. Kamp, and T.J.Schep. Simulation of laser wakefield acceleration of an ultrashort electron bunch. *Phys. Rev. E*, 63:046502, 2001.

[**64**] J. Cary, R. Giacone, C. Nieter, E. Esarey, G. Fubiani, and W. P. Leemans. All-optical beamlet train generation. In *Part. Accel. Conf.*, volume 72, page 490, 2003.

[**65**] W. L. Kruer. *The Physics of Laser Plasma Interactions.* Westview Press, 2003.

[**66**] V. L. Ginzburg. *The propagation of electromagnetic waves in plasmas.* Pergamon Press, 1970.

[**67**] P. Lapostolle, A.M. Lombardi, E. Tanke, S. Valero, R.W. Garnett, and T.P. Wangler. A modified space charge routine for high intensity bunched beams. *NIM A*, 379:21–40, 1996.

[**68**] M. Reiser. *Theory and design of charged particle beams.* Wiley & Sons, 1994.

[**69**] T. P. Wangler. *RF Linear Accelerators.* Wiley & Sons, 1998. pp. 270-272.

[**70**] S. Chandrasekhar. *Ellipsoidal Figures of Equilibrium.* Dover Publications, 1969.

[**71**] A. W. Chao, R. Pitthan, T. Tajima, and D. Yeremian. Space chage dynamics of bright electron beams. *Phys. Rev. STAB*, 6:024201, 2003.

[**72**] B. van der Geer and M. de Loos. *The General Particle Tracer code.* PhD thesis, Technische Universiteit Eindhoven, 2001.

[**73**] F. Sacherer. Rms envelope equations with space charge. *IEEE Trans. Nuc. Sci.*, NS-18:1105, 1971.

[**74**] R. Ryne. Finding matched rms envelopes in rf linacs: A hamiltonian approach. Technical Report LA-UR-95-391, Los Alamos National Laboratory, 1995.

[**75**] P. Lapostolle. Possible emittance increase through filamentation due to space charge in continuous beams. *IEEE Trans. Nuc. Sci.*, NS-18:1101, 1971.

[**76**] J. Qiang, R. D. Ryne, S. Habib, and V. Decyk. An object-oriented parallel particle-in-cell code for beam dynamics simulation in linear accelerators. *J. Comp. Phys.*, 163:434–451, 2000.

[**77**] R. C. Davidson and H. Qin. *Physics of intense charged particle beams in high energy accelerators.* World Scientific, 2001.

[**78**] E. J. Konopinski. *Electromagnetic fields and relativistic particles.* McGraw-Hill, 1981. Page 433.

[**79**] P.C. Clemmow and J.P. Dougherty. *Electrodynamics of Particles and Plasmas.* Addison-Wesley, 1969.

[**80**] F. S. Tsung. Private communication.

[**81**] E. M. Lifshitz and L. D. Landau. *The Classical Theory of Fields.* Pergamon Press, 1987.

[**82**] F. Rohrlich. *Classical Charged Particles.* Addison-Wesley, 1990.

[**83**] J. Huschilt, W. E. Baylis, D. Leiter, and G. Szamosi. Numerical solution to two-body problems in classical electrodynamics: Straight-line motion with retarded fields and no radiation reaction. *Phys. Rev. D*, 10(7):2844–2850, 1973.

[**84**] K. Floettmann. Some basic features of the beam emittance. *Phys. Rev. STAB*, 6:034202, 2003.

[**85**] S. Fritzler, E. Lefebvre, V. Malka, F. Burgly, A. E. Dangor, K. Krushelnick, S. P. D. Mangles, Z. Najmudin, J.-P. Rousseau, and B. Walton. Emittance measurements of a laser-wakefield-accelerated electron beam. *Phys. Rev. Lett.*, 92(16):165006, 2004.

[**86**] J. Cary. Private communication.

[**87**] K. Nakamura, G. Fubiani, C. G. R. Geddes, P. Michel, J. van Tilborg, C. Toth, E. Esarey, C. B. Schroeder, and W. P. Leemans. Laser triggered injection of electrons in a laser wakefield accelerator with the colliding pulse method. In *Advanced Accelerator Concepts*, volume 737, page 901. AIP Conf. Proc, 2004.

[**88**] D. Nicholson. *Introduction to plasma theory.* John Wiley & Sons, 1983.

[**89**] S. Ichimaru. *Statistical plasma physics*, volume 1. Frontiers in Physics, 1992.

[**90**] N. A. Krall and A. W. Trivelpiece. *Principles of Plasma Physics.* San Francisco Press, Inc, 1986.

[**91**] R. D. Hazeltine and F. L. Waelbroeck. *The framework of plasma physics.* Frontiers in Physics, 1998.

[**92**] X. L. Chen and R. N. Sudan. Two-dimensional self-focusing of short intense laser pulse in underdense plasma. *Phys. Fluids B*, 5(4):1336–1348, April 1993.

[**93**] P. Mora and T. M. Antonsen. Kinetic modeling of intense, short laser pulses propagating in tenuous plasmas. *Phys. Plasmas*, 4(1):217–229, January 1997.

[**94**] W. B. Mori. Advances in simulation capability: A path towards modeling 10-100 gev plasma accelerators stages. In *Advanced Accelerator Concepts*, volume 737, pages 75–85. AIP Conf. Proc, 2004.

[**95**] D. F. Gordon, B. Hafizi, R. F. Hubbard, and P. Sprangle. Raman sidescatter in numerical models of short pulse laser plasma interactions. *Phys. Plasmas*, 9(4):1157–1163, April 2002.

[**96**] J. Aharoni. *The Special Theory of Relativity.* Dover publications, 1985. Page 113, 160.

[**97**] J. D. Jackson. *Classical Electrodynamics.* John Wiley & Sons, 1998.

[**98**] J. D. Jackson. Private communication.

[**99**] G. Ripken. Non-linear canonical equations of coupled synchro-betatron motion and their solution within the framework of a non-linear 6-dimensional (symplectic) tracking program for ultra-relativistic protons. Technical Report 85-084, DESY, 1985.

[**100**] D. P. Barber, G. Ripken, and F. Schimdt. A non-linear canonical formalism for the coupled synchro-betatron motion of protons with arbitrary energy. Technical Report 87-036, DESY, 1987.

[**101**] H. Goldstein. *Classical Mechanics*. Addison-Wesley, 1980.

[**102**] I. Borchardt, E. Karantzoulis, H. Mais, and G. Ripken. Calculation of transverse and longitudinal space charge effects within the framework of the fully six-dimensional formalism. Technical Report 88-013, DESY, 1988.